Impact and Cause of Sensitivity Ripple in Radio Astronomy Reflector Antennas

by

William Jacques Cerfonteyn

Thesis presented in partial fulfilment of the requirements for the degree of Doctorate of Philosophy in Electrical and Electronic Engineering in the Faculty of Engineering at Stellenbosch University

Supervisor: Prof. Dirk I.L. de Villiers

December 2023

Stellenbosch University https://scholar.sun.ac.za

Declaration

By submitting this thesis electronically, I declare that the entirety of the work contained therein is my own, original work, that I am the sole author thereof (save to the extent explicitly otherwise stated), that reproduction and publication thereof by Stellenbosch University will not infringe any third party rights and that I have not previously in its entirety or in part submitted it for obtaining any qualification.

Date: December 2023

Copyright © 2023 Stellenbosch University
All rights reserved.

Stellenbosch University https://scholar.sun.ac.za

Abstract

Impact and Cause of Sensitivity Ripple in Radio Astronomy Reflector Antennas

W.J. Cerfonteyn
Department of Electrical and Electronic Engineering,
University of Stellenbosch,
Private Bag X1, Matieland 7602, South Africa.

Thesis: PhD (Electronic)

December 2023

This dissertation presents a study on the impact and cause of the frequency ripple in receiving sensitivity of electrically small reflector antennas. Knowledge of the shape and spectral content of the ripple is important in some radio astronomy applications. Although no alternative to high fidelity sampling of the antenna response, using appropriate computational electromagnetic simulations, was found to accurately characterize the ripple response, the different physical causes of the ripple, and their relative impact on the final response, is comprehensively considered. For next-generation telescopes using wide-band room temperature low-noise amplifiers (LNA), as opposed to extremely cold cryogenic systems, it is shown that the ripple may, in many cases, be reliably ignored during the initial design phase of the system - even for electrically very small systems. It is further illustrated how the ripple characteristics vary as a function of antenna pointing angle, and how, in some cases, the spillover energy onto the hot ground may dominate the effect. To date, such characterizations have been ignored in the literature, and focus has mainly been on the behaviour of the antenna main beam - which normally points at a relatively cold sky.

The dissertation describes that the cause of the frequency ripple in receiving sensitivity is due to non-ideal effects. The sensitivity ripple is influenced only by the ripple in the antenna noise temperature (ANT), and the ripple in the aperture efficiency (AE), while the antenna and LNA are well matched. Furthermore, the ripple of the ANT and AE is determined only by the radiation intensity ripple, which is caused by stray radiation, due to non-ideal effects,

Stellenbosch University https://scholar.sun.ac.za

interfering with the radiation pattern of the full reflector system. Non-ideal radiation or effects occur, when the reflector does not operate ideally, which occurs when the reflector is not infinitely large. The extent of the non-ideal radiation is correlated to the electrical size of the reflector, and thus electrically small reflectors start to diverge more from the ideal radiation proposed by geometric optics.

Furthermore, it is highlighted that the ANT is a function of all directions, and thus the sensitivity is also. This results in certain directions or regions being significantly more important than others for the ANT calculation, in a specific pointing angle. In these regions, the ripple in the radiation pattern is observed in the ripple of the ANT, as expected. Heatmaps are constructed to illuminate these important angles which can be used to gain insight into which non-ideal effects dominate the ripple contribution, and prove the strong dependence of the ANT ripple on the pointing angle. Besides being a function of all directions, the ANT is also a function of many physical parameters. Some of these parameters and their effect on the ANT is investigated.

During the design of radio telescope projects, such as the ngVLA, state-of-the-art estimations for ANT and AE are used. The accuracy of these approximations for ANT and AE are investigated, and characterised. These strategies used for rapid approximation are fast, however, often neglect modeling the ripple. This is because precise calculation of the ripple is often expensive in terms of computation and storage, and usually not necessary during the optimisation phase. The modeling efficiency of these techniques is interrogated, which is a key component in the effective designing of reflectors for radio astronomy.

Physical Optics (PO) simulation strategies are often used in larger radio telescope designs, compared to Method of Moments (MoM). For smaller designs, the accuracy between these techniques becomes important to consider. MoM accounts for more non-ideal effects, compared to PO, and as such models the ripple more accurately. In small designs, the Physical Theory of Diffraction (PTD) can be used in conjunction with PO, to more accurately model the influence of non-ideal effects. There is a breakpoint in frequency, where the ripple modeled with MoM and PO (with PTD) will converge, as the electric size of the reflector increases. These techniques are compared and analysed, to characterise their impact for use in modeling the ripple of the ANT in smaller designs.

Finally in the conclusion, future work is considered, where possible ripple prediction methods are discussed. One of these methods uses a combination of techniques (including Validated Exponential Analysis or VEXPA) to recover a unique signal composition, from a sampling rate under the Nyquist rate. Besides this method, the viability of geometric arguments, or applying

Stellenbosch University https://scholar.sun.ac.za

a preprocessed ripple, is considered for ripple prediction. The exclusive use of far-fields in the sensitivity calculation, without considering the near-field, is also discussed, with suggestions to aid the investigation of its effect.

Stellenbosch University https://scholar.sun.ac.za

Opsomming

Gevolg en Oorsprong van Sensitititeit Riffel in Radio Astronomie Reflektor Antennas

W.J. Cerfonteyn

Departement Elektriese en Elektroniese Ingenieurswese,
Universiteit van Stellenbosch,
Privaatsak X1, Matieland 7602, Suid Afrika.

Tesis: PhD (Elektronies)

December 2023

Hierdie proefskrif bied 'n studie aan oor die impak en oorsaak van die frekwensie-rimpeling in die ontvangsensitiwiteit van elektriese klein weerkaatsantennas. Kennis van die vorm en spektrale inhoud van die rimpeling is belangrik in sommige radiosterrekunde toepassings. Alhoewel daar geen alternatief vir hoëtrou simulasie van die antenna-weergawe, wat gebruik maak van toepaslike berekende elektromagnetiese simulasies, gevind was om die rimpelweergawe akkuraat te karakteriseer nie, word die verskillende fisiese oorsake van die rimpeling, en hul relatiewe impak op die finale gedrag, omvattend oorweeg. Vir die volgende generasie teleskope wat breëband kamertemperatuur laeruis versterkers (LNA) gebruik, in teenstelling met uiters koue kryogeniese stelsels, word getoon dat die rimpeling in baie gevalle betroubaar geïgnoreer kan word tydens die aanvanklike ontwerpfase van die stelsel - selfs vir elektries baie klein stelsels. Dit word verder geïllustreer hoe die rimpeleienskappe verskil as 'n funksie van die antenna se wyshoek, en hoe, in sommige gevalle, die oorspoelenergie na die warm grond die effek kan oorheers. Tot op hede is sulke karakteriserings in die literatuur geïgnoreer, en fokus was hoofsaaklik op die gedrag van die antenna hoofbundel - wat normaalweg na 'n relatief koue lug wys.

Die proefskrif beskryf dat die oorsaak van die frekwensie-rimpeling in ontvangsensitiwiteit te wyte is aan nie-ideale effekte. Die sensitiwiteitsrimpeling word slegs beïnvloed deur die rimpeling in die antenna ruistemperatuur (ANT), en die rimpeling in die stralingsvlak benuttingsgraad (AE), terwyl die antenna en LNA goed aangepas is. Verder word die rimpeling van die ANT en AE slegs bepaal deur die stralingsintensiteitrimpeling, wat veroorsaak word deur verstrooiing, as gevolg van nie-ideale effekte, wat inmeng met die stralingspatroon

Stellenbosch University https://scholar.sun.ac.za

van die volle weerkaatser stelsel. Nie-ideale stralingseffekte vind plaas wanneer die weerkaatser nie ideaal werk nie, wat plaasvind wanneer die weerkaatser nie oneindig groot is nie. Die omvang van die nie-ideale straling is gekorreleer met die elektriese grootte van die reflektor, en dus begin elektries klein weerkaatsers meer afwyk van die ideale straling wat deur geometriese optika voorspel word.

Verder word dit uitgelig dat die ANT 'n funksie van alle rigtings is, en dus is die sensitiwiteit ook. Dit lei daartoe dat sekere rigtings, of gebiede, aansienlik belangriker is as ander vir die ANT-berekening, vir 'n spesifieke wyshoek. In hierdie gebiede word die rimpeling in die stralingspatroon waargeneem in die rimpeling van die ANT, soos verwag. Hittekaarte word gekonstrueer om hierdie belangrike hoeke uit te wys wat gebruik kan word om insig te verkry in watter nie-ideale effekte die rimpelbydrae oorheers, en om die sterk afhanklikheid van die ANT-rimpeling op die wyshoek toe te lig. Behalwe dat dit 'n funksie van alle rigtings is, is die ANT ook 'n funksie van heelwat fisiese parameters. Sommige van hierdie parameters en hul effek op die ANT word ondersoek.

Tydens die ontwerp van radioteleskope, soos die ngVLA, word innoverende afskattingstegnieke van ANT en AE gebruik. Die akkuraatheid van hierdie benaderings vir ANT en AE word ondersoek en gekarakteriseer. Hierdie strategieë wat vir benadering gebruik word is vinnig, maar ignoreer tipies die modellering van die rimpeling. Dit is omdat presiese berekening van die rimpeling normaalweg duur is in terme van berekeningstyd, en gewoonlik nie nodig is tydens die optimeringsfase nie. Die modelleringsdoeltreffendheid van hierdie tegnieke word ondersoek, wat 'n sleutelkomponent is in die effektiewe ontwerp van weerkaatsers vir radiosterrekunde.

Fisiese Optika (PO) simulasiestrategieë word dikwels vir die analise van groter weerkaatsantennas gebruik, in teenstelling met die moment metode (MoM) wat vir kleiner stelsels verkies word. Vir kleiner ontwerpe word die akkuraatheid van hierdie tegnieke belangrik om te oorweeg. MoM neem meer nie-ideale effekte in ag, in vergelyking met PO, en modelleer die rimpel dus meer akkuraat. In klein ontwerpe kan die Fisiese Teorie van Diffraksie (PTD) saam met PO gebruik word om die invloed van nie-ideale effekte meer akkuraat te modelleer. Daar is 'n breekpunt in frekwensie, waar die rimpeling gemodelleer met MoM en PO (met PTD) sal konvergeer, soos die elektriese grootte van die reflektor toeneem. Hierdie tegnieke word vergelyk en ontleed om hul impak te karakteriseer vir gebruik in die modellering van die rimpeling van die ANT in kleiner ontwerpe.

Laastens in die slothoofstuk, word toekomstige werk oorweeg, waar moontlike rimpelvoorspellingsmetodes bespreek word. Een van hierdie metodes gebruik

Stellenbosch University https://scholar.sun.ac.za

’n kombinasie van tegnieke (insluitend Gevalideerde Eksponensiële Analise of VEXPA) om ’n unieke seinsamestelling te voorspel vanaf ’n stel monsters wat geneem word stadiger as die Nyquist-tempo. Benewens hierdie metode, word die lewensvatbaarheid van meetkundige argumente, of die toepassing van ’n voorafverwerkte rimpeling, oorweeg vir rimpelvoorspelling. Die eksklusiewe gebruik van ver-velde in die sensitiwiteitsberekening, sonder om die naby-veld in ag te neem, word ook bespreek, met voorstelle om die ondersoek na die effek daarvan moontlik te maak.

Stellenbosch University https://scholar.sun.ac.za

Acknowledgements

I would like to express my sincere gratitude to ...

God, for giving me the perseverance, ability and circumstances, to successfully complete this difficult project.

My family for supporting me, especially my father Henk Cerfonteyn, and my mother Mariaan Cerfonteyn. I also want to thank my brother Rickus Cerfonteyn for his advice, and my brother Danie Cerfonteyn and his wife Cisca Cerfonteyn, for always making me feel at home. Finally, the complaining is over.

My girlfriend Biancha Alberts for her love and understanding, and her mother Loulana Alberts, for her support. It has been a trying time.

All my friends, especially Petrus Schoonwinkel and Ben Nell for their understanding. It is finally done.

Prof. Dirk I.L. de Villiers and Fahmi Mokhupuki, for assisting me with my PhD research project. I really appreciate the help, and I am sorry it was such a frustrating process, but I have grown immensely through it.

The SKA for funding.

My colleagues for supporting me and being friends.

University Stellenbosch, for providing me the opportunity to do this PhD degree project.

Stellenbosch University https://scholar.sun.ac.za

Dedications

This dissertation is dedicated to God, for always providing a way through even the most seemingly impossible situations. I have learnt to be patient, and have faith.

Stellenbosch University https://scholar.sun.ac.za

Contents

Stellenbosch University https://scholar.sun.ac.za

Stellenbosch University https://scholar.sun.ac.za

List of Figures

Stellenbosch University https://scholar.sun.ac.za

Stellenbosch University https://scholar.sun.ac.za

Stellenbosch University https://scholar.sun.ac.za

Stellenbosch University https://scholar.sun.ac.za

Stellenbosch University https://scholar.sun.ac.za

Stellenbosch University https://scholar.sun.ac.za

Stellenbosch University https://scholar.sun.ac.za

Stellenbosch University https://scholar.sun.ac.za

Stellenbosch University https://scholar.sun.ac.za

Stellenbosch University https://scholar.sun.ac.za

Stellenbosch University https://scholar.sun.ac.za

Stellenbosch University https://scholar.sun.ac.za

List of Tables

Stellenbosch University https://scholar.sun.ac.za

Chapter 1

Introduction

Reflector antenna systems are often used in radio astronomy. This is because reflectors are highly directive antennas, which allows for high sensitivity. In many radio astronomy projects they are used in an array format, to increase the sensitivity and resolution of the system. Sensitivity is a primary figure of merit for radio astronomy, and often times have a frequency ripple which is ignored in the design of the reflector system. Modeling this ripple is both computationally expensive and requires more storage, however, not modeling the ripple leads to a decrease in accuracy. This dissertation studies the cause, effect, and implications of this sensitivity frequency ripple to provide future designers of reflector systems for radio astronomy with some guidelines on how the effectively include, or ignore, the ripple effects in their designs.

1.1 Radio astronomy

The universe consists of many celestial objects which radiate electromagnetic energy. This energy is detectable on Earth and can come from any direction in any polarisation, and at different frequencies.

Astronomy is the study of the universe, while radio astronomy is a subset of astronomy and is about detecting emissions from celestial objects at radio frequencies and using this information to characterize the universe. These emissions are noise-like, mostly incoherent and broad-band [2]. They are studied to determine and analyse their sources, which include stars, galaxies, radio galaxies, quasars, pulsars, and masers [3]. The first detection of radio emissions happened in 1933, when Karl Jansky detected them from the milky way while working at Bell Telephone laboratories. He is considered one of the founding fathers of radio astronomy.

Detection of these emissions require some physical instrument, namely an an-

Stellenbosch University https://scholar.sun.ac.za

tenna. These antennas are typically large parabolic reflector antennas. Generally different reflectors need to be developed for different radio astronomy projects to be able to detect emissions at different frequencies. The aperture of a reflector is the projected area of its surface, onto a plane normal to the direction that the reflector receives or radiates the most energy. This aperture is the collecting area the reflector has available, to receive or radiate energy from.

These emissions tend to be very small signals. To allow these signals to be detectable, a large collecting area is required. This can be achieved by creating a single very large antenna. An example of this is Arecibo, which was a 305 m diameter spherical reflector radio telescope, and was the main instrument in the Arecibo Observatory [4]. Diameter refers to the diameter of the projected aperture area. It was constructed near Arecibo, in Puerto Rico, at the Arecibo Observatory in a natural sinkhole. In 2020 the Arecibo telescope was decommissioned, and a partial collapse of the telescope also occurred, with no plans to rebuild the telescope. Another example is FAST [5], which is a 500 m diameter spherical reflector. It is located in the Dawodang depression, which is a natural basin in Pingtang County, Guizhou, southwest China.

Creating a single large antenna is a difficult and expensive engineering feat. With the advent of faster computers, data transfer techniques, interferometry and aperture synthesis techniques (which will be discussed soon), a large collecting area can be formed by combining data from multiple telescopes, to virtually form a single very large telescope. This became a popular design choice, as very large telescopes could be formed without the mechanical difficulty of physically building one. A collection of antennas working together is called an array. Array design is fundamentally plausible as a single large parabolic reflector can be dissected into many smaller parabolic reflectors with the same focus point as shown in Fig. 1.1. Note that this figure does not represent how array designs are commonly physically realised, it simply presents a fundamental argument to why array designs can work.

Array design does have drawbacks. Each antenna element in the array requires its own electronics back-end, and the back-end correlator scale squarely with the number of elements. For single element radio telescopes, the cost scaling associated with the reflectors, feeds, and back-end in arrays does not occur. This makes them notably cheaper to operate than arrays and still viable in radio astronomy [6].

Many modern array radio telescope designs use interferometry and aperture synthesis [7]. Interferometry is a method which uses the interference characteristics of signals, to combine them from multiple antennas [8]. Consider a 2-element interferometer, which has a single baseline connecting them. A baseline is the vector connecting two antennas that are both a part of the

Stellenbosch University https://scholar.sun.ac.za

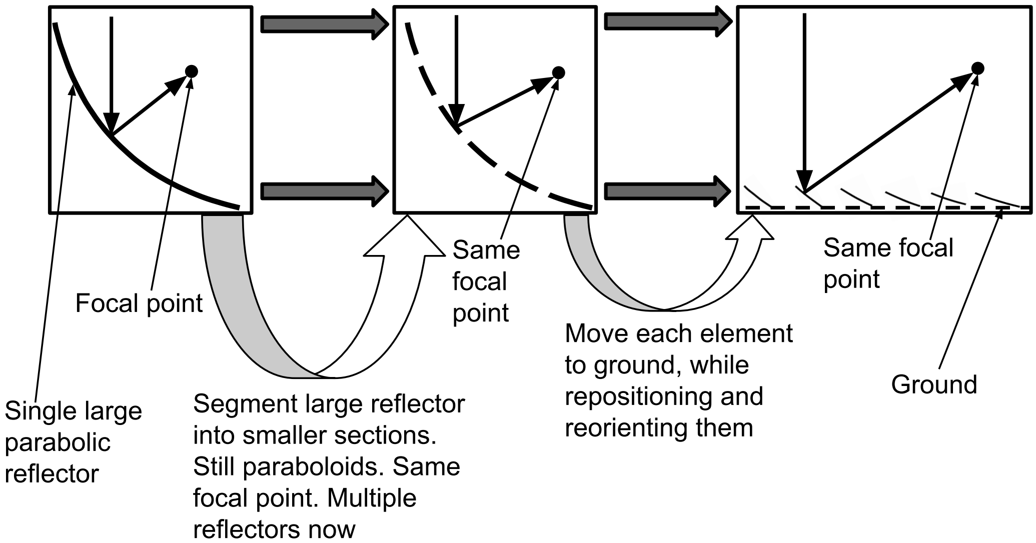

Figure 1.1: Array design is fundamentally plausible as a single large parabolic reflector can be dissected into many smaller parabolic reflectors with the same focus point

same larger array. By using interferometry, these two antennas can obtain an angular resolution similar to an antenna with an aperture the size of the baseline. The angular resolution is the ability of the interferometer to observe fine detail, or small objects, in the sky [9]. Large baselines allows efficient imaging at high resolutions [10]. However, since there are only two antennas collecting energy, the collection area is small, which leads to low sensitivity. Sensitivity will be discussed soon.

Two antennas that are synchronously connected as an interferometer, and separated by a large distance, gives rise to the formation of fringes, or grating lobes. Fringes or grating lobes are images of the signal received from the antennas. This is because of the spacing requirement for arrays which states that in a uniform array, the element can be at most a half wavelength spaced apart, to suppress grating lobes. This requirement in turn is due to the Nyquist sampling rate, which states that for a certain aperture, a certain amount of samples (antennas) are required to avoid aliasing (grating lobes). It is interesting to note that when using reflectors, the baselines will naturally be large. This is because the electric size of reflectors are much larger than half a wavelength, in any sensible case, and they are placed even further apart. The baseline length

Stellenbosch University https://scholar.sun.ac.za

is exacerbated at high frequencies, in wideband situations, which increases the electric size of the reflectors even more, and places them even further apart.

In aperture synthesis, antennas are placed at varying baselines between the original two antennas [11]. The combination of fringes generated from these different baseline antennas, suppress the total fringes in the system. This results in the original received signal being dominant. This technique also allows large collecting areas to be formed, because there are many antennas, which gives rise to a more sensitive system [12]. Aperture synthesis, or synthesis imaging, is thus a type of interferometry that mixes signals from a collection of antennas to generate pictures or information having the same angular resolution as an instrument the size of the entire collection.

Interferometry can be used to tune the system to observe fine details in [10] by choosing large baselines. It can also be used to give sensitivity to larger objects in space, by choosing shorter baselines, but smaller objects can then not be observed [9].

The rotation of the Earth also rotates these baselines, giving sensitivity in different directions on the sky. If many long and short baselines are available, and they rotate with the Earth, a detailed image of various scales and resolutions can be formed. Aperture synthesis has led to radio interferometers becoming true imaging devices, with resolution far in excess of that available to optical telescopes [11].

Sensitivity is a primary figure of merit (FoM) for radio astronomy. It can be described as the minimum detectable signal that can be observed on a given collecting area. Maximizing sensitivity is preferred, as this allows smaller signals to be detected. A certain collecting area can have a varying sensitivity, depending on how effective the area is being used. Optimising the elements in the array indirectly optimises the array as well. Engineers often optimise the reflectors to optimally use the collecting area, to maximize sensitivity.

Arrays can be designed with a large number of elements or antennas, N, with small element diameters, D, to reach the same collecting area compared to using fewer elements with a larger diameter. This big-N-small-D strategy is used in radio astronomy to obtain a large collecting area. There are several radio astronomy projects already using this principle, including the Square Kilometer Array, or the SKA. The SKA, has the goal of reaching a combined collecting area of about a square kilometre [13]. The project will have 64 MeerKAT (precursor) dishes with a 13.5 m diameter and 133 reflectors with a 15 m diameter for the SKA mid-frequency (SKA1-mid) telescope array [14]. The SKA1-mid is the part of the SKA that will be built in South-Africa, with the SKA1-low and SKA1-survey being built in Australia. The SKA can be

Stellenbosch University https://scholar.sun.ac.za

interpreted as a compromise between the number of elements, N, and their aperture, D, compared to other arrays such as the Deep Synoptic Array 2000-antenna (DSA-2000) which also use this principle. As technology continued to improve, projects with even more and smaller elements were developed like the DSA-2000, as the computational and data transfer burden could now be handled. The DSA-2000 has a much larger number of elements with a much smaller diameter compared to the SKA with 2000 elements with a 5 m diameter [15].

In this dissertation for comparative reference, the SKA reflector antennas can be seen as 'medium' sized and the DSA-2000 reflector antennas as 'small', for the L-band (0.7 - 2.0 GHz) frequency range.

1.2 Purpose of this study

Smaller reflector designs may be desirable, however, the decrease in the electrical size of a reflector presents new engineering challenges. These challenges need to be investigated to be able to effectively design small antennas.

One of the reasons why smaller reflector designs are desired is their faster survey speed. Survey speed is heavily dependent on the size of the antenna beam [16]. An antenna that has a wide beam enables a faster surveying speed than one that has a narrow beam. The width of an antennas beam is generally dependant on how large the antenna is, or particularly how large its aperture is. Smaller reflectors have wider beams compared to larger reflectors.

With 2000 5 m dishes, the DSA-2000 has comparable sensitivity to SKA1-mid, but has notably faster survey speed [17]. Survey speed is an important metric for the DSA-2000 and perhaps future projects. The demand for effective smaller dish designs are thus high, which makes the effective design of these reflectors a priority.

Another reason why certain projects prefer using smaller reflectors is, that they are notably more cost effective compared to larger ones. Small 5 m reflectors can be manufactured using single piece manufacturing, to create a single-piece reflector, which is not possible for larger 13.5 m and 15 m dishes. This reduces capital cost investment notably, as the per unit cost is much less.
One of the challenges in small reflector design is the effect of the low noise amplifier (LNA) temperature on the sensitivity. LNAs are part of the receiver back-end of a reflector system in radio astronomy [18]. Historically LNAs did not have acceptable performance in ambient temperature, making cryogeni-

Stellenbosch University https://scholar.sun.ac.za

cally cooling them a requirement for high sensitivity systems [19].

The operational costs of large radio astronomy array projects can be 10% of capital costs per annum. A major cost factor for operational costs involved are cryogenic cooling of components, because it requires a substantial amount of power and maintenance. Many current systems require cryogenic cooling to keep the physical temperature low, which reduces the noise temperature significantly [20]. This is because the gain of the LNA is typically provided by several indium phosphide (InP) high electron mobility transistors (HEMTs), which according to the Pospieszalski noise model, shows that the standard four noise parameters can be expressed in terms of HEMT equivalent circuit parameters and two frequency-independent noise temperatures. The first parameter T_g, associated with the gate-source resistance r_{gs}, scales linearly with temperature [21].

Projects with smaller reflectors generally have significantly more elements. Installing a cryostat and maintaining it for many elements is a notably larger operational and capital investment cost [22].

With the advancement in ambient temperature LNA technology, due to improvement by Dr. Sander Weinreb in the field of ambient LNAs [15], the DSA-2000 has elected to use them. Ambient temperature LNAs do not require cryostats and as such the capital cost investment is lower [23]. Since cryocooling is also not required, the operational costs are also lower. The unit cost for the DSA-2000 antenna/receiver package is lower than \$20, 000, including hardware and labour. This is significantly lower than the per unit cost of the SKA.

Generally non-cryocooled LNAs have worse performance than cryocooled LNAs. The impact of the receiver or LNA temperature on the sensitivity has to be investigated to quantify and analyse the impact of using non-cryogenically cooled LNAs.

Regarding the radiation pattern of smaller reflector antennas, diffraction effects start to play a larger role as the size of the antennas decrease. These effects are non-ideal behaviour, which deviate from the intended electrical design of a reflector, that become more pronounced as reflector electrical size decreases. Non-ideal effects will be described in detail in Chapter 2 and Chapter 3. The expected result from these effects is to cause a ripple behaviour on the sensitivity over frequency. Another challenge in small reflector design might be this ripple becoming a large contributor to the sensitivity, as it is generally negligible and ignored in larger systems.

The effectivity of simplified calculation techniques [24], for use in the calcu-

Stellenbosch University https://scholar.sun.ac.za

lation of sensitivity for smaller reflector designs, also need to be investigated. These techniques will be discussed in detail in Chapter 4, but in short they use simplifications, which leads to fast approximations with relatively high accuracy, for use in electrically medium or large reflectors. These modern sensitivity calculations simplify diffraction effects. This is in part due to the computational burden to accurately characterise it over the entire band, but also because larger reflectors have less pronounced edge diffraction effects, which is why simplifying the effects still provides accurate enough results. Smaller reflectors have a larger circumference to surface area ratio, and thus have larger diffraction effects. For electrically small reflectors it is expected that the sensitivity will have a larger ripple over frequency than for electrically larger reflectors. The modern sensitivity calculation techniques are sufficient to design large and medium sized reflectors, however, these techniques might become inadequate when decreasing the electrical size of the reflectors. A major part of the design of these reflectors for radio astronomy is the quick and accurate calculation of the sensitivity.

It is possible to not use simplifications and simply perform a very dense analysis over frequency to capture the ripple, however, this will require significantly more time to simulate and design small reflectors, to the point of being possibly being unviable. In this dissertation, the terms analyse and simulate will be used interchangeably. This is because computational electromagnetic (CEM) design tools are used to analyse the electric behaviour of antennas, by simulating its behaviour. If the omission of the ripple during the design of smaller reflector systems is notable to the accuracy of simulating the electrical behaviour of the reflector system, then these simplifications will not be viable to design small reflectors. If these techniques can not be readily used for smaller reflector design, methods to quickly and accurately identify and predict the ripple will be necessarily to update these techniques to be viable for small reflector design.

Another challenge is that small reflectors might not be accurately characterised electrically with the use of the asymptotic Physical Optics (PO) analysis method, which is often times used for larger reflector design, as reflector electric size becomes very small. Full wave analysis methods such as Methods of Moments (MoM), which is generally not used for larger reflector designs, as it is not notably more accurate and significantly slower, might become a relevant design technique for smaller reflector designs.

The primary purpose of this PhD research project is to investigate the ripple over frequency of the sensitivity for electrically small reflectors. The causes of the ripple is investigated. The prominence of the ripple is also interrogated, to determine the viability of using these simplifications in the design of electrically small reflectors. With the advances in LNA technology, the viability of

Stellenbosch University https://scholar.sun.ac.za

the modern non-cryocooled LNAs are also essential to review, by considering the impact of the LNA temperature on the sensitivity ripple. Finally, the viability of analysis techniques for use in electrically small reflectors is analysed.

1.3 Contributions

1. Characterisation of the causes of the ripple on the sensitivity for electrically small reflector designs. A thorough analysis into the origin of the ripple could perhaps aid in the prediction of the ripple or the mitigation of it. Possible ripple prediction techniques are also discussed.

2. Characterisation of the impact of the ripple on the sensitivity for electrically small reflector designs, and the viability of using simplifications to calculate the sensitivity for small reflector designs.

3. Characterisation of the impact of the receiver or LNA temperature on the ripple of the sensitivity. With the advent of low temperature non-cryocooled LNAs, the impact of the LNA temperature on the sensitivity ripple could indicate for which LNA temperatures it is important to model the ripple.

1.4 Dissertation layout

Following this basic high-level introduction, Chapter 2 will discuss reflectors, including the rise of non-ideal effects with smaller reflectors. Analysis technique ability to identify non-ideal effects are discussed.

Non-ideal effects are then described in detail in Chapter 3, followed by the interference process through which non-ideal effects influence the radiation pattern of the reflector system to inject a ripple on it over frequency.

The effect of the radiation pattern on the antenna noise temperature (ANT) ripple is discussed in Chapter 4, followed by an investigation into the angle dependency of the ANT.

The cause of the ripple in the sensitivity is then investigated in Chapter 5, followed by the impact of the ANT and aperture efficiency ripple on the sensitivity.

Finally the conclusion is given in Chapter 6.

Stellenbosch University https://scholar.sun.ac.za

Chapter 2

Characterisation of reflector systems

2.1 Introduction

A reflector antenna is a large metal surface, which approaches a perfect electrical conducting (PEC) surface, so that it optimally scatters or reflects most of the energy incident on it. Any reflector system consist of one or multiple reflector antennas and a feed. The feed receives or radiates energy. The reflector antenna is designed to redirect a large amount of energy to the feed in the receiving case, or radiate a large amount of energy from the feed in specific directions in the transmitting case. This translates to reflectors having a relatively high directivity, which is generally why reflectors are used over other antenna types. To achieve this, they are often relatively large constructions compared to other types of antennas. This is especially useful in radio astronomy as a larger collecting area leads to more sensitivity.

In this dissertation the electrical size is implied when referring to size. Electrical size measures a reflector in wavelengths at a particular frequency, and is thus a function of frequency. Higher frequencies will lead to a larger electrical reflector size, for constant physical size, as the wavelength decreases. Reflector antennas are often designed to operate over a certain frequency band and as such will have an increasing electrical size as the frequency increases over the band, while the physical size remains constant.

Stellenbosch University https://scholar.sun.ac.za

2.2 Geometric Optics design of reflector antennas

Electromagnetic fields propagate as spherical waves, when not in close proximity to a radiating source, and when in free space. A feed antenna, which radiate electromagnetic energy, is an example of a radiating source. Geometric Optics (GO) is a simplification of the behaviour of electromagnetic waves and it is relevant for electrically large structures. It assumes that electromagnetic spherical waves travel in rays, or straight lines, in free space and can be reflected. Ray tracing techniques traces the path a ray would propagate or reflect in. These techniques can thus be used to determine the behaviour of electromagnetic waves following the model proposed by GO.

Snell's law states that for an incident ray reflected from a surface, the reflected ray would have the same angle as the incident ray, relative to the tangent (or normal) of the surface. This law is also relevant for GO analysis, where the rays reflected from the surface of the reflector follow this law, $\theta_i = \theta_r$. The electric field (E-field) and magnetic field (H-field) components, are orthogonal to each other, and to the propagation direction $\bar{s}_{[\cdot]}$.

Consider a reflected GO field propagating along parallel rays towards the antenna aperture, $\bar{s}_p = \bar{z}$. The reflected E-field at a certain distance from a radiating source can be calculated as follows,

$$\overline{E}_p(s) = \overline{E}_i(0)e^{-jks}, \tag{2.1}$$

where s is the distance measured from the field source along the ray path, and the wavenumber is defined as k. The e^{-jks} term thus accounts for phase oscillation for the E-field in the direction of propagation. The $\overline{E}_i(0)$ term assumes no spatial attenuation present.

The GO method is discussed in detail in [25]. It explains the E-field amplitude attenuation due to propagation effects, reflection coefficient and polarisation orientation.

The incident field of the reflecting surface, as well as the scattering effects of the surface due to this incident field, have to be known to calculate the full reflector system radiation pattern. Additionally the electrical properties and geometry of the reflecting surface have to be known too, however, the geometry is generally chosen. Thus, the full radiated field of a reflector system can be calculated as follows,

$$\overline{E}_{\text{tot}} = \overline{E}_i + \overline{E}_p, \tag{2.2}$$

Stellenbosch University https://scholar.sun.ac.za

where $\overline{E}_p$ is the electric field component that is caused by scattering or reflection effects, which reflects away from the reflector surface, $\overline{E}_i$ is the incident electric field on the reflector surface, and $\overline{E}_{\text{tot}}$ is the total radiated field of the reflector system.

The electric field component, $\overline{E}_p$, is unknown. Approximation methods are often times used to calculate this quantity quickly and relatively accurately. These approximation methods are asymptotic methods, which means they are asymptotically accurate on electrically large structures, but become less accurate for smaller systems. GO is such a method. When the reflected E-field is calculated and the incident E-field is known, the total radiated field can be calculated with GO by using (2.2)

For GO, the geometrical theory of diffraction (GTD) is a compensation technique, which uses ray tracing to include diffracted rays and describe diffracted fields [26], to improve the GO method.

The ray trace simplification allows conic sections, or idealised geometric forms, to be used for the design of reflector antennas which directs rays in a predictable manner in the ideal case. The ideal case refers to the perfect redirection of energy according to one of these conic sections. Theoretically this is realisable with an infinitely large conic section. A conic section is formed from the resulting intersection curve between an intersecting plane and a cone. Different curves can be formed depending on orientation of plane intersection. These curves have names, such as the classical parabola, ellipse or hyperbola. This process is shown in Fig. 2.1

These different curves direct rays in different ways, however, all of these curves direct rays through two specific focus points. An example for an ellipse is shown in Fig. 2.2 and an example for a parabola is shown in Fig. 2.3. Notice how the one focus point for the parabola is at infinity, this has the implication of directing the rays in parallel.

The reciprocity theorem in antenna literature state that the transmitting or receiving of electromagnetic waves in antennas result in the same electrical behaviour of the antenna. Thus, the ray orientation can be inverted. This also applies to the feed. In this dissertation receiving and transmitting cases will be used interchangeably.

In the case of the parabola the feed can be placed on the nearest focus point, which will then collect incoming rays from a single direction as the parabola collimates in one direction. In the ideal case it is a Dirac delta response over angle, which creates a perfect narrow beam that can be completely controlled to collect a large amount of radiation from a specific direction. This is useful

Stellenbosch University https://scholar.sun.ac.za

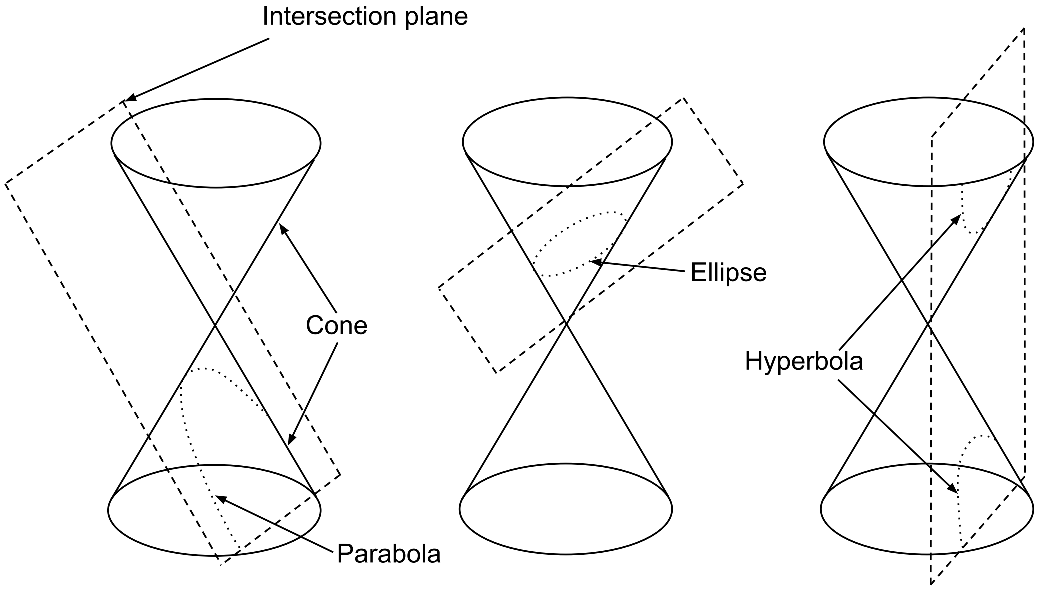

Figure 2.1: Conic sections reflector cut

for radio astronomy, as extremely weak signals from specific sources in the universe can then be detected and studied. In Fig. 2.4 this is shown.

These 2D conic designs can be used in their 3D forms to create physical reflectors with the same geometric properties, as shown in Fig. 2.5 for the parabola case. A 2D parabola is rotated around the symmetry axis of the 3D paraboloid to form it. A section of this parabola, which represents the cross section of the reflector design, is selected. A cutting plane is inserted from the one outer edge to the other. The volume below the cutting plane is a 3D paraboloid, representing the physical reflector antenna design. The reflector is symmetric around its cross section. In this dissertation, reflector antennas will be presented in their cross section form.

The parabola geometry can be used as a single or primary reflector. A single reflector refers to one reflector used as a reflector system, where a primary reflector refers to the first reflector in a reflector system, where energy from space is incident on it, in the receiving perspective. Most radio astronomy projects use a parabola geometry as a single or primary reflector due to the reasons mentioned earlier. A possible configuration from a single reflector is shown in Fig. 2.6. This is a centre fed configuration where the feed is placed

Stellenbosch University https://scholar.sun.ac.za

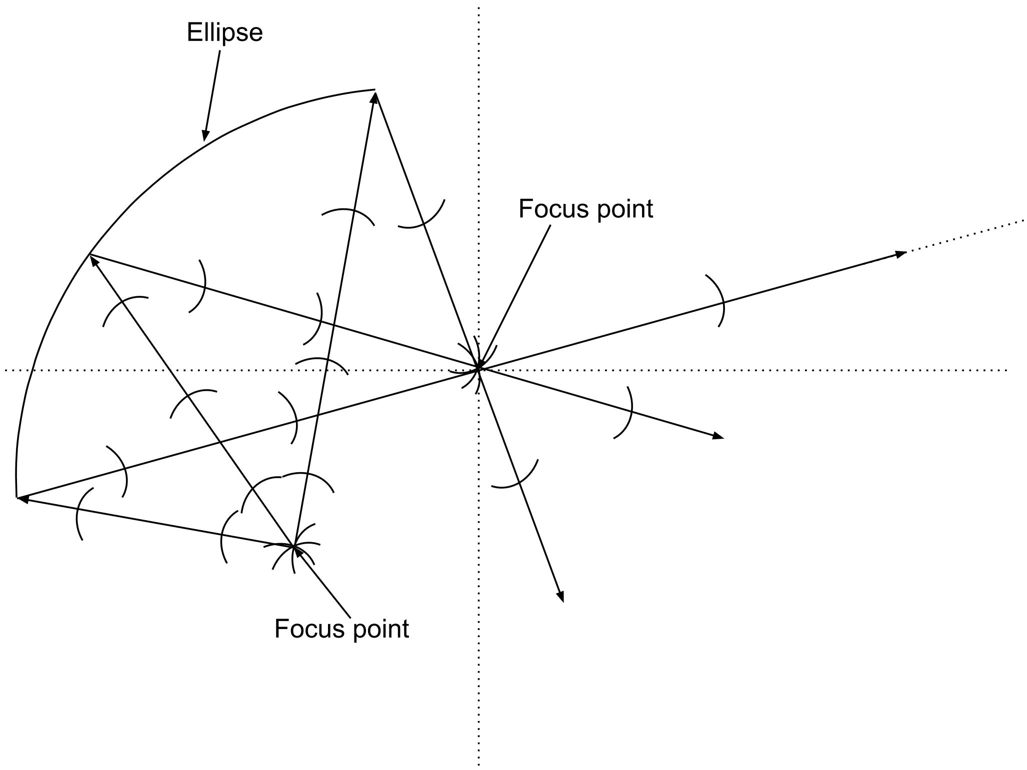

Figure 2.2: Ellipse focus points

in front of the reflector.

The ellipse is generally not used as a single or primary reflector, but is very useful as subreflector in a dual reflector system. The ellipse directs energy over an angle arc in the ideal case, instead of in a single direction. This is shown in Fig. 2.7. In the ideal case, this allows the elliptically shaped subreflector to direct all the energy from a feed onto a parabola shaped primary reflector, which then radiates all the energy in a single direction (or reversed in the receiving perspective), and is shown in Fig. 2.8. This is referred to as a highly directive antenna system, as it receives (or transmits) most energy from (to) a specific direction. This is the direction of maximum radiation intensity, and around it is the main lobe, or main beam. Directions outside the mainlobe, is called the sidelobes, and radiation to the back of the antenna is called the backlobe. This type of reflector configuration is called the Gregorian dual reflector system and many radio astronomy projects have preferred or highly considered this optics configuration for high performance systems.

This definition of the Gregorian system is not standard, however, it is useful for the discussion of the effect of non-ideal radiation on the radiation pattern, which is later discussed in the dissertation. The standard definition of a

Stellenbosch University https://scholar.sun.ac.za

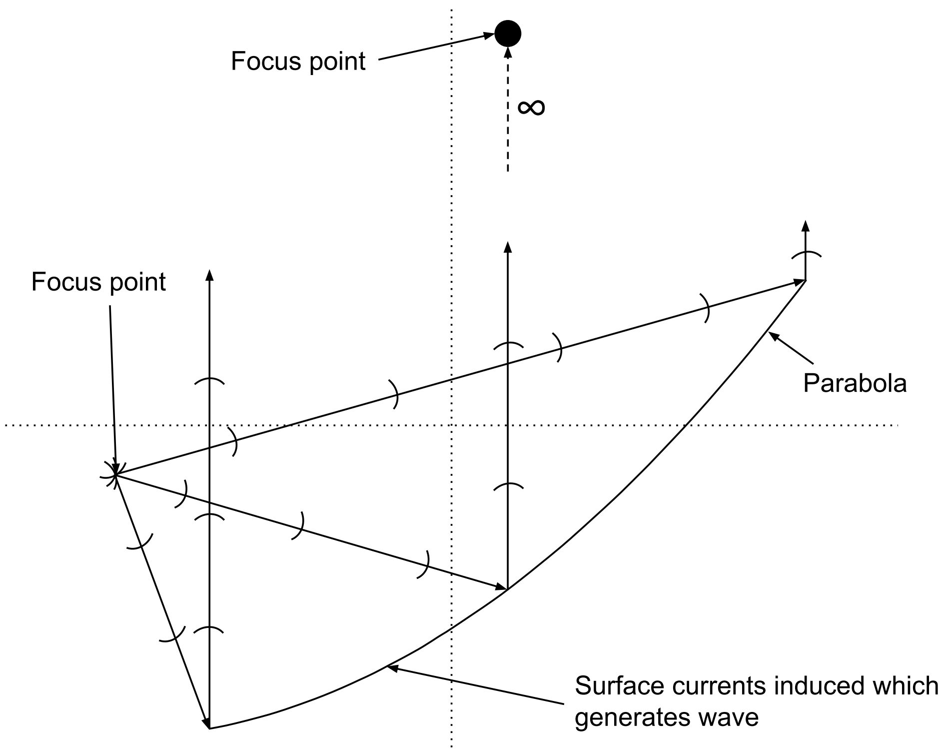

Figure 2.3: Parabola focus points

Gregorian system states that the (non-infinite) focus of the parabola is positioned on the secondary focus of the ellipse. The overlapping of the two focus points, allows the reflector system to achieve high transmission efficiency and low spillover levels (which will be discussed in Chapter 3) over a wide frequency band [27]. This is because the relative position of their focuses is independent of frequency, allowing largely predictable energy transmission in any electrically large situation. Theoretically, all of the energy of the parabola is transferred to the ellipse through the shared focus, which is then transferred to a feed. This leads to high transmission efficiency.

Additionally, both reflectors can be positioned outside of the aperture plane of the other. This allows both reflectors to be designed electrically large, without causing aperture blockage. It is also possible to design them rotationally, or axially, symmetric. In this case there is aperture blockage, however, it provides a uniform phase distribution over the illuminated portion of the aperture, which increases polarisation performance [28]. Rotationally symmetric dual reflectors are usually designed for Cassegrain antennas, to reduce the subtended angle of the feed, or feed taper angle, for use with deep primary reflectors. Offset dual reflector systems are usually designed for Gregorian antennas, where the feed taper angle is similar or larger compared to primary focus systems. A larger

Stellenbosch University https://scholar.sun.ac.za

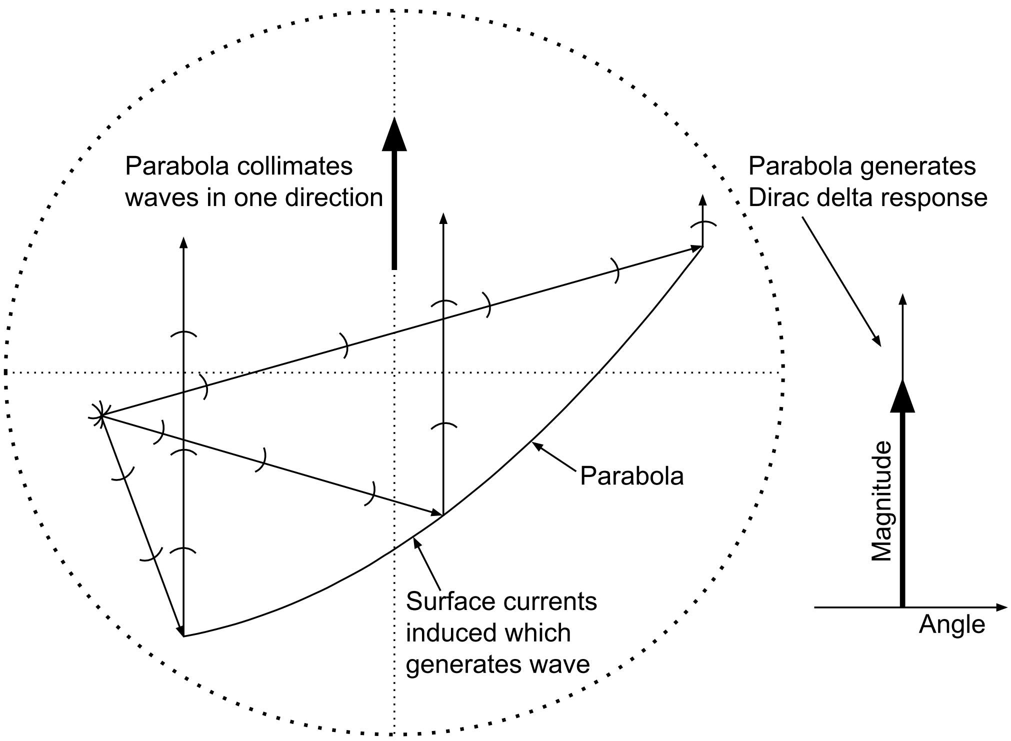

Figure 2.4: The parabola creates a Dirac delta response over angle in the ideal case, which is theoretically realisable for an infinitely large parabola

taper angle requires a smaller feed. A smaller feed is usually lighter, easier to mount, requires less physical support and can be easier to manufacture.

Using the design equations from [29], the offset Gregorian dual reflector antenna system which has an unblocked aperture without supporting struts was created, and is shown in Fig. 2.9 along the xz-symmetry plane. The design is based on practical size dimensions satisfying the Mizugutch condition to reduce cross polarisation [27]. The polarization characteristics of a reflector system is influenced by the symmetry of the reflectors. The cross polarised component over the aperture plane due to the asymmetrical reflector configuration can be canceled by making effective use of a another asymmetrical reflector and by properly arranging them with a primary radiator. The condition to cancel the cross-polarized component in such a reflector system is expressed as follows,

$$\tan(\alpha) = \frac{|1 - e^2|\sin(\beta)}{(1 + e^2)\cos(\beta) - 2e}, \tag{2.3}$$

where alpha is the angle between the horn axis and the rotation axis of the subreflector, beta is the angle between the rotation axis of the subreflector and that of the paraboloidal main reflector, and e is the eccentricity of the subre-

Stellenbosch University https://scholar.sun.ac.za

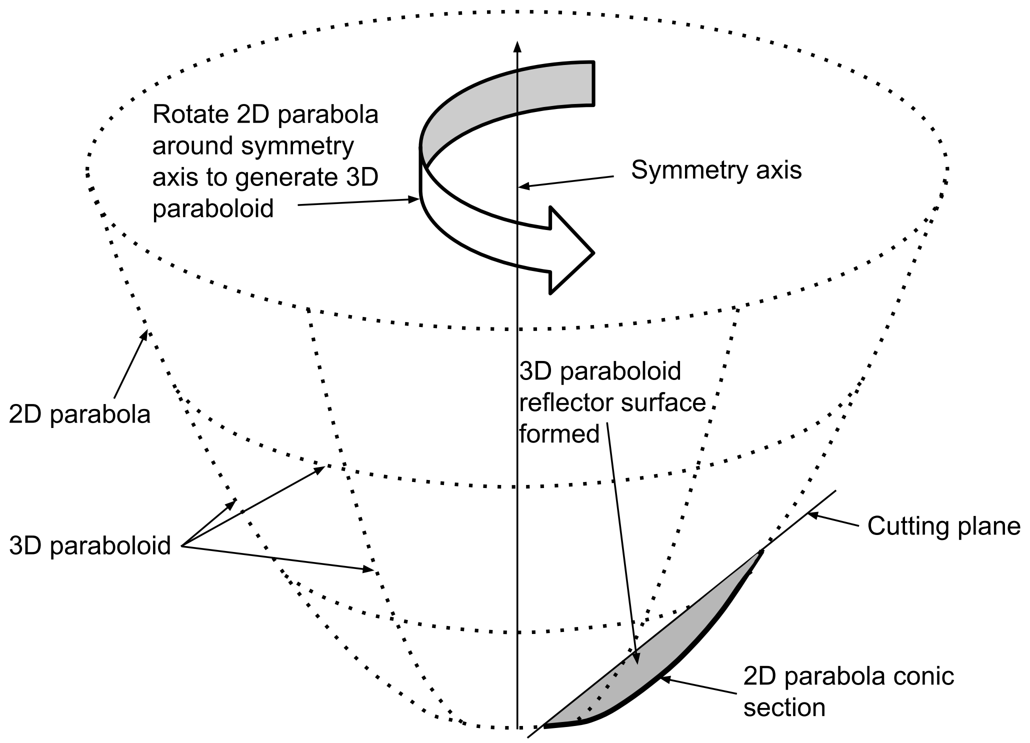

Figure 2.5: 3D paraboloid reflector antenna formed from 2D parabola conic section

flector. This condition is known as the Mizugutch condition. Offset technically refers to the reflector system not being axially symmetric, and practically this occurs when the feed is placed offset to this axis. The subreflector subtended half-angle is denoted by θ_e and the projected aperture diameter by D_m. The feed-up and feed-down pointing angle directions are denoted by $+\theta_\mathrm{p}$ and $-\theta_\mathrm{p}$, respectively. The feed-up pointing angle refers to the feed rotating up towards the sky, where the feed-down tipping angle refers to the feed rotating down towards the ground.

Reflector antennas in radio astronomy are usually highly directive. They are commonly rotated, or tipped, so that they can observe radiation from different directions, which originates from celestial objects that are scattered throughout the universe. The tipping angle, or pointing angle, is defined as the angle between zenith and the vector normal to the aperture plane of the reflector system and is shown in Fig. 2.10. The reflector is not rotated in azimuth. This is not necessary as the reflector system is symmetric around its shown cross section.

In this dissertation, unless otherwise stated, an arbitrary relatively small offset Gregorian dual reflector antenna system is used as the standard reflector

Stellenbosch University https://scholar.sun.ac.za

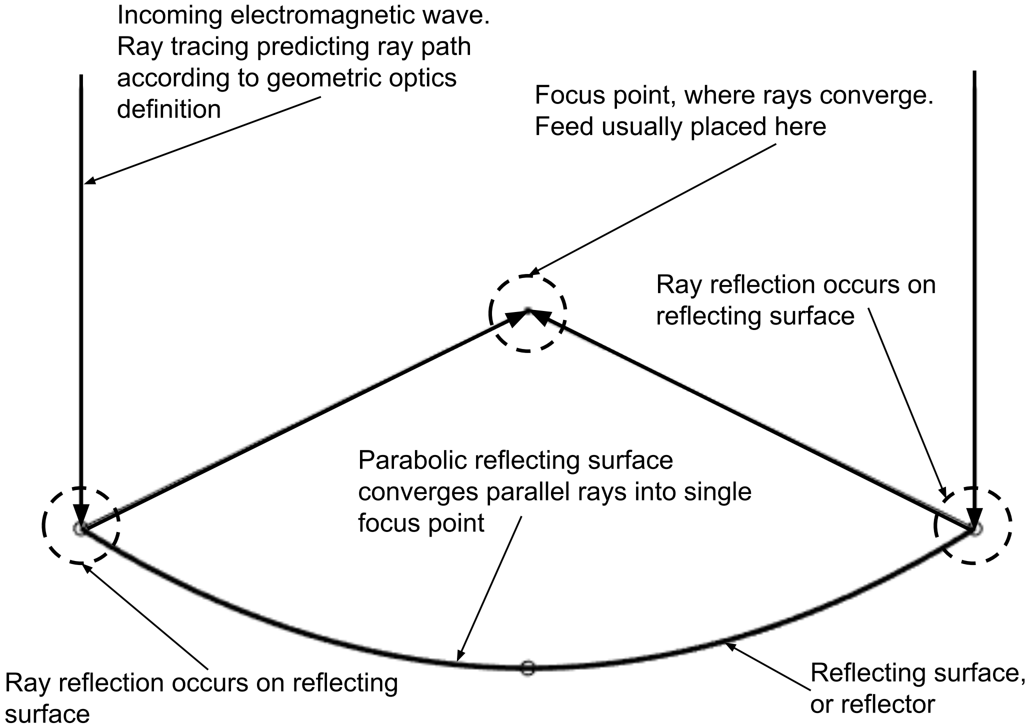

Figure 2.6: A single reflector configuration

configuration for analysing ANT, aperture efficiency (AE) and sensitivity. A standard reflector was chosen, to serve as a constant throughout the analysis, to make it more tractable. It is explicitly stated in cases where the reflector design changes, and the effect it has. A relatively small reflector is chosen to illustrate the implication of the non-ideal effects on the radiation pattern based responses of the system, as non-ideal effects become less important for larger reflectors. Any electrically small reflector could be chosen for the analysis, including a single reflector. Although the influence of the non-ideal effects in this case might be different, the analysis remains relevant for any electrically small reflector. The reflector has maximum main and subreflector chord lengths of 5 m and 2 m respectively, and features a main-reflector projected aperture diameter of 4 m. Chord length refers to the length of the line drawn from one cross section outer edge, to the other. Finally, a similar reflector was used for the analysis of non-ideal effects in the AE calculation in [30], which is discussed and compared in Chapter 5.

Stellenbosch University https://scholar.sun.ac.za

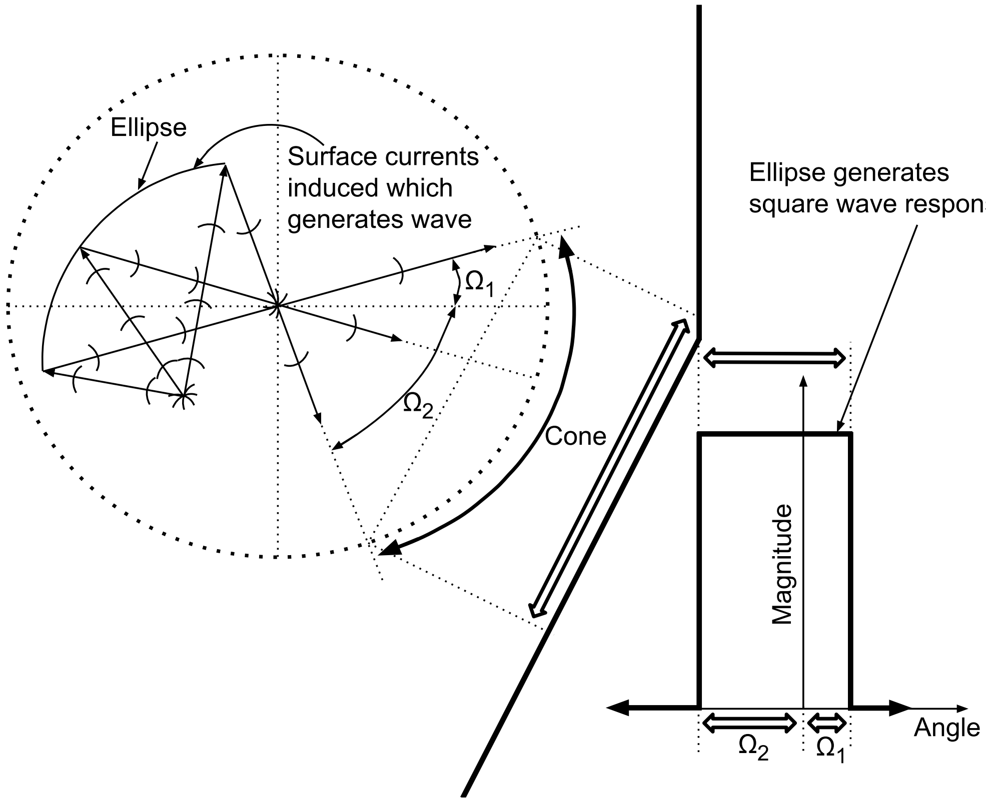

Figure 2.7: Ellipse creates a square response over angle in the ideal case, which is theoretically realisable for an infinitely large ellipse

2.3 Analysis techniques

The assumption thus far have been for idealised cases. In practise, however, there are non-ideal effects that influence the radiation pattern generated from a reflector system. These non-ideal effects will cause a parabola geometry for example to radiate some energy in all directions, instead of just a single direction. Non-ideal effects become more pronounced as the reflector size decreases. Non-ideal effects include diffraction effects, which will be discussed in detail in the next chapter. GO does not take non-ideal effects into account, and is thus commonly only useful for an initial design, as it is usually not accurate enough for a comprehensive electrical analysis of the design. Techniques such as PO, Physical theory of Diffraction (PTD) and MoM, account for these non-ideal effects, and are commonly used to analyse antenna electric behaviour. Each of these techniques account for various levels of non-ideal effects, and the technique chosen is thus dependent on the size of the reflector.

Stellenbosch University https://scholar.sun.ac.za

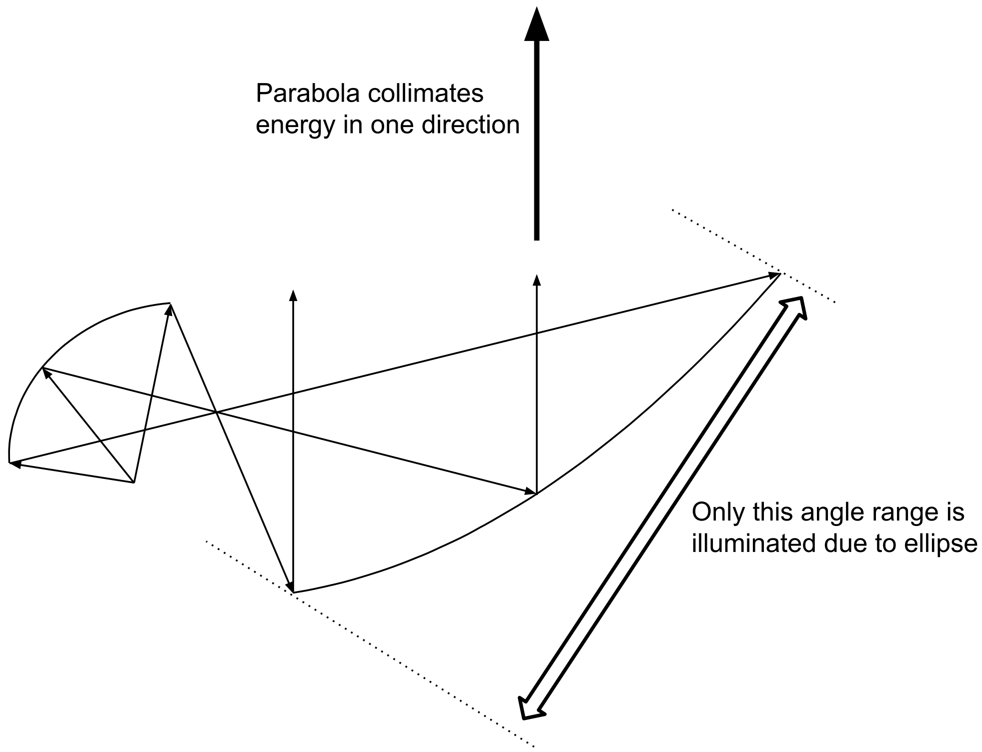

Figure 2.8: Ellipse parabola interaction

2.3.1 Physical Optics and Physical Theory of Diffraction

PO is an asymptotic current distribution approximation method. The PO method require the discretization of a surface, to allow it to calculate the current distribution on the surface. Without discretization, there is technically infinite currents, which is computationally intractable. The discretization of a surface can be realised through meshing the antenna geometry, and can be seen in Fig. 2.11. It can also be achieved by creating a point cloud of the surface, and will also be presented as shown in Fig. 2.11 for brevity, where the centre of each element will be a point in the cloud. Meshing is the process of segmenting the antenna into smaller sections. Combining all these sections forms the entire antenna geometry again. Note that the mesh elements are usually edge-to-edge packed, but they are seperated some distance from each other in Fig. 2.11, for the purpose of illustration. Each of these mesh elements are numbered, and have a surface current associated with it. Since the current distribution is technically continuous, large discretized sections will result in a low resolution and inaccurate representation of the current distribution. Smaller discretized sections have to be balanced with the computational burden of solving more currents.

Stellenbosch University https://scholar.sun.ac.za

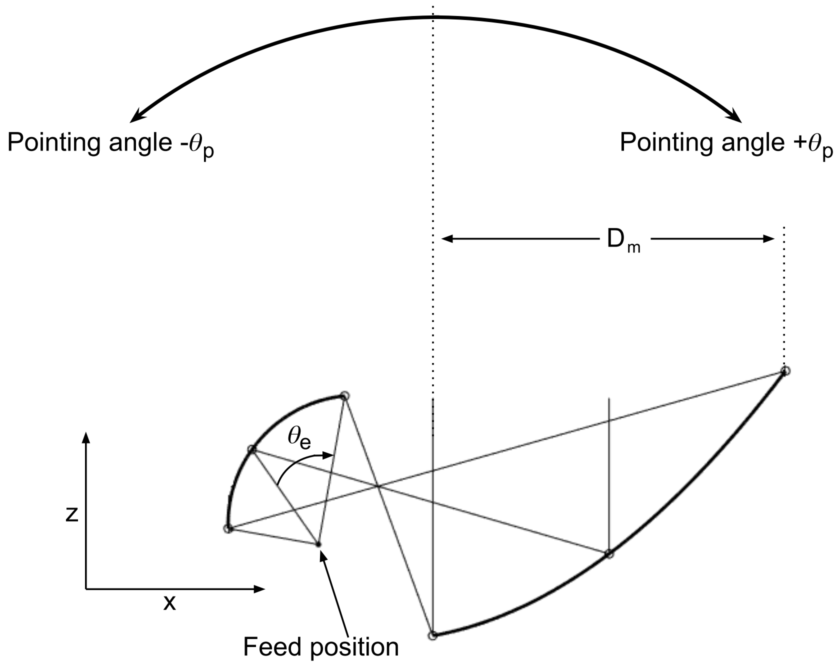

Figure 2.9: An arbitrary offset Gregorian dual reflector antenna is shown along the xz-symmetry plane. The subreflector subtended half-angle is denoted by θ_{e} and the projected aperture diameter by D_{m}. The feed-up and feed-down pointing angle directions are denoted by $+\theta_{\mathrm{p}}$ and $-\theta_{\mathrm{p}}$, respectively

The PO method can be solved using a point based method, or using a meshing scheme. For mesh based PO, the current on each of the mesh elements can be calculated with the use of a basis function. The Rao-Wilton-Glisson (RWG) functions are a set of basis functions, and arbitrarily shaped surfaces can be modeled by using them. This is because such surfaces can be modeled using a tetrahedral mesh and the RWG can realise it. The RWG is a special set of basis functions, and their normal components are continuous across all surface edges. Each shared edge in the mesh has a single basis function associated with it.

The PO method makes the assumption that the surface current on a tangential infinitely large flat surface, is the same as the surface current at a specific point on a perfectly conducting curved scatterer. An incident plane wave on an infinitely large flat surface, generates a reflected plane wave. This can be seen in Fig. 2.12. The surface current at any point on this surface is simply [31],

Stellenbosch University https://scholar.sun.ac.za

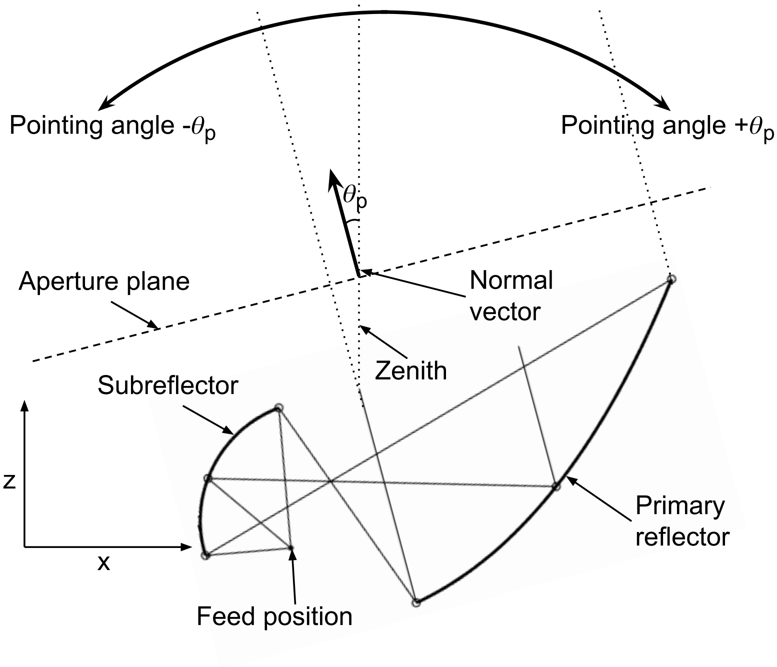

Figure 2.10: Offset Gregorian dual reflector, tipping in $-\theta_\mathrm{p}$ to demonstrate the definition of pointing or tipping angle for radio astronomy

$$\bar{J}_s = 2\hat{n} \times \overline{H}_i, \tag{2.4}$$

with the incident magnetic field denoted as $\overline{H}_i$, and $\hat{n}$ the unit vector normal to any point on the surface. When using this assumption on a specific point on the curved scatterer, then $\hat{n}$ is the unit vector normal to any the specific point on the curved scatterer. It is important to note that this PO current calculation requires line-of-sight visibility to the source of the radiation.

From this, the $\overline{E}_p$ from (2.2), which is the electric field component that is caused by scattering or reflection effects, can instead be treated as the scattered electric field radiated by the current distribution from (2.4).

The surface current assumption becomes inaccurate at the edge of the reflector. This can be seen in Fig. 2.13. This is because the edge is a discontinuity, without an approximate flat surface surrounding it. The current assumption at the centre of the reflector is accurate, if the reflector is electrically large enough, for the surrounding surface area to appear approximately flat.

Stellenbosch University https://scholar.sun.ac.za

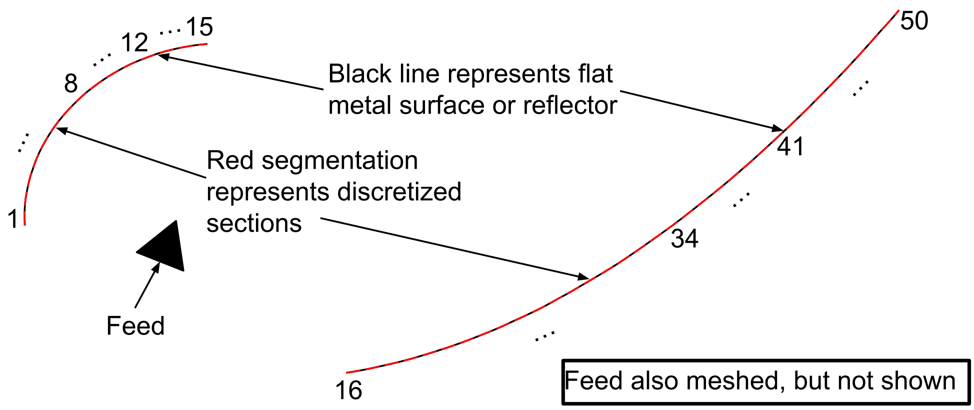

Figure 2.11: Both PO and MoM discretizes the surface of the antenna, to create a finite number of currents to calculate, which is required for any numerical calculation technique. The discretization of a surface can be realised through meshing or creating a point cloud of the surface

For PO, the PTD is a compensation technique, that can be used to more accurately calculate the radiation from the edges of a reflector surface. It is a current approximation based method, and improves the accuracy by including edge diffraction effects on the rim of the reflector surface. It instead assumes that a plane wave illuminating an infinite, perfectly conducting half plane [32] is the reason for the induced currents.

The surface current assumption used in PO, also omits certain interactions. It assumes the current at each mesh element (or point) is only due to the incoming wave, however, this is not entirely correct. The current at each mesh element (or point) radiates and could induce currents at mesh elements (or points) over the reflector, which will change the currents at these mesh elements (or points). This can be seen in Fig. 2.16.

The PO described and used in this dissertation is single reflection PO (SRPO), however, Multi-reflection PO (MRPO) also exist. The MRPO applies the PO approximation to the field radiated by the present current solution towards the scatterer itself, to account for successive internal reflections. The visibility

Stellenbosch University https://scholar.sun.ac.za

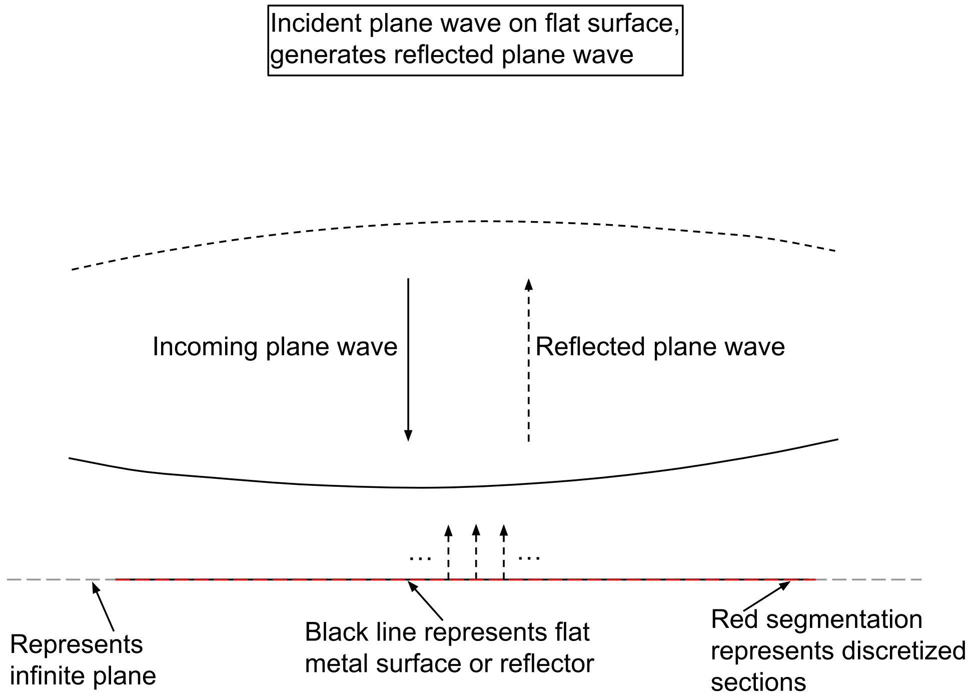

Figure 2.12: An infinite flat surface generates a reflected plane wave, from an incident plane wave

status between every pair of basis functions is required, taking into account all geometry [33]. MRPO includes some non-ideal effects in its calculation, that SRPO does not. This allows it to model some re-radiation and self-coupling non-ideal effects. These effects will be discussed in more detail in Chapter 3.

In many cases the PO simulations are also performed in a sequential manner, as seen in Fig. 2.15. The scattering of the subreflector, due to the energy radiated from the feed, is calculated. Then, the scattering of the primary reflector, due to the scattering from the subreflector and the feed radiation is calculated. Finally, the total radiation pattern is calculated due to the scattering from the primary reflector, the subreflector, and the radiation from the feed. In this case, the effect of the primary reflector scattering, on the scattering of the secondary reflector is omitted. Technically this can be simulated, however, then the scattering of the secondary reflector on the first has to be simulated again. This process can then be repeated until convergence, which would make the method extremely slow. In this dissertation, the PO calculation is performed as shown in Fig. 2.15.

These assumptions allow the PO method (and even the GO method) to present fast and relatively accurate estimations of the reflector system radiation pat-

Stellenbosch University https://scholar.sun.ac.za

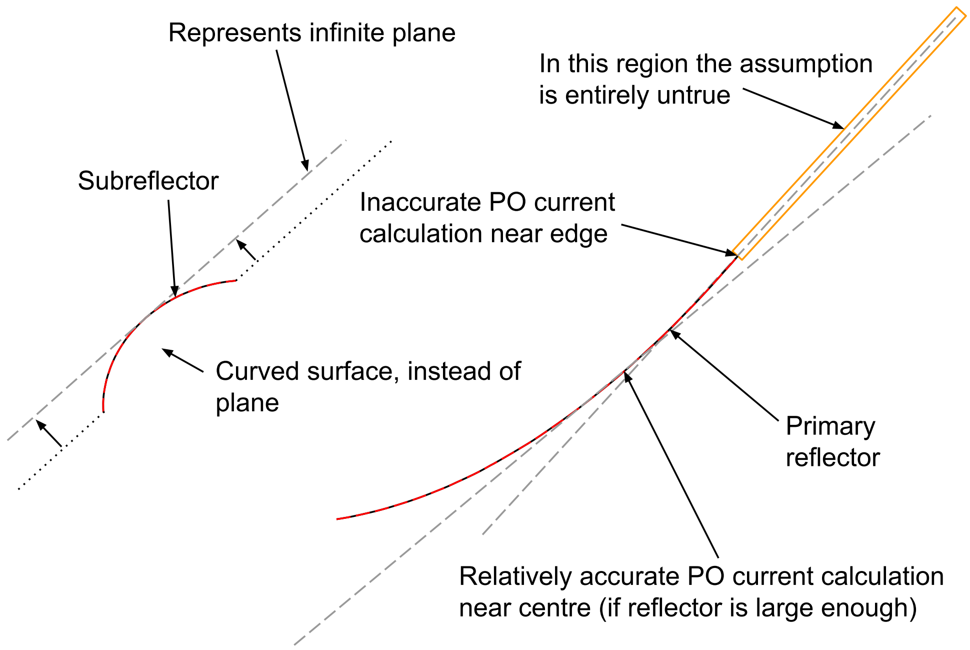

Figure 2.13: PO current calculation near the edges of a reflector is very inaccurate, while PO current calculation near the centre is more accurate, if the reflector is electrically large enough

tern, especially for electrically large reflector systems. With a reduction in size, these assumptions become more inaccurate. The assumptions lead to an incomplete description of the non-ideal effects. The field effects on the edge of the scatterer, for example, are not comprehensively considered to account for edge diffractions (which is a non-ideal effect and will be described in the next chapter). Compensation techniques can, however, be used to improve the initial approximations and their ability to account for non-ideal effects.

When the PO currents are calculated for a surface, then the radiated field can be calculated with the radiation integral analysis procedure. In this procedure the magnetic current sources $\bar{J}_m$, together with the electric current sources $\bar{J}_e$, cause the surface current distribution $\bar{J}_s$. This surface current distribution, $\bar{J}_s$, is then integrated to obtain the electric vector potential $\bar{A}_e$ and the magnetic vector potential $\bar{A}_m$ as follows,

$$\bar{A}_e = \frac{\mu}{4\pi} \iint_S \bar{J}_e(\bar{r}') \frac{e^{-jkR}}{R} \, ds', \tag{2.5}$$

Stellenbosch University https://scholar.sun.ac.za

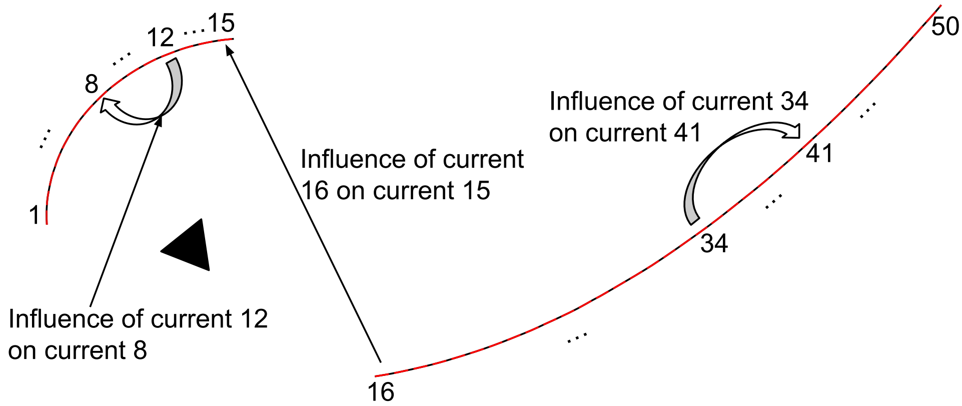

Figure 2.14: Coupling between currents is not taken into account using PO, but is when using MoM

$$\bar{A}_m = \frac{\varepsilon}{4\pi} \iint_S \bar{J}_m(\bar{r}') \frac{e^{-jkR}}{R} \, ds', \tag{2.6}$$

with the permittivity as ε and the permeability as μ. The euclidean distance is defined as $R = |\bar{r} - \bar{r}'|$, with $\bar{r}$ being an observational point in the far-field and $\bar{r}'$ being the source coordinates over the reflecting surface. The integral is bounded by the surface limit S, and each prime variable, denoted with $[\cdot]'$, is in reference to the integration over the scatterer surface. The scattered electric field $\overline{E}_p$ can be calculated as follows,

$$\overline{E}_p = -j\omega[\bar{A}_e + \frac{1}{k^2}\nabla\nabla \cdot \bar{A}_e] - \frac{1}{\varepsilon}\nabla \times \bar{A}_m, \tag{2.7}$$

with the angular frequency denoted as ω. From this, the entire radiated field can be calculated as previously shown in (2.2). Next, the MoM will be discussed.

Stellenbosch University https://scholar.sun.ac.za

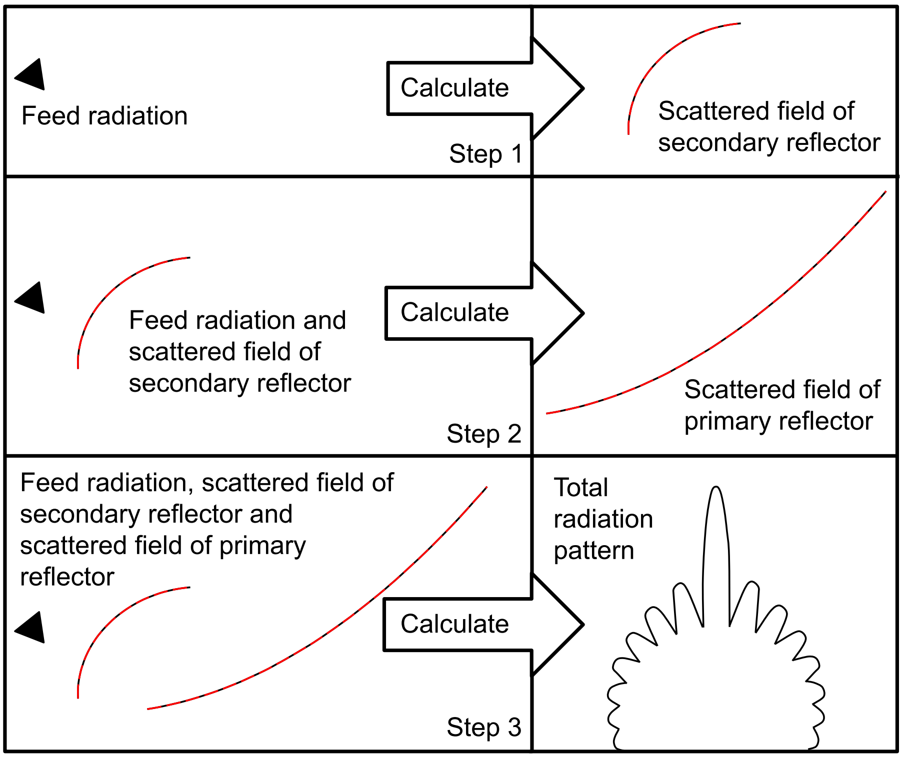

Figure 2.15: A possible calculation process of a PO simulation to calculate the total radiation pattern

2.3.2 Method of Moments

The MoM is a full-wave method, and not an asymptotic method like the PO. This means that MoM calculates all the surface current interactions, and does not use the same assumptions that PO uses, which allows it to be accurate for all reflector sizes. The MoM calculates the integral form of Maxwell's equations. It does this by creating a solvable matrix equation from the electric field integral equation (EFIE), by first transforming it into a boundary value problem. The EFIE can describes the electrical behaviour of the antenna system by using a known current distribution, $\boldsymbol{J}(\boldsymbol{r}')$, to calculate the electric field.

The EFIE can be described as follows [34],

$$\boldsymbol{E} = -j\omega\mu \int_V \overline{\overline{\boldsymbol{G}}}(\boldsymbol{r}, \boldsymbol{r}') \cdot \boldsymbol{J}(\boldsymbol{r}')\, d\boldsymbol{r}', \tag{2.8}$$

or as

$$\boldsymbol{E} = \mathcal{L}\{\boldsymbol{J}\} = -j\omega\mu \int_V \overline{\overline{\boldsymbol{G}}}(\boldsymbol{r}, \boldsymbol{r}') \cdot \boldsymbol{J}(\boldsymbol{r}')\, d\boldsymbol{r}', \tag{2.9}$$

Stellenbosch University https://scholar.sun.ac.za

where $\mathcal{L}$ is the integral operator and $\overline{\overline{\boldsymbol{G}}}(\boldsymbol{r}, \boldsymbol{r}')$ is the dyadic homogeneous Green function defined as,

$$\overline{\overline{\boldsymbol{G}}}(\boldsymbol{r}, \boldsymbol{r}') = \frac{1}{4\pi}\left[\mathbf{I} + \frac{\nabla\nabla}{k^2}\right]\frac{e^{-jk|\boldsymbol{r}-\boldsymbol{r}'|}}{|\boldsymbol{r}-\boldsymbol{r}'|}. \tag{2.10}$$

The EFIE has a unique solution in the case where the tangential field components are required to be zero at the surface of the PEC antenna, ($\boldsymbol{E}_{\text{tan}} = 0$), which is the case for the boundary condition of a perfect electrical conductor (PEC). In this case an analytical solution is usually not possible, but a numerical approximation is. The MoM is a numerical approximation and has shown to be an accurate approximation of Maxwell‘s equations.

If the source ($\boldsymbol{E}_{\text{inc}}$) induces the current distribution $\boldsymbol{J}$, then the scattered field can effectively be calculated by (2.9).

The boundary condition of a perfect electrical conductor (PEC) also provides a relation between the incident field and the scattered field as follows,

$$\mathcal{L}\{\boldsymbol{J}_{\boldsymbol{s}}\}_{\text{tan}} = -\boldsymbol{E}_{\text{inc,tan}}. \tag{2.11}$$

The induced current, and the incident field, can be used to solve the integral equation, by using the formulation described in (2.9). The MoM also has to mesh the antenna, to be able to solve it.

A sum of coefficients for the basis function, defined on the mesh, can be used to approximate the induced current as shown below,

$$\mathbf{J} = \sum_{n=1}^{M} \alpha_n \bar{f}_n. \tag{2.12}$$

The basis function is denoted as $\bar{f}_n$, and the unknown coefficients as α_n. When using the RWG basis functions, with each shared edge in the mesh having a single basis function associated with it, there are no artificial charge densities along the edges and the total charge in the mesh is zero. This makes modelling of the current densities easier. When using the approximation from (2.11) in (2.9), it creates a solution with a single equation and M unknowns. Note that the RWG functions are not used in all MoM solvers. While RWG is used in this dissertation for illustration, higher order basis functions can also be used.

The terms testing or weighting refers to the process of changing an integral equation to a set of linear equations. Weighting or testing is defined as follows,

Stellenbosch University https://scholar.sun.ac.za

$$\sum_{n=1}^{M} \alpha_n \iint_S w_m(\boldsymbol{r}) \cdot \mathcal{L}\{f_\mathrm{n}\}\, dS = \iint_S w_m(\boldsymbol{r}) \cdot \boldsymbol{E}_\mathrm{inc}\, dS \tag{2.13}$$

where the electric field is weighted and integrated over the testing function (w_m).

The integral equation can be tested using a Dirac delta function or a constant. It can also be tested by using Galerkin testing. Galerkin testing is when the basis function itself is used as the testing function. This form of testing constraints the boundary condition across the entire surface domain [35], unlike point matching [36]. It is also computationally simple.

Thus, by using a RWG, Galerkin, EFIE-based MoM to solve the surface current density, it generates a system of linear equations for a single antenna with M number of DoFs as follows,

$$\begin{bmatrix} Z_{11} & Z_{12} & Z_{13} & \dots & Z_{1M} \\ Z_{21} & Z_{22} & Z_{23} & \dots & Z_{2M} \\ Z_{31} & Z_{32} & Z_{33} & \dots & Z_{3M} \\ \vdots & \vdots & \vdots & \ddots & \vdots \\ Z_{M1} & Z_{M2} & Z_{M3} & \dots & Z_{MM} \end{bmatrix} \begin{Bmatrix} \alpha_1 \\ \alpha_2 \\ \alpha_3 \\ \vdots \\ \alpha_M \end{Bmatrix} = \begin{Bmatrix} v_1 \\ v_2 \\ v_3 \\ \vdots \\ v_M \end{Bmatrix}. \tag{2.14}$$

Furthermore, the system can be segmented per array element as follows,

$$\begin{bmatrix} \mathbf{Z}_{11} & \mathbf{Z}_{12} & \mathbf{Z}_{13} & \dots & \mathbf{Z}_{1N} \\ \mathbf{Z}_{21} & \mathbf{Z}_{22} & \mathbf{Z}_{23} & \dots & \mathbf{Z}_{2N} \\ \mathbf{Z}_{31} & \mathbf{Z}_{32} & \mathbf{Z}_{33} & \dots & \mathbf{Z}_{3N} \\ \vdots & \vdots & \vdots & \ddots & \vdots \\ \mathbf{Z}_{N1} & \mathbf{Z}_{N2} & \mathbf{Z}_{N3} & \dots & \mathbf{Z}_{NN} \end{bmatrix} \begin{Bmatrix} \mathbf{J}_1 \\ \mathbf{J}_2 \\ \mathbf{J}_3 \\ \vdots \\ \mathbf{J}_N \end{Bmatrix} = \begin{Bmatrix} \mathbf{V}_1 \\ \mathbf{V}_2 \\ \mathbf{V}_3 \\ \vdots \\ \mathbf{V}_N, \end{Bmatrix} \tag{2.15}$$

for an array of N disjoint antennas.

This formulation allows MoM to solve currents on each mesh element coupling with each other, as shown in Fig. 2.16, which PO does not. It also calculates scattering between the scatterers. MoM thus calculates for more non-ideal effects, compared to PO.

2.4 Conclusion

In this chapter it was shown that reflectors are designed from idealised geometric forms using Geometric Optics. Reflector antennas, however, do not be-

Stellenbosch University https://scholar.sun.ac.za

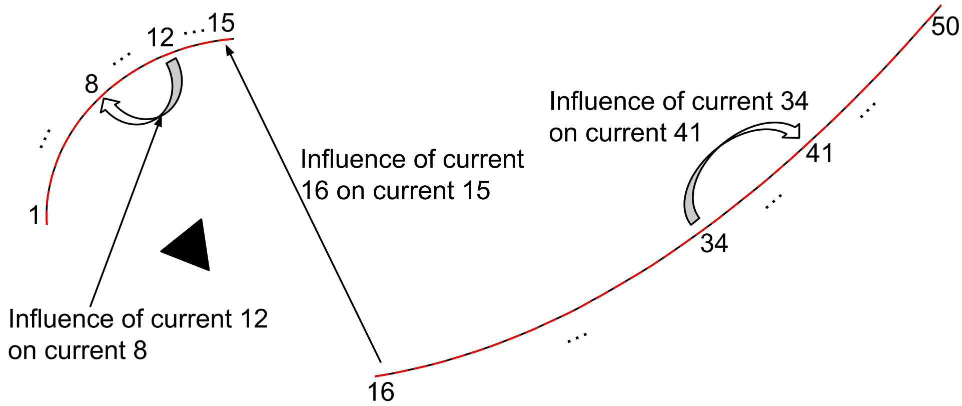

Figure 2.16: Coupling between currents is not taken into account using PO, but is when using MoM

have ideally and have non-ideal effects which cause extra radiation. When the electrical size of the reflectors reduces, these non-ideal effects become larger. Finally, the different analysis techniques and their ability to model non-ideal effects are discussed. These non-ideal effects will have an impact on the radiation pattern of the reflector system and will be discussed in detail next.

Stellenbosch University https://scholar.sun.ac.za

Chapter 3

Interference effects in antenna radiation patterns

Non-ideal effects influence the radiation pattern of the reflector system. This chapter will describe and discuss non-ideal effects, the interference process through which they influence the radiation pattern, and their influence on the radiation system response of a reflector system.

3.1 Non-ideal effects

There are many types of non-ideal effects. These effects include diffraction, spillover, self-coupling and re-radiation effects. Non-ideal effects, or radiation, occur when an antenna does not operate ideally. A reflector antenna operates ideally when it is infinitely large. Ideal radiation operates as described by GO, with PO and MoM able to account for non-ideal effects. As the electrical size of the reflector reduces, non-ideal effects become more pronounced. These non-ideal effects, and the reason for their occurrence, will be discussed in detail next.

3.1.1 Diffraction

Edge diffraction causes waves to bend around the edges of a metal surface, which causes radiation to occur in the shadow region behind the surface, as can be seen in Fig. 3.1. This effect occurs as surface currents induced on the edges of the reflector radiate spherical waves in all directions as can be seen in Fig. 3.2. This radiation behind the reflector is in contrast to the ideal GO description.

Stellenbosch University https://scholar.sun.ac.za

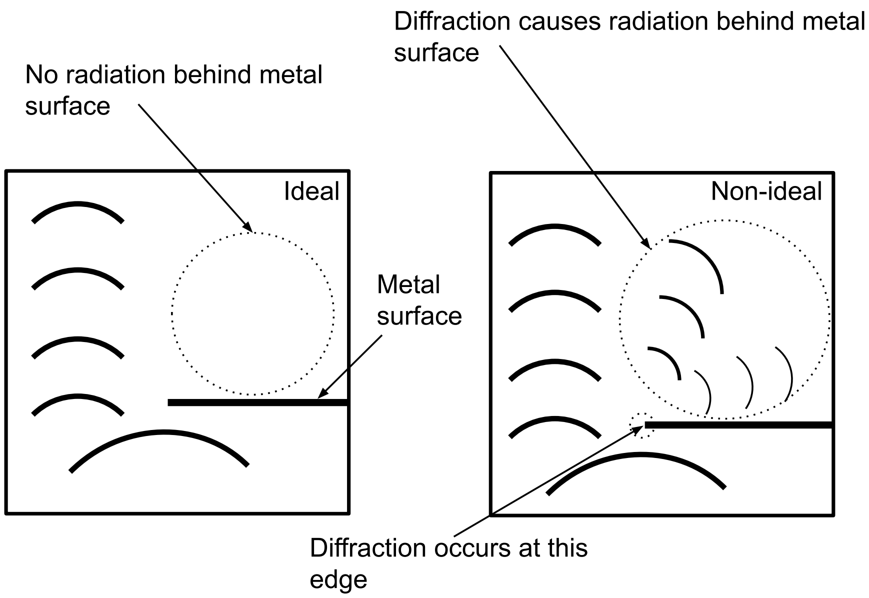

Figure 3.1: Diffraction occurring as waves travels over terminating metal surface

Edge diffraction effects become worse as the size of the reflector reduces. As the reflector size reduces, the ratio of the circumference over the area increases, as the area scales quadratically and the circumference linearly with radius. The normal radiating area will direct the energy as proposed by GO, while the radiation on the circumference will scatter the energy in all directions. As the size decreases, the ratio of energy being scattered in all directions, instead of being directed, will increase. This leads to more dominating non-ideal effects in the total radiation pattern response of the reflector system. In this case the frequency was adjusted to change the size of the reflector.

3.1.2 Spillover non-ideal effect

Spillover refers to radiation outside of the solid-angle of the ideal design as proposed by GO. This occurs for the ellipse, and the radiating feed, which can be seen in Fig. 3.3. Ideally, a feed would radiate similarly to the ideal ellipse radiation to illuminate only the reflector surface, however, practically this is impossible. Radiation from the back or sides of the feed is also non-ideal since it causes radiation outside of the solid-angle.

Stellenbosch University https://scholar.sun.ac.za

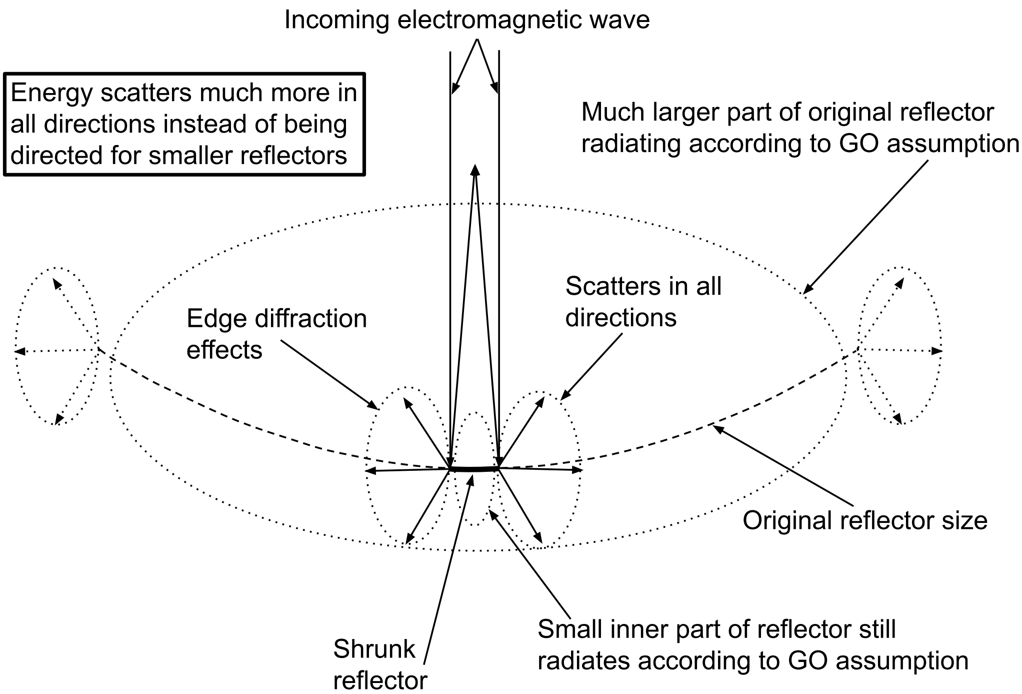

Figure 3.2: Electrically small reflector antennas scatter more energy in all directions, instead of in the designed direction, due to diffraction effects radiating energy in all directions and being more dominant in the total radiated field

As the size of the reflector or feed decreases, the spillover energy will increase. This is because the ability for the reflector or feed to radiate as desired reduces as the electrical size decreases, causing more energy to radiate in unintended directions.

3.1.3 Self-coupling non-ideal effect

The GO design, idealises a reflector surface scattering all the energy in a specific direction or set of directions, however, practically non-idealised radiation occurs in the form of self-coupling. This idealisation is used in PO as well. Self-coupling in this context refers to the reflector surface scattering energy to other parts of the same surface, causing additional radiation, as seen in Fig. 3.4. From Fig. 3.4, the radiation of one current influences the radiation of other currents, as described in Chapter 2. The matrix solution of MoM accounts for the influence of all currents, on all other currents. This non-ideal effect includes mutual coupling, which involves currents on different surfaces influencing each other.

Stellenbosch University https://scholar.sun.ac.za

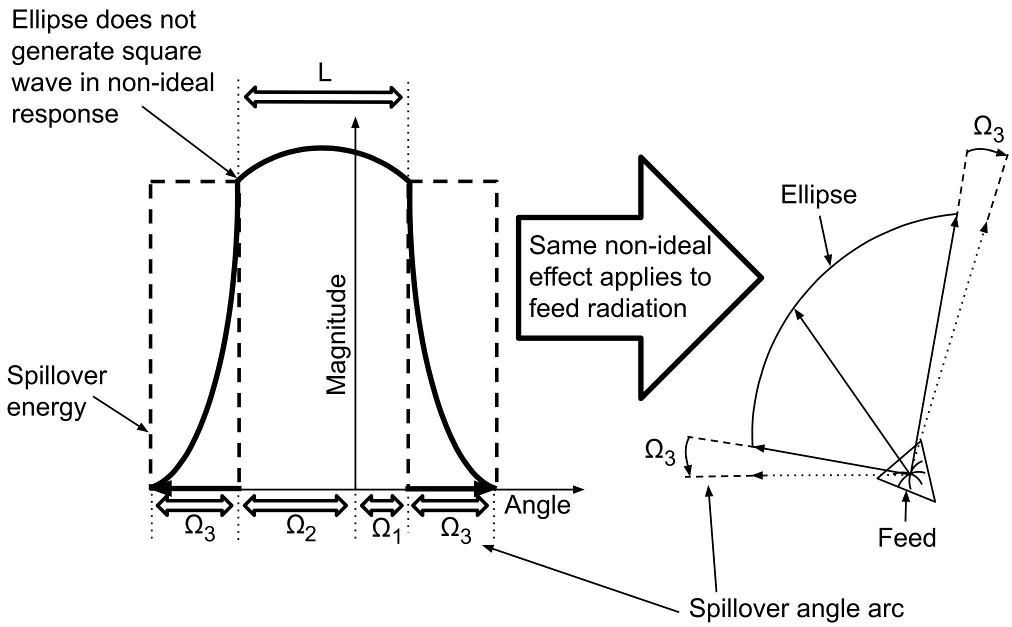

Figure 3.3: Spillover non-ideal radiation shown for ellipse and feed

The f/d ratio is a ratio used to design a parabolic reflector antenna and defines how deep or shallow a reflector dish is. The distance from the closest focal point of the reflector antenna where the feed would be positioned, to the apex of the reflector, is the focal length f. The diameter of the projected aperture is d. A smaller f/d ratio leads to a deeper dish, which is more curved. Increasing the focal length, while keeping the diameter constant, will result in a shallower and less curved dish as can be seen in Fig. 3.5. More coupling occurs for a smaller f/d ratio as a reflector antenna has a larger curvature, and more of the radiated energy is incident on the reflector surface, compared to a flatter curvature. This can be seen in Fig. 3.6.

If the shape of the reflector antenna is kept constant (no change in f/d ratio), with only its size increasing, it will lead to a less curved surface per unit length compared to a smaller reflector as can be seen In Fig. 3.7. Thus, as the reflector size increases, the non-ideal radiation from self-coupling decreases.

3.1.4 Re-radiation non-ideal effect

The re-radiation non-ideal effect occurs from reflections within the reflector system, which also creates standing waves, and will be discussed next.

Stellenbosch University https://scholar.sun.ac.za

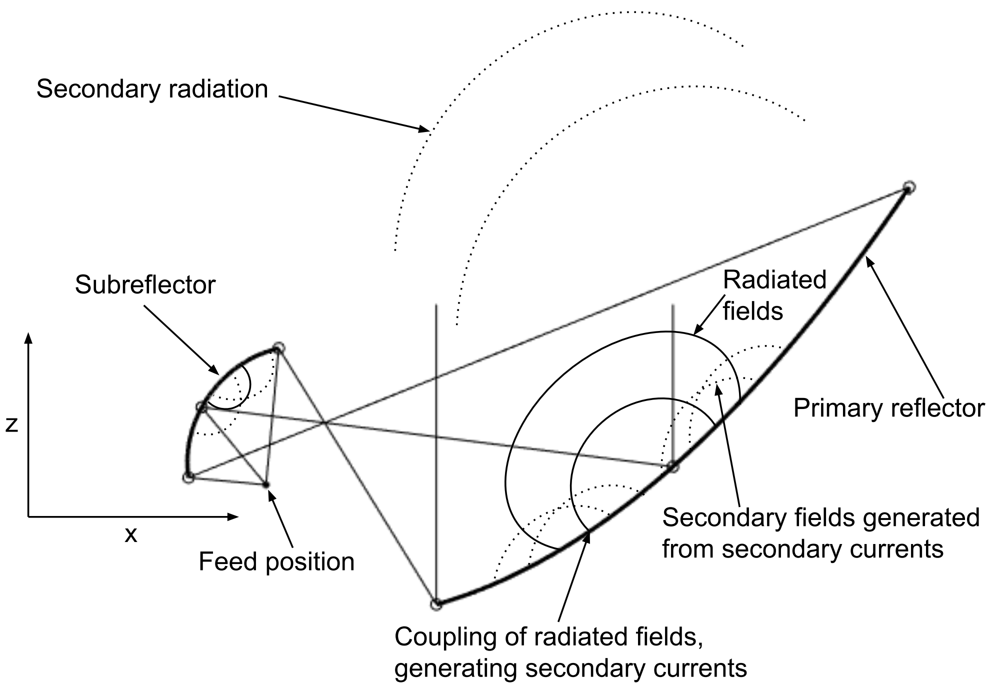

Figure 3.4: Self-coupling causing secondary radiation in reflector systems

3.1.4.1 Standing waves

In Fig. 3.8 the formation of standing waves are shown. When energy travels from one medium into the next, some or all of the energy can be reflected. This depends on how similar the impedance, or how well matched, the second medium is compared to the first, and in this case medium two is completely mismatched. This mismatch causes all the energy to get reflected back into medium one, with no energy entering medium two. The reflected wave moves in the opposite direction of the incident wave over time. As they superimpose, the resulting standing wave is formed. The standing wave does not propagate in a direction, but oscillates in the orthogonal direction of the reflected and incident waves' propagation over time.

In reflector systems, medium one can be the region between the reflector and the horn, where medium two can be the region between the horn and the receiver. The reflection can happen inside the receiver or between the horn and the receiver, when they are mismatched. In reality, many systems are not completely mismatched and some of the incident energy will pass into the second medium, which will result in the reflected energy being less and the standing wave being smaller. A standing wave can also occur between the primary reflector and secondary reflector. In the ideal case, no standing wave

Stellenbosch University https://scholar.sun.ac.za

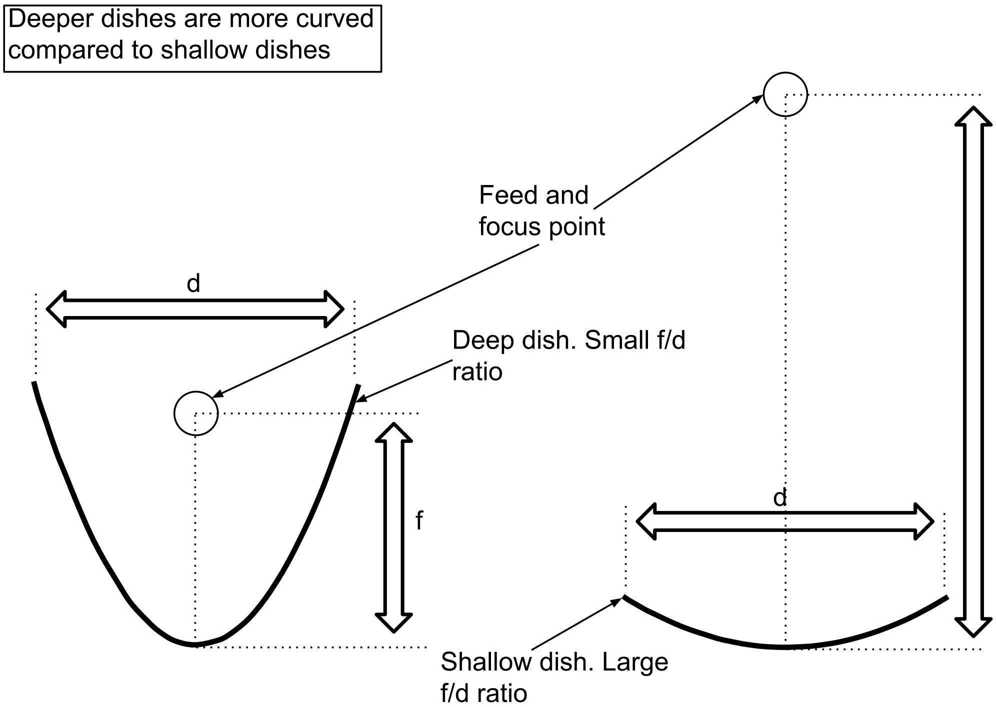

Figure 3.5: Deeper dishes, which are more curved, are generated by using a smaller f/d ratio for reflectors

occurs and all the energy is received.

The standing wave forming between the feed and the reflector antenna (or between different reflectors) is a near-field effect and can be seen in Fig. 3.9. The near-field relates to field effects close to the reflector system, where the far-field relates to field effects further away. The radiation pattern of a reflector system is usually calculated in the far-field. This is because it is expected that the energy will be transmitted (or received) to a receiver (from a source) far away, where the field effects close to the system is not important. While the mutual coupling forms a standing wave in the near-field, the effect in the far-field might not be a traditional standing wave. The effect, however, is similar. A ripple over frequency will form, which is described in detail later.

3.1.4.2 Re-radiation

The formation of a standing wave is due to the reflection of energy from a mismatch. Thus, when a standing wave exists, there is reflected energy. This reflected energy from the receiver will re-radiate the reflector as shown in Fig. 3.10. Some of the initial energy radiated from the horn to illuminate the re-

Stellenbosch University https://scholar.sun.ac.za

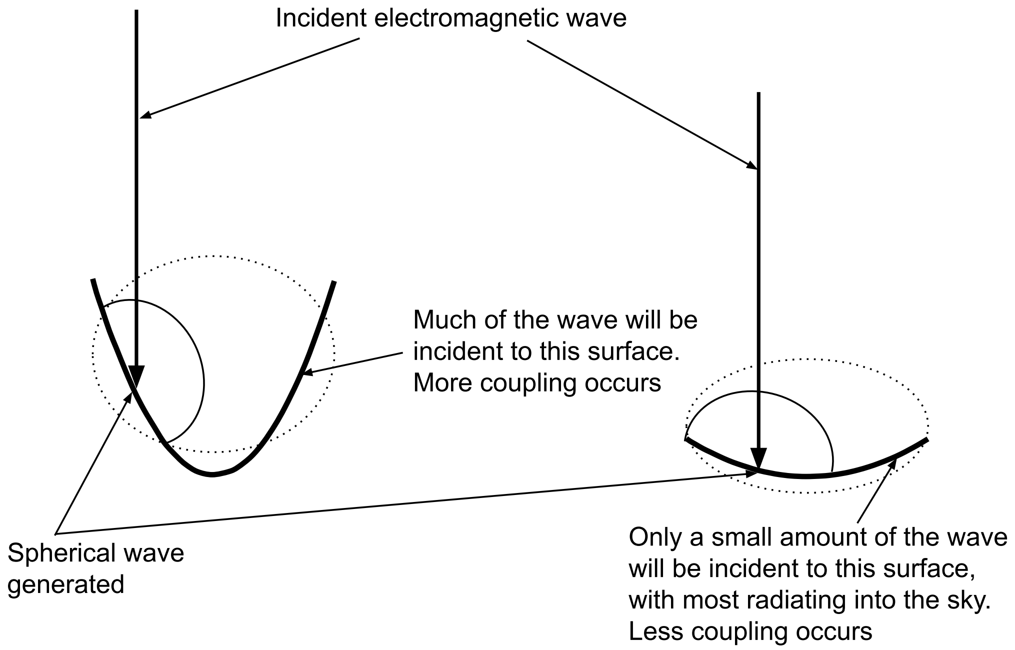

Figure 3.6: Larger curvature for reflector leads to more coupling, because more of the radiating wave gets intercepted by the reflector surface, compared to a flatter reflector

flector gets scattered back into the horn, as the reflector radiates. The receiver will generally be mismatched to some degree, since there are too many effects to match for, and energy will then be reflected back into the horn from the receiver. The horn will then re-illuminate the reflector, which will cause the reflector to re-radiate.

Reducing the size of the reflector antenna will have little direct effect on re-radiation, as re-radiation is a non-ideal effect due to system mismatches. Indirectly, however, it could impact the re-radiation. A size increase will likely improve the ability of the reflector antenna to direct energy, causing less energy to scatter in unwanted directions. If the feed is positioned outside of the primary direction of radiation of the reflector system, as shown previously in the Gregorian dual reflector system, less energy will scatter back into the horn after radiation. This will reduce the amount of energy that can reflect and cause less re-radiation.

These non-ideal effects impact the radiation pattern response of the reflector system through the process of interference, which will be discussed next.

Stellenbosch University https://scholar.sun.ac.za

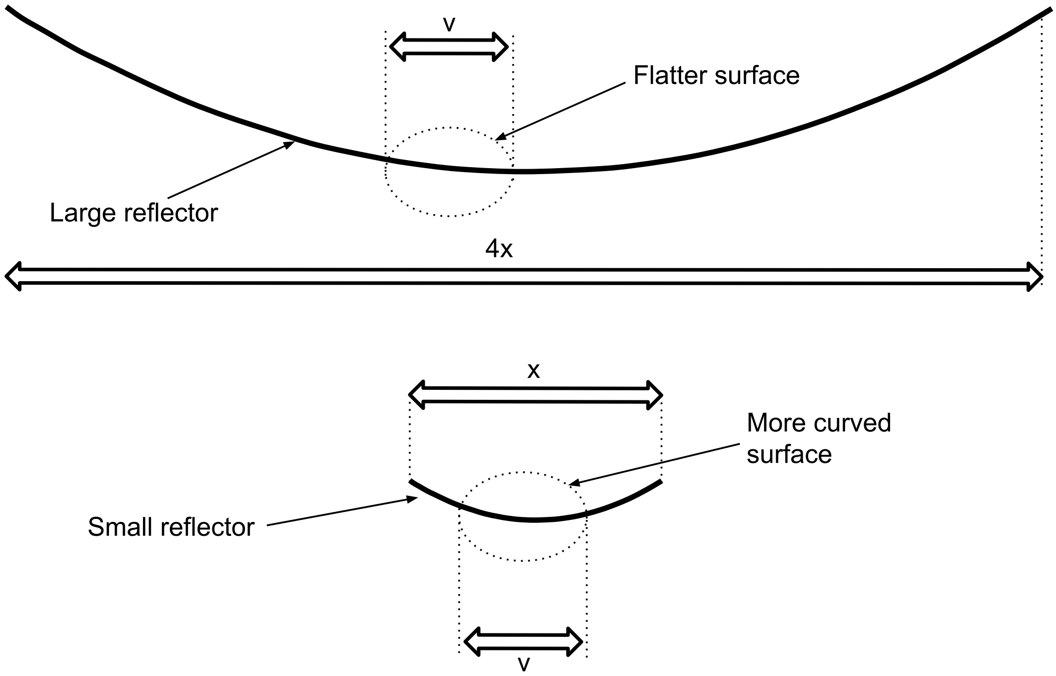

Figure 3.7: Electrically larger reflector antennas have less curvature per unit length, compared to smaller reflector antennas. This leads to a flatter surface per unit length compared to smaller reflector antennas

3.2 Wave interference

Interference is the addition of signals or (electromagnetic) waves in space. These terms will be used interchangeably. The effect happens when signals occupy the same space, which results in the signals combining to form a single signal at the collision location, which is the sum of the signals occupying the space. The combined signal is a function of the individual signals' phases and amplitudes at the interfering location. Higher amplitudes and different relative phases will result in a significantly different combined signal, compared to the original interfering signals.

3.2.1 Interference first principles and relation to reflector antenna radiation

Interference can be described with the addition of vectors in space. In Fig. 3.11 the process of adding vectors in a 2D space is shown, specifically in the complex plane. This is because it is fully descriptive for the interference interaction investigated in this dissertation, as electromagnetic waves and their

Stellenbosch University https://scholar.sun.ac.za

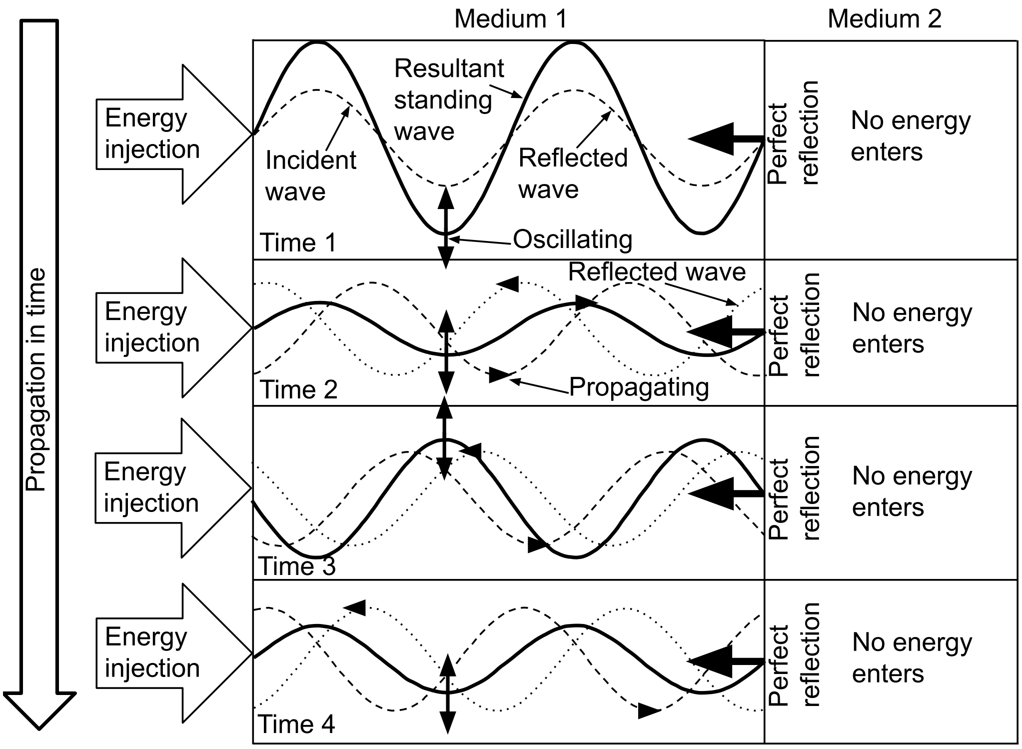

Figure 3.8: The formation of standing waves

interaction can be fully described in the complex plane. In theory, these concepts described here expands to vectors in any n-dimensional space.

The vectors $\boldsymbol{V_1}$ and $\boldsymbol{V_2}$ each represents an arbitrary vector in 2D space, with relatively different phases and magnitudes. In this case, the vector $\boldsymbol{V_3}$ is the sum of the vectors $\boldsymbol{V_1}$ and $\boldsymbol{V_2}$. To calculate the magnitude of $\boldsymbol{V_3}$ the Pythagoras theorem is used, and the angle of $\boldsymbol{V_3}$ is obtained using trigonometry, as shown below for quadrants one and two,

$$\boldsymbol{V_3} = \boldsymbol{V_1} + \boldsymbol{V_2}, \tag{3.1}$$

where, each vector can be represented with $A_n e^{j(wt+\sigma_n)}$ as,

$$\boldsymbol{V_1} = A_1 e^{j(wt+\sigma_1)}, \tag{3.2}$$
$$\boldsymbol{V_2} = A_2 e^{j(wt+\sigma_2)}, \tag{3.3}$$

where j is the imaginary unit, $w = 2\pi f$ the angular velocity, f is the frequency, t is time, A is the magnitude, and σ is the phase shift. This results in,

$$\boldsymbol{V_3} = A_1 e^{j(wt+\sigma_1)} + A_2 e^{j(wt+\sigma_2)}, \tag{3.4}$$

Stellenbosch University https://scholar.sun.ac.za

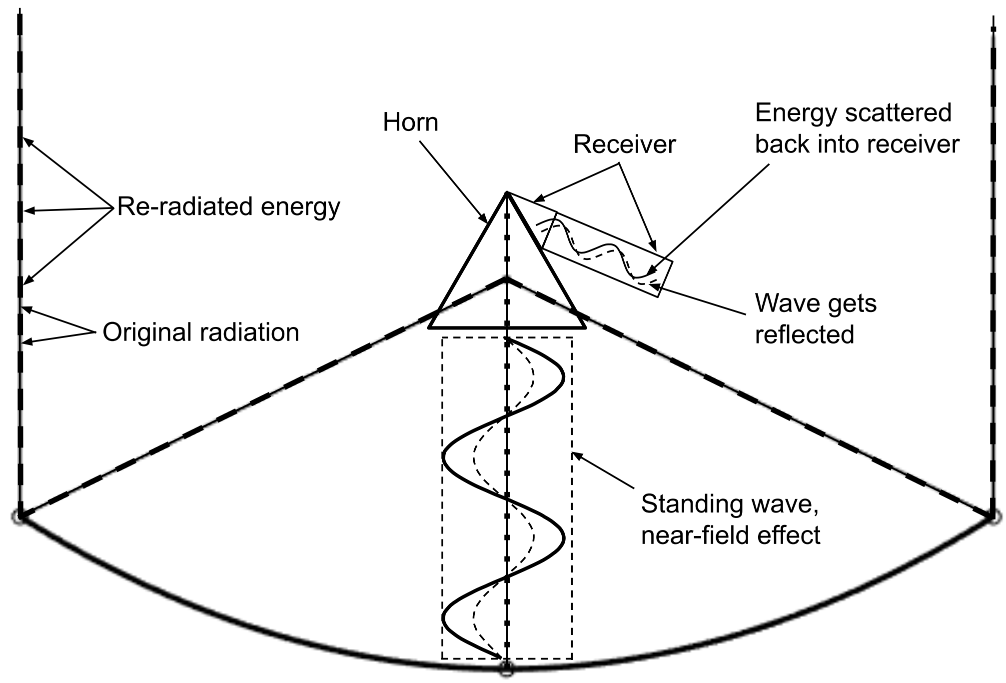

Figure 3.9: Standing waves form and they are a near-field effect

which expands into,

$$\boldsymbol{V_3} = A_1 e^{jwt} e^{j\sigma_1} + A_2 e^{jwt} e^{j\sigma_2}, \tag{3.5}$$

and factorises into,

$$\boldsymbol{V_3} = (A_1 e^{j\sigma_1} + A_2 e^{j\sigma_2}) e^{jwt}, \tag{3.6}$$

which simplifies to,

$$\boldsymbol{V_3} = A_3 e^{j(wt+\sigma_3)}, \tag{3.7}$$

or,

$$\boldsymbol{V_3} = A_3 e^{j\sigma_3} e^{jwt}, \tag{3.8}$$

where A_3 and σ_3 is the magnitude and phase shift, respectively, of the combined vector $\boldsymbol{V_3}$, with,

Stellenbosch University https://scholar.sun.ac.za

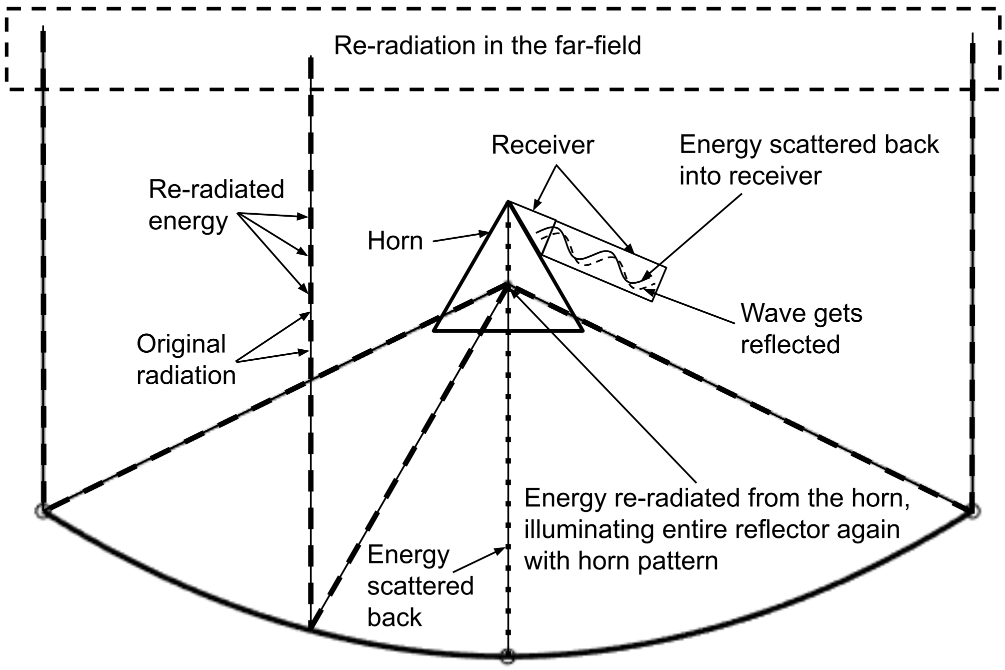

Figure 3.10: How re-radiation occurs and that it is a far-field effect

$$e^{j\sigma_3} = \arccos\left(\frac{(\Re(\boldsymbol{V_3}))}{A_3}\right), \tag{3.9}$$

where $\Re$ is the real component and,

$$\Re(\boldsymbol{V_3}) = \Re(\boldsymbol{V_2}) + \Re(\boldsymbol{V_1}), \tag{3.10}$$

where the real component of $\boldsymbol{V_3}$ is thus simply the addition of the real components of each of the vectors. Finally A_3 expands to,

$$A_3 = (\Re(\boldsymbol{V_2}) + \Re(\boldsymbol{V_1}))^2 + (\Im(\boldsymbol{V_1}) + \Im(\boldsymbol{V_2}))^2, \tag{3.11}$$

where $\Im$ is the imaginary component.

In this dissertation time-harmonic electromagnetic fields or waves are assumed. Electromagnetic waves propagate when the source currents vary quickly in time. In the case of steady sinusoidal time variation for source currents, all resulting waves must also be time-harmonic. A steady sinusoidal time varying source current can be described as [32],

Stellenbosch University https://scholar.sun.ac.za

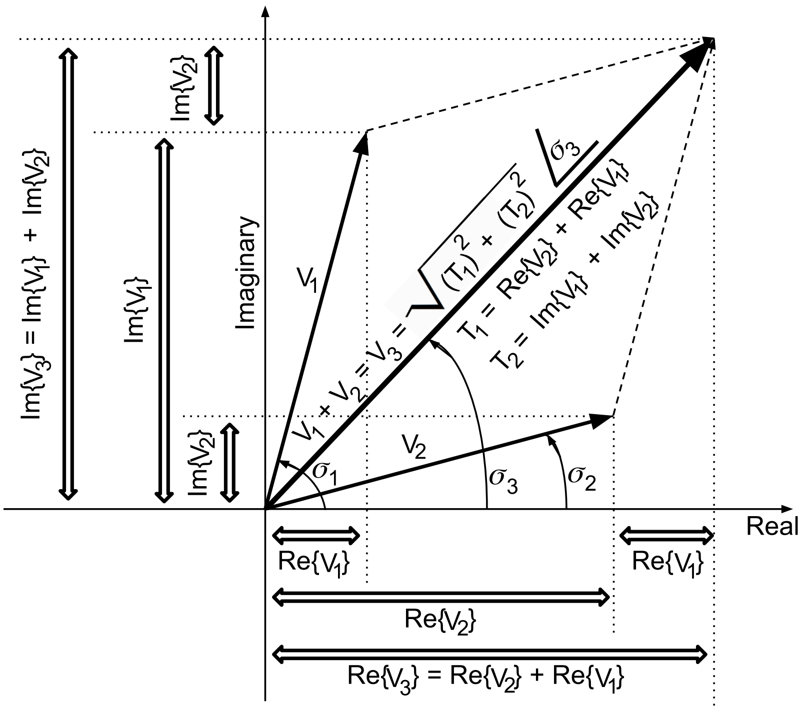

Figure 3.11: Mathematical process of adding vectors

$$\cos(wt + \phi) = \Re(e^{j(wt+\phi)}), \tag{3.12}$$

where ϕ is phase in radians. The instantaneous values of the electromagnetic waves can be rewritten as,

$$\overline{\boldsymbol{E}}(x, y, z, t) = \Re(\boldsymbol{E}(x, y, z)e^{jwt}), \tag{3.13}$$
$$\overline{\boldsymbol{H}}(x, y, z, t) = \Re(\boldsymbol{H}(x, y, z)e^{jwt}), \tag{3.14}$$

because the waves are generally vector functions of space and time. The E field is denoted by $\boldsymbol{E}$, and the H field by $\boldsymbol{H}$, but electromagnetic waves will be discussed in more detail later in this chapter. The waves are time-harmonic and can be expressed as time-harmonic vector fields of the form,

$$\boldsymbol{E} = E_x(x, y, z)\hat{\boldsymbol{x}} + E_y(x, y, z)\hat{\boldsymbol{y}} + E_z(x, y, z)\hat{\boldsymbol{z}}, \tag{3.15}$$

where $E_x(x, y, z)\hat{\boldsymbol{x}}$, $E_y(x, y, z)\hat{\boldsymbol{y}}$ and $E_z(x, y, z)\hat{\boldsymbol{z}}$ are all complex functions. Due to this, only the real part is used to describe the waves in this dissertation.

The Maxwell equations describing electromagnetic waves are linear, implying electromagnetic waves are linear, in linear mediums such as free space. The interaction between electromagnetic waves are thus also linear. The implication

Stellenbosch University https://scholar.sun.ac.za

of this is that only waves with the same frequency can interact, or interfere. While interference effects can only occur between waves with the same frequency, these effects are often between waves with different phases.

Consider an arbitrary vector,

$$\boldsymbol{V_p} = A_p e^{j\sigma_p} e^{jwt}. \tag{3.16}$$

If time increases from t_1, to t_2, the angle of the vector will increase, $e^{j\sigma_p} e^{jwt_2} > e^{j\sigma_p} e^{jwt_1}$. As time progresses, the vector rotates around the origin of the coordinate system at an angular rate of w. The value of the real component of the vector will oscillate as the vector spins over time, which will produce a cosine function waveform, and is shown in Fig. 3.12. An arbitrary cosine function, C_p, can be described as,

$$C_p = \Re(Ae^{j(wt+\sigma_0)}), \tag{3.17}$$

$$C_p = A\text{cos}(wt + \sigma_0). \tag{3.18}$$

Finally, a higher angular velocity w (or faster spinning vector) will increase the frequency f, as shown in Fig. 3.13.

In Fig. 3.14 a propagating plane wave is shown. The wave has an electric field component, or E field, which is described in (3.19). It also has a magnetic field component, or H field, as described in (3.20). The wave impedance in freespace is $\eta = 377\ \Omega$, the wavenumber is $k = \frac{2\pi}{\lambda}$, and the wavelength is $\lambda = \frac{c}{f}$. The speed of light, or phase velocity, in freespace $c = 2.99790 \times 10^8\ \frac{m}{s}$. E_x and E_y each denotes E fields in each direction respectively in the Cartesian plane, with the unit vectors denoted as $\hat{\boldsymbol{x}}$ and $\hat{\boldsymbol{y}}$. The direction of propagation is z [32]. Furthermore, each wave component presents as a propagating cosine function.

$$\boldsymbol{E} = \boldsymbol{E_t} e^{-jkz} = [E_x\hat{\boldsymbol{x}} + E_y\hat{\boldsymbol{y}}]e^{-jkz} \tag{3.19}$$

$$\boldsymbol{H} = \frac{1}{\eta}\hat{\boldsymbol{z}} \times \boldsymbol{E} = \frac{1}{\eta}\hat{\boldsymbol{z}} \times \boldsymbol{E_t} e^{-jkz} = \frac{1}{\eta}[-E_y\hat{\boldsymbol{x}} + E_x\hat{\boldsymbol{y}}]e^{-jkz} \tag{3.20}$$

The region closest to the antenna is called the reactive near-field and is dominated by reactive fields. The region just beyond the reactive fields, is the radiating near-field region. The region beyond the radiating near-field, extending to infinity, is called the far-field. The near-field region is defined up to a distance smaller than $\frac{2D^2}{\lambda}$ from the antenna, where λ is the wavelength,

Stellenbosch University https://scholar.sun.ac.za

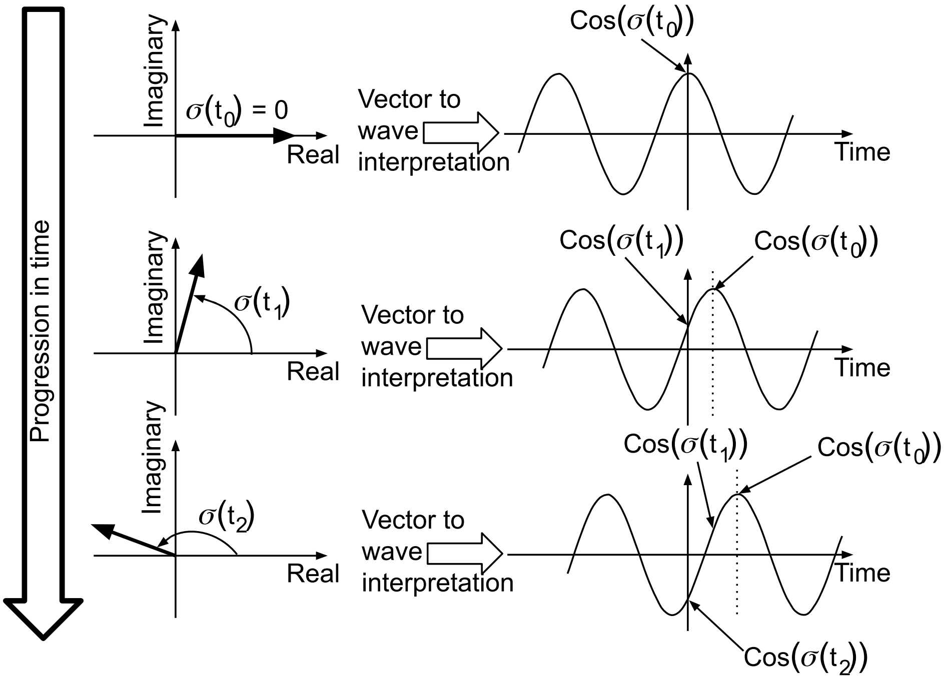

Figure 3.12: Link between vectors and cosine functions

and D is the circle with the smallest diameter, that can enclose the antenna structure. For reflector antennas, however, it is usually acceptable to assume D is the aperture diameter of the antenna. This assumption might become less accurate for small offset systems.

The far-field region is dominated by radiating fields and is also independent of the radial component of the field or distance from the antenna. This is because reactive fields become negligible in the far-field. The region between the near-field and the far-field is the transition region.

Due to the reciprocity theorem, radiation received from far away from the antenna is also in the far-field. This is usually the case, which is why the far-field radiation pattern is usually simulated and used in design. For the work discussed in this dissertation, radiation is often from the sky which is far away from the antenna and thus in the far-field. For this reason, the far-field radiation pattern is preferred.

When electromagnetic waves propagate from a source, such as a reflector feed, they start to imitate a plane wave when they have travelled far enough and is in the far-field. This is shown in Fig. 3.15. The field variation along the

Stellenbosch University https://scholar.sun.ac.za

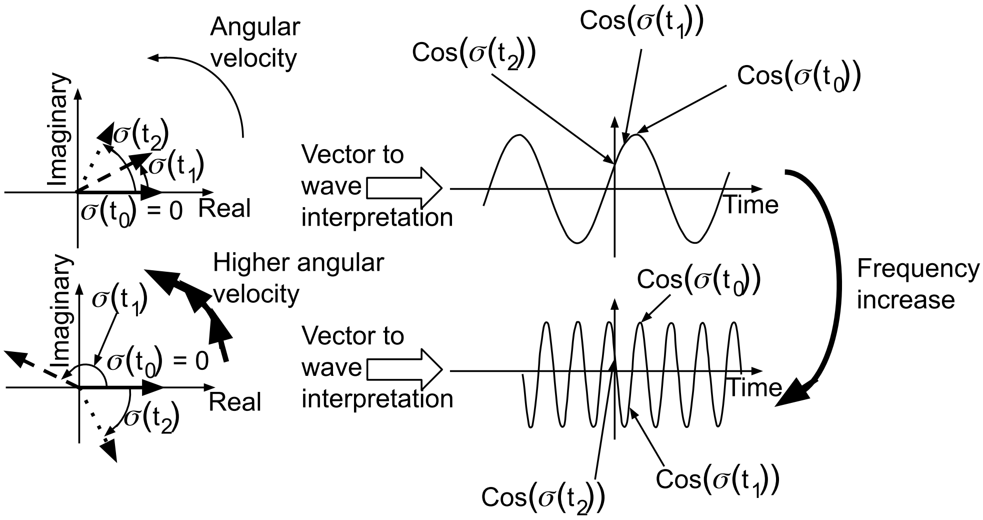

Figure 3.13: Angular velocity of vector effect on wave

direction of propagation is assumed to be negligible in the far-field region. Antennas thus generate plane waves, with components presenting as cosine functions, in the far-field as shown in Fig. 3.16.

3.2.2 Wave phase effect on type of interference occurring

Interference between waves can range from perfect constructive to perfect destructive interference, with general interference occurring between these extremes. In Fig. 3.17 perfect constructive interference is shown. This is the case where the vectors or waves have exactly the same phases, resulting in a wave with an amplitude which is the sum of each individual interfering wave. In Fig. 3.18 perfect destructive interference is shown. This is the case where the vectors or waves are completely out of phase, resulting in a wave with an amplitude which is the difference of each individual interfering wave. In Fig. 3.19 general interference is shown. This is the general case where the vectors or waves have different relative phases, resulting in a wave with an amplitude which is the sum or difference of each individual interfering wave and with a different phase compared to each individual interfering wave. All these vectors

Stellenbosch University https://scholar.sun.ac.za

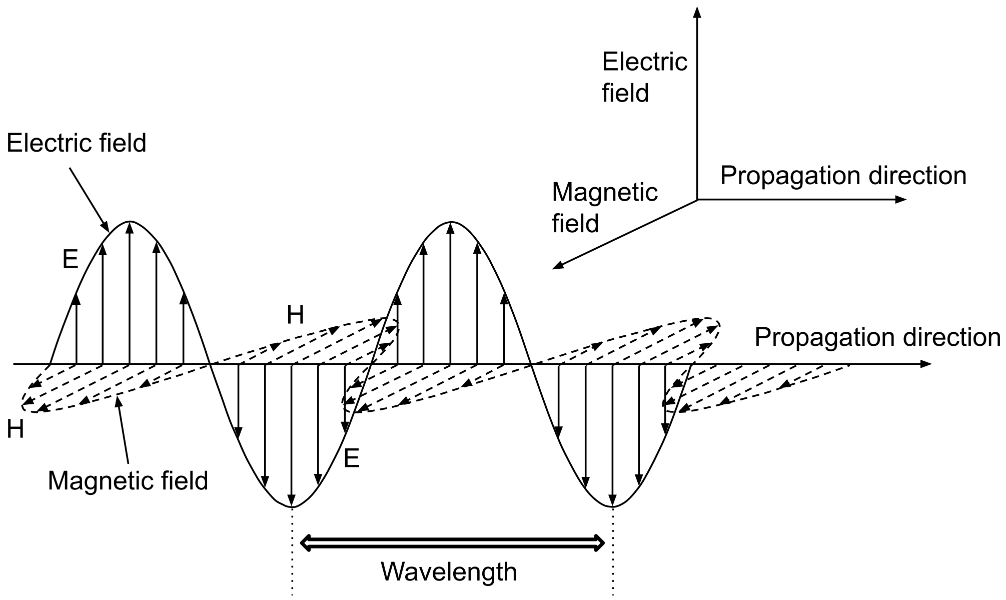

Figure 3.14: Plane waves linked to cosine function

or waves discussed here have the same angular velocity or frequency.

3.2.3 Interference source position effect

Non-co-located sources will cause phase interference effects due to the different apparent path lengths that plane waves travel to a common observation point. This type of radiation occurs for the feed of the reflector system, in the ideal case, and will later be used in a ray tracing approach to explain the ripple phenomenon on the radiation pattern. In this chapter, these types of sources will be assumed. Fig. 3.20 shows the different cases. If the relative path length differs between the waves, it will cause different individual phases in the locations they interfere, which will cause different interference results.

3.2.4 Interference requires at least two sources

Multiple non-co-located (or co-located) sources can cause interference effects. The simplest form of interference happens between two sources. A scatterer can also be seen as a source of energy radiation, for the purpose of interference analysis, as it scatters energy. A simple example of a situation that can cause

Stellenbosch University https://scholar.sun.ac.za

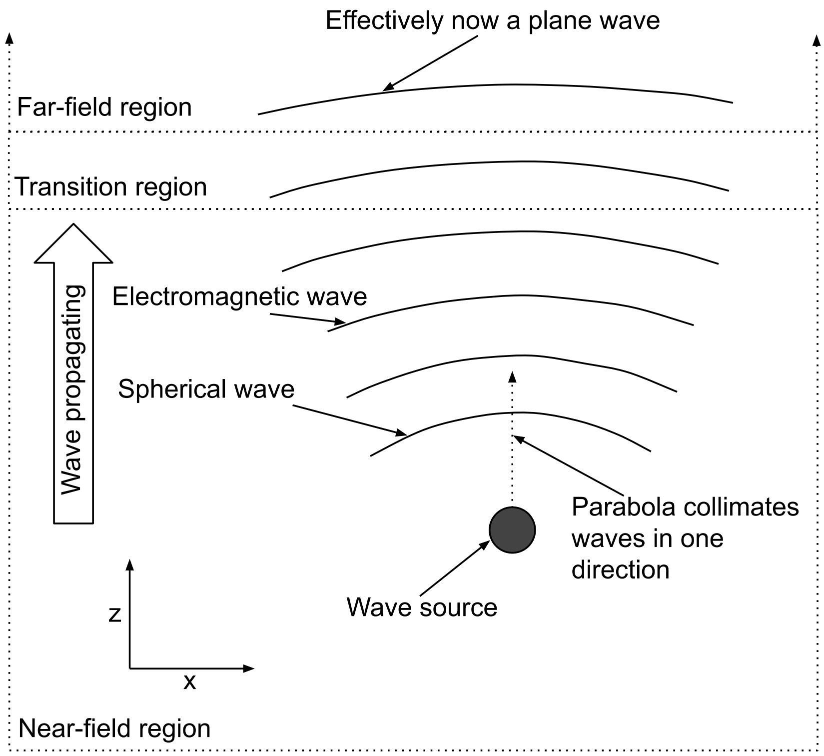

Figure 3.15: Electromagnetic waves become plane waves after travelling far enough

interference is a single source radiating energy, and a scatterer reflecting it. The interference happens because the scatterer redirects waves back into the paths of radiation of the source.

Interference can also occur between two sources if they are co-located. If the sources radiate waves with the same frequency and initial phase, then perfect constructive interference will occur, while general interference will occur for sources with different phases and amplitudes.

A symmetric single reflector is a good example of a physical configuration causing interference, by using a single source and a single scatterer, and supports why interference occurs within reflector systems. For example, radiation from the back of the feed can interfere with the scattered fields from the reflector.

Far-field interference is dependent on the angle of observation, and the interference effects of importance in this dissertation is in the far-field. This dependence is illustrated through Fig. 3.21, where the interference is caused between the (red) diffracted wave, and the (blue) radiation as predicted by GO. The path length difference between these rays determine the effect of the interference, and changing the angle of observation will change these path

Stellenbosch University https://scholar.sun.ac.za

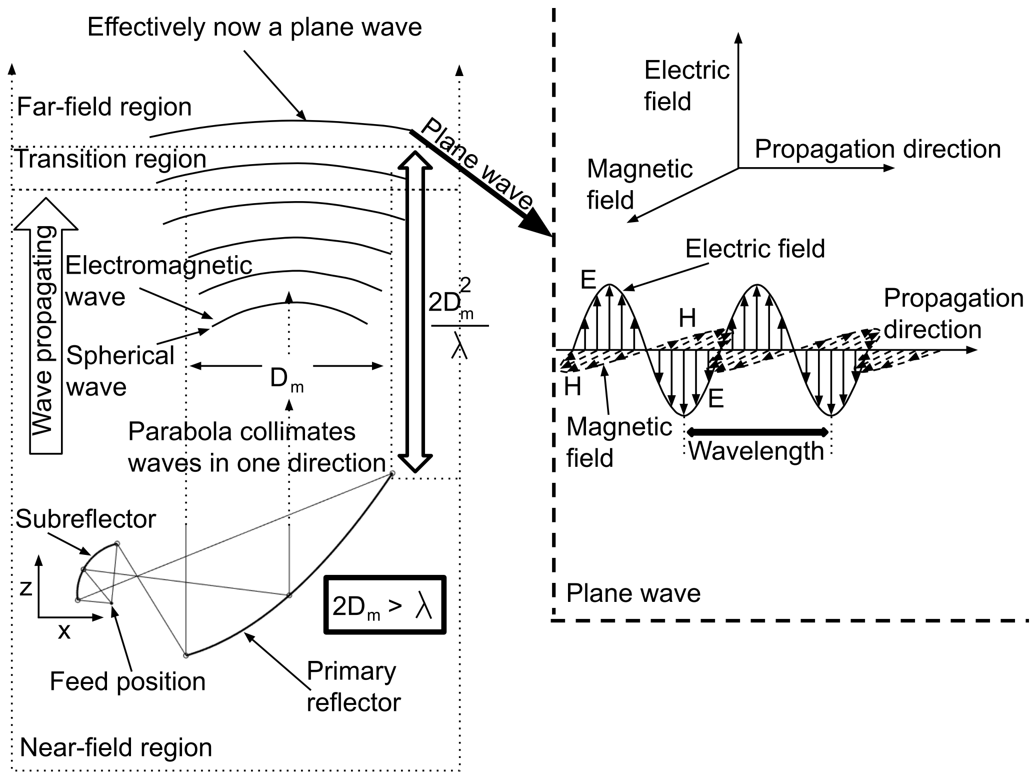

Figure 3.16: Reflector generates plane waves in far-field

length differences.

As multiple sources will also cause interference, it also applies to multi reflector setups. Interference is a linear process that uses superposition, and thus there will just be more interference occurring. All physical reflector systems have non-co-located sources and will usually experience general interference.

3.2.5 Interference function of angle: Wave phase

As non-co-located sources will generally cause interference between waves with different phases, Fig. 3.22 shows how interference is a function of phase, which is a function of angle. The relative phases of the waves will be a function of the angle between their propagation directions, and the joining line between the non-co-located sources. It is possible for the waves to still have the same phases, even if they do not come from co-located sources, if their individual propagation axis' are both orthogonal to a joining line between their sources. This can be seen in Fig. 3.22. Their relative phases are also a function of the frequency of the waves and the path length difference between the waves.

Stellenbosch University https://scholar.sun.ac.za

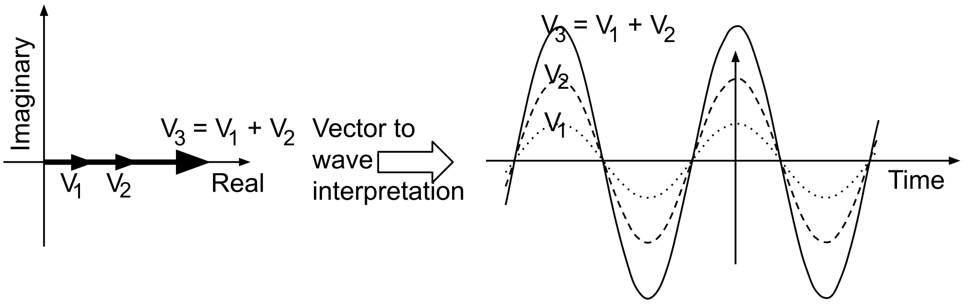

Figure 3.17: Perfect constructive interference

3.2.6 Interference function of angle: Wave amplitude

While interference is a function of wave phase, it is also a function of wave amplitude, which is generally a function of angle around a specified source. Interfering waves will occur in all directions for a reflector system, as some energy scatters or radiates in all directions, while most energy scatters or radiates in the direction of maximum radiation of the reflector system.

The interference experienced will depend on the interfering waves. Different non-ideal effects and their magnitudes are experienced in different directions. The reflectors also radiate differently across angle, and this radiation interferes with the non-ideal effect radiation. The resulting wave amplitude, due to these interfering waves, will vary over angle and is thus strong function of direction. Interference is thus a strong function of angle, which will become an important concept in the next chapter.

Stellenbosch University https://scholar.sun.ac.za

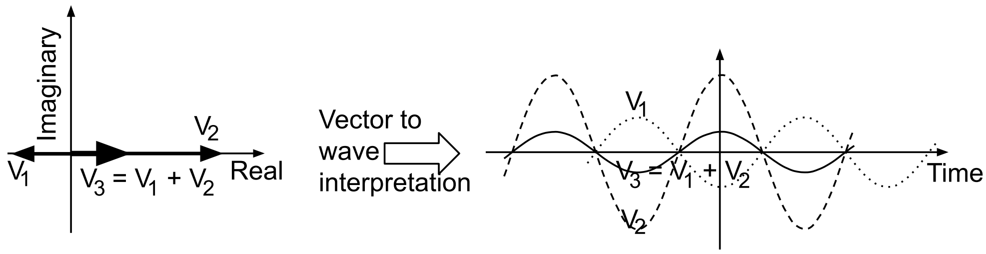

Figure 3.18: Perfect destructive interference

3.3 Effect of interference on radiation pattern

Assume the frequency of a wave were to increase by a factor n, then the wavelength would shrink by a factor n, as shown in (3.21), and visually in Fig. 3.23.

$$\frac{\lambda}{n} = \frac{c}{nf} \tag{3.21}$$

When the wavelength decreases or the frequency increases by a factor n, it effectively shifts the wave on its propagation axis z by a factor n, as each position on the axis will now have a new phase value. This can be observed in Fig. 3.23, and also mathematically below,

$$nk = \frac{2\pi}{\frac{\lambda}{n}}, \tag{3.22}$$

$$nk = \frac{n2\pi}{\lambda}, \tag{3.23}$$

$$\boldsymbol{E_s} = \boldsymbol{E_t}e^{-j(nk)z} = [E_x\hat{\boldsymbol{x}} + E_y\hat{\boldsymbol{y}}]e^{-j(nk)z}, \tag{3.24}$$

$$\boldsymbol{E_s} = [E_x\hat{\boldsymbol{x}} + E_y\hat{\boldsymbol{y}}]e^{-jk(nz)}. \tag{3.25}$$

Stellenbosch University https://scholar.sun.ac.za

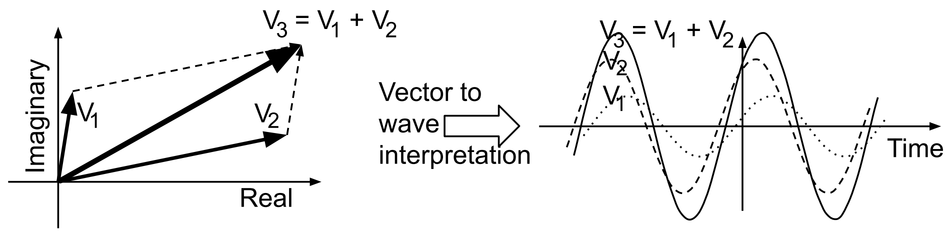

Figure 3.19: General interference

Conversely, shifting a wave in its propagation axis, leads to a different phase value for each position on the axis. If two waves interfere with one wave relatively shifted compared to the other, it will lead to a different interference result depending on how much the wave is shifted, as the waves will probably have different phase values where they interfere.

Consider two waves that interfere, with identical frequencies. The one wave has a shorter propagation path compared to the other, as described visually in Fig. 3.24. The first wave can be described as,

$$\boldsymbol{E_1} = \boldsymbol{E_{t1}} e^{-jkz}. \tag{3.26}$$

The second wave, $\boldsymbol{E_2}$, experiences a shift of a in the propagating axis, which leads to a phase shift, and can be described as,

$$\boldsymbol{E_2} = \boldsymbol{E_{t2}} e^{-jk(z+a)}. \tag{3.27}$$

The interference of the two waves create $\boldsymbol{E_3}$,

$$\boldsymbol{E_3} = \boldsymbol{E_1} + \boldsymbol{E_2} = \boldsymbol{E_{t1}} e^{-jkz} + \boldsymbol{E_{t2}} e^{-jk(z+a)}, \tag{3.28}$$

Stellenbosch University https://scholar.sun.ac.za

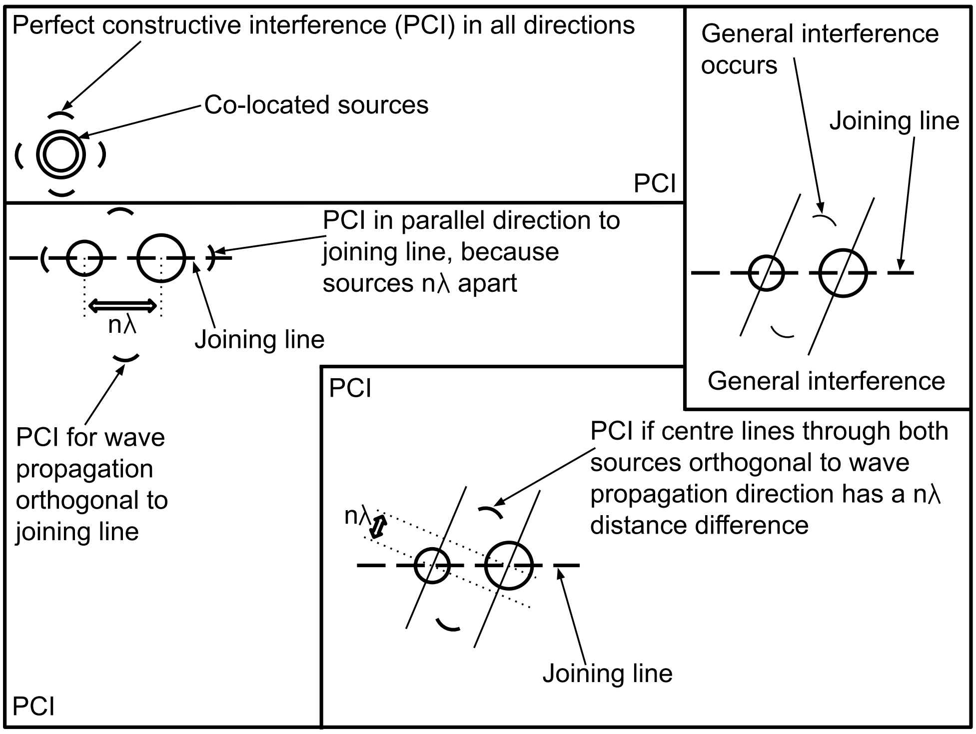

Figure 3.20: Possible interference effects for co- and non-co-located sources

which expands to,

$$\boldsymbol{E_3} = \boldsymbol{E_{t1}} e^{-jkz} + \boldsymbol{E_{t2}} e^{-jkz} e^{-jka}, \tag{3.29}$$

and can be rewritten as,

$$\boldsymbol{E_3} = (\boldsymbol{E_{t1}} + \boldsymbol{E_{t2}} e^{-jka}) e^{-jkz}, \tag{3.30}$$

or as,

$$\boldsymbol{E_3} = \boldsymbol{M_3} e^{-jkz}, \tag{3.31}$$

where the amplitude of $\boldsymbol{E_3}$ can be described as,

$$\boldsymbol{M_3} = \boldsymbol{E_{t1}} + \boldsymbol{E_{t2}} e^{-jka}. \tag{3.32}$$

The phase term, e^{-jka}, can be unpacked as shown in (3.33) below, which translates to a spinning vector in the complex plane as k (or a) increases, shown in Fig. 3.25,

Stellenbosch University https://scholar.sun.ac.za

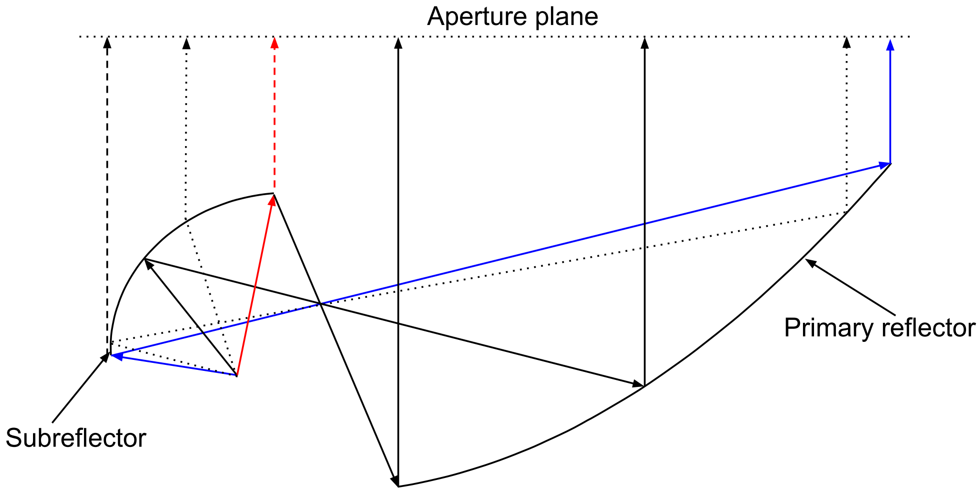

Figure 3.21: Far-field interference shown for a dual reflector system

$$e^{-jka} = \cos(-ka) + j\sin(-ka) = \cos(ka) - j\sin(ka), \tag{3.33}$$

where the real component of this vector is a cosine function. This cosine function is periodic, and thus the added phase shift of e^{-jka} will also be periodic. The component, e^{-jka}, will cause $\boldsymbol{M_3}$ to oscillate over frequency, due to constructive and destructive interference of the terms in $\boldsymbol{M_3}$, as k is a function of frequency. If a is larger, it will cause the vector e^{-jka} to have a higher angular velocity, or spin faster, as the frequency is steadily increased over a band. The variation in $\boldsymbol{M_3}$ presents as a ripple over frequency, and can be seen in Fig. 3.26.

The relative position a between the two wave origins can be assumed constant, in a specific direction, for this dissertation. This is because in the context of reflector systems, the origin of each interfering wave is dependent on the position of the components in the system, and the angle in which the interference occurs. In this case, the interference direction was in the z-axis. The relative position of the components to each other, do not change after they are constructed.

Stellenbosch University https://scholar.sun.ac.za

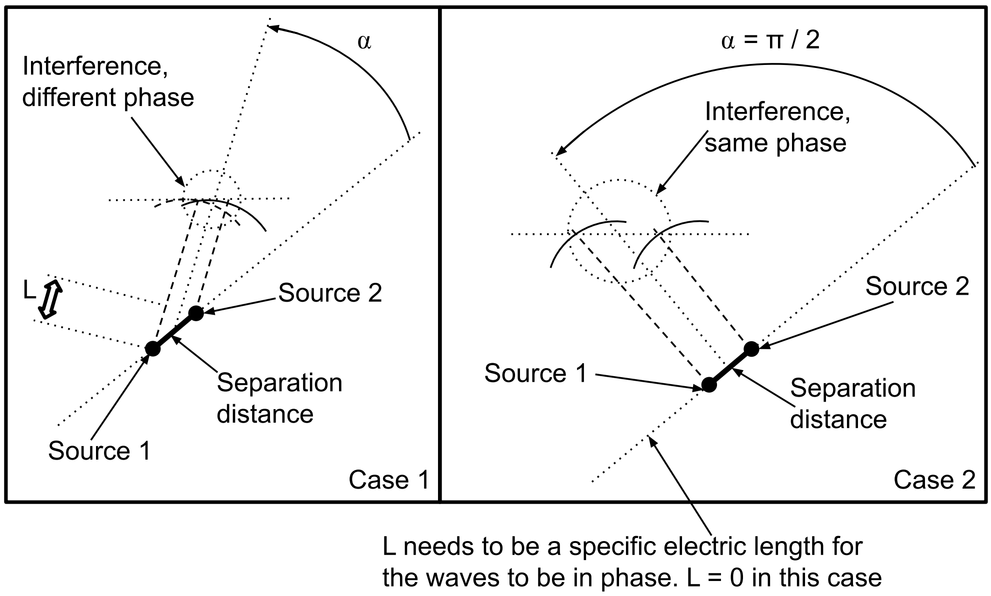

Figure 3.22: Interference is a function of phase which is a function of angle. It is possible for the waves to still have the same phases, even if they do not come from co-located sources, if their individual propagation axis are both orthogonal to a joining line between their sources

In Fig. 3.27 this ripple behaviour due to interference is shown practically for a dual reflector setup, where non-ideal diffracted waves interfere with the ideal radiation of the reflector system. As frequency increases, the electric path length differences between the diffracted fields from the subreflector, and the fields from the main reflector, cause general interference. The diffracted fields are smaller than the fields from the main reflector, which will result in a small ripple effect on the fields from the main reflector over frequency. Ripple, or also known as chromatic aberration, effects will become more pronounced as the electrical size of the reflector reduces as non-ideal effects become more dominant.

3.3.1 Non-ideal interference specifics and analysis techniques ability

Finally, the Fig. 3.29 shows how each non-ideal effect interferes with the radiation response of the reflector system. Fig. 3.29a shows how interference from edge diffraction occurs, due to waves generated from diffraction. Fig. 3.29b

Stellenbosch University https://scholar.sun.ac.za

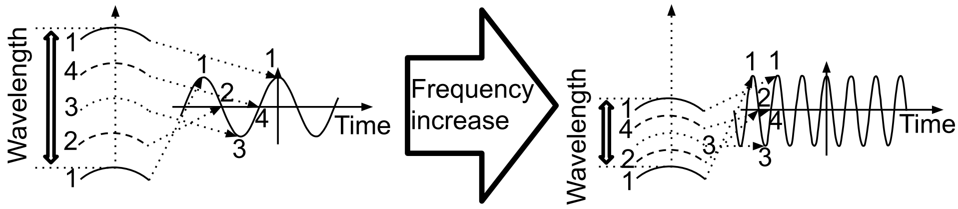

Figure 3.23: Wavelength reduces as frequency increases

shows how interference from feed spillover occurs. This includes interference due to waves generated from the side or back radiation of feed. Fig. 3.29c shows how interference from self-coupling occurs due to secondary waves interfering. Fig. 3.29d shows how interference from re-radiation occurs.

Prime focus centre fed reflector systems will have larger re-radiation interference, compared to offset systems, where the feed is not in front of the reflector. This is due to the large amount of collimated energy in zenith re-radiating from the horn, causing interference. In offset systems, sidelobe energy from the field from the reflector will cause re-radiation causing a much smaller re-radiation interference.

Similarly, in prime focus centre fed systems, back radiation from the feed will interfere with the field from the primary reflector in zenith. When the system is offset, energy radiated from the side of the feed will now interfere with the field from the primary reflector in zenith. These, and many other interference causing effects, are thus a function of geometry. In Fig. 3.28 shows the case for back radiation, assuming the feed has larger back radiation compared to side radiation.

Stellenbosch University https://scholar.sun.ac.za

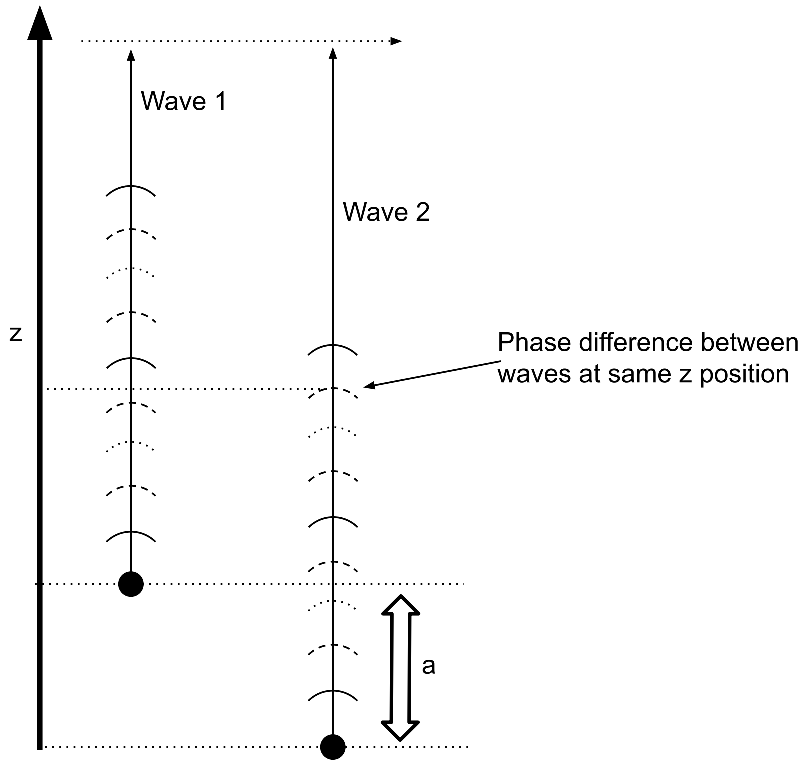

Figure 3.24: Waves with same frequency, but different path lengths interfering

PO (single-reflection PO) can not calculate coupling effects between the geometric structures and re-radiation effects, due to the arguments made in Chapter 2. It can calculate diffraction and spillover effects, with PTD enhancing the ability of PO to calculate diffraction effects, as previously described. MoM can calculate coupling effects such as re-radiation and self coupling between the geometric structures, as well as, diffraction and spillover effects. MoM thus accounts for more interference effects.

3.4 Conclusion

In this chapter it was shown how non-ideal effects use the process of interference to cause ripple behaviour in the radiation pattern response of the reflector system. Non-ideal effects become more pronounced as the electrical size of the reflector reduces and can be categorised as diffraction, spill-over, re-illumination and self-coupling effects. Interference between plane waves is described and it is shown that reflectors generate plane waves in the far-field. It is shown that the interference effects experienced by electromagnetic waves between non-ideal radiation and ideal radiation, presents as the addition of vectors, to cause the resultant wave, due to interference effects, to exhibit a

Stellenbosch University https://scholar.sun.ac.za

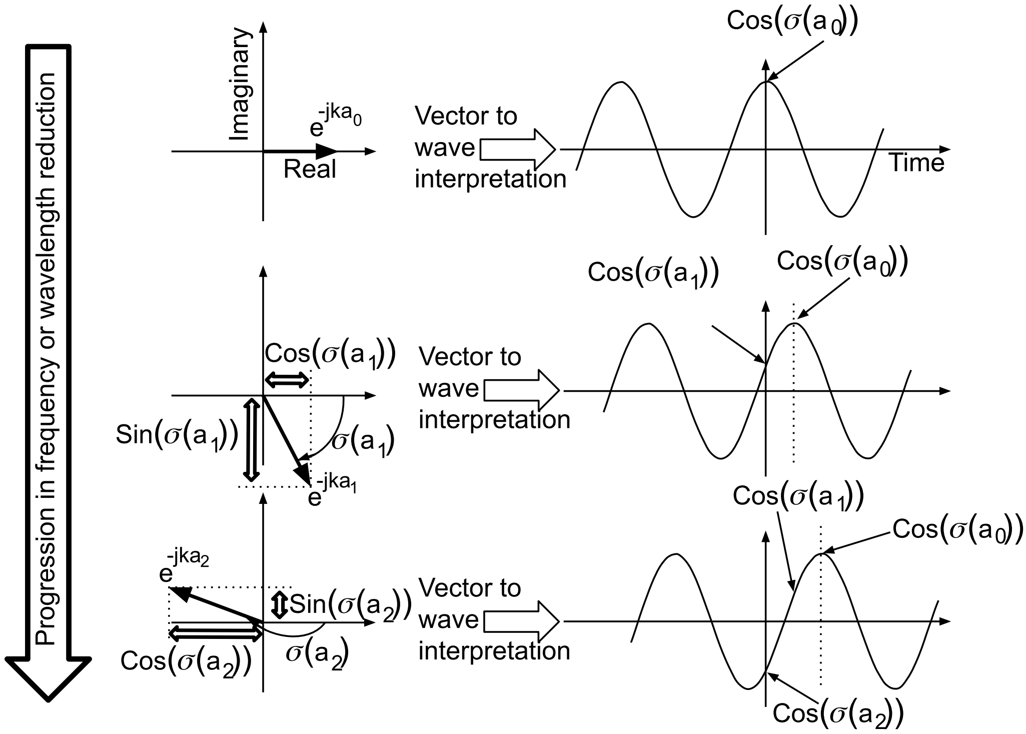

Figure 3.25: Spinning vector in complex plane as k (or a) increases

ripple on its underlying base form. In the next chapter, the ANT and the implication of the ripple on the radiation pattern will be discussed. The ANT is influenced by many factors, and so its level of complexity is high, and will be investigated next.

Stellenbosch University https://scholar.sun.ac.za

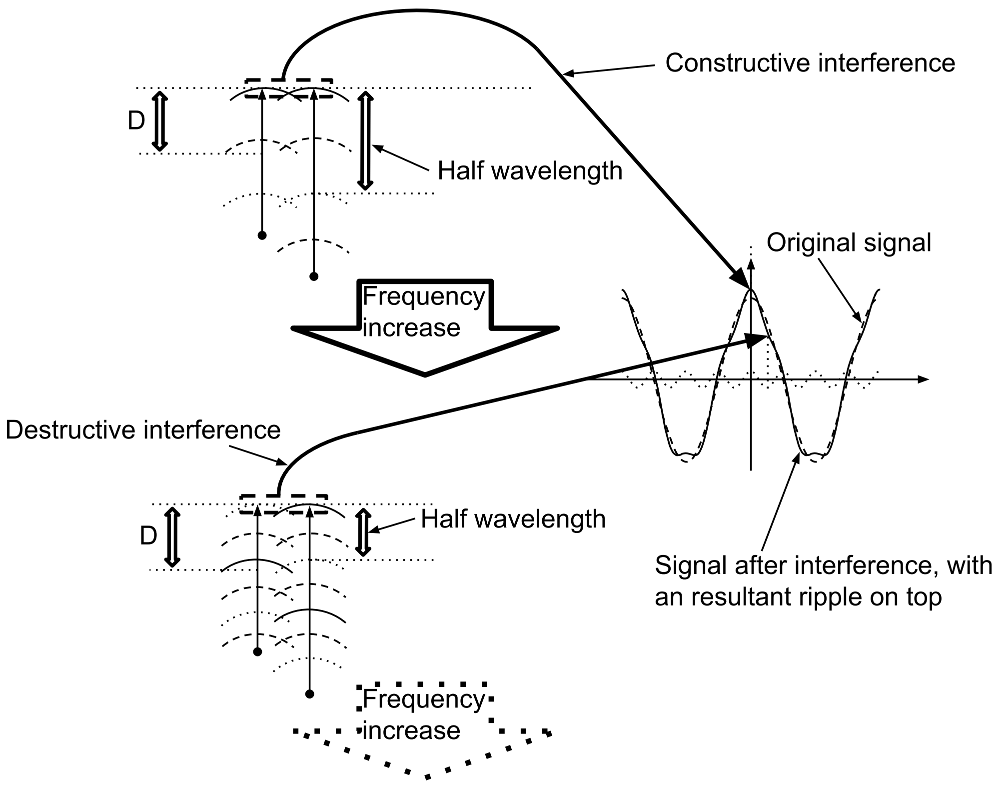

Figure 3.26: Ripple caused by interference due to frequency increase

Stellenbosch University https://scholar.sun.ac.za

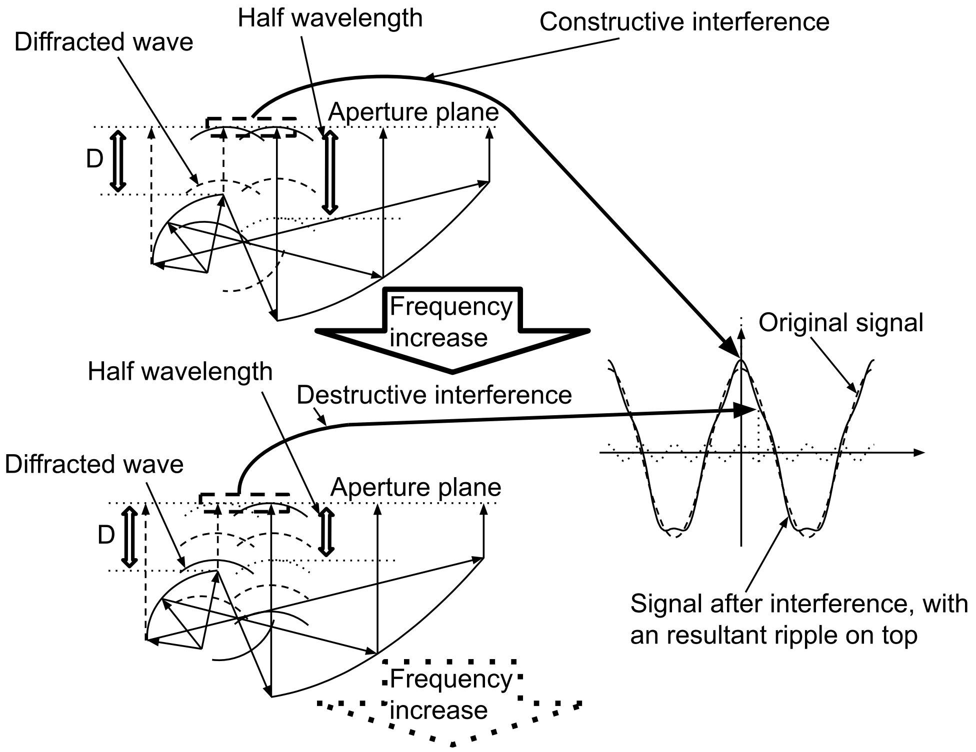

Figure 3.27: Interference causing a ripple response, for dual reflector system

Stellenbosch University https://scholar.sun.ac.za

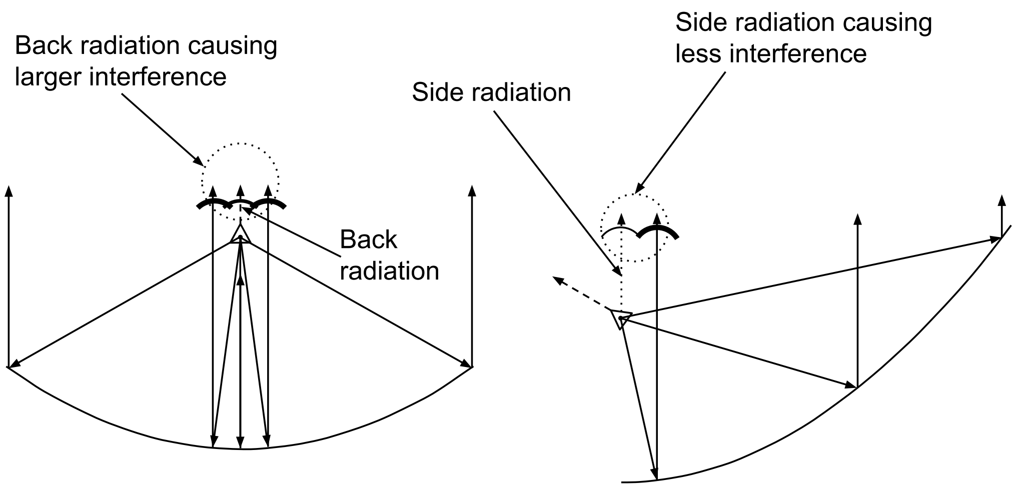

Figure 3.28: Example of feed non-ideal radiation interference being a function of geometry, in this case assuming the feed has a higher back radiation compared to side radiation

Stellenbosch University https://scholar.sun.ac.za

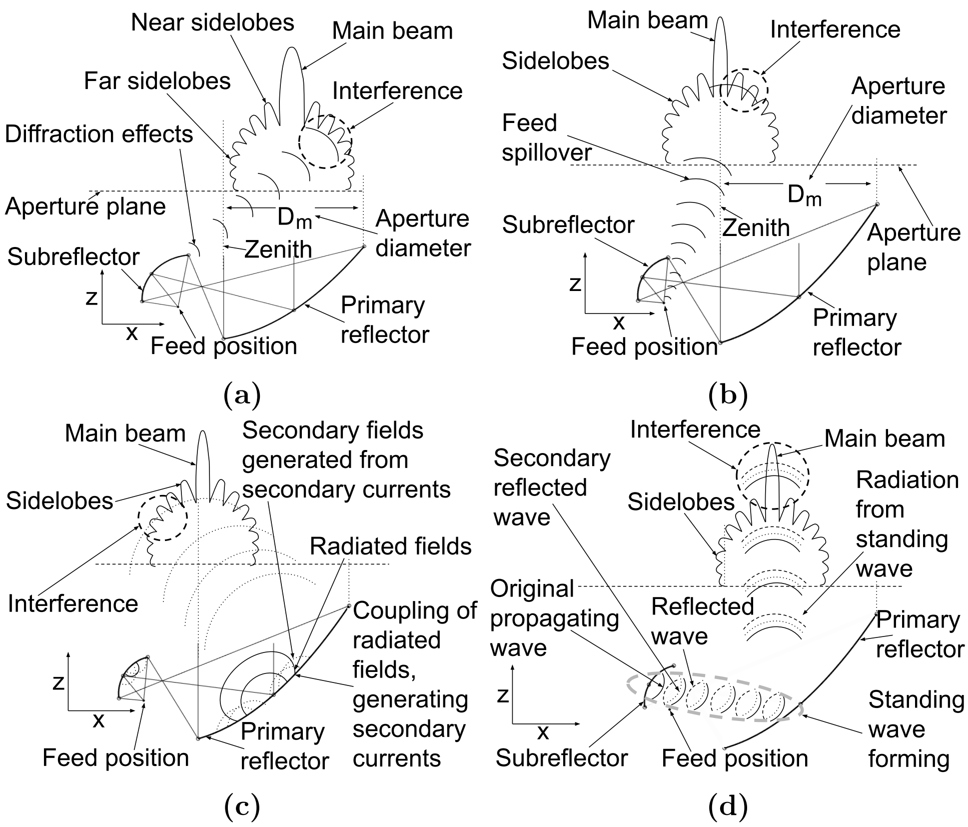

Figure 3.29: How non-ideal effects interfere. In (a) the interference of diffracted fields on the radiation pattern of the reflector system is shown. In (b) the interference from feed spillover is shown. In (c) the interference from secondary waves generated from self-coupling is shown. In (d) the interference from fields generated from re-radiation is shown

Stellenbosch University https://scholar.sun.ac.za

Chapter 4

Characterization of antenna noise temperature ripple

The previous chapter explained how non-ideal effects use the process of interference to cause a ripple on the radiation pattern response of the reflector system over frequency. In this chapter the effect of the ripple on the radiation pattern on the antenna noise temperature (ANT) will be analysed.

4.1 Antenna noise temperature ripple analysis

The ANT, or radiometric noise temperature, is part of the sensitivity calculation which will be discussed in detail in the next chapter, at a given frequency f as follows [1],

$$T_{\mathrm{A}}(f|\hat{\mathbf{r}}_0) = \frac{\iint_{4\pi} N(f,\Omega|\hat{\mathbf{r}}_0)\sin\theta d\Omega}{\iint_{4\pi} U(f,\Omega)\sin\theta d\Omega}, \tag{4.1}$$

where T_{A} denotes the ANT and where,

$$N(f,\Omega|\hat{\mathbf{r}}_0) = T_{\mathrm{b}}(f,\Omega)U(f,\Omega|\hat{\mathbf{r}}_0). \tag{4.2}$$

$N(\cdot)$ is a product of the background noise temperature (or surrounding brightness temperature) $T_{\mathrm{b}}(\cdot)$ with the total reflector antenna radiation intensity $U(\cdot)$ [1], when the reflector system is pointing in the direction $\hat{\mathbf{r}}_0$, at an operating frequency f in the spherical coordinate system $\Omega = (\theta,\phi)$. The background noise temperature $T_{\mathrm{b}(\cdot)}$, is a model of the radiation from the universe at a specific position on Earth, and will be discussed in more detail next.

The background noise temperature $T_{\mathrm{b}}(\cdot)$, or apparent radiometric temperature distribution, is also known as the brightness temperature distribution from the "scene" surrounding the antenna at a particular frequency [1]. There are different source contributions to the brightness temperature distribution surrounding the antennas, one is the emission from the gasses in the atmosphere, the second is the apparent temperature of the background sky seen

Stellenbosch University https://scholar.sun.ac.za

through the atmosphere and the other is the emission and scattering from the ground. The ground emission occurs through blackbody radiation. Blackbody radiation can be summarised as the spectrum of radiation emitted due to the thermal temperature of any object. The ground scattering occurs due to the reflection (or scattering) of the sources from the sky interacting with the ground.

The background noise temperature contribution from the sky, and ground, can be separated. The integrand $N(\cdot)$ can then also be separated into two cases. For brevity, only the estimation of the integrand, under certain simplified conditions, will be discussed. The full description can be found in [1]. These conditions include using unpolarised sources, and the assumption that the ground is dry, with a relative permittivity of the ground $\epsilon_2 \approx 3.5$. It also requires that the far side lobes of the co-polar radiation antenna pattern are significantly lower, at about -40 dB less, compared to the main beam maximum, and that it is comparable in value to the cross-polar pattern. Finally, it also requires that the antenna is not pointing at the ground. In this case, the reflection coefficient can be simplified to a single average reflection coefficient for the ground, as the co-polar $\Gamma_{\|}(\theta_1)$ and cross-polar $\Gamma_{\perp}(\theta_1)$ reflection coefficients are similar [1]. These coefficients will be discussed in more detail soon. This approximation for the integrand can be calculated as follows,

$$N(f,\Omega|\hat{\mathbf{r}}_0) = \begin{cases} U(f,\Omega|\hat{\mathbf{r}}_0)T_{\mathrm{b}}^{\mathrm{sky}}(f,\theta), & \text{if } 0 \le \theta \le \frac{\pi}{2} \\ U(f,\Omega|\hat{\mathbf{r}}_0)[(1-\tilde{\Gamma}(\theta_1))T_{\mathrm{gnd}} + \tilde{\Gamma}(\theta_1)T_{\mathrm{b}}^{\mathrm{sky}}(f,\theta_1)], & \text{if } \frac{\pi}{2} \le \theta \le \pi, \end{cases} \tag{4.3}$$

where $\theta_1 = \pi - \theta$, $\tilde{\Gamma}(\theta_1)$ is the average reflection coefficient for the ground, T_{gnd} is the ground temperature, and it is normally assumed to be 300K. Finally, $T_{\mathrm{b}}^{\mathrm{sky}}(f,\theta)$ is the sky noise model, which is discussed soon.

The average reflection coefficient is defined as,

$$\tilde{\Gamma}(\theta_1) = \frac{\Gamma_{\|}(\theta_1) + \Gamma_{\perp}(\theta_1)}{2}, \tag{4.4}$$

where,

$$\Gamma_{\|}(\theta_1) = \left| \frac{\cos(\theta_1) - \sqrt{\epsilon_2 - \sin^2(\theta_1)}}{\cos(\theta_1) + \sqrt{\epsilon_2 - \sin^2(\theta_1)}} \right|^2, \tag{4.5}$$

$$\Gamma_{\perp}(\theta_1) = \left| \frac{\epsilon_2\cos(\theta_1) - \sqrt{\epsilon_2 - \sin^2(\theta_1)}}{\epsilon_2\cos(\theta_1) + \sqrt{\epsilon_2 - \sin^2(\theta_1)}} \right|^2. \tag{4.6}$$

In Fig. 4.2 the sky noise model, sky brightness temperature, or model of the surrounding scene brightness temperature is shown over frequency. This is only for the sky region, thus above the horizon. It includes the temperature due to

Stellenbosch University https://scholar.sun.ac.za

the cosmic microwave background (CMB) and the galactic emission (mostly synchrotron emission), which follows a power law spectrum. Synchrotron emission is a type of non-thermal radiation, unlike blackbody radiation, which is thermal radiation. Synchrotron emission occurs from charged particles rotating, at almost the speed of light, around magnetic field lines. These charged particles are usually electrons, and they are constantly changing direction, which in effect accelerates and emits photons with frequencies depending on the speed of the electron at that moment [37]. The model also includes the temperature due to atmospheric absorption. It is shown over various observations angles from zenith. It is important to note that these observation angles are not related to the tipping angle of the reflector, and provides the surrounding scene brightness temperature over frequency for that angle. It is created as described in [1].

In Fig. 4.2 it is shown that Galactic synchrotron radiation, which has an average $\frac{1}{f^{2.75}}$ power law response, dominates the system noise temperature at frequencies in the lower part of the bandwidth. With increasing frequency, the noise contribution from extra-terrestrial sources is reduced and becomes almost constant over frequency. It starts to rise again near the 20 GHz frequency point and higher.

In Fig. 4.1 the background noise temperature from both the sky and ground contribution can be seen, for various frequencies. From Fig. 4.1, the contribution from the sky and ground is somewhat similar for frequencies below 5 GHz, with only a few kelvin difference. For higher frequencies, the sky region becomes notably hotter, as expected from Fig. 4.2. Finally, the background temperature converges over angle for all frequencies.

In Fig. 4.2, at 100 MHz the sky temperature is 1000 K, where the ground temperature is generally much lower, as seen in Fig. 4.1. The sky noise model thus has a higher kelvin value, than the ground temperature, at low frequencies. This can also be described as the sky being hotter than the ground. At 1 GHz, however, the ground temperature generally dominates the sky temperature of under 100 K. The region contribution which dominates, is thus dependent on the frequency.

The local peak at 22.235 GHz in Fig. 4.2 is due to an absorption line. For brevity, a short description will be given on absorption lines and molecular transitions, with a detailed description provided in [1]. An absorption line will appear in a spectrum, if an absorbing material is placed between a source, such as a star, and the observer, such as a radio telescope. The absorbing material could be the outer layers of a star, a cloud of interstellar gas or a cloud of dust. An absorption line occurs at the frequency where an element absorbs a photon. According to quantum mechanics, an atom, element or

Stellenbosch University https://scholar.sun.ac.za

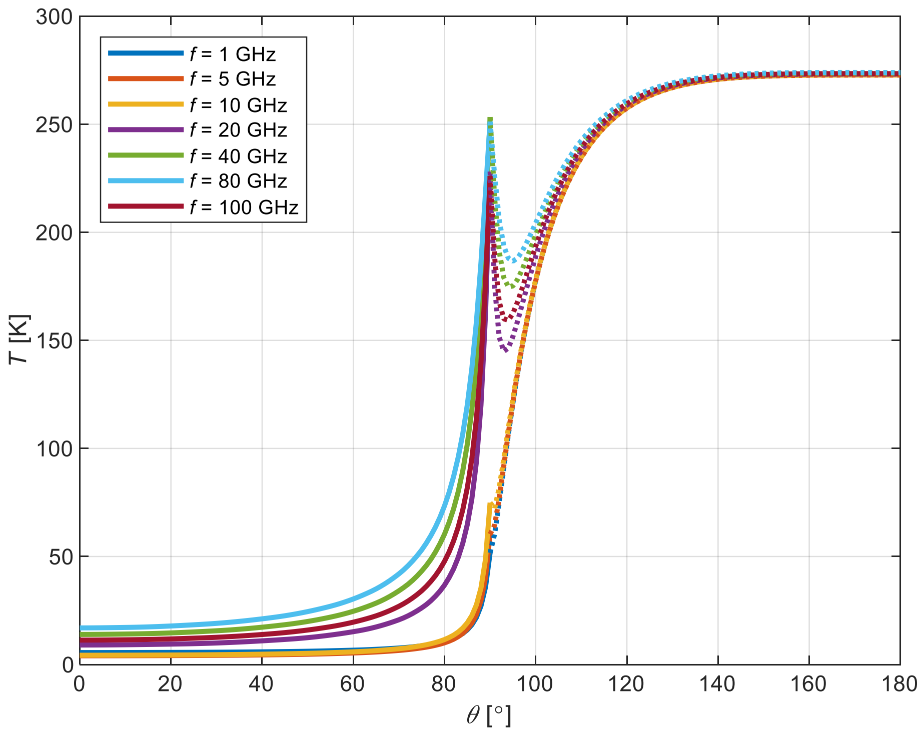

Figure 4.1: The sky and ground contribution to the background noise temperature over frequency. θ refers to the observation angle from zenith. The Cortes model is used, as described in [1]

molecule can absorb photons with energies equal to the difference between two energy states. As the frequency of a photon is directly linked to its energy, this means only certain frequency photons are absorbed or emitted. The frequencies where absorption lines exist are unique for each element. Absorptions can occur due to molecular transitions. Transitions in a molecule can occur in various states, including the rotational state. Rotational transitions occur at various frequencies, including microwave. These transitions occur due to the absorption (or emission) of photons, to enter a new rotational state, and these absorptions lead to absorption lines. The peak in Fig. 4.2 at 22.235 GHz, is a water vapour absorption line. The peak at 118.75 GHz is an oxygen absorption line. There are more absorption lines not shown, including a water vapour absorption line at 183.31 GHz.

The sky brightness temperature can further be described through intensity. The radiation field, of radiation propagating in a media such as the atmosphere, can be described in terms of the specific intensity, I_v. The specific intensity can further be described as the power per unit area, per unit frequency interval at a specific frequency, and per unit solid angle, flowing in a given direction [32].

Stellenbosch University https://scholar.sun.ac.za

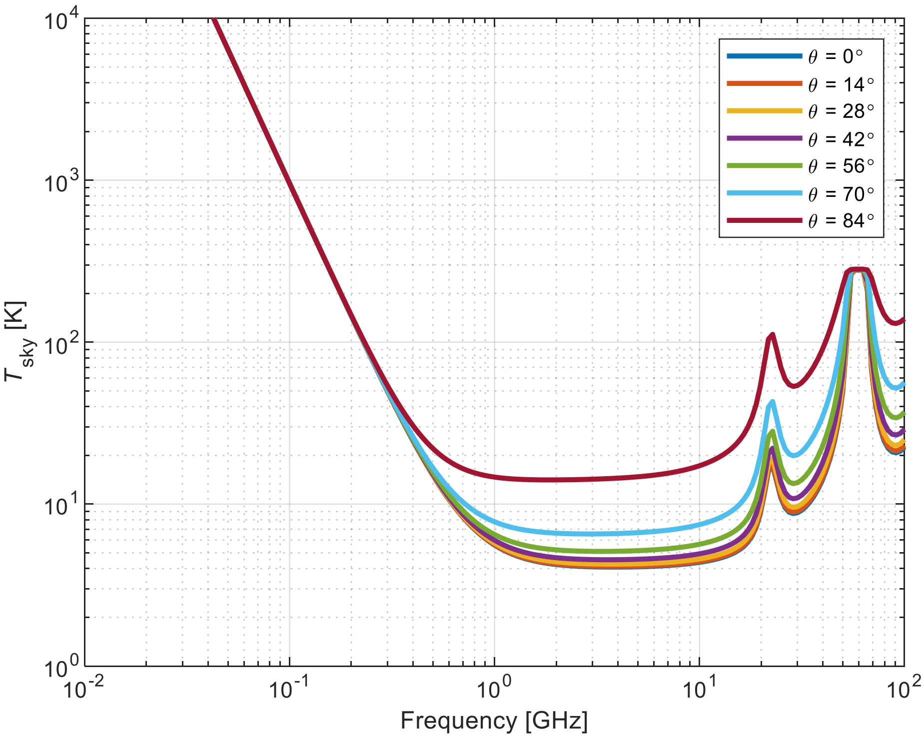

Figure 4.2: Sky noise model over frequency, or sky brightness temperature, over frequency. θ refers to the observation angle from zenith. The Cortes model is used, as described in [1]

Radiation emitted by molecules which propagates through the atmosphere, is in part attenuated by atmospheric absorption, where the energy absorbed is then re-emitted as thermal radiation. The radiation will be attenuated more, as it travels through the atmosphere for longer. The specific intensity, I_v, can be defined as,

$$I_v = I_v(s_o)e^{-\tau_v(0,s_o)} + \int_{s_o} k_a(f,s)B_v(T)e^{-\tau_v(0,s)}ds, \tag{4.7}$$

when received from a specific direction in the atmosphere. In (4.7), the background intensity is defined as $I_v(s_o)$, at a specific distance s_o. The atmospheric absorption coefficient is defined as $k_a(f,s)$. The absorption coefficient is a macroscopic parameter that represents the interaction of the incident electromagnetic radiation with the constituent molecules of the atmosphere. The source in the medium is defined as $B_v(T)$, where T is the temperature in Kelvin. When the medium is isothermal, which means it has a constant temperature, then the source, $B_v(T)$, corresponds to the Planck's function,

$$B_v(T) = \frac{2hf^3}{c^2}\frac{1}{e^{\frac{hf}{kT}} - 1}, \tag{4.8}$$

Stellenbosch University https://scholar.sun.ac.za

where h is the Planck's constant, k is the Boltzmann constant, f is the frequency, and c is the speed of light. The opacity of the medium, or the optical depth, is defined by τ_v, and can be calculated as,

$$\tau_v(s_o, s) = \int_{s_o}^{s} k_a(f, \xi) d\xi. \tag{4.9}$$

The Planck's function can be approximated as,

$$B_v(T) \approx \frac{2kT}{\lambda^2}, \tag{4.10}$$

in the microwave frequency range, with $hf \ll kT$, which is known as the Rayleigh-Jeans approximation. The Rayleigh-Jeans approximation is acceptable for radio astronomy at almost all frequencies - certainly for frequencies under 10 GHz. The Planck's function (specific intensity) approximation has a linear dependence on the physical temperature, and this allows the definition of the sky brightness temperature, T_b^{sky}, as follows,

$$T_b^{sky} = \frac{\lambda^2}{2k} I_v, \tag{4.11}$$

where the brightness temperature is defined as the physical temperature an equivalent blackbody source would require, to be able to generate the intensity I_v. This definition allows (4.7), to be rewritten in terms of,

$$T_b^{sky}(f) = T_{bc}(f)^{-\tau_v(0,s_o)} + \int_{s_o} k_a(f, s) T(s) e^{-\tau_v(0,s)} ds, \tag{4.12}$$

where $T_{bc}(f)$ is the brightness temperature due to cosmic emission.

.

The reflector antenna radiation intensity $U(f, \Omega)$ is a function of the radiation pattern of the reflector system. The radiation intensity can be defined as,

$$U(f, \Omega) = \frac{1}{2\eta} |G(f, \Omega)|^2, \tag{4.13}$$

where $G(\cdot)$ is the complex far-field function or the radiation field function. The radiation pattern is a graphical representation of the far-field function $|G(\cdot)|$ [32]. When referring to the radiation pattern in the ANT, the radiation intensity is implied. The complex far-field function relates to the electric field through,

$$\boldsymbol{E}(f, \Omega) = \frac{e^{-jkr}}{r} \boldsymbol{G}(f, \Omega), \tag{4.14}$$

when the radiated fields are observed in the far-field, at a specific point r [32].

Stellenbosch University https://scholar.sun.ac.za

4.2 Ripple properties, Reflector types and geometry used in analysis

To illustrate the details of the ANT calculation, and the effects of interference ripple on the result, the following generic example is considered. The analysis performed for ANT, aperture efficiency (AE) and sensitivity in this dissertation is done using an ideal Gaussian feed. The feed has a 12 dB edge taper at the subreflector subtended half-angle, of 45°, to illuminate the reflector system. A physical feed, is not required to demonstrate the concepts introduced and discussed in this chapter. Any specific physical feed will only lead to slightly different results, however, these results will still be a function of the concepts described in this chapter.

The analysis is done at $\theta_\mathrm{p} \in [0°, -40°, -80°]$ pointing angles. This covers a generous portion of the sky from zenith close to the horizon, in a resolution that can highlight the different ripples observed for each angle, which will be discussed later.

Furthermore, the analysis is also performed over a 3:1, L-band $[0.7 - 2.1]$ GHz frequency band. It is useful to perform the analysis at a low frequency band, as electrically small reflectors are important at low frequencies. The creation of electrically large reflectors at low frequencies, would likely require large physical structures, and thus it is more likely that an electrically small reflector will be preferred. Furthermore, the frequency in this band is low enough to allow the observation of the Milky Way radiation (galactic emission), without absorption lines in the band. It is high enough, however, to not allow the sky noise temperature to completely dominate, while the receiver noise temperature has a negligible impact.

The simulations performed for the ANT, AE and sensitivity are done using PO with the PTD added. Henceforth PO simulations will imply the inclusion of PTD. PO calculates only a subset of the non-ideal effects calculated by MoM, however, PO is used in this dissertation to describe the basic principles, concepts and primary effects of ripple in the sensitivity. For more detail in specific situations, or when the inclusion of the effect of mutual coupling is desired, MoM can be used.

The reflector setup used is an offset Gregorian dual reflector system, with maximum chord lengths of 5 m and 2 m for the primary reflector and subreflector, respectively. The primary reflector has a projected aperture diameter of 4 m.

The background model used is the Cortes model, as described earlier.

Stellenbosch University https://scholar.sun.ac.za

Finally, the validation set of AE, ANT and sensitivity $\boldsymbol{\upsilon}$ is used to generate the fine models for the ANT, AE and sensitivity. A validation set is the data used for verification of the validity of any model or set compared to it, whereas a fine model is a highly accurate representation of the relevant quantity. A coarse model is a fast approximation of the relevant quantity, and often times not highly accurate. The number of equally spaced radiation pattern samples across the frequency band required for the validation set, is discussed next. While this setup is standard for most of the analysis, some parts are altered in some tests. In these cases it will be explicitly described what changed.

In order to characterize the frequency ripple of interest here, the Fast Fourier transform (FFT) is used extensively in this dissertation. The FFT is useful to extract the frequency components of a signal, but its ability is limited by the sample rate of the signal. Recall that Nyquist sampling is required to avoid aliasing when calculating an FFT of a broadband signal, implying a sampling rate F_s of $F_s > 2f_f$ is required to accurately capture the fastest frequency component f_f in the broadband signal. The FFT creates images of the frequency components in the upper half of the Fourier band, which is why only the lower half of the band is used to identify the frequency components in the signal. When $2f_f > F_s > f_f$, under sampling occurs as all of the frequency components of a signal can not be captured, which shifts (image) components from the lower half of the band into the upper half, and visa versa. Aliasing can start to occur when under sampling a signal. Aliasing is an effect where calculated frequency components from the FFT interfere, distorting the output of the transform and misidentifying frequency components.

The reflector system used is shown in Fig. 4.3. One of the longest possible path length differences could be described by the difference between the feed radiating to the leftmost edge of the subreflector in Fig. 4.3, compared to the feed radiating to the leftmost edge of the subreflector, then to the rightmost edge of the primary reflector, and then back to the leftmost edge of the subreflector. This path length difference is 13.13 m. The ripple period is approximated as $R_{\mathrm{p}} \approx \frac{c}{(L_{\Delta})(10^6)}$ [38], where c is the speed of light, and L_{Δ} is the path length difference between interfering waves. The ripple period decreases, as the path length difference increases. The path length difference of 13.13 m, leads to a ripple period of $R_{\mathrm{p}} \approx \frac{c}{L_{\Delta}} \approx \frac{c}{13.13} \approx 22.83$ MHz, which leads to,

Stellenbosch University https://scholar.sun.ac.za

$$R_{\mathrm{p}} = \frac{2S_{\mathrm{p}}}{10^6}\ \mathrm{MHz}, \tag{4.15}$$

$$S_{\mathrm{p}} = \frac{R_{\mathrm{p}}(10^6)}{2}, \tag{4.16}$$

$$S_{\mathrm{p}} = \frac{(22.83)(10^6)}{2}, \tag{4.17}$$

$$S_{\mathrm{p}} = 11.42 \times 10^6 \frac{\mathrm{Hz}}{\mathrm{sample}}, \tag{4.18}$$

where S_{p} is the bandwidth per sample. Using (4.18), the number of samples required can be calculated through,

$$S_{\mathrm{p}} = \frac{B_{\mathrm{W}}}{N_{\mathrm{S}}}, \tag{4.19}$$

$$N_{\mathrm{S}} = \frac{B_{\mathrm{W}}}{S_{\mathrm{p}}}, \tag{4.20}$$

$$N_{\mathrm{S}} = \frac{(1.4)(10^9)}{(11.42)(10^6)}, \tag{4.21}$$

$$N_{\mathrm{S}} = 122.60\ \mathrm{samples}, \tag{4.22}$$

where the number of frequency samples is N_{S}, and the bandwidth is described as B_{W}. While 123 samples would be enough to capture one of the smallest ripple periods, $R_{\mathrm{p}} \approx 22.83$ MHz, a conservative 201 equally spaced radiation pattern samples across the frequency band is chosen instead for the validation set. The validation set samples are generated through PO augmented by PTD analysis of the full reflector system, using the commercial solver GRASP [39]. This densely sampled set is used to capture the ripple on the ANT, AE and sensitivity which will be discussed in detail later.

The 201 samples over the 1.4 GHz band allows for,

$$S_{\mathrm{p}} = \frac{(1.4)(10^9)}{201}, \tag{4.23}$$

bandwidth per sample, which allows ripple periods of up to,

$$R_{\mathrm{p}} = \frac{2S_{\mathrm{p}}}{10^6} = 13.93\ \mathrm{MHz} \tag{4.24}$$

to be captured without under sampling and aliasing. For $R_{\mathrm{p}} = 13.93$ MHz, $L_{\Delta} \approx \frac{c}{(13.93)(10^6)} \approx 21.52$ m. Thus $R_{\mathrm{p}} = 13.93$ MHz, allows for $L_{\Delta} \leq 21.52$ m. It is thus expected that the limit of $L_{\Delta} \leq 21.52$ m will allow most, if not all,

Stellenbosch University https://scholar.sun.ac.za

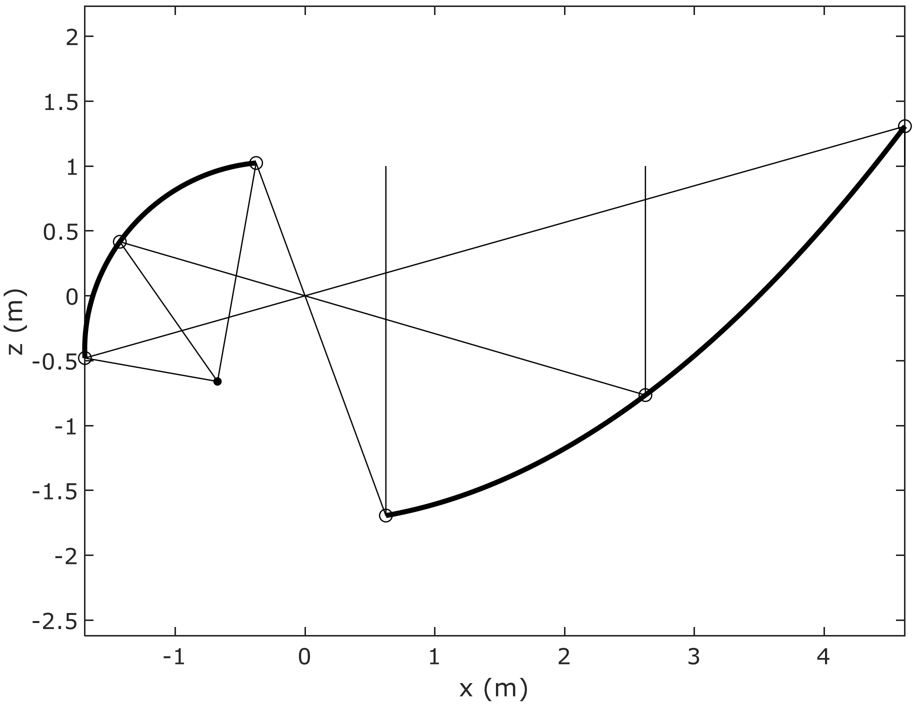

Figure 4.3: The standard reflector used in the dissertation

possible ripple periods in the ANT, AE and sensitivity to be captured.

Modern antenna design usually requires an initial antenna design, followed by an optimisation phase. The optimisation phase is a phase of rapid design iteration, which includes iterative simulations, to tweak the antenna design for better performance. It is usually not possible to have a perfect initial antenna design, as it is too complicated to choose the correct values for all the design parameters. It is often also too computationally expensive to test all the possible values in the optimisation phase, for each design parameter, to find the optimal design. Optimisation strategies are often developed in an attempt to find the optimal design parameters, without explicitly testing each possible value. These strategies usually sacrifice some measure of accuracy for each design iteration, to allow them to be completed much faster, and are often necessary to optimise in a reasonable time frame.

Such strategies exist for the ANT, AE and sensitivity as well. They include fast, and relatively accurate, calculations of the ANT, AE and sensitivity, respectively. These fast approximations are known as the low-fidelity data. Conversely, the high-fidelity data, or fine model, represent the very accurate, and usually slowly calculated, data. While the high-fidelity data set enables

Stellenbosch University https://scholar.sun.ac.za

many relevant ripples to be captured, it is prohibitively large and would not be practical in the calculation of ANT, AE and sensitivity during the optimisation phase, as it will require too much computation time and resources.

In Fig. 4.4 the ANT response fine model, in specific pointing angles for the reflector, is shown as the solid lines. The high sample rate exposes the relatively fast oscillation, or ripple, over frequency of the ANT. The dashed lines are coarse models, low order approximations, or low-fidelity approximations. In this case the coarse models are generated using the strategy in [24], which details the entire process, however, a condensed description will be provided next to convey the limitations of the strategy.

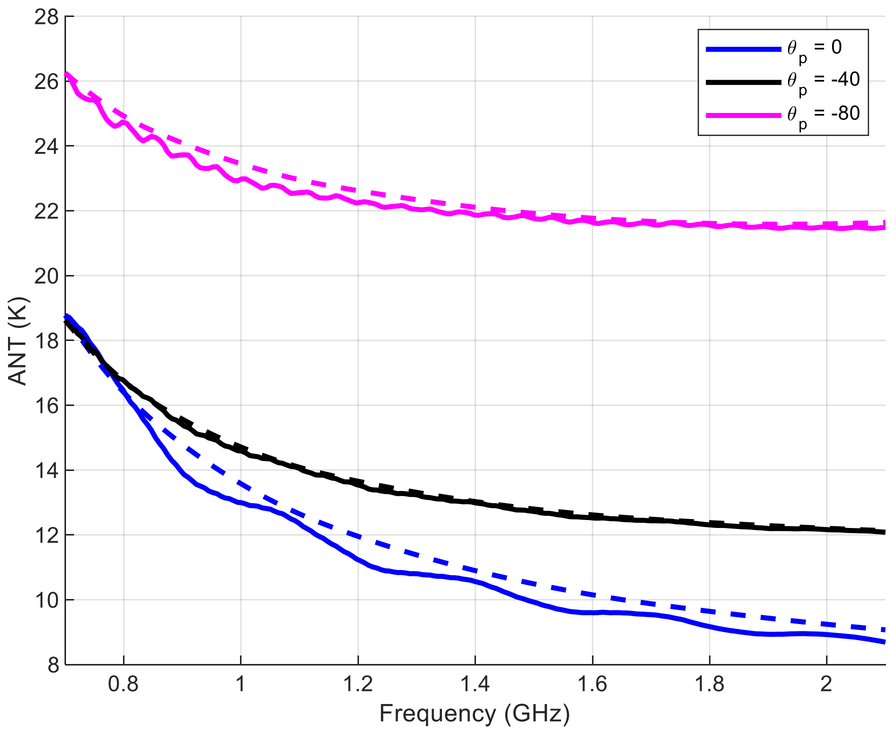

Figure 4.4: The high-fidelity approximation is compared to the low-fidelity approximation, for the ANT, over three pointing angles. The solid lines display the high-fidelity approximation from (4.1). The dashed lines display the low-fidelity approximation, which excludes the ripple

4.2.1 Strategies for rapid ANT approximation

The strategy in [24], uses a masking technique to accelerate the calculation of the ANT by using approximations. In Fig. 4.5 an approximation is shown.

Stellenbosch University https://scholar.sun.ac.za

The masking strategy assumes that the feed radiates most energy onto the subreflector as seen in Fig. 4.5a. The subreflector then radiates most energy onto the primary reflector as seen in Fig. 4.5b. Finally the primary reflector radiates most energy into the sky into the direction of maximum radiation intensity of the reflector system as seen in Fig. 4.5c.

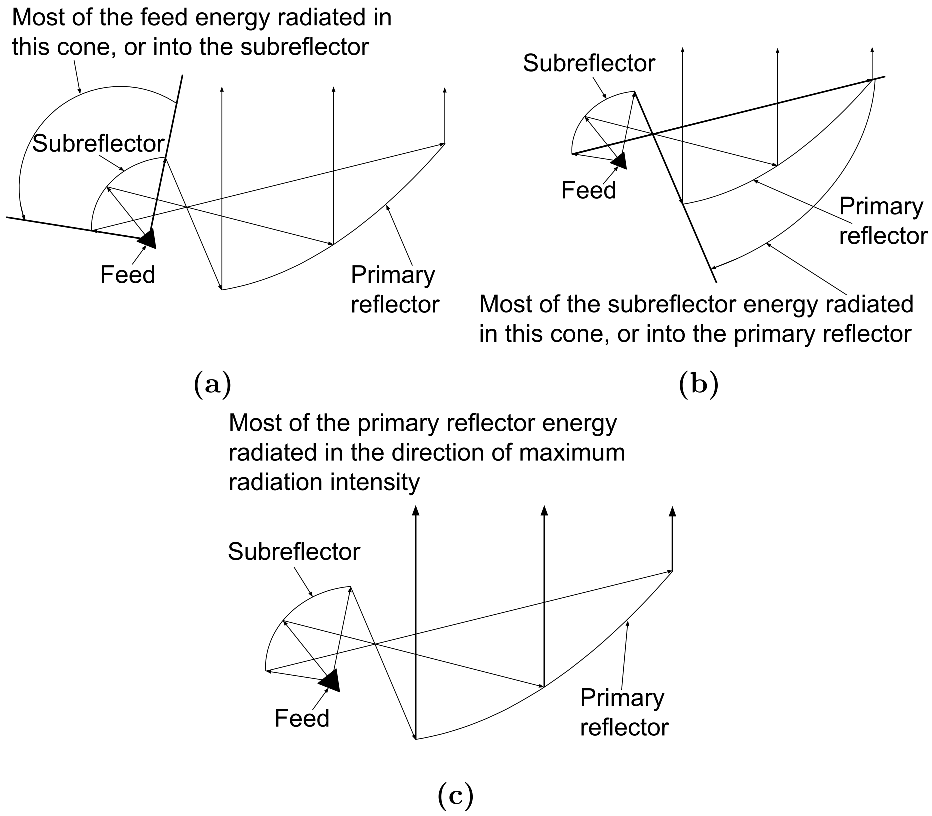

Figure 4.5: Feed radiate most energy onto the subreflector. Subreflector radiate most energy onto the primary reflector. Primary reflector radiate most energy in the direction of maximum radiation intensity

By using this assumption, it can be predicted where most of the energy will radiate without including the reflecting surfaces, as shown in Fig. 4.6. In Fig. 4.6a it can be predicted that most of the radiation from the subreflector will reflect from the primary reflector into the direction of maximum radiation intensity. This means that the primary reflector can be excluded from the simulation and the ANT (which would have included the primary reflector) can be relatively accurately predicted. This can be extended to exclude the subreflector as shown in Fig. 4.6b, and it can be predicted that most of the feed energy will be reflected from the subreflector, onto the primary reflector and then into the direction of maximum radiation intensity. The subreflector can thus also be excluded, and only the feed pattern can be simulated to

Stellenbosch University https://scholar.sun.ac.za

relatively accurately predict the ANT. Excluding the primary and secondary reflector simulations significantly decreases the computation time required to calculate the ANT.

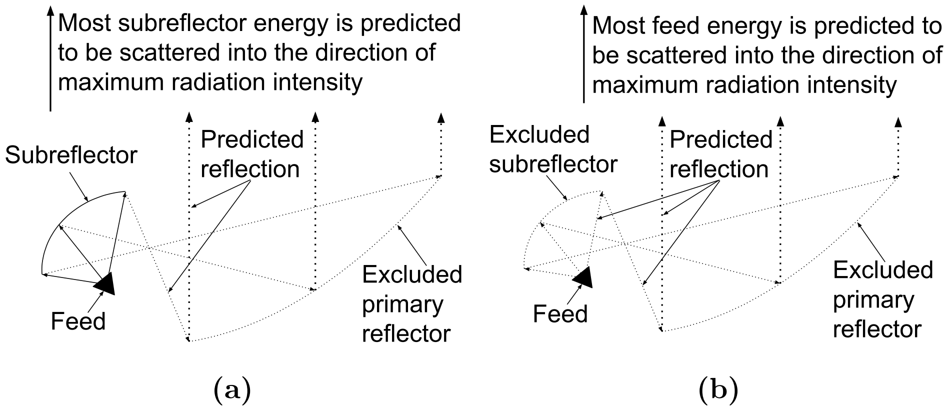

Figure 4.6: Most subreflector energy is predicted to be scattered into the direction of maximum radiation intensity. Most feed energy is predicted to be scattered into the direction of maximum radiation intensity

This approach, however, is not perfect and as the reflector size reduces, the assumptions will become less reliable and the strategy less accurate. Diffraction effects are also not taken into account. To compensate for diffraction effects, the strategy then uses simulations. It requires the simulation of the far-field radiation pattern of the full reflector system (which includes the primary reflector), at up to three frequencies, uniformly separated over the band. Usually only the lowest frequency is simulated. It also requires the simulation of the far-field radiation pattern of the reflector system, excluding the primary reflector, at three frequencies uniformly separated over the band. Finally the feed pattern (which is the reflector system, excluding the subreflector and the primary reflector) needs to be simulated at a high sample rate over the band, similar to the fine model or validation set resolution.

Using the simulated data, the strategy then adjusts the background noise temperature, in the direction of the main beam, to change the ANT over frequency. It is adjusted until the ANT at the simulated frequencies, match the ANT calculated through the simulated data. Rays are launched in each direction from the feed, and where these rays hit reflectors, they are reflected. The background noise temperature is adjusted in the final direction of these rays. This compensates for extensions, such as a subreflector extension, and for radiation directly on the primary reflector. An account of the mathematics to correct the approximated temperature, using simulated data, is provided in subsection 4.4.10. In this subsection, the impact of the strategy on the ANT

Stellenbosch University https://scholar.sun.ac.za

is investigated.

Part of the success of this strategy is due to the power law base form of the ANT, which is mostly due to the galactic emission which follows a power law spectrum, as mentioned earlier. The base form refers to the form of the ANT, without its ripple included. This allows the ANT to be relatively accurately predicted, from only a few simulated frequencies, as a power law requires only a few points to be accurately described. The power law, however, is more accurately described if a few frequencies are simulated, instead of only one. The ANT can thus be predicted from simulating the radiation pattern of the full reflector system at a single frequency, however, using three will increase the accuracy of the predicted ANT. While the prediction of the power law base of the ANT is relatively accurate, it does not include the ripple in the ANT. The ripple is thus not modeled using this strategy.

Coarse models generated from this strategy, by using only one full system simulation, is considered the standard case in this dissertation. The ripple can now be obtained or isolated by taking the difference between the high-fidelity approximation (fine model) of the ANT, and a low-fidelity approximation (low order) of the ANT that is calculated by using the strategy in [24].

4.2.2 Fourier Transform application

An FFT is applied on the isolated ripple of each tipping angle, to extract the frequency components and compare them. Ripple isolation protects the FFT results from being dominated by slow varying components, potentially obscuring the ripple information. The FFT application and results are discussed in detail next.

The FFT in this dissertation is performed over frequency, instead of time. By simply interpreting the function or signal which is a function of frequency, as a function of time instead, the result from the FFT can be interpreted as the frequency of the periodic terms that constitute the response of the frequency signal, instead of the time signal. Thus, no mathematical change has to be done and the transform can be applied in exactly the same manner.

The FFT is performed on the isolated ripple of the signal. This is useful, because the ripple is only a small oscillation on the signal. If the FFT of the original signal is calculated, it will be dominated by other frequency components, which will obscure the ripple component information. The output of the transform in this dissertation shows the period, that is required for each term to oscillate, naturally implying that peaks with a smaller period will correspond to the high frequency terms that are associated with the ripple

Stellenbosch University https://scholar.sun.ac.za

component. In some cases, the logarithm with base 10 is taken of the period, to highlight the dominant ripple component. The dominant ripple will always be located at the highest magnitude in the FFT. In the case of the logarithm, it will be displayed on the x-axis. Period is easier to interpret as seen in Fig. 4.7. In Fig. 4.7b, the FFT of the ANT ripple displays the period of the frequency components. The marked period on the peak, corresponds to the distance between the two marked frequencies in Fig. 4.7a. These two marked frequencies, roughly displays the distance between two ripple peaks. It is thus intuitive to interpret the marked period of Fig. 4.7b. In Fig. 4.7c, the FFT of the ANT ripple is shown in frequency, instead of period. It is less intuitive to interpret the relation of this marked frequency, in regards to the ripple in the ANT. Notice that the period format of the FFT, displays high (fast) frequency components to the left, and low (slow) frequency components to the right of the graph.

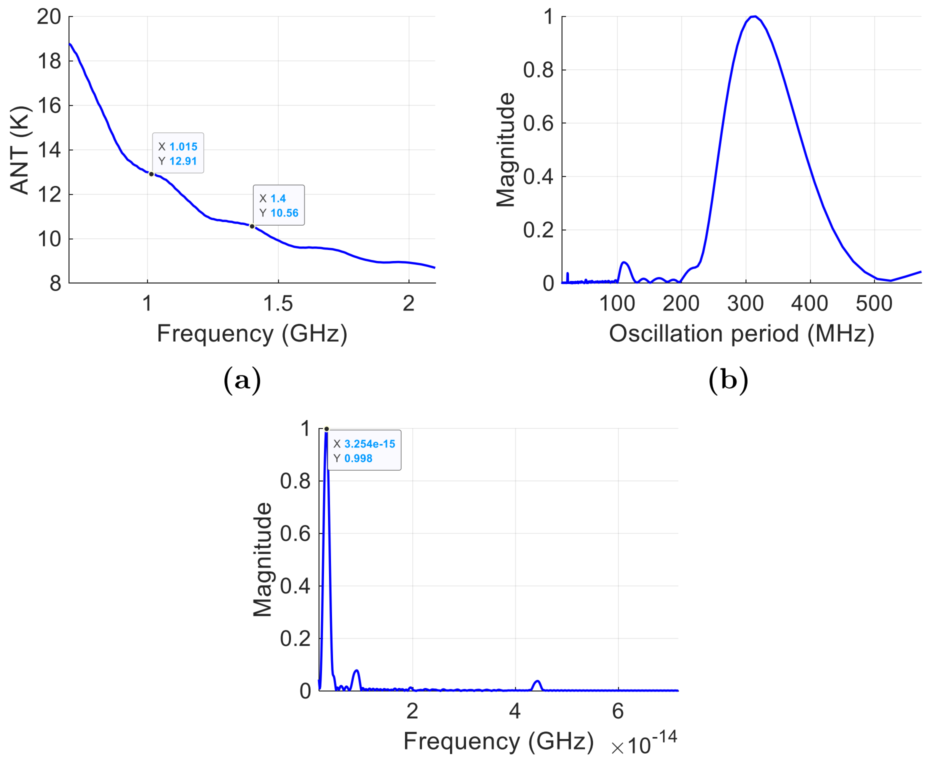

(a) (b) (c)

Figure 4.7: Period is easier to interpret compared to frequency for FFT. In (a) the ANT is shown, and in (b) the FFT of the ANT ripple, showing the period of the ripple. In (c) the FFT of the ANT ripple is shown in frequency, instead of period

A rectangular window is used implicitly before the FFT is performed, however, the effect of applying a hamming window on the signal before the FFT is

Stellenbosch University https://scholar.sun.ac.za

also investigated. Hamming windows often improve the accuracy of the FFT, in many cases. The FFT process is designed to extract the frequency components of periodic signals, however, in many cases the provided signals are not periodic. In these cases, there exist discontinuities at the start and end of the signal. These discontinuities present as high-frequency components in the FFT, which are not part of the original signal, and can have much higher frequencies than the Nyquist frequency, which causes aliasing to occur. This effect is known as spectral leakage. The hamming window reduces spectral leakage, by suppressing the discontinuities.

In Fig. 4.8 a hamming window is applied on an arbitrary isolated ANT ripple. In Fig. 4.8a the ripple of the original signal is shown accompanied by the same ripple with a hamming window applied to it. In Fig. 4.8b the FFTs of both these ripples are shown. While it is apparent that the hamming window produces a more clear transform, the dominant frequency components are the same in both transforms. Due to this, the importance of choosing the ideal window is neglected in this dissertation. The hamming window, however, is applied in many cases.

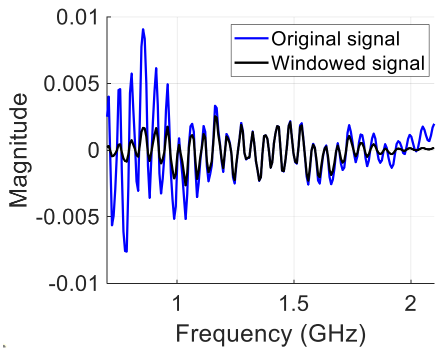

(a)

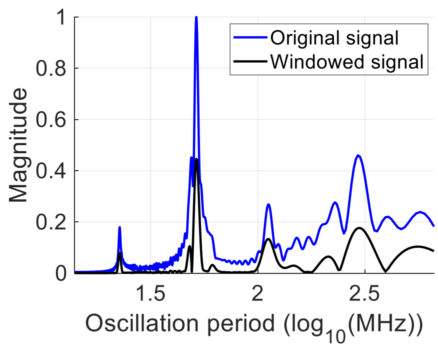

(b)

Figure 4.8: A hamming window is applied on an arbitrary isolated ANT ripple. In (a) the ripple of the original signal is shown accompanied by the same ripple with a hamming window applied to it. In (b) the FFTs of both these ripples are shown

The ripple is isolated either as described above, through subtracting a fine model from a low order approximation created through some strategy, or by subtracting a fine model from a specific power law fitted through it. The latter approach is determined through an algorithm which uses an iterative power law fitting processes, combined with analysing the impact of each fit, to determine the best fit and extract the ripple effectively. The benefit of using the low order approximation approach, is that the approximation accuracy can be tested, along with identifying the ripple (and general frequency) components

Stellenbosch University https://scholar.sun.ac.za

it does not model. The benefit of using the iterative power law, is that a more distinct and defined ripple can be isolated more confidently.

In both cases a coarse model, without ripple, is generated. The iterative power law technique will be discussed soon. It is expected that a power law will fit the ANT well, due to its base form resembling a power law. This implies that the ripple on the signal can effectively be isolated by using a power law. Polynomial fitting is also more prone to rapidly oscillate, compared to power laws, which can cause it to extract the ripple as well as the base form and possibly inject ripple components. This will be discussed in more detail soon. For these reasons, Polynomial fitting is thus not used to isolate the ripple in many cases.

4.2.3 Iterative power law ripple extraction

While a 1st-order power law is sufficient to extract some ripple from a signal, the iterative n-order power law technique was developed to increase the confidence that the extracted ripple is indeed the ripple of the signal, and to analyse the impact on the extracted components, due to the power law fitting. A 1st-order power law can be described as follows,

$$\text{Order 1:} \qquad c_0 x^{c_2} + c_1, \tag{4.25}$$

where each c represents an unknown constant or coefficient to be determined through the fitting process, and x is the independent variable representing the frequency in this case.

The iterative power law technique is described in Fig. 4.9. It starts by fitting a 1st-order power law through the fine model, or signal. Two FFTs are calculated, one for the fitted power law and the other for the provided signal. These two FFTs are then divided by each other, to produce a quotient over frequency. These quotients are produced as follows,

$$Q_n = \frac{\text{FFT}(T_\text{A}(f|\hat{\mathbf{r}}_0))}{\text{FFT}(P_n)} \tag{4.26}$$

where Q_n denotes the quotient for an n order fit, FFT denotes the FFT operation or function, T_A is the ANT as discussed earlier, and P_n is the power law for an n order fit.

An example of a signal with a 3rd order power law fit is shown in Fig. 4.10, their FFTs in Fig. 4.11, and the quotient graph in Fig. 4.12. The signal is normalised in both magnitude and frequency to enhance numerical stability

Stellenbosch University https://scholar.sun.ac.za

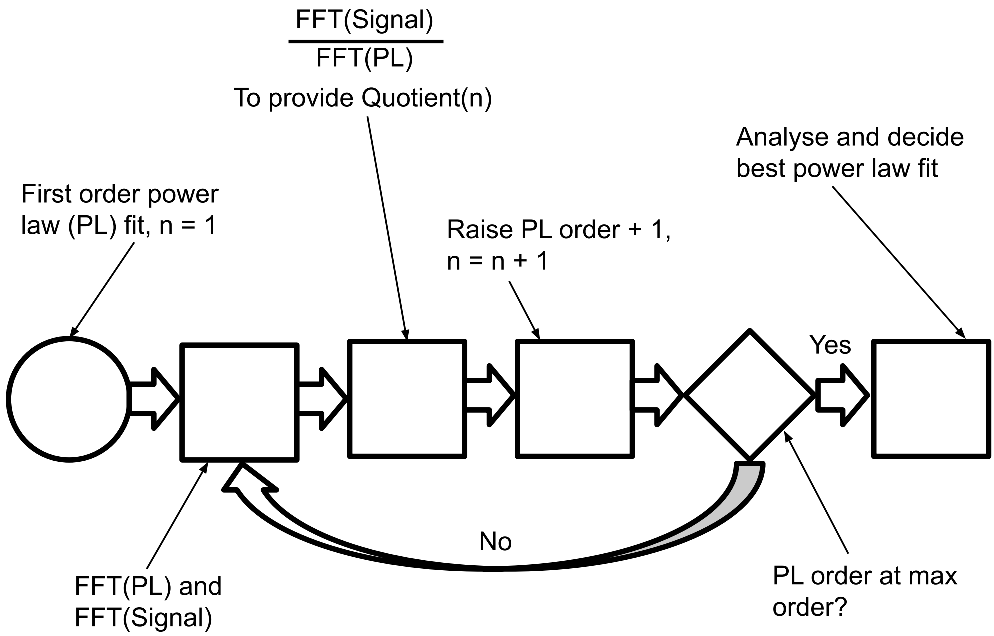

Figure 4.9: A flow chart describing the iterative power law algorithm

and fitting accuracy, when performing the power law fitting. The normalisation is performed by independently scaling both axes to a maximum value of one. This is done for each axis, by divided their values by the maximum value for that axis. The process is then partially repeated. Another power law is then fitted. This power law is a single order higher than the previously fitted power law, thus a $(n+1)$ order power law instead of a n order power law, described as follows,

$$\text{Order 2:} \quad c_0 x^{(c_3 x^1 + c_2)} + c_1, \tag{4.27}$$

$$\text{Order 3:} \quad c_0 x^{(c_4 x^2 + c_3 x^1 + c_2)} + c_1, \tag{4.28}$$

$$\text{Order 4:} \quad c_0 x^{(c_5 x^3 + c_4 x^2 + c_3 x^1 + c_2)} + c_1, \tag{4.29}$$

$$\text{Order n:} \quad c_0 x^{(\sum_{i=1}^{n-1} c_{(i+2)} x^i + c_2)} + c_1, \tag{4.30}$$

$$\text{Order n+1:} \quad c_0 x^{(\sum_{i=1}^{n} c_{(i+2)} x^i + c_2)} + c_1. \tag{4.31}$$

An FFT is then calculated for this power law. This FFT is again divided by the FFT of the provided signal, to produce another quotient over frequency. The process is then partially repeated again, for a higher order power law. It repeats up to a 19-th order power law, each time providing another quotient

Stellenbosch University https://scholar.sun.ac.za

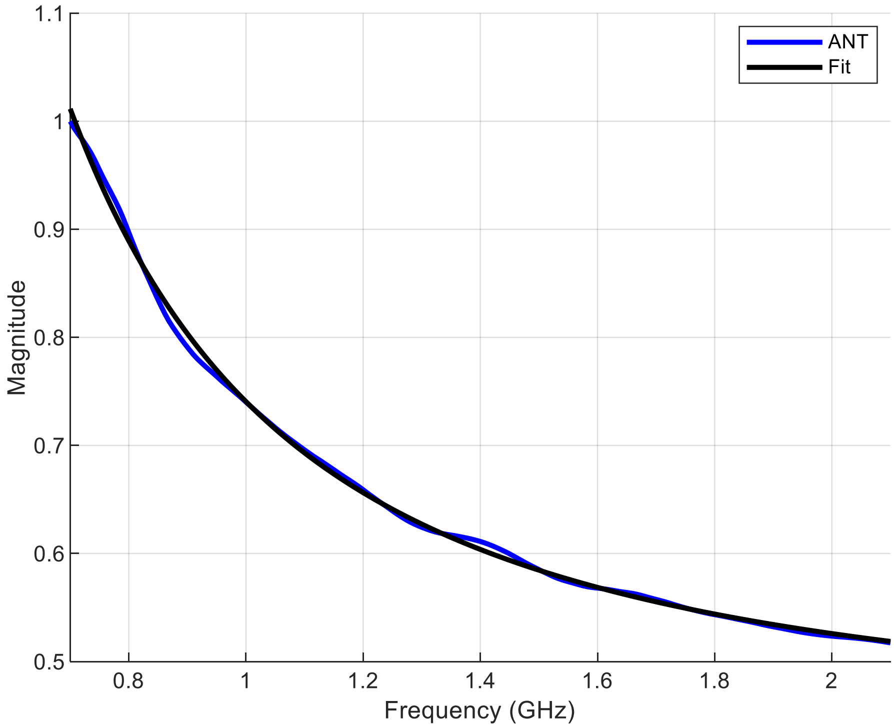

Figure 4.10: A signal plotted with a 3rd order power law fit

over frequency.

In Fig. 4.13 the quotient is shown for orders one, two and three. Notice that the 3rd order power law quotient mostly remains closer to one, from the right (∼1500 MHz) to the left at about ∼250 MHz, compared to the others. This will be explained shortly, but informs that this power law thus suppresses the slow components present in the original signal better than the others.

These quotients gives insight into how well the power law fits the signal. The power law would fit the signal perfectly if the quotient is a constant value of one over the entire band. It is expected that a power law will not perfectly fit the signal, and will model the underlying power law, without the ripple. This is because the ripple does not have a power law baseform.

This assumption stems from the general slow (or non-existent) oscillation of power laws as shown in Fig. 4.14, where a third order polynomial is compared to a third order power law, when both are used to fit an ANT calculation. This is due to the predominance of slow Fourier components, as shown in its FFT in Fig. 4.11. From Fig. 4.14, polynomials tend to be more oscillatory, compared to power laws. The polynomial is calculated as follows,

Stellenbosch University https://scholar.sun.ac.za

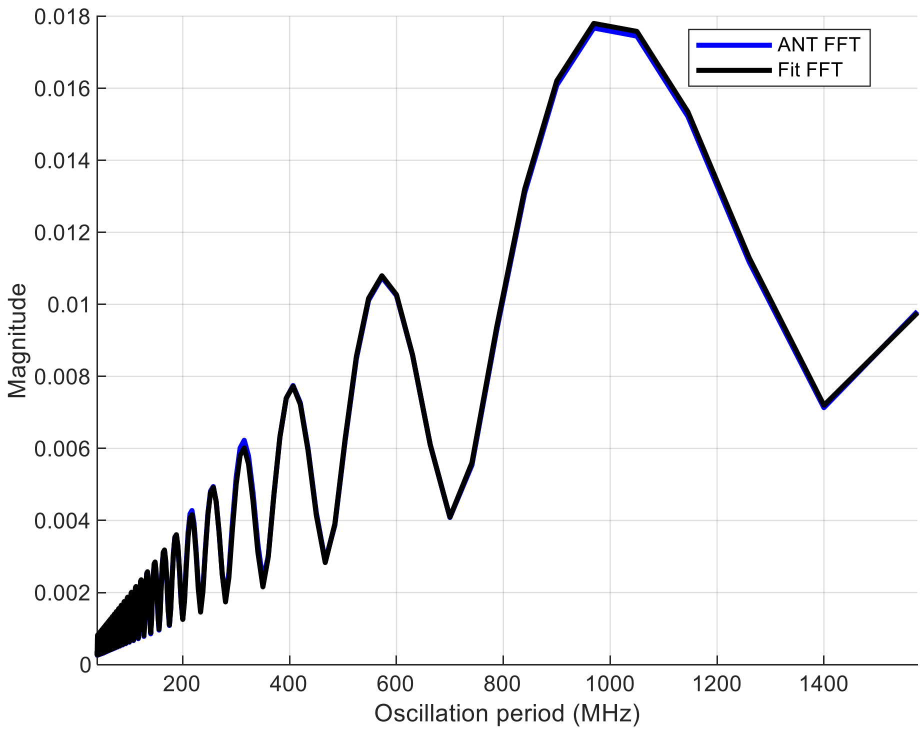

Figure 4.11: FFT of signal and a 3rd order power law fit

$$\text{Order 1:} \qquad a_1x + a_0, \tag{4.32}$$
$$\text{Order 2:} \qquad a_2x^2 + a_1x + a_0, \tag{4.33}$$
$$\text{Order n:} \qquad \sum_{i=0}^{n} a_{(i)}x^i. \tag{4.34}$$

In this case, both functions do not manage to fit the ripple of the ANT.

In Fig. 4.15 a 15th order of both is used, and compared. Notice that the 15th order polynomial fits the ripple of the ANT, where the power law does not. This is not desired. While it is intended that this process remove the slow varying components of the signal, it should not remove the ripple, which is why polynomial fitting is generally not used for ANT ripple extraction. From this even a 15th order power law will struggle to model the ripple in most cases. This reduces the risk notably of the ripple being modeled out. This behaviour of power laws allows it to generally characterise slower variation more effectively, compared to fast variation.
There is also the risk of ripple, or frequency component, injection. This occurs when the power law has some frequency components which are stronger, than in the signal it fits. These components are called artifact components.

Stellenbosch University https://scholar.sun.ac.za

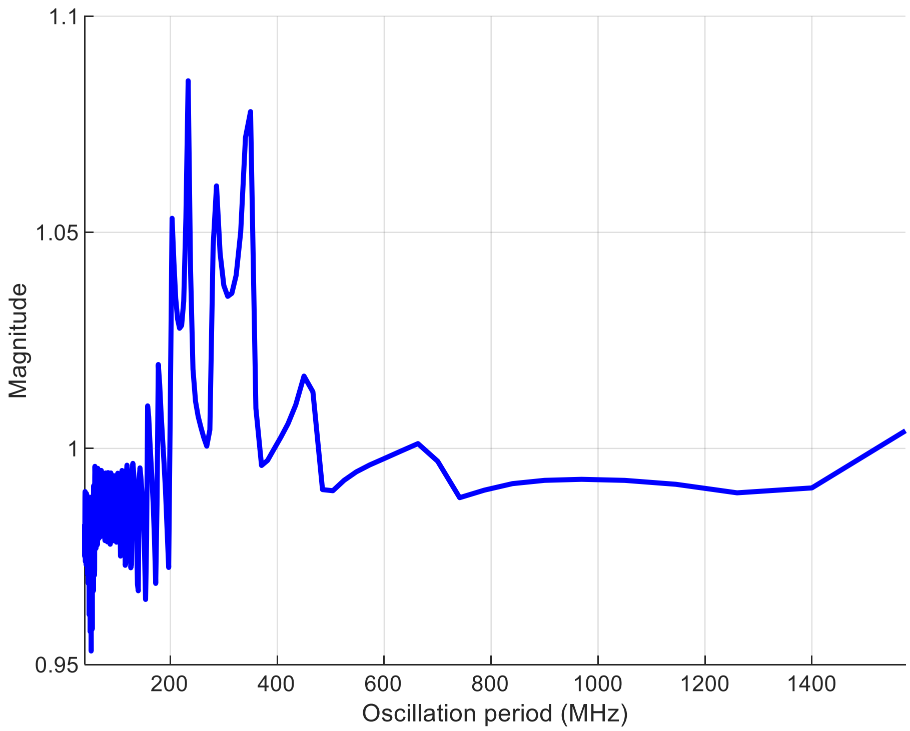

Figure 4.12: An example of the quotient graph for a 3rd order power law fit

Any value on the quotient graphs below 1 technically represents an artifact component. These components will be stronger after the subtraction. This could lead to these components becoming dominant in the subtracted result, even though they do not exist in the original signal. This is only a concern if the injected components are notable, compared to the dominant components in the signal, which is usually not the case. It is also generally unlikely, as the power law does not usually oscillate fast enough.

There is also the risk of insufficient frequency component suppression. This occurs when the power law does not have the same strong slow frequency components that the original signal has, which is then not removed in the subtraction. This results in the subtracted signal still having undesired slow components present, which can dominate and obscure the ripple components. Any value on the quotient graphs above 1 technically represents a component that is not fully suppressed. Insufficient suppression is also only a concern, if the slow components are still notable in the subtracted signal.

Both of these risks are, however, considered in the algorithm. The peaks above and below the quotient graph for each power law is compared against the probable ripple components in the signal. The probable ripple components have

Stellenbosch University https://scholar.sun.ac.za

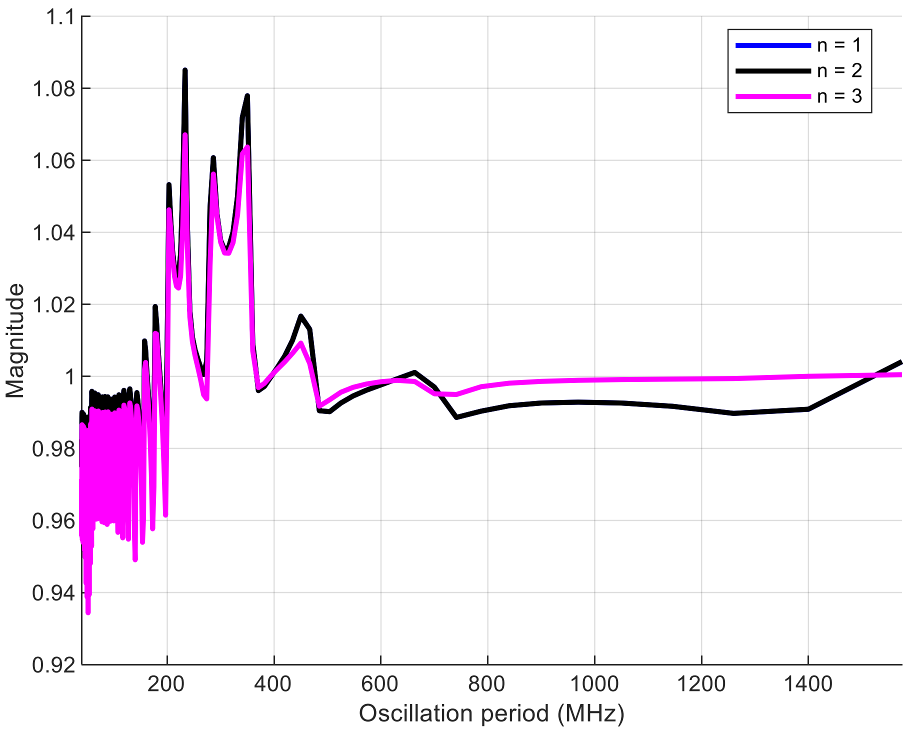

Figure 4.13: The quotient is shown for orders one, two and three

to be estimated, as the ripple that has to be extracted is not known. This is because the ripple is obscured by multiple other components. To determine the probable ripple components, the components that appear frequently across each subtracted result is collected. Any injection or lack of suppression that any power law might have on the subtracted result, will probably not be repeated by most of the other fits, as their form changes due to their order changing. The components that remain frequently unsuppressed, across all the different order power law fits, are thus probably ripple components.

The collected quotient graph peaks, for each power law fit, represent the dominant lack of component suppression, and dominant component injection. The peaks above the quotient is for the former, and below for the latter. This collection of peaks is then processed, for each power law, to determine a power law score. The purpose of the power law score is to determine the best power law fit, for low component injection and high slow component suppression. The power law order that provides the lowest score is considered the best for ripple extraction.

The power law score is determined as follow,

$$S_n = L_n Z_n + I_n X_n, \tag{4.35}$$

Stellenbosch University https://scholar.sun.ac.za

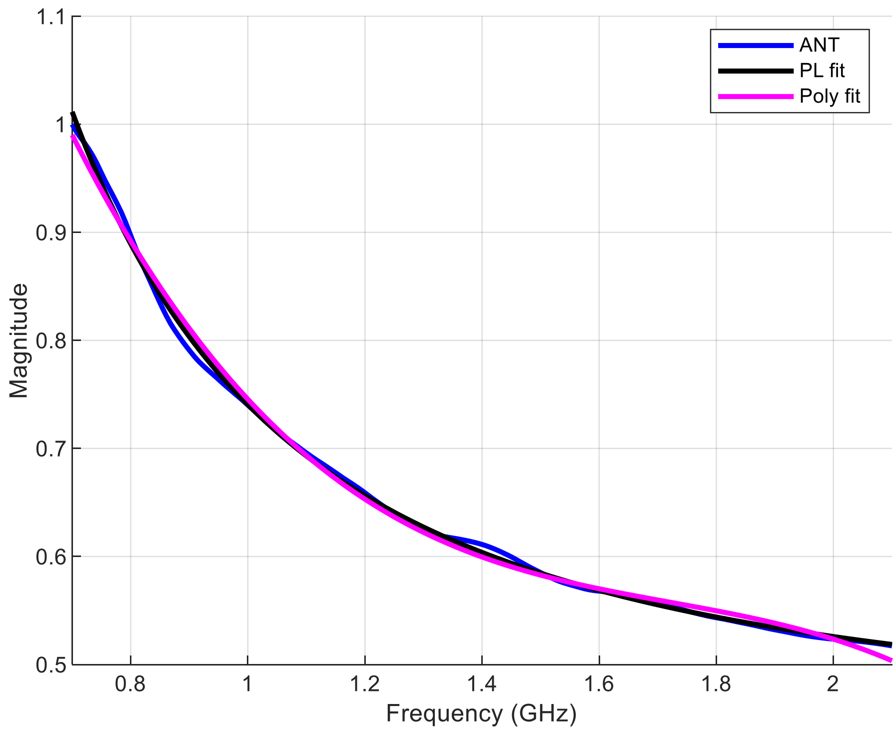

Figure 4.14: A third order polynomial fit is compared to a third order power law fit, when both are used to fit the ANT

where the n denotes the current power law order, S_n is the score, L_n is the suppression coefficient, Z_n is a collection of the dominant insufficient suppression, near each probable ripple component. The injection coefficient is I_n, and X_n is a collection of the dominant component injection, near each probable ripple component. The purpose of the coefficients is to decide the relevance of the quantity.

As mentioned earlier, only probable ripple components are considered. If other dominant components are found in the final result, where a chosen power law order is subtracted from the signal, then these components are removed. This is acceptable, as these components are probably injected components and not ripple components.

The coefficient values are separated into a ripple and non-ripple region. The separation between these regions is predicted by calculating the distance between the quotient graph suppression peaks, and choosing the separation point at the peak where an outlier distance occurs. This can be seen in Fig. 4.16. A suppression peak is a local peak, where all the marked values are suppression peaks. The distance between each peak pair, is their period difference.

Stellenbosch University https://scholar.sun.ac.za

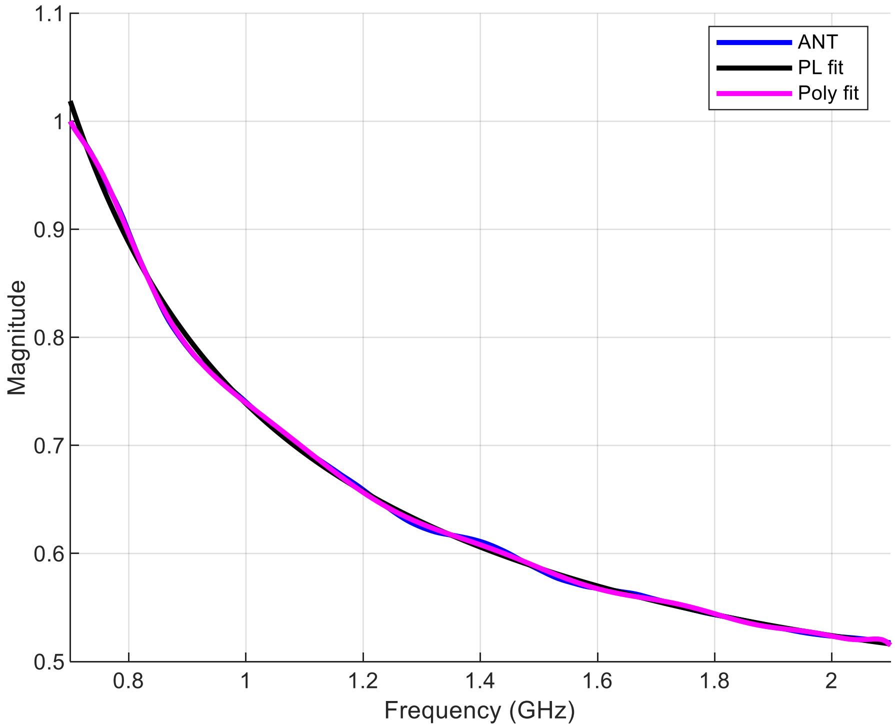

Figure 4.15: A 15th order polynomial fit is compared to a 15th order power law fit, when both are used to fit the ANT

The separation point is the discontinuity, in the region separation plot. The distance between each successive peak pair, from the left, is calculated. The outlier distance is calculated as the first suppression peak pair that has a value larger than double the average distance. The outlier peak is the right-most marked value. Only the suppression peaks is used, as the ripple will likely occur when the power law can not suppress the fast ripple components of the signal. The ripple region will likely occur where the power law rapidly struggles to suppress the fast components, which is why the region is defined at the peak where an outlier distance occurs.

It is also worth mentioning that although only probable ripple components are analysed, some of these predicted components might be outside of the ripple region, although it is unlikely. If this occurs, the component is either a slower ripple component or it is a slow component which the various power law fits struggle to suppress.

The coefficient $L_n = 5$ and $I_n = 10$, in the non-ripple region. It is unlikely that this case will occur, but if a non-ripple region component exists, it will be insufficiently suppressed by most power law fits. If a power law manages

Stellenbosch University https://scholar.sun.ac.za

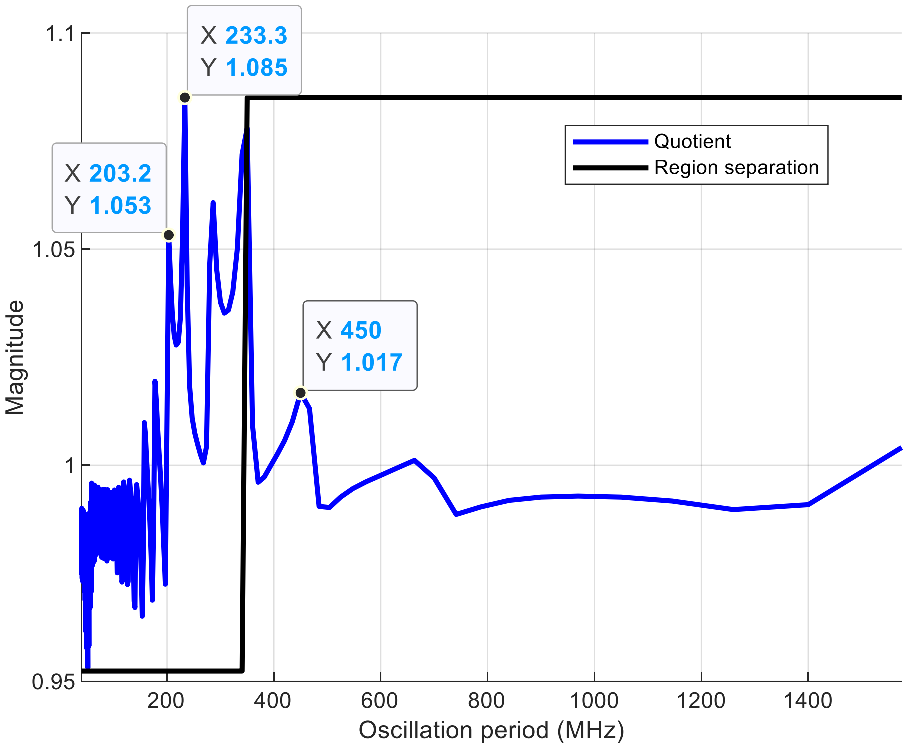

Figure 4.16: The predicted ripple region and non-ripple region separation, is displayed. The separation is predicted at the peak where an outlier distance occurs

to suppress it, then this component is probably not a real ripple component, as a power law fit will struggle to suppress a ripple component. In this case it is likely a difficult to suppress slow component, and the power law that suppresses it will be the best. Additionally, if a power law injects this component, then it is very likely to not be a ripple component. For these reasons, the coefficients are assigned high values in this range.

The coefficient $L_n = -1$ is assigned a negative value in the ripple region. This is because the lack of suppression of ripple components in this region is desired. It is assigned a lower value, as the lack of suppression of ripple will likely occur in all fits, and the contribution would dominate if assigned a higher value. The coefficient $L_n = 4$ in the ripple region, as injection of ripple is strongly discouraged. These coefficients are relative to each other, and can be chosen arbitrarily to prioritise the desired output of the fit.

The result of the iterative power law used on an example fine model of the ANT is shown in Fig. 4.17. The signal and the chosen power law is shown in Fig. 4.17a, followed by their quotient in Fig. 4.17b. The subtracted result is shown in Fig. 4.17c, where the power law is subtracted from the signal.

Stellenbosch University https://scholar.sun.ac.za

Finally, the FFT of the subtracted result is shown in Fig. 4.17d. The chosen order for the power law is one. Even though the third order power law suppresses the slow components more than a first order power law, the first order power law in this case extracts the ripple components more effectively. This is because these slow components are known not to be ripple components, and can be removed if dominant.

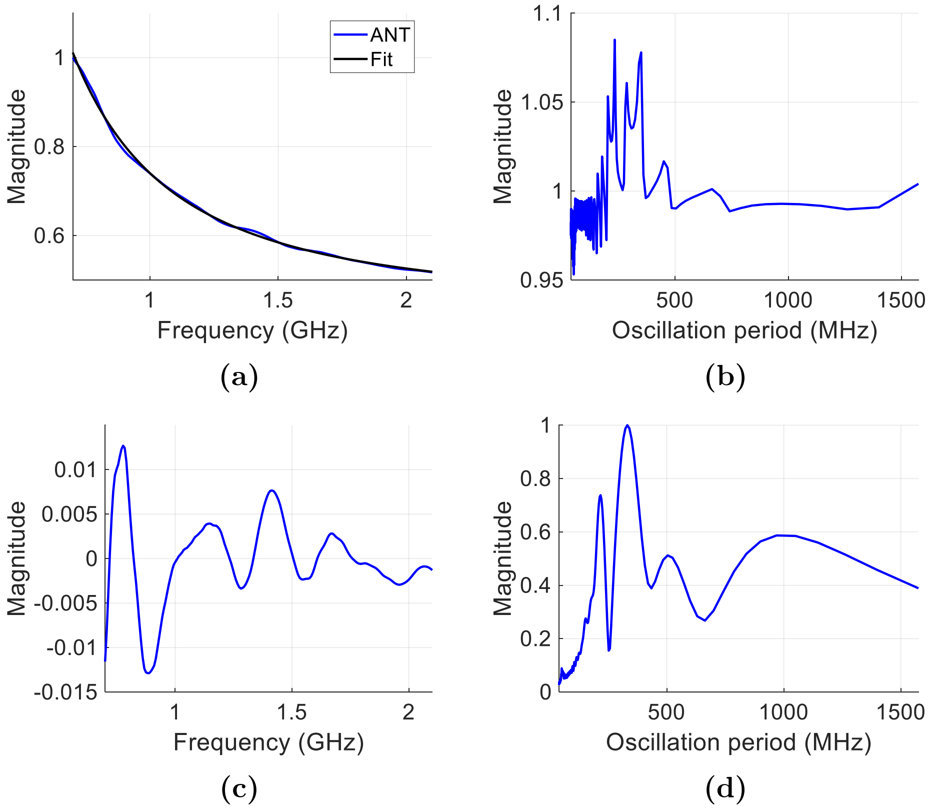

Figure 4.17: The iterative process result shown when used on an example fine model of the ANT. In (a) the signal and the chosen power law is shown. In (b) their quotient. In (c) the subtracted result, where the power law is subtracted from the signal. In (d) the FFT of the subtracted result is shown

4.2.4 Characterisation of ripple in the ANT: Direction impact

At this point the ANT has been described, including the terms necessary to calculate it. The tools to allow ripple extraction from the ANT, have also been developed and explained. The ANT ripple will be investigated and characterised next.

Stellenbosch University https://scholar.sun.ac.za

In Fig. 4.18 a normalised FFT of the ANT ripple at each pointing angle is shown on linear-log scale to highlight the frequency components of the ripple. From the FFT, it is shown that the ANT ripple feature many dominant frequency components across the observed pointing angles.

These different ripples, at different pointing angles, can be attributed to the background noise temperature effectively changing in each direction, when the reflector system rotates. In reality, the radiation pattern will rotate when the reflector system rotates, however, the background noise temperature can instead be rotated, with the radiation pattern remaining unchanged, to produce the same result.

The radiation pattern has a different ripple in each direction. This occurs because the interference effects, causing the ripple, is different in each direction. In some directions it might be mostly due to diffraction effects, and in others due to spillover effects, etc. It also occurs because the path length difference between interfering fields will change in each direction. Interference effects was discussed in detail, in Chapter 3. Recall that the ANT integral is calculated over the entire 4π steradian sphere, and is thus influenced by radiation pattern and background noise temperature in all directions, as shown again below,

$$T_{\mathrm{A}}(f|\hat{\mathbf{r}}_0) = \frac{\iint_{4\pi} N(f,\Omega|\hat{\mathbf{r}}_0)\sin\theta d\Omega}{\iint_{4\pi} U(f,\Omega)\sin\theta d\Omega}, \tag{4.36}$$

$$N(f,\Omega|\hat{\mathbf{r}}_0) = T_{\mathrm{b}}(f,\Omega)U(f,\Omega|\hat{\mathbf{r}}_0). \tag{4.37}$$

In the ANT integral, the radiation pattern is multiplied with the background noise temperature. As the background noise temperature changes, the radiation pattern in each direction will be multiplied with a different background noise temperature value. Since the radiation pattern has a different ripple in each direction, the ripple in each direction will be weighed differently, as the background noise temperature changes. This changes the total answer in the ANT, as the integral is calculated, to lead to different ripples behaviour for each pointing angle. Since the ripple in each direction are weighed differently, certain directions contribute more to the ANT calculation, and are thus more important. These directions will change, depending on the pointing angle.

The ANT is normalised to the total radiated power, as seen in the denominator of (4.1). The denominator is a constant scalar over frequency, and as such only scales the result of the numerator of the ANT. This multiplicative scaling has a slight impact on the ripple, because the change in the numerator at each frequency, is a function of the numerator at each frequency.

The ANT is shown in Fig. 4.19a, followed by its numerator in Fig. 4.19b. It is plotted for a -80° tipping angle. In Fig. 4.19c the ripple of the ANT and its

Stellenbosch University https://scholar.sun.ac.za

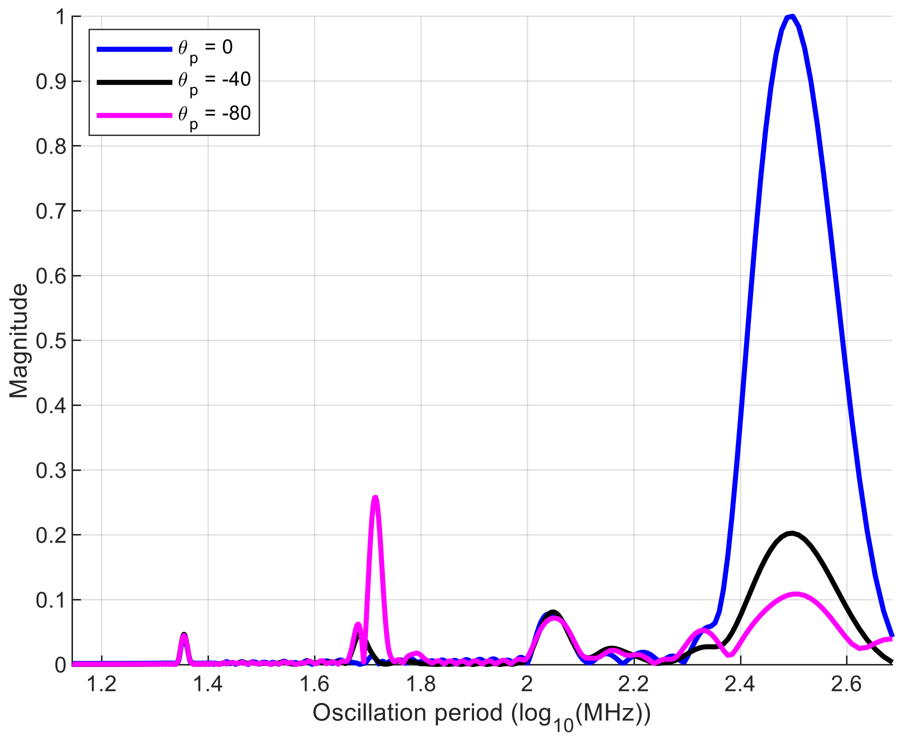

Figure 4.18: A normalised FFT of the ANT ripple at each pointing angle is shown on linear-log scale to highlight the frequency components of the ripple

numerator is shown. In Fig. 4.19d the FFT of the ripple is shown for the ANT and its numerator. From Fig. 4.19 a slight change can be seen in the ripple, however, it does not change the frequency of the dominant ripple components. Furthermore, the denominator is not a source of ripple in the ANT calculation, as it is a scalar.

4.2.5 Characterisation of ripple in the ANT: ANT ripple origin

To investigate where the ripple comes from, recall that the numerator of (4.1) requires a product, $M_{\mathrm{TbUS}}(f, \Omega|\hat{\mathbf{r}}_0) = N(f, \Omega|\hat{\mathbf{r}}_0)\sin\theta$, of the background noise temperature, the radiation pattern of the full reflector system and a sinus function. The sinus function is not a function of frequency, so it can not contribute to a frequency ripple in the ANT. Also recall that the model of the surrounding scene brightness temperature from Fig. 4.2 (figure repeated again in Fig. 4.20 below), which is used to generate the background noise temperature, has Galactic synchrotron radiation. This radiation dominates the system noise temperature at frequencies in the lower part of the bandwidth, and has an

Stellenbosch University https://scholar.sun.ac.za

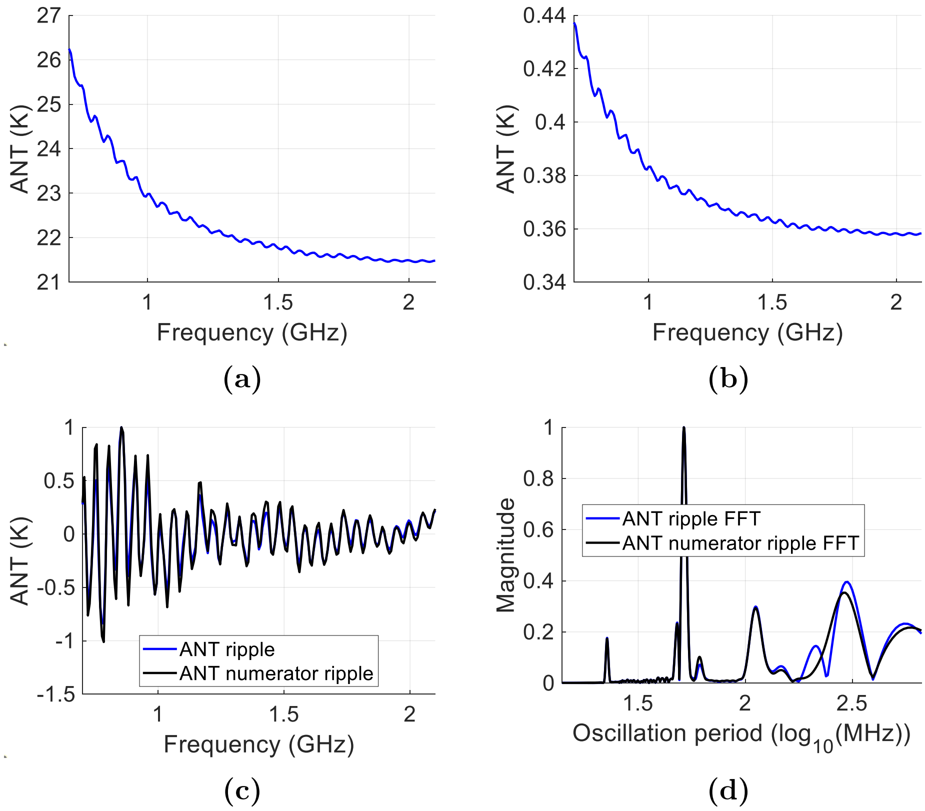

Figure 4.19: The ANT is shown in (a), followed by its numerator in (b). It is plotted for a -80° tipping angle. In (c) the ripple of the ANT and its numerator is shown. In (d) the FFT of the ripple is shown for the ANT and its numerator

average $\frac{1}{f^{2.75}}$ power law response, which does not include a ripple.

The only remaining part that can possibly contribute to the ripple is the radiation pattern of the full reflector system, which does have a ripple over frequency, as explained in Chapter 3. There is another mechanism, instead of interference, that adds ripple over frequency. In Fig. 4.21 this mechanism is shown and the reason why it leads to a ripple over frequency for the radiation pattern of a full reflector system. When the frequency increases, the electrical size of the reflector increases. This increase in size leads to a higher effective aperture diameter which leads to a narrower main beam. As the main beam narrows, the sidelobes moves closer to the direction of maximum radiation intensity. The sidelobes also become smaller. as more energy is radiated in the main beam, which will become larger. If a specific direction is chosen, and the radiation pattern is observed over frequency, a ripple is seen. This is because for one frequency the sidelobe at the observed angle might be at a peak, and as the frequency increases and the sidelobes moves in, the directivity at the observed angle will oscillate from a seeing a peak to a null and back to a peak continuously. Additionally, this directivity will also decrease for the observed

Stellenbosch University https://scholar.sun.ac.za

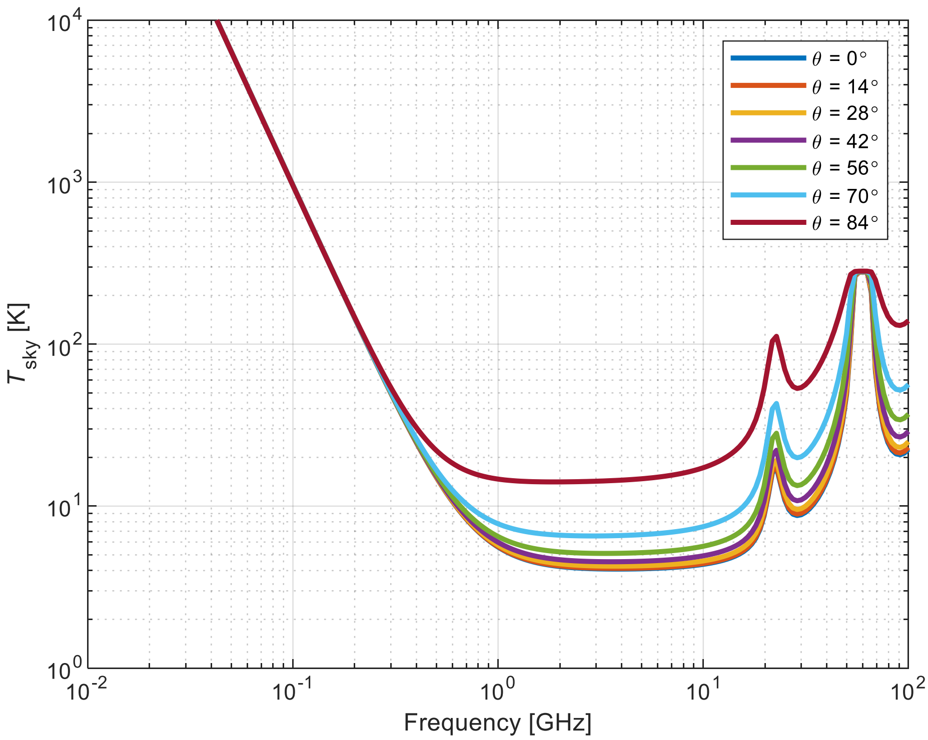

Figure 4.20: Sky brightness temperature over frequency

angle over frequency, as more and more energy is added into the main beam and the sidelobes becomes smaller, which relates to the ripple reducing over frequency.

Important to note, is that the direction of maximum radiation intensity does not experience this ripple. This is especially profound when discussing AE ripple, and the prediction of this ripple, in the next chapter. The AE ripple is calculated only from the direction of maximum radiation intensity, and as such, is not influenced by the ripple mechanism mentioned above. This makes the prediction of the AE ripple easier than the ANT ripple prediction.

The radiation pattern is the cause of the ripple in the ANT over frequency, however, it can also be observed that the ripple in the ANT is a function of tipping angle as seen in Fig. 4.4. This implies the ripple in the ANT is not simply the ripple in the radiation pattern. The origin of this tipping angle dependency, and the impact it has on the ripple of the ANT, is discussed soon.

Non-ideal effects that interfere with the radiation pattern from the reflector system, will radiate in all directions causing interference in all directions. The entire full system radiation pattern in all directions thus contributes to the

Stellenbosch University https://scholar.sun.ac.za

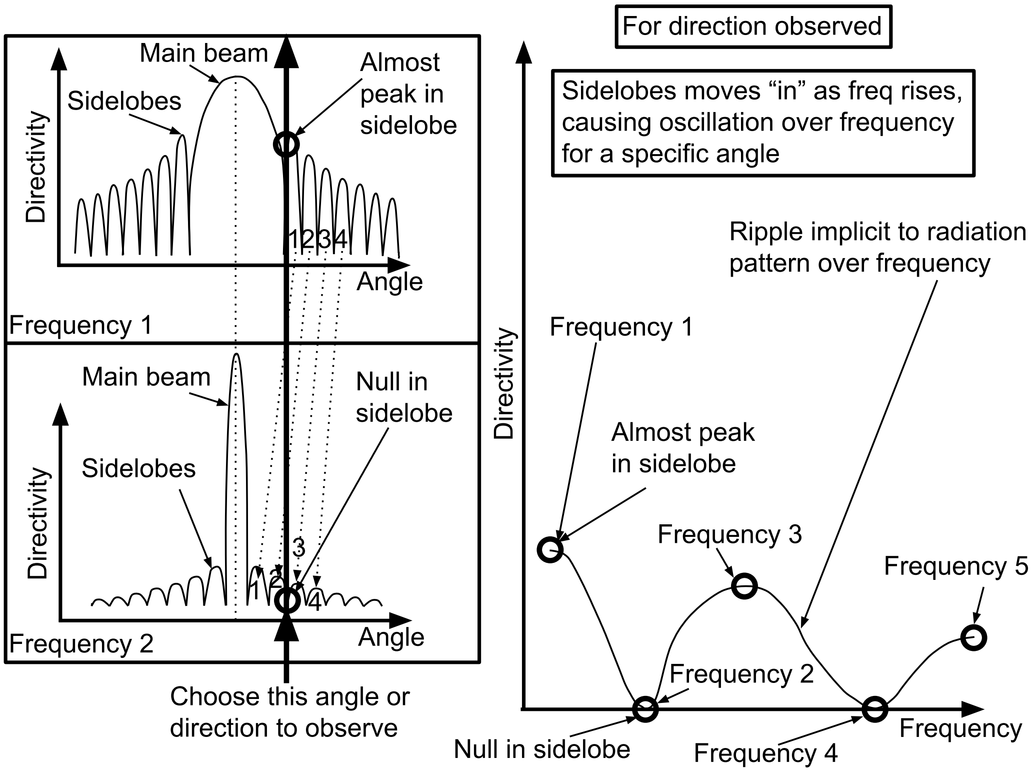

Figure 4.21: A full reflector system radiation pattern implicitly has a ripple over frequency

ripple in the ANT. The contribution to the ANT calculation (and ripple) from the mainlobe of the radiation pattern will be significantly higher than the contributions due to the sidelobes, assuming a uniform background noise temperature over angle. Fig. 4.22 shows why the ripple contribution for the ANT is larger for the main beam compared to the sidelobes' contribution. This is because the main lobe of the radiation pattern of a reflector system has significantly more energy compared to the sidelobes.

Interference is an additive process. The relative energy added from a specific non-ideal effect interfering in the main lobe, will be less, compared to the relative power added in the sidelobes. The ripple effect caused in the radiation pattern by this non-ideal effect will thus be smaller in the main lobe, compared to the sidelobes. Fig. 4.23 shows how the relative energy added to zenith, or the main beam, from interference is less than that added to the sidelobes.

Stellenbosch University https://scholar.sun.ac.za

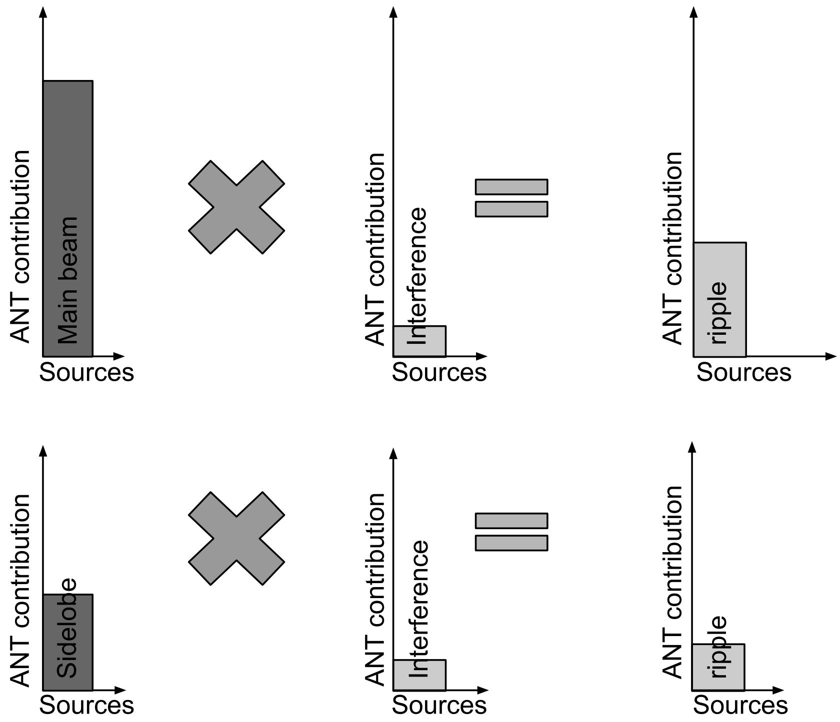

Figure 4.22: Ripple contribution for the ANT is larger for the main beam, compared to the sidelobes

4.3 Antenna noise temperature ripple as a function of tipping angle

4.3.1 True-View Projections

True-View projections are used in this chapter to investigate important angles regarding ripple contribution to the ANT, and thus a quick overview of true-view projections will be given to allow the reader to interpret their results.

Spherical projections usually attempt to project the full 4π steradian sphere onto a 2-D plane or grid. This can not be done by directly projecting onto the plane, as duplicate values will be created as shown in Fig. 4.24. The duplication is a result of the sphere not being a one-to-one function, with multiple combinations of range elements resulting in the same domain answer. The projection is thus an implicit function of the range elements, from which multiple combinations can lead to the same projection.

Instead different spherical projection strategies have been developed. Examples include the stereographic projection, the Mercator projection or the true-

Stellenbosch University https://scholar.sun.ac.za

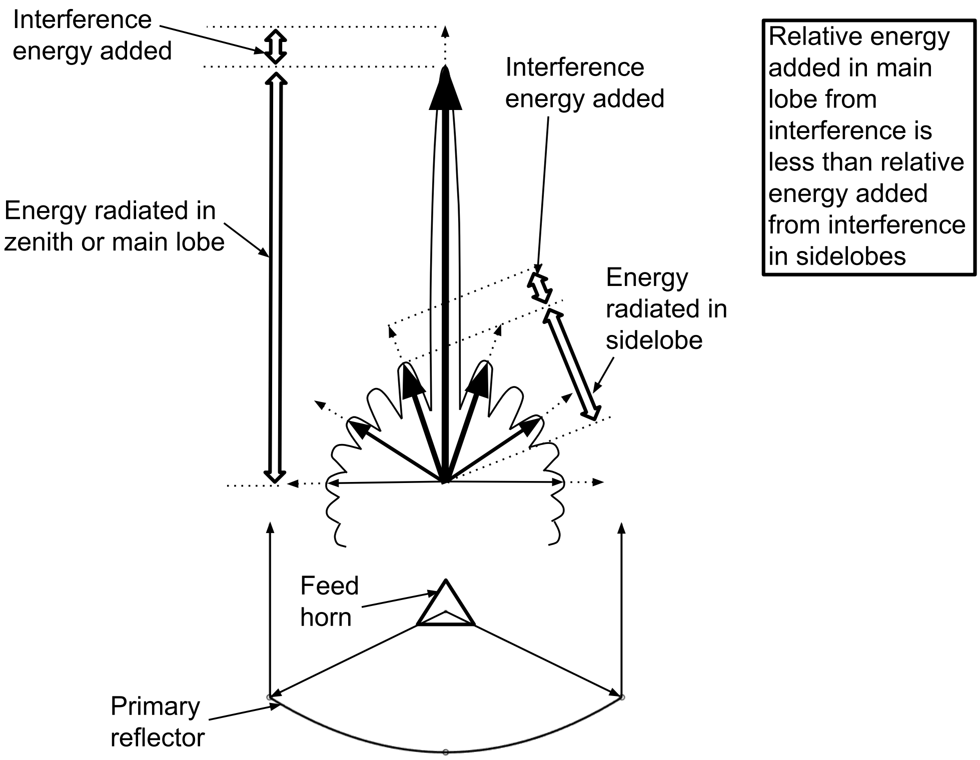

Figure 4.23: The relative energy added by interference effects is less in zenith, or the main beam, than it is in the sidelobes. This is because the main beam has much more energy than the sidelobes, yet the interference effect energy added will be relatively similar. This results in a smaller ripple over frequency for the far-field in the direction zenith, compared to the sidelobe directions

view projection among others. All spherical projections cause distortions in the projection, as it is impossible to project a sphere onto a 2D plane without distortion, and the different types of projection strategies distort different parts of the projection. The true-view coordinate system is a polar (circle) representation of the polar spherical (θ,ϕ) coordinate system [40], and not a rectangular 2D plot such as the popular Mercator projection generally used to project Earth onto a 2D plane. The true-view projection is often used in antenna design to project the far-field radiation pattern sphere onto a 2D grid. The benefit of a true-view projection is that it does not notably distort the projected data to the centre of the 2D grid, which is in the $\theta = 0°$ direction. The projection does, however, distort more outside of this direction. The highest distortion occurs in the $\theta = 180°$ direction.

The centre of the 2D grid is usually the projected main beam for an antenna system. The main beam is thus centered in the $\theta = 0°$ direction. The main beam is the cone in which most of the power is radiated from the antenna system, and thus is the most important to correctly display. Most of the

Stellenbosch University https://scholar.sun.ac.za

distortion from the true-view projection occurs when the backlobe is projected, which is in the $\theta = 180°$ direction. The backlobe is thus the radiation in the opposite direction of the main beam, and contains significantly less power than the main beam. A distorted backlobe is relatively insignificant. This makes the true-view projection a good choice for radiation pattern projections and the true-view projection is used extensively in this dissertation for its benefits [40]. A true-view projection casts the two orthogonal components of the grid as described in the following (4.38) for the y-axis,

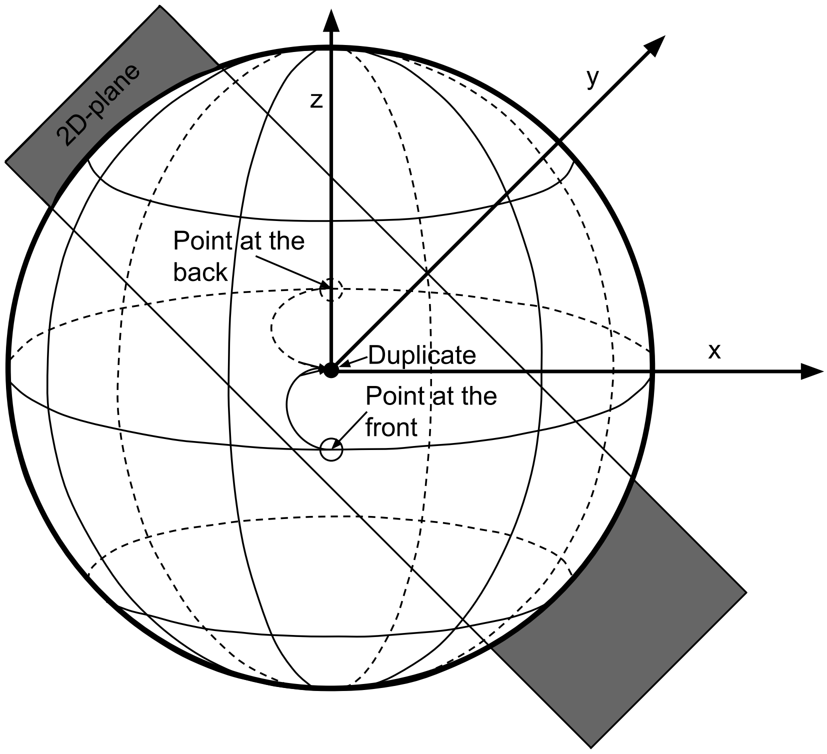

Figure 4.24: Directly projecting sphere to plane causes duplicate values

$$\mathrm{Y_g} = \theta \sin(\phi)^\circ \tag{4.38}$$

and the following transform (4.39) for the x-axis,

$$\mathrm{X_g} = \theta \cos(\phi)^\circ \tag{4.39}$$

to map the sphere onto a 2-D plane.

An ideal Gaussian pattern is used to demonstrate the projection. An ideal Gaussian pattern is an idealised feed pattern, which has no sidelobes. It is

Stellenbosch University https://scholar.sun.ac.za

useful, as it can be used to approximate a physical feed [41]. The Gaussian pattern can be defined by,

$$U_{\text{gndB}}(\theta) = T_{\text{dB}} \left(\frac{\theta}{T_\theta}\right)^2, \tag{4.40}$$

where U_{gndB} is the normalised radiation intensity in dB, T_{dB} is the feed edge taper in dB, and T_θ is the feed edge taper angle in radians. The normalised radiation intensity in dB, is defined to have the value of the edge taper, at the edge taper angle. In Fig. 4.25a, the edge taper is chosen as $T_{\text{dB}} = -12$ dB, and the taper angle as $T_\theta = 45°$, which is converted to radians in the calculation. Furthermore, the normalised radiation pattern in dB is shown in Fig. 4.25b, and its true-view plot in Fig. 4.25c. The pattern is independent of frequency and ϕ. Any arbitrary scalar can be added to the normalised radiation intensity in dB, to tailor the response outside of a normalised version.

The centre of the true-view plot will be directly up or in the z-direction. The edge of the true-view plot will be directly down, or in -z. It can seen that the direction of maximum radiation intensity, in the z direction, is also the brightest region in the true-view plot. A region in this context can be described as a cluster of angles around a specific direction.

4.3.2 Analysis of ANT calculation terms

Recall that to fully calculate the ANT as seen in (4.1), the integral of the product, M_{TbUS}, of multiple terms have to be calculated, and the ANT has to be normalised. These terms include the radiation pattern or radiation intensity $U(f, \Omega|\hat{\mathbf{r}}_0)$, the background noise temperature $T_\text{b}(f, \Omega)$ and the sin function $\sin\theta$. It is not necessary to consider the normalisation of the ANT, in regards to the investigation of angle dependence of the ANT, as it simply scales the ANT.

Assume the antenna is pointing to a 0° tipping angle. In Fig. 4.26 the terms required to calculate the ANT in this case is shown, including M_{TbUS}. Every figure presents information on a true-view grid with HEALPix resolution reduction. HEALPix is discussed soon in the HEALPix subsection. It is calculated for $f = 0.7$ GHz. The normalisation factor is excluded.

The primary and subreflector projected positions are also shown on each true-view plot. The projection is realised by projecting the rim coordinates of each reflector, from spherical coordinates, to true-view coordinates. The projection for the primary reflector is performed from the primary focus, in the classical conic section case. The projection of the subreflector is performed from the

Stellenbosch University https://scholar.sun.ac.za

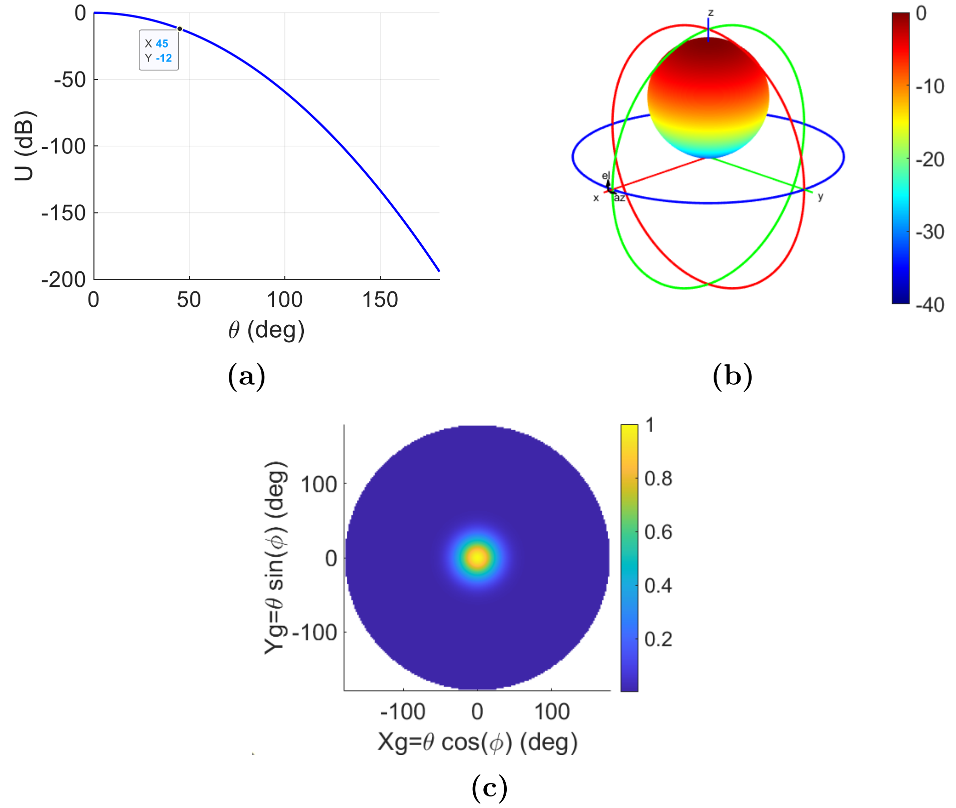

Figure 4.25: The radiation pattern of an ideal Gaussian feed, with a -12 dB edge taper. In (a) the normalised radiation intensity is shown to have a -12 dB edge taper, at 45° angle. The normalised radiation pattern is shown in 3D in (b), and in true-view in (c)

feed position, or the secondary focus in the classical system. The reflectors are projected from these positions, as the feed is the dominant approximated beam focus associated with the SR, and the primary focus is the dominant approximated beam focus associated with the primary reflector [42]. By using this approach, it can be seen where the radiation energy is concentrated, and its origin. This presentation can be useful in the identification of the non-ideal effect, which dominantly influences the radiation pattern, and will be discussed more in the final section of this chapter, before the conclusion. Thus, the projected subreflector is located in the area near the centre, enclosed by the black border. The projected primary reflector is located in the area near the edge, enclosed by the black border.

In Fig. 4.26a the radiation intensity of the full reflector system is shown, with most energy in the direction of maximum radiation intensity, as expected. In Fig. 4.26b the background noise temperature is shown. The background noise temperature has a distinct colour, or temperature, transition at around the 90° angle in either axis. This is expected, as this angle marks the transition

Stellenbosch University https://scholar.sun.ac.za

between the sky region and the ground region at the horizon of Earth. In this case, the sky region is in the blue area near the centre. The ground region is in the remaining yellow area. Since the background noise temperature is calculated in L-band, the sky region is much colder than the ground. If the background noise temperature was calculated at a low frequency of 100 MHz, then the sky region would be much hotter (1000K) compared to the ground (300K). In Fig. 4.26c, the sinus function can be seen, which oscillates into peaks and valleys over angle. Finally, in Fig. 4.26d M_{TbUS} from these terms is shown. Thus, the product of the radiation intensity (Fig. 4.26a), the background noise temperature (Fig. 4.26b), and the sinus function (Fig. 4.26c).

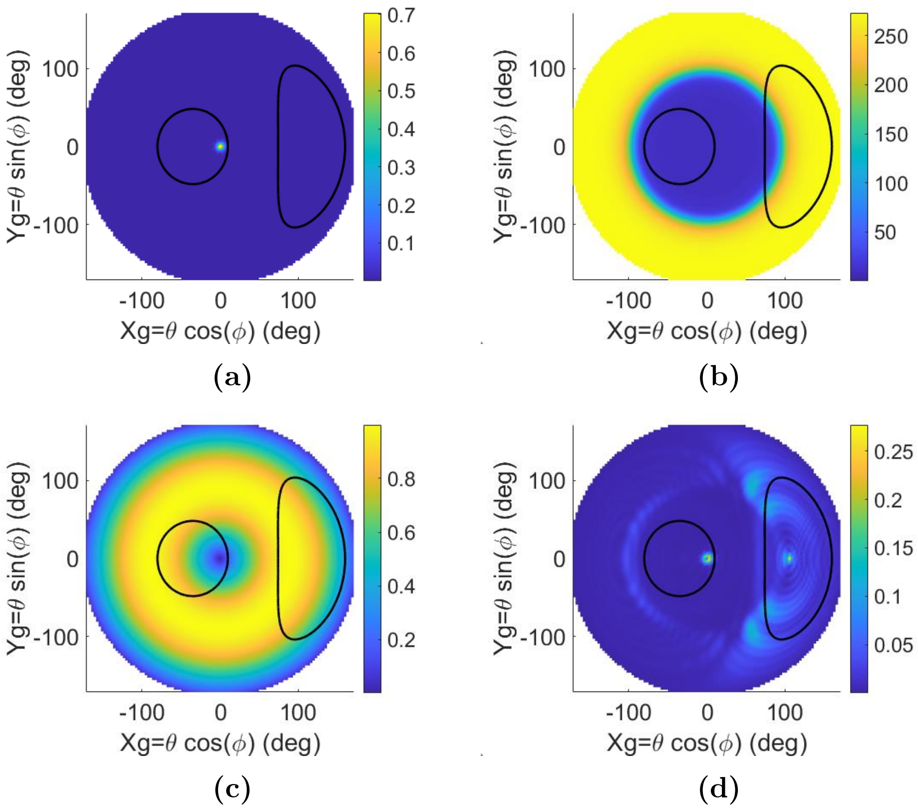

Figure 4.26: Each term required to evaluate the integral of the ANT, excluding the normalisation, is shown. M_{TbUS} from these terms is also shown. In (a) the radiation intensity of the full reflector system is shown. In (b) the background noise temperature is shown. In (c) the sinus function is shown. In (d) M_{TbUS} from the factors is shown. Each figure is presented on a true-view grid with HEALPix resolution reduction. The primary and subreflector positions are also shown on the true-view grid. This is shown for 0.7 GHz

Stellenbosch University https://scholar.sun.ac.za

4.3.3 HEALPix

HEALPix was created in order to have a mathematical structure which allows a suitable discretization of functions on a sphere, at high and varying resolutions. The purpose of this was to enable efficient statistical and astrophysical analysis of full sky data sets. This is because these data sets are large and cumbersome to analyse. The data sets are created through satellite missions which measure the cosmic microwave background (CMB) anisotropy, and is then used to create data sets, at various frequencies, which are used to synthesise full-sky maps of the microwave sky. The synthesise is accurate to a few arcminutes for angular resolution [43].

HEALPix can create this structure due to three properties. The first is because the sphere is hierarchically tessellated into curvilinear quadrilaterals, as shown in Fig. 4.27. Each shape used in the tessellation is known as a pixel. The lowest resolution consist of only 12 pixels. Increasing the resolution of the tessellation (or HEALPix projection) results in each pixel divided into four new pixels. This resolution increase is shown in Fig. 4.28. The resolution is increased from the base level, resulting in 12 pixels, to a level higher, resulting in 48 pixels. The second property, is that each pixel has approximately the same area, at a specific resolution. The final property is that the pixels are distributed on lines of constant latitude, which is critical for all harmonic analysis applications involving spherical harmonics.

The true-view projections used in this dissertation, is projected from a sphere. Spheres in this dissertation, and in most EM simulation software, is defined on the standard theta-phi grid. HEALPix can be applied to spheres, to change the non-uniform resolution of the sphere, to an approximate uniform area grid instead. This is useful for various presentations, which will later be described in more detail. In the context of this dissertation, when HEALPix is applied to a sphere, its true-view projection will display pixels or polygons. Each pixel, or polygon, consists of a cluster of similar angles, instead of individual angles. The terms pixel, polygon, or angle, are used interchangeably in this chapter, as they imply a similar direction.

The angular variation of the functions described in true-view is generally slower over most of the grid, compared to the fast variation found at the horizon of the background noise temperature, or around the main beam of the radiation pattern. Due to this, the application of HEALPix can be used to reduce the number of angles, to increase the speed of the analysis, with a smaller sacrifice to accuracy, in the slower angular variation regions. While using HEALPix in the fast variation regions might lead to a larger sacrifice to accuracy, these regions are far smaller, compared to the slower regions, and the impact is thus less severe. The HEALPix projection, or averaging, will refer to the applica-

Stellenbosch University https://scholar.sun.ac.za

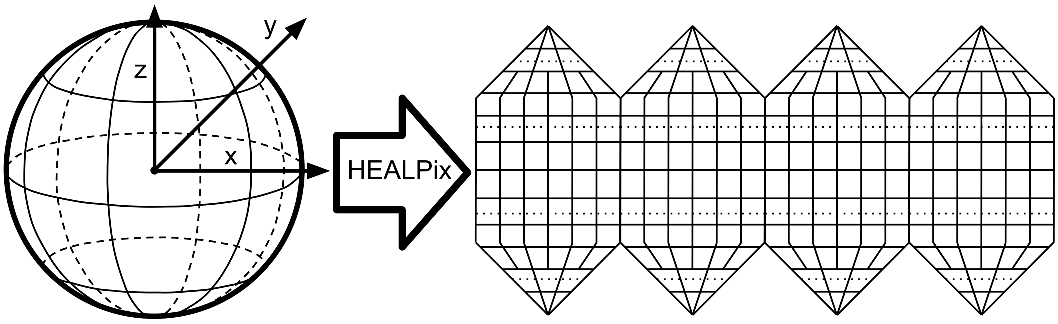

Figure 4.27: Sphere hierarchically tessellated into curvilinear quadrilateral, using HEALPix

tion of HEALPix on the applicable sphere.

The speed increase is especially notable due to only requiring fitting each pixel, by using a power law for example, instead of fitting each angle. The speed increase is important, as fitting each angle can take multiple days (or a week) to calculate, with the HEALPix projection increasing the speed by more than x30 times. The HEALPix averaging reduces the number of angles, by grouping angle clusters into an attempted equispaced polygon grid. HEALPix pixelisation is especially useful for the poles of a sphere, since they have many duplicate values for phi at $\theta = 0°$ and $\theta = 180°$. HEALPix packs the poles as a single pixel, eliminating the duplicate information.

4.3.4 Ripple contribution approximation through true-view regions

The ripple contribution to the ANT ripple, from each angle in the radiation pattern, can be approximated through true-view plots. This is possible, because the integral of M_{TbUS}, can be calculated by the summation of M_{TbUS}

Stellenbosch University https://scholar.sun.ac.za

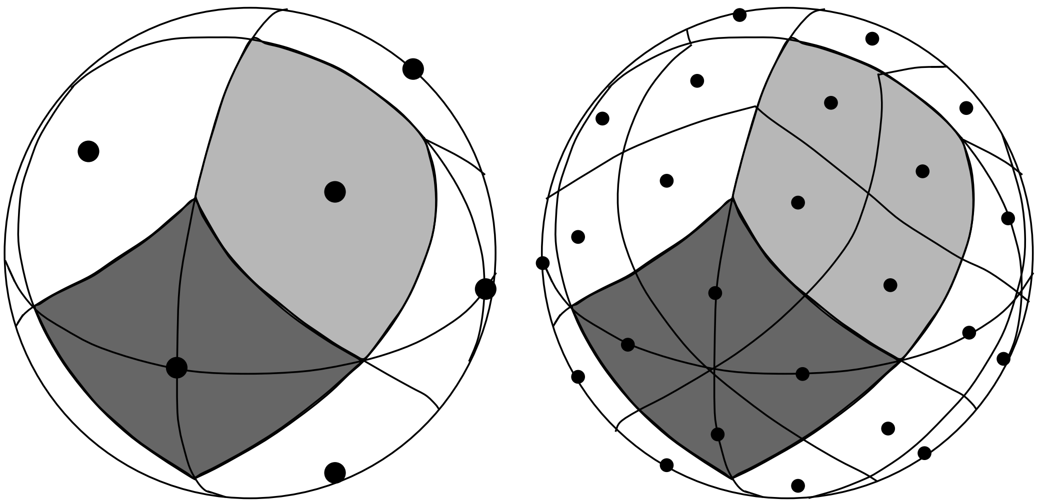

Figure 4.28: Resolution increase from the base level seen in the left image, to a higher resolution seen in the right image

over the entire projection. This is discussed in detail in Appendix A. Furthermore, in Appendix A it is proven that the angular resolution used for the full radiation pattern, in this dissertation, is high enough for the ANT integral to converge.

The benefit of calculating the integral as a summation over the grid, is that it allows immediate insight into the calculation of the ANT, by observation of the grid or figure. Calculation of the integral (or the entire ANT) would only yield a scalar value, at a specific frequency, which would not provide any insight into the origin of the ANT ripple. M_{TbUS} from the factors required to calculate the ANT, is shown again below in Fig. 4.29. From Fig. 4.29 it is immediately apparent that the brighter or higher magnitude regions, will contribute more to the calculation of the ANT, than the other regions will. Remember that these regions refer to specific angles, or angle clusters in the case of the HEALPix application. Thus, certain regions or angles contribute more to the calculation of the ANT, than others. Furthermore, a large number of angles have relatively low contributions, while a selection of other angles largely dominate the calculation. This allows the identification of important angles for the calculation, and to disregard other less important angles. These important angles can then be used to create a relatively close approximation

Stellenbosch University https://scholar.sun.ac.za

of the ANT.

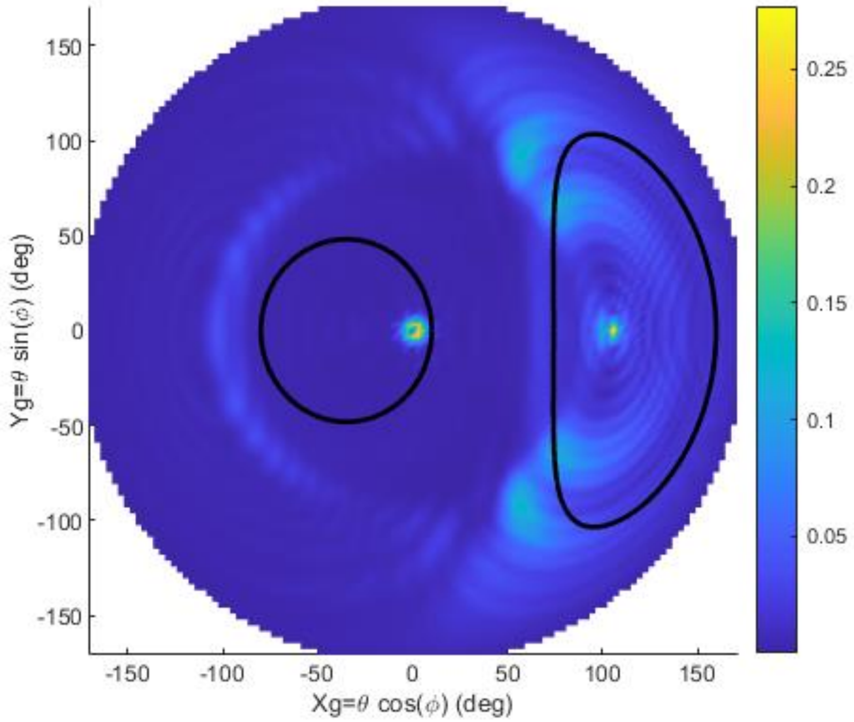

Figure 4.29: M_{TbUS} from the factors required to calculate the ANT. The contribution of each angle in the calculation of the ANT, is determined by the brightness or magnitude at the angle. This is shown for 0.7 GHz

Recall that these important angles are determined from M_{TbUS}, which is calculated from the product of the radiation pattern, or intensity, the background noise temperature and the sinus function. Naturally, an important angle will only occur where M_{TbUS} have a high magnitude. The radiation pattern will largely contribute in the region where its main beam is located. For L-band, the background noise temperature will contribute much more, below the horizon, in the ground regions. Finally, the sinus function is part of the surface area element of the surface integral of a sphere to regulate the contributions near the poles, as smaller area elements are required for the denser grids. It is still, however, part of M_{TbUS} and will contribute in an oscillatory manner over angle.

It is expected that the ripple contributions observed in these important angles, will largely determine the ripple observed in the ANT. Recall that the radiation pattern is the only term which can contribute to the ripple of the ANT, and thus the only relevant term in this context. The radiation pattern

Stellenbosch University https://scholar.sun.ac.za

$U(f, \phi, \theta|\hat{\mathbf{r}}_0)$, is a function of frequency, angle and pointing direction of the reflector system. If the reflector is tipped to a specific direction, then the radiation pattern reduces to $U_\mathrm{p}(f, \phi, \theta)$. Furthermore, assume a specific angle is selected, then the radiation pattern reduces to $U_\mathrm{pa}(f)$. Thus, for a specific angle and pointing direction, a function over frequency is observed. This can be conceptually seen in Fig. 4.30, and practically in Fig. 4.31 for two arbitrary chosen angles. This function has a ripple over frequency, which is expected, as the radiation intensity is the only ripple contributor to the ANT ripple.

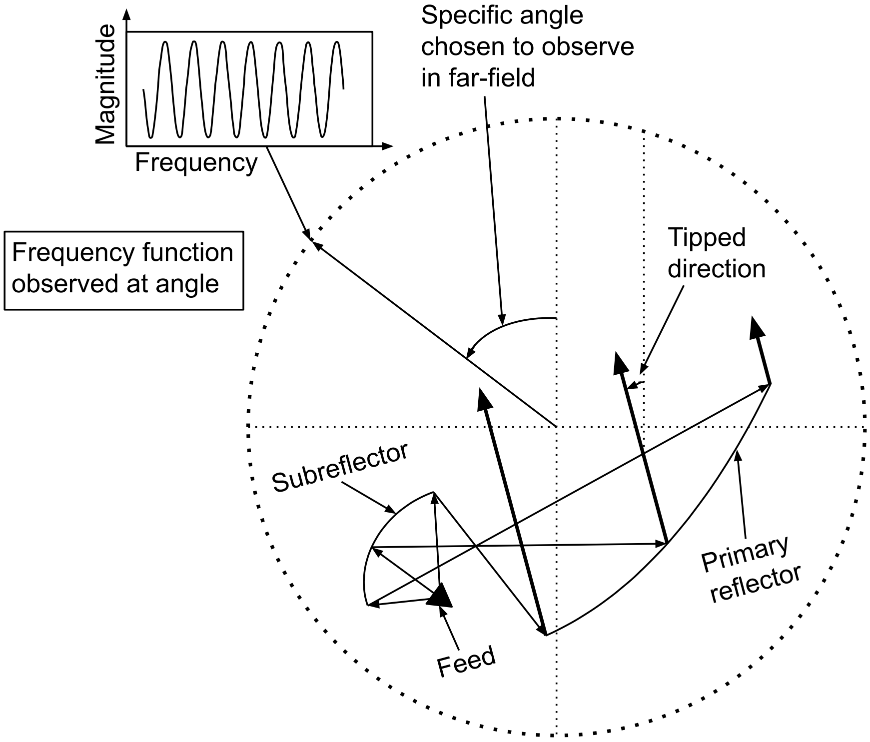

Figure 4.30: Function of frequency observed for radiation intensity, when a specific angle is chosen to be observed, when the reflector is pointed in a specific direction

An FFT can be performed on this function $\mathrm{FFT}(U_\mathrm{pa}(f))$, as seen in Fig. 4.32 and Fig. 4.33, to provide insight into the frequency component composition. Before this transform, the ripple can be isolated using a ripple extraction technique, and the FFT can be applied on the ripple instead. This is useful to support extracting ripple components.

Before discussing ripple extraction on the radiation intensity, $U_\mathrm{pa}(f)$, the concept of a base form will be discussed. This concept, attempts to cast the applicable function into a summation of a base form and a ripple. This con-

Stellenbosch University https://scholar.sun.ac.za

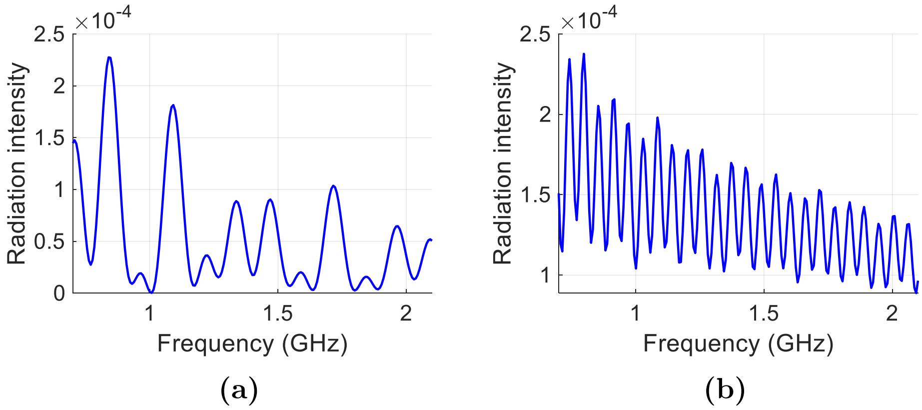

Figure 4.31: Radiation intensity observed for arbitrary chosen angles, when the reflector is pointed in a specific direction

cept applies well to the ANT, because there is a clear distinction between the base form and the ripple, and is the basis of ripple extraction using the iterative power law technique. This distinction might not be as clear for the radiation intensity, $U_{\mathrm{pa}}(f)$. If the radiation intensity, however, has a distinct power law base form and a ripple, then the iterative power law technique will likely extract the ripple successfully. In all cases, the goal of ripple extraction in this dissertation is to remove the base form, and retain the ripple, where the fitting process is used in an attempt to model the base form.

The developed iterative power law technique, in subsection 4.2.3, usually performs well in extracting the ripple from the radiation intensity, sometimes *even* in cases where a power law base form is not explicit, as seen in Fig. 4.32. This gives some leverage to the task of accurate ripple extraction, as the technique is somewhat robust. Power law fitting also performs well if the base form is monotonically increasing, or decreasing. The iterative power law technique, however, does not *always* perform well when a power law base form is not explicit, and a solution to this will be discussed soon.

In Fig. 4.32a the radiation intensity as seen in Fig. 4.31a is shown. In Fig. 4.32b the FFT of this radiation intensity is shown. In Fig. 4.32c the extracted ripple with the use of the iterative power law technique is shown, of this radiation intensity. In Fig. 4.32d the FFT of this extracted ripple is shown. A similar situation occurs in Fig. 4.33, for Fig. 4.31b.

In some cases, a polynomial fit is better suited to extract the ripple of the radiation intensity. Polynomial fitting is prone to ripple removal, including important ripple information, and thus it is important to correctly choose the situation in which polynomial fitting is required. A process is implemented to test if $U_{\mathrm{pa}}(f)$ has a power law base form, which is fundamental to choosing

Stellenbosch University https://scholar.sun.ac.za

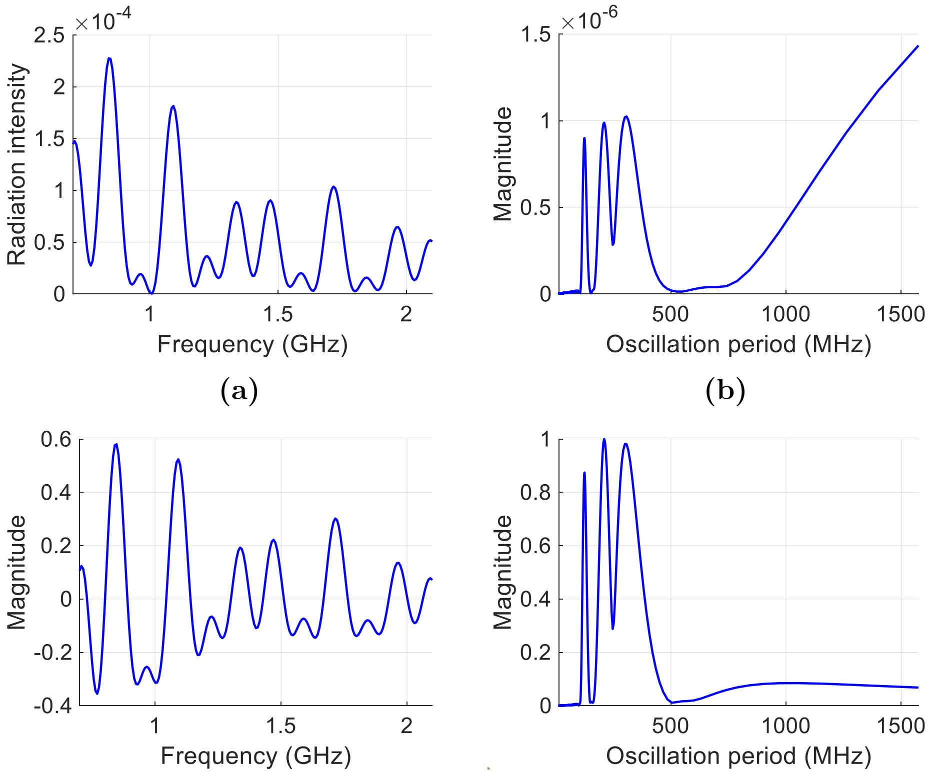

(a) (b) (c) (d)

Figure 4.32: The iterative power law technique performs well to extract the ripple from the radiation intensity, for the first arbitrary angle. In (a) the radiation intensity as seen in Fig. 4.31a is shown. In (b) the FFT of this radiation intensity is shown. In (c) the extracted ripple with the use of the iterative power law technique is shown, of this radiation intensity. In (d) the FFT of this extracted ripple is shown

which fitting process will be used for ripple extraction.

Before explaining the process in detail, a brief overview of the objective will be discussed. In the event that a distinct power law base form is not present, it is likely that either the ripple dominates or the base form is oscillating. In either case, this oscillating behaviour can be modeled using a polynomial fit, and used to decide if a distinct power law base form is present.

The process to test if $U_{\mathrm{pa}}(f)$ has a power law base form, includes calculating the oscillatory nature of the radiation intensity base form. A power law base form will likely oscillate less than a polynomial base form. The base form is determined by fitting the radiation intensity with an arbitrary 9th order polynomial fit. A higher order fit is chosen to enable modeling more oscillating base forms, which have higher oscillation magnitudes and faster oscillation cycles.

A polynomial fit will likely oscillate more when performed on $U_{\mathrm{pa}}(f)$ with a

Stellenbosch University https://scholar.sun.ac.za

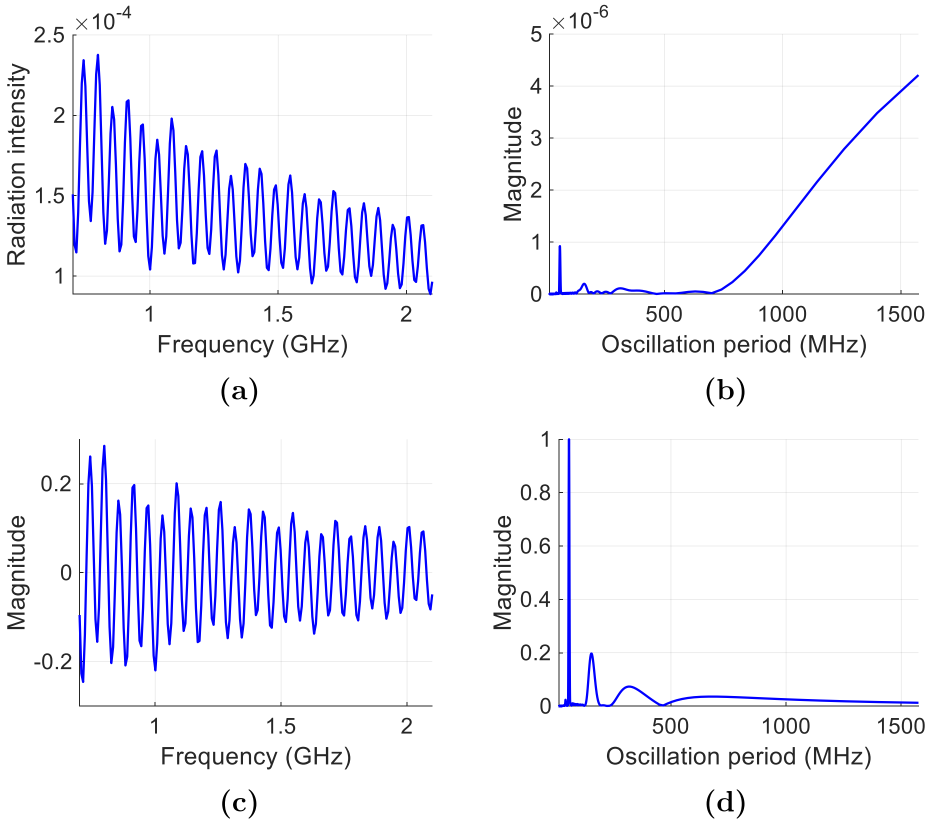

Figure 4.33: The iterative power law technique performs well to extract the ripple from the radiation intensity, for the second arbitrary angle. In (a) the radiation intensity as seen in Fig. 4.31a is shown. In (b) the FFT of this radiation intensity is shown. In (c) the extracted ripple with the use of the iterative power law technique is shown, of this radiation intensity. In (d) the FFT of this extracted ripple is shown

more oscillatory base form, compared to $U_{\mathrm{pa}}(f)$ with a power law base form. An oscillation threshold can thus be defined and calculated, to predict if $U_{\mathrm{pa}}(f)$ has a power law base form. To determine this threshold, a calibration is required. The calibration will be discussed soon.

To define an oscillation threshold, it is required to have a method of determining how oscillatory the base form is. The oscillation of the fit is determined through calculating its turning or inflection points, by using first and second order derivatives, and by calculating a measure of its oscillation through,

$$O_f = n_f \sum_{i=1}^{n_f} |F_p(i)''|, \tag{4.41}$$

where n_f is the number of (frequency) samples for the fit, and $F_p(i)''$ is the second order derivative of the fitted polynomial. The absolute value is calculated, to allow every value in F_p'' to rise the oscillation measure (OM), as

Stellenbosch University https://scholar.sun.ac.za

desired. The summation is used to account for the oscillation over the entire band, to increase the confidence in the OM. Finally, the result is scaled with n_f to account for the number of samples used. Thus, this OM does not increase, as the number of samples increases. The fit is further normalised to its maximum value, before F_p'' is calculated, so that the OM does not scale with the magnitude of the fit. The oscillation measurement using (4.41), can thus be used on any fit in this dissertation, to compare the OM of fits directly.

To conclude if the fit represents a power law base form, requires calibration as discussed earlier. To do this, the OM of an arbitrary calibration signal is calculated using (4.41), and its value is used as the oscillation threshold. The calibration signal can be defined by taking an arbitrary number of samples, 101, from a sinusoidal function with a single oscillation over the band, $\sin(2\pi\boldsymbol{B})$. The band, $\boldsymbol{B}$, is defined as a uniformly sampled vector (101 samples) between 0 and 1. This calibration signal is used, as it is likely more oscillatory than a power law base form, but not too oscillatory to raise the calibration value too high for a power law base form to be chosen when it is unlikely to be the base form. The fit is predicted to represent a more oscillatory base form, if its OM is higher than the oscillation threshold, and if it has a turning or an inflection point. Otherwise, it is predicted to represent a power law base form.

In the case where a power law base form is not detected, the radiation intensity has its mean removed, and is passed through an FFT process. The assumption is that $U_{\mathrm{pa}}(f)$ is oscillatory enough, and that its oscillatory components qualifies as ripple components, without the need for further slow component removal. There is, however, an exception to this choice. Polynomial fits are prone to ripple removal, likely only retaining fast ripple components. If the dominant ripple component is very slow, then $U_{\mathrm{pa}}(f)$ is fitted through a polynomial process to extract the fast ripple components, and remove the slow (unlikely ripple) components. This threshold is chosen somewhat arbitrarily, at a ripple period slower than half the bandwidth in period (700 MHz period, for 1.4 GHz bandwidth). The safety in this choice, is discussed next.

Recall that earlier in this chapter, the ripple period in relation to the path length difference was calculated. For 201 samples over the 1.4 GHz band, a ripple period of $R_{\mathrm{p}} = 700$ MHz requires a path length difference of $L_\Delta \approx \frac{c}{(700)(10^6)} \approx 0.43$ m. The standard reflector system used is shown again in Fig. 4.34. The ripple period increases, as the path length difference decreases. Thus, $R_{\mathrm{p}} \geq 700$ MHz, requires $L_\Delta \leq 0.43$ m. This is more than twice as small as the shortest path length distance, which is from the feed to the nearest subreflector edge, at 1.04 m. While some path length difference could possibly be smaller than $L_\Delta \leq 0.43$ m, it is highly unlikely.

An FFT can be performed on the radiation intensity in a similar way for all

Stellenbosch University https://scholar.sun.ac.za

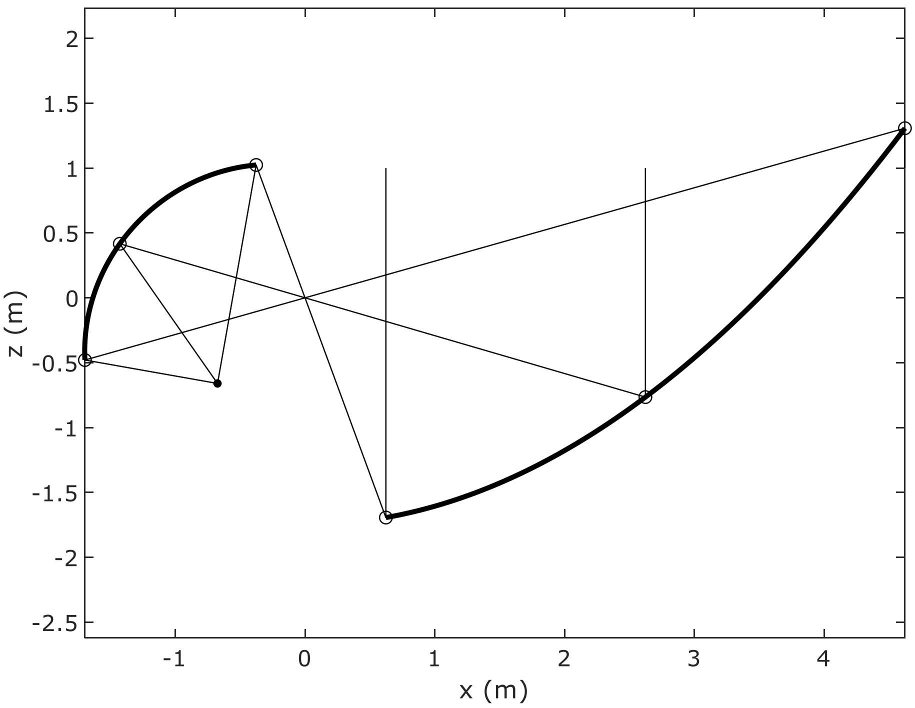

Figure 4.34: The standard reflector used in the dissertation

the other angles, and its ripple can be isolated. Remember, each isolated ripple is still a function of frequency $R_{\mathrm{i}}(f, \phi, \theta)$, as seen in Fig. 4.33d and in Fig. 4.32d. The dominant ripple component can be chosen for each isolated ripple, in all angles, to produce the dominant isolated ripple $R_{\mathrm{di}}(\phi, \theta)$. The dominant ripple component $R_{\mathrm{di}}(\phi, \theta)$ for the radiation intensity can thus be described over a theta-phi grid, or on a unit sphere. Since it is a sphere, it can be projected with true-view and HEALPix, as seen in Fig. 4.35. The dominant ripple component $R_{\mathrm{di}}(\phi, \theta)$ for the radiation intensity, is often referred to as the dominant ripple period in this dissertation, as it describes the components in period. Thus in summary, the dominant ripple period, refers to the dominant frequency component from the FFT of the radiation intensity fit, in all directions. The radiation intensity fit is produced through fitting the radiation intensity, in all directions, to extract the ripple. The dominant ripple period, $R_{\mathrm{di}}(\phi, \theta)$, is thus a set of scalar values, for each angle, representing the dominant ripple period of the radiation intensity in each angle.

The important angles can thus be identified through M_{TbUS}, and for every angle a dominant ripple component can be calculated. Recall that M_{TbUS}, refers to the product of the factors required to calculate the ANT integral. Thus, the product of the background noise temperature, the radiation pattern of the full

Stellenbosch University https://scholar.sun.ac.za

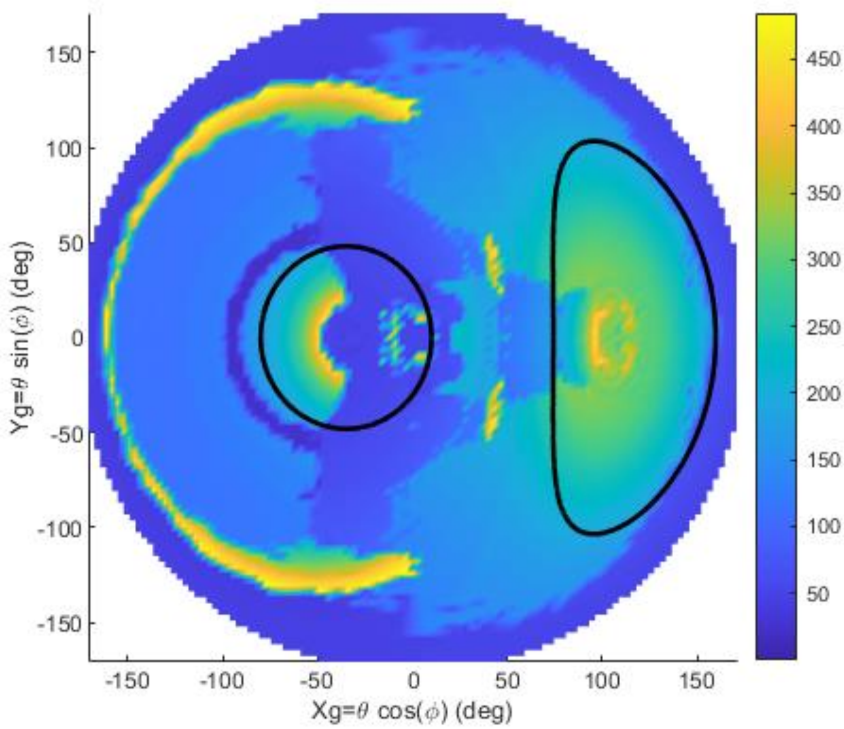

Figure 4.35: The dominant ripple of the radiation intensity in true-view and HEALPix format

reflector system and a sinus function. M_{TbUS} is displayed on a true-view grid with HEALPix resolution reduction. In this case, it is calculated for $f = 0.7$ GHz.

M_{TbUS} can now be applied as a mask over the dominant ripple component $R_{\mathrm{di}}(\phi, \theta)$, to highlight the important dominant ripple components. The mask is generated by creating an alpha map from M_{TbUS}. The term alpha map in this context refers to an external transparency layer that can be used as an overlay, to highlight certain regions, and exclude others. This is shown conceptually in Fig. 4.37. The purpose of this is two fold. Firstly, to confirm that the important dominant ripple components indeed does lead to the ripple observed in the ANT. Secondly, to determine which angles are important for the ripple in the ANT, and possibly develop methods to predict the ripple or predict the dominant causes of the ripple for a specific system. In Fig. 4.38, the mask is applied over the dominant ripple components, so that only the regions with colour are important dominant ripple components.

The alpha map is not always directly correlated to the values in M_{TbUS}. In some cases custom scaling can be used to change the opacity of the regions to

Stellenbosch University https://scholar.sun.ac.za

highlight subtle changes, or highlight the strongest contributing regions. One of these scaling methods is named sin scaling, and is shown in Fig. 4.36, where low contributing values are essentially completely transparent. The purpose of this scaling method is to highlight the strongest contributing regions.

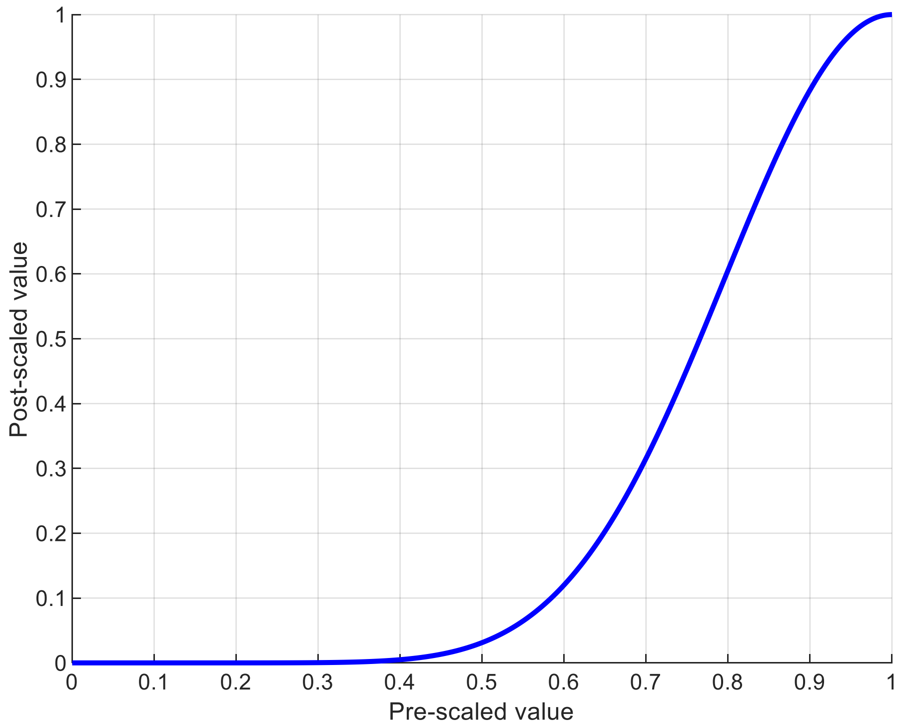

Figure 4.36: Custom scaling used to highlight the strongest contributing regions

The important regions, and dominant ripple components, change as a function of the tipping or pointing angle of the reflector. This can be seen in Fig. 4.40. In Fig. 4.40a the background noise temperature is shown at -80°, in Fig. 4.40c at -40°, in Fig. 4.40e at 40°, and in Fig. 4.40g at 80°. In Fig. 4.40b the dominant ripple components of the full radiation pattern, with the applied alpha map from M_{TbUS}, is shown at -80°. In Fig. 4.40d it is shown at -40°, in Fig. 4.40f at 40°, in Fig. 4.40h at 80°. Each figure is presented on a true-view grid with HEALPix resolution reduction. The primary and subreflector positions are also shown as the solid black shapes. The horizon is additionally plotted as the dotted black shape.

Notice in Fig. 4.40 that the background noise temperature is shifted as a function of tipping angle, instead of the radiation intensity. This produces the same result, as previously described. In Fig. 4.40 the high contribution

Stellenbosch University https://scholar.sun.ac.za

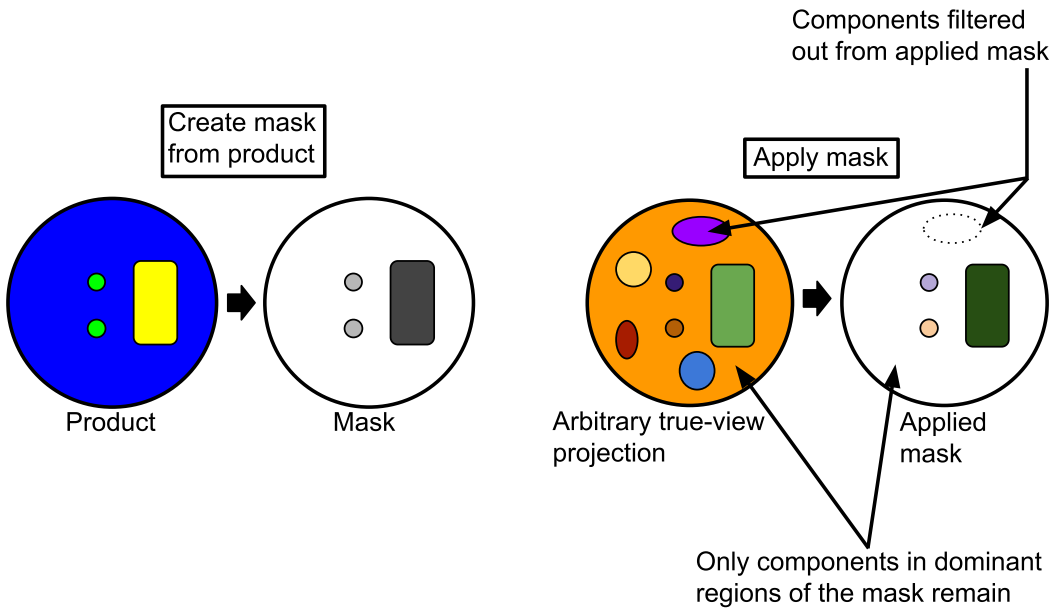

Figure 4.37: Mask generated from M_{TbUS}. The mask is used as a transparency layer to isolate important dominant ripple components

regions change, as the background noise temperature is shifted.

The sinus function will be identical in all cases. The radiation pattern will also be similar in most cases, with a high magnitude main beam, especially in radio astronomy reflector systems. Remember, however, that the background noise temperature is a strong function of frequency. The sky model is shown again in Fig. 4.39 below. At low frequencies, for example 100 MHz, the sky region of the background noise temperature will dominate the ground region. At higher frequencies, for example 1 GHz, the ground region will dominate the sky region. Due to this, the important regions will thus be strongly dependent on the frequency at which the analysis is done.

It is also important to note that M_{TbUS} is calculated at 0.7 GHz in this case, which is the lowest frequency in the $[0.7 - 2.1]$ GHz bandwidth. The background noise temperature is relatively stable over frequency between $[0.7-2.1]$ GHz, which can be seen in Fig. 4.39, with only a few kelvin difference. Due to this, the background noise temperature will only slightly change over this band. The radiation intensity form will also not drastically change over frequency, with a dominating main beam and much less radiation in other directions. The sinus function is independent of frequency, and the radiation pattern dominant

Stellenbosch University https://scholar.sun.ac.za

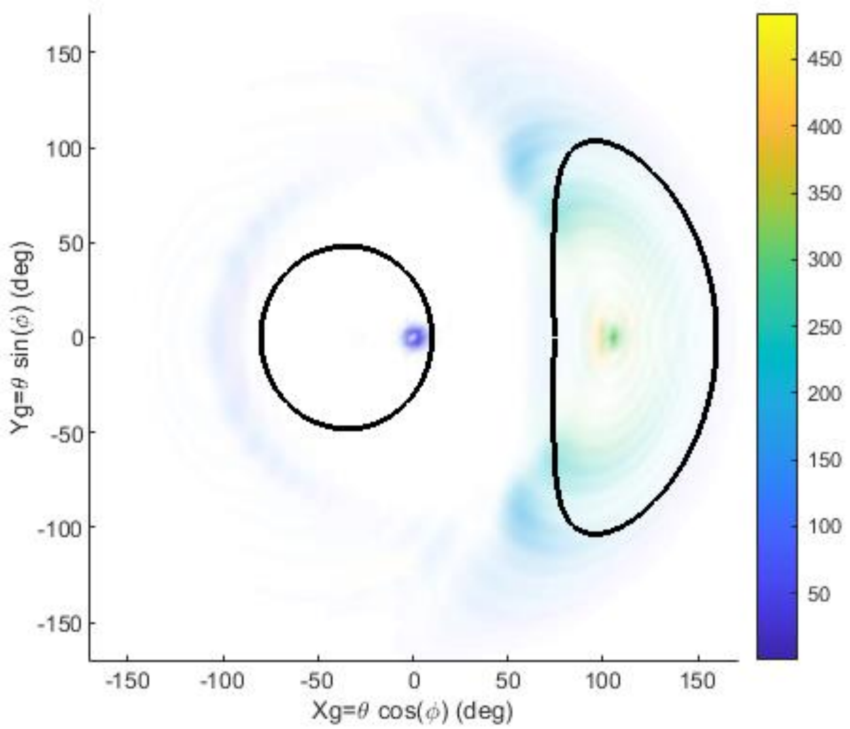

Figure 4.38: M_{TbUS} used to apply an alpha map over the dominant ripple components of the radiation pattern to highlight the important dominant ripple components, in true-view for a tipping angle of 0°. The colour scale represents the period of the dominant ripple component. Only the regions with colour are important dominant ripple components. The regions inside the black shapes, represent the projected subreflector and primary reflector

ripple periods $R_{\mathrm{di}}(\phi, \theta)$ are also independent of frequency. To keep the discussion and analysis tractable, M_{TbUS} is assumed frequency independent over this range. While this is not entirely accurate, it is a relatively close approximation, and enables useful interactions to be derived from M_{TbUS}. This means that the important regions are also calculated frequency independent for this bandwidth. If for example a bandwidth of $[0.1 - 1]$ GHz is analysed, M_{TbUS} will have to be calculated at various frequencies over the band, and applied, as the important regions will be a strong function of frequency.

4.3.5 Visually presented origin of ANT ripple

Now a specific angle will be selected, to observe if the dominant ripple component in the radiation intensity matches the ANT ripple, for a specific pointing direction. This subsection will also demonstrate the notable impact of the tipping angle on the ANT ripple. In Fig. 4.41a the ANT for the zenith direction

Stellenbosch University https://scholar.sun.ac.za

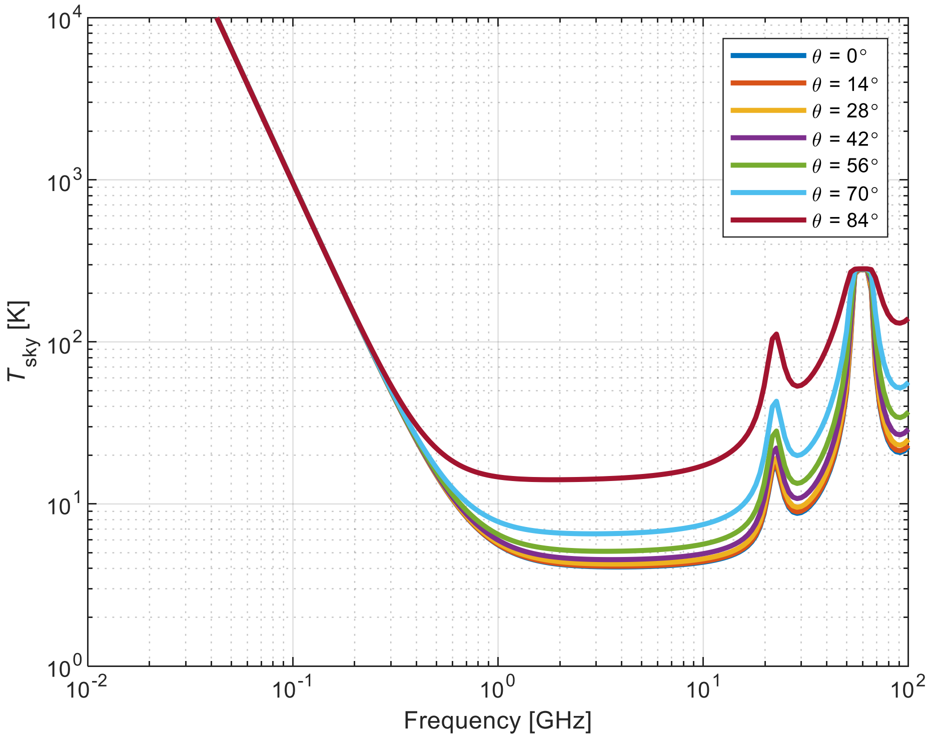

Figure 4.39: Sky brightness temperature over frequency

is shown. In Fig. 4.41b the FFT of its ripple is shown. The ANT ripple has a dominant ripple period of 315 MHz for this angle.

In Fig. 4.42a the true-view projection with an applied alpha map is shown. In Fig. 4.42a it is shown non-marked, to not obscure information. Many of the coloured regions have ripple periods around $\sim$ 300 MHz, seen from the z value. Remember, it is expected that the ripple of the ANT is the sum of these regions. A high contributing (high opacity) region is marked in Fig. 4.42b. For this region, a $\sim$ 300 MHz dominant ripple period is observed from the z value, for the radiation pattern over frequency. These marked directions will often times not exactly match the dominant ripple period of the extracted angle, due to interpolation effects in the construction of these plots. This marked direction is near the angle shown in Fig. 4.42c.

For this marked angle, the radiation pattern over frequency is shown in Fig. 4.43a. The ripple of this direction for the radiation pattern is shown in Fig. 4.43b. The dominant ripple seen corresponds closely to the ripple observed for the marked angle in Fig. 4.42b as expected. The other $\sim$300 MHz regions further dominate the contribution to the ANT ripple.

Stellenbosch University https://scholar.sun.ac.za

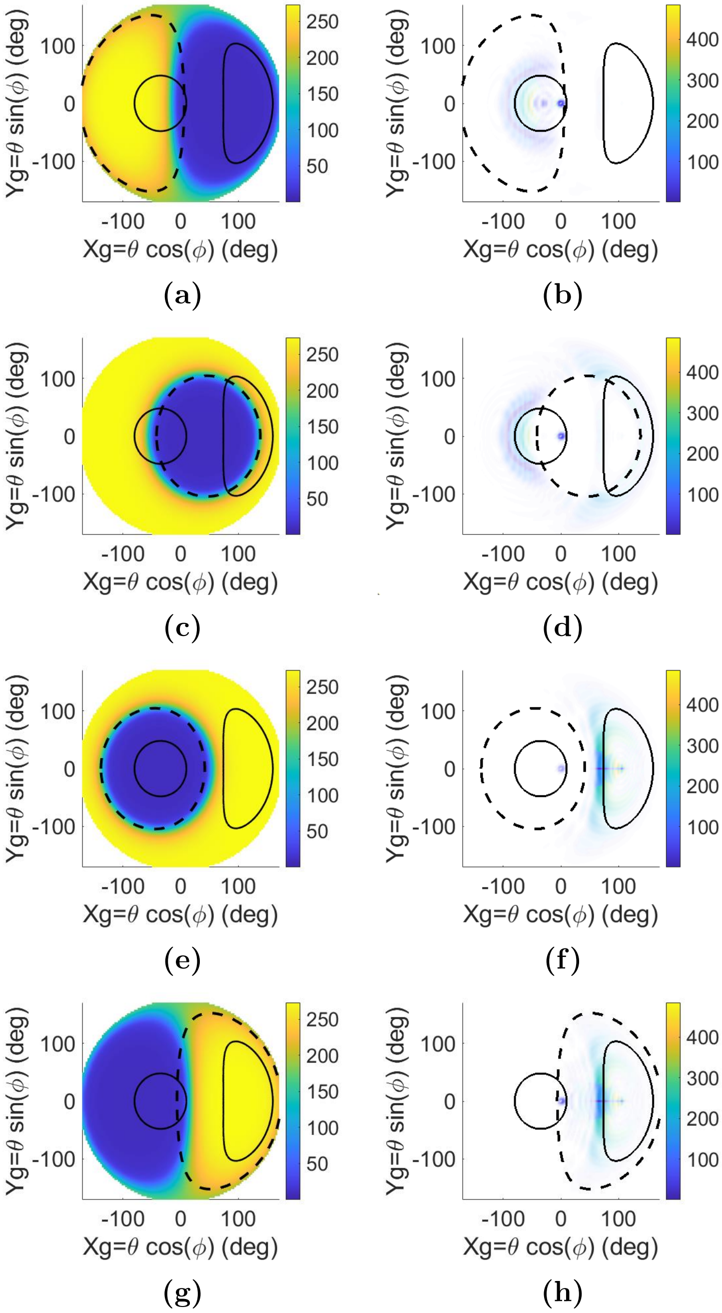

Figure 4.40: The important regions, and dominant ripple components, change as a function of the tipping or pointing angle of the reflector. In (a) the background noise temperature is shown at -80°, in (c) at -40°, in (e) at 40°, and in (g) at 80°. In (b) the dominant ripple components of the full radiation pattern, with the applied alpha map from M_{TbUS}, is shown at -80°. In (d) it is shown at -40°, in (f) at 40°, in (h) at 80°. Each figure is presented on a true-view grid with HEALPix resolution reduction. The primary and subreflector positions are also shown as the solid black shapes. The horizon is also plotted as the dotted black shape

Stellenbosch University https://scholar.sun.ac.za

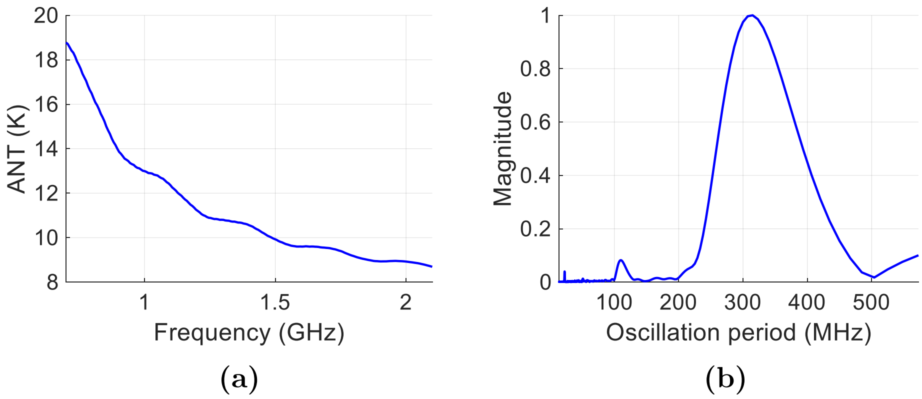

Figure 4.41: ANT for zenith in (a) and the FFT of the ANT ripple in (b)

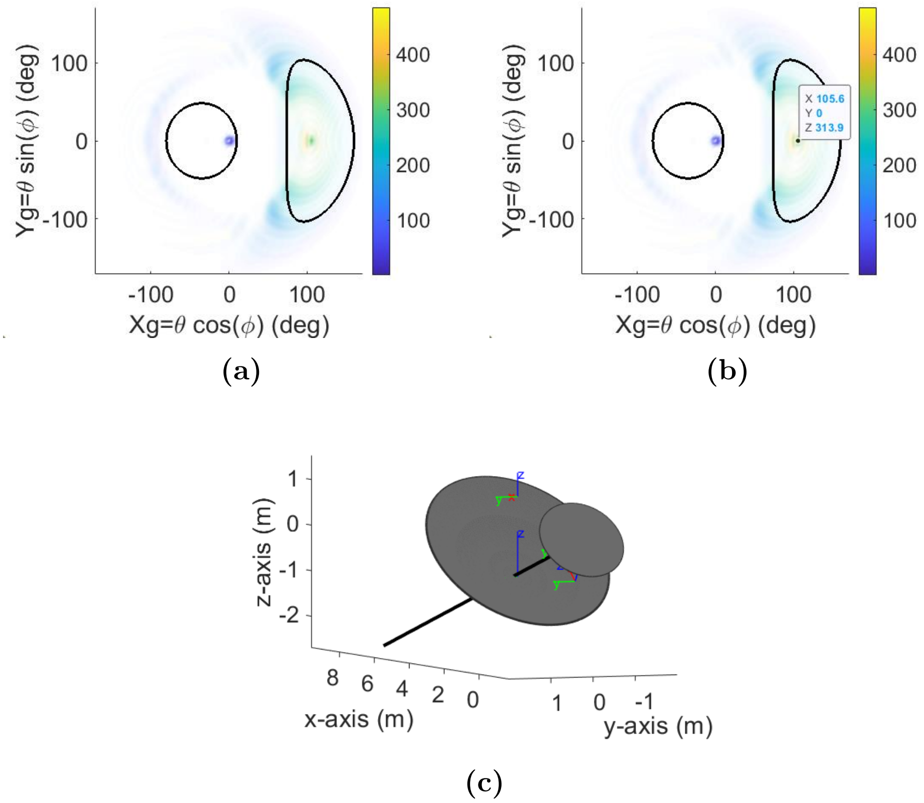

Figure 4.42: The true-view projection of the dominant ripple periods of the radiation pattern, in all directions, with an applied alpha map, for the zenith tipping angle, in (a) and (b). In (b) a specific direction is marked. A vector is drawn in (c), near the marked direction in (b)

From this, the ~300 MHz ripple seen in the ANT in zenith is also observed in the radiation pattern, in a high contributing region.

In Fig. 4.44 the ANT and its ripple is shown for a -80° tipping angle. From

Stellenbosch University https://scholar.sun.ac.za

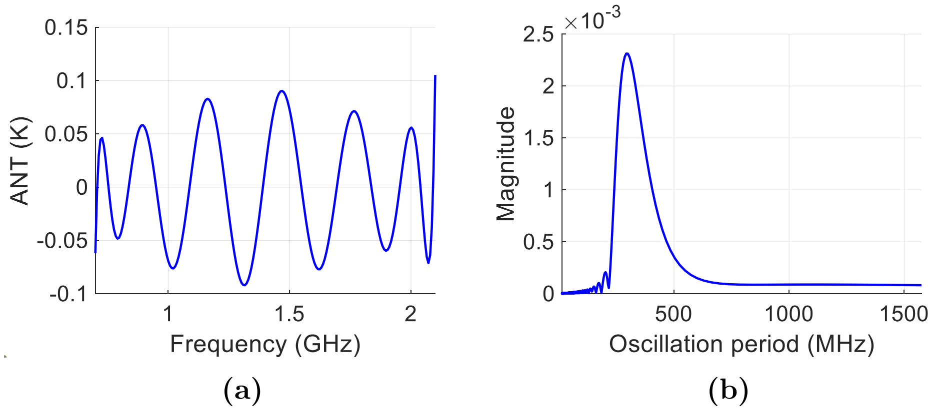

Figure 4.43: In (a) the ripple of the radiation pattern for the marked angle as seen in Fig. 4.42b. In (b) the FFT of this ripple is shown

Fig. 4.44 it is clear that there is a dominant ripple at ∼50 MHz. In Fig. 4.45, the true-view projection of the dominant ripple period of the radiation intensity is shown, with a alpha map applied. A non-marked and marked version is shown. Many contributing ∼50 MHz regions can be seen, as expected, and dominate the ANT ripple.

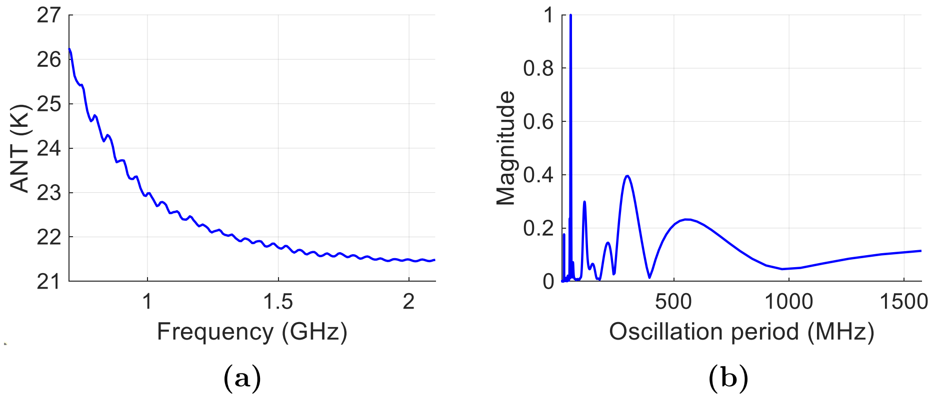

Figure 4.44: ANT and its ripple at -80° tipping angle. In (a) the ANT is shown and in (b) its ripple

Each bar, in the bar chart in Fig. 4.47, displays a measure of the contribution to the ANT ripple, from a specific dominant ripple period of the radiation intensity, in all the angles where it is dominant. The numbers above each bar identifies the period in MHz, of the specific dominant ripple period. The chart is normalised to the bar with the highest contribution.

For example, if the ANT for a specific tipping angle has a dominant ∼50 MHz ripple, then it is expected that there will be many angles, in high contributing

Stellenbosch University https://scholar.sun.ac.za

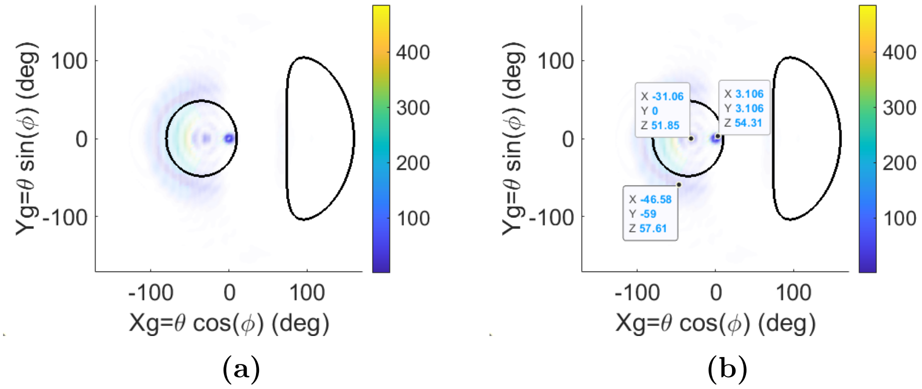

Figure 4.45: The true-view projection of the dominant ripple period of the radiation intensity is shown, with a alpha map applied. In (a) the non-marked version is shown, and in (b) the marked version is shown

regions, containing dominant ∼50 MHz ripple periods in the radiation pattern, which causes the ∼50 MHz ANT ripple. The measure is thus calculated, by summing the specific dominant ripple period, over all regions containing this ripple, in the true-view projection of the dominant ripple period of the radiation intensity, and scaling it with the alpha map, to account for the variable relevance of each region.

Thus, the bar chart in Fig. 4.47 is calculated by individually summing the specific dominant ripple periods in Fig. 4.45, over all regions containing the ripple, to provide a measure of its contribution to the ANT ripple. While the true-view projections of the radiation intensity dominant ripple periods, with an applied alpha map, gives a visual indication of the ripple that will be present in the ANT, the bar charts gives a more quantitative indication.

From Fig. 4.47 it can be seen that the ∼50 MHz ripple dominates, as expected. It should also be noted that the dominant ripple contributions observed in Fig. 4.47 will not be entirely match the ripple contributions seen in the ANT, which can be seen in Fig. 4.44. This is expected, as the process to extract the ripple, and the HEALPix averaging introduce some error. Furthermore, only the dominant ripple contributions are considered, and not all the components in the FFT. It is important to note that the radiation pattern might not always have a single dominant ripple components, and can have multiple notable components, as seen in Fig. 4.46. In Fig. 4.46 the notable components is extracted out of the FFT for the radiation intensity ripple, in each pixel.

In Fig. 4.48, the dominant ripple period in each region is summed, and a collection of ripple periods are shown, as previously described. It is done in Fig. 4.48a for a -80° tipping angle, and in Fig. 4.48b for a 0° or zenith tipping angle. In Fig. 4.48 it can clearly be seen that the ∼50 MHz ripple does not

Stellenbosch University https://scholar.sun.ac.za

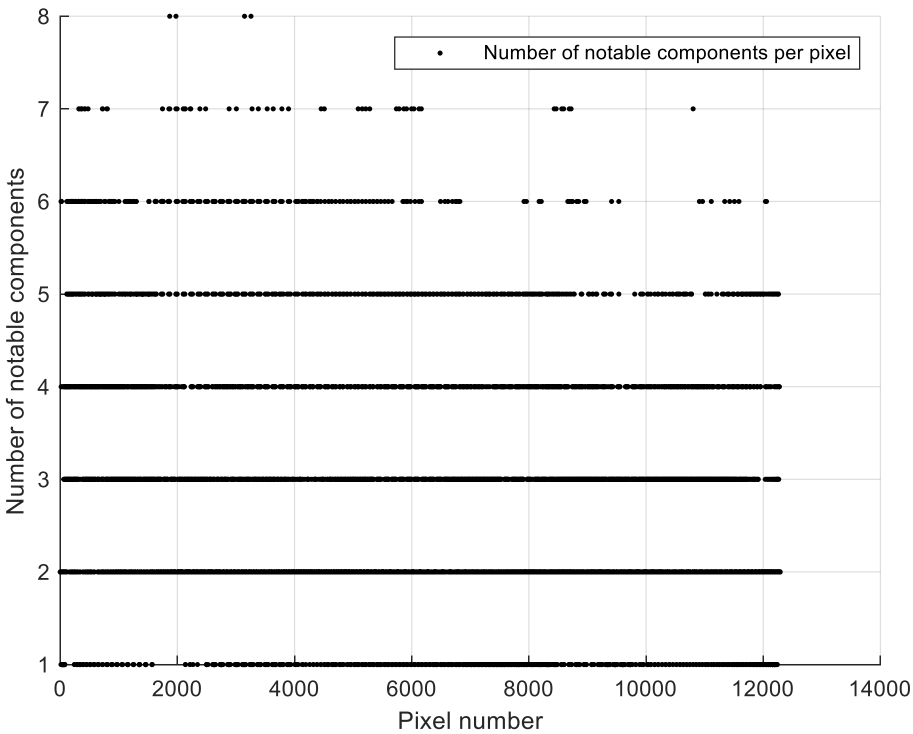

Figure 4.46: The radiation intensity has many notable components in its FFT, per pixel

dominate the ANT ripple for a zenith tipping angle, but the ∼300 MHz ripple does, as expected.

Furthermore, from Fig. 4.48, the notable impact of the tipping angle is also demonstrated, where both tipping angles have different ripple profiles. These results also confirm that the ripple in the radiation pattern causes the ripple in the ANT, and that certain dominating regions constitute most of the ANT calculation.

In conclusion, the radiation intensity ripple exists in all angles. It is partly due to various non-ideal effects causing interference. This ripple also exists due to the mechanism shown previously in Fig. 4.21, which adds a ripple on the radiation intensity due to the frequency changing. From these ripples, only the relevant ripples can be isolated using the product, M_{TbUS}, of the factors required to calculate the ANT. These important ripples largely determine the ripple in the ANT. Furthermore, when observing a specific galactic object, such as a star, the reflector has to tip to track the star throughout the year. The ANT ripple is influenced by the tipping angle, and thus the ANT measurement changes throughout the year, which is important to account for in

Stellenbosch University https://scholar.sun.ac.za

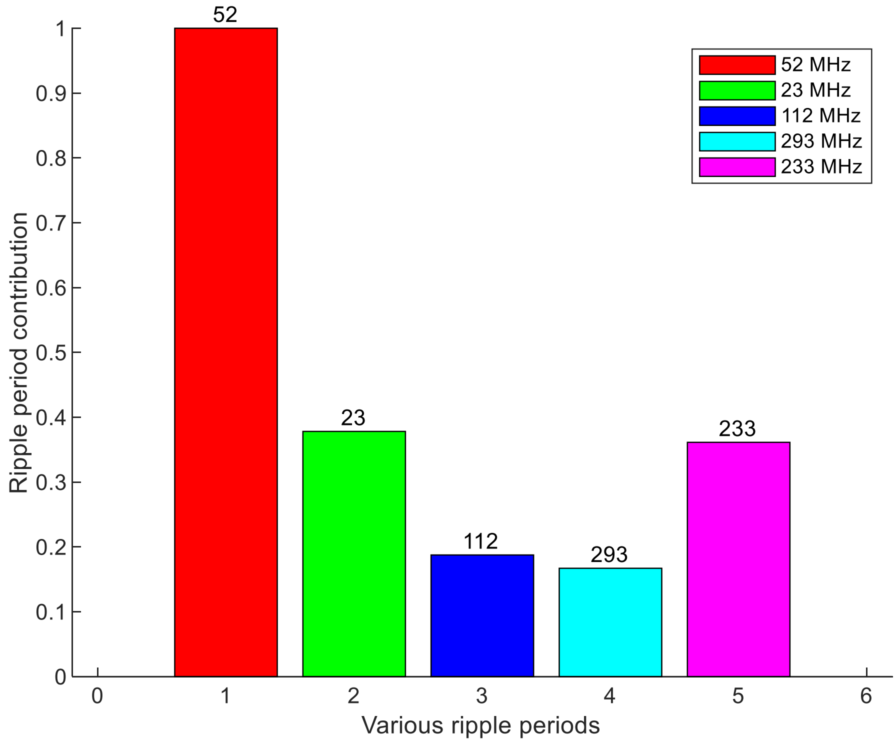

Figure 4.47: The contribution from a collection of dominant ripple periods is shown for a -80° tipping angle. It can clearly be seen that the ∼50 MHz ripple dominates as expected, when comparing to the dominant ripple in the ANT at -80° tipping angle, seen from the ANT ripple FFT at this tipping angle

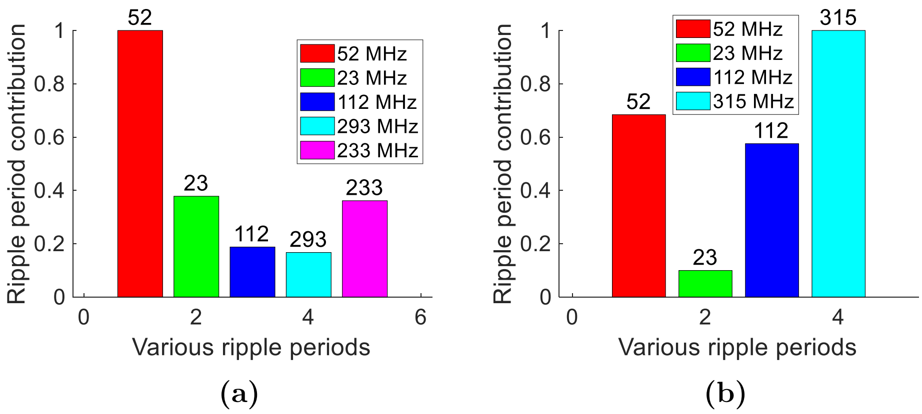

Figure 4.48: The contribution from each dominant ripple period is shown for a -80° and 0° tipping angle. In (a) it is shown for -80° and in (b) for 0°

certain experiments.

Stellenbosch University https://scholar.sun.ac.za

4.4 Practical considerations for ANT ripple and ANT

The ANT ripple is a function of many different factors. In this section certain cases will be analysed with the aid of the tools developed throughout the dissertation, to view their impact on the ANT and its ripple. Some of these cases include changing the frequency band or the reflector type. The developed tools refer to the ripple extraction processes, such as the iterative power law, or the analysis tools, such as the bar charts or contribution regions.

4.4.1 ANT as a function of reflector geometry

The ANT ripple is a function of reflector geometry, as it will result in different interference patterns forming from the different path lengths of the different sized reflectors. A smaller dish is used in this case to compare against the standard dish used in this dissertation, and is shown in Fig. 4.49. This dish has maximum chord lengths of 4 m and 1 m for the primary reflector and subreflector, respectively. The primary reflector has a projected aperture diameter of 3 m. In Fig. 4.50 the ANT is shown for both the smaller reflector and the standard reflector as well as both their ripples. It can clearly be seen that the ANT ripple changes based on reflector geometry.

In Fig. 4.51 the dominant ripple periods of the radiation intensity is shown in all directions, with an alpha map overlay, for the zenith pointing direction. It is shown for the smaller reflector in Fig. 4.51a and the standard reflector in Fig. 4.51b. From these figures, it can clearly be seen that the dominant ripple is different in many directions. In Fig. 4.52, the dominant ripple period in each region is summed, and a collection of ripple periods are shown.

Remember, the dominant ripple period, $R_{\mathrm{di}}(\phi, \theta)$, refers to the dominant frequency component from the FFT of the radiation intensity fit, in all directions. The radiation intensity fit is produced through fitting the radiation intensity, in all directions, to extract the ripple. The dominant ripple period, $R_{\mathrm{di}}(\phi, \theta)$, is thus a sphere of scalar values, for each angle, representing the dominant ripple period of the radiation intensity in each angle.

From Fig. 4.52 it can clearly be seen that the contributing regions with ~420 MHz ripple is much more dominant for the smaller reflector, than for the standard reflector. Conversely, the contributing regions with ~300 MHz ripple is much more dominant for the standard reflector, than for the smaller reflector. These results are reflected in the FFT in Fig. 4.50.

Stellenbosch University https://scholar.sun.ac.za

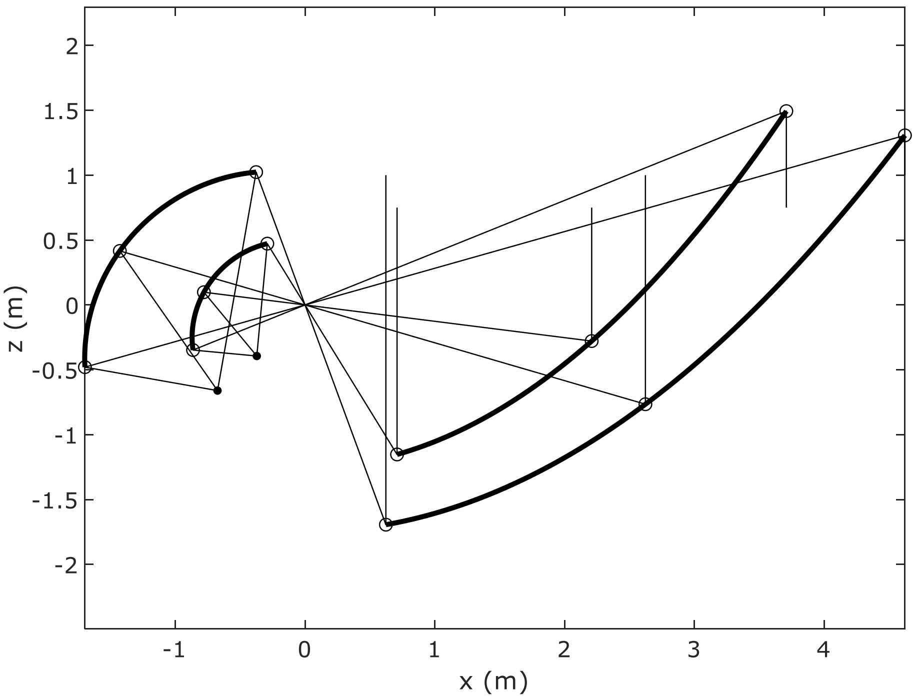

Figure 4.49: The smaller dish used in this case, compared against the standard dish used in this dissertation

Finally in Fig. 4.53 the contributing regions for each of the displayed dominant ripple periods in Fig. 4.52 are shown, for both reflectors. Each contributing region displays each angle in true-view, that has the specific dominant ripple period, scaled with the alpha map to account for the variable relevance of each region. The colour scale represents the contribution, with a maximum possible contribution of one. The contribution is directly correlated to the alpha map, normalised to the highest value of the alpha map. Thus all the brightly lit angles in a contributing region, recognised by a high value on the colour scale, represent angles where the specific dominant ripple period exists and is important to the ANT ripple.

From Fig. 4.52 it can clearly be seen that different regions are highly contributing to the ANT ripple, in each reflector setup. Notice that the contribution from the edges of the primary reflector, in the case of the smaller reflector setup, is much stronger than in the case of the standard reflector. This is expected, as edge diffraction will be larger for smaller reflector setups.

Stellenbosch University https://scholar.sun.ac.za

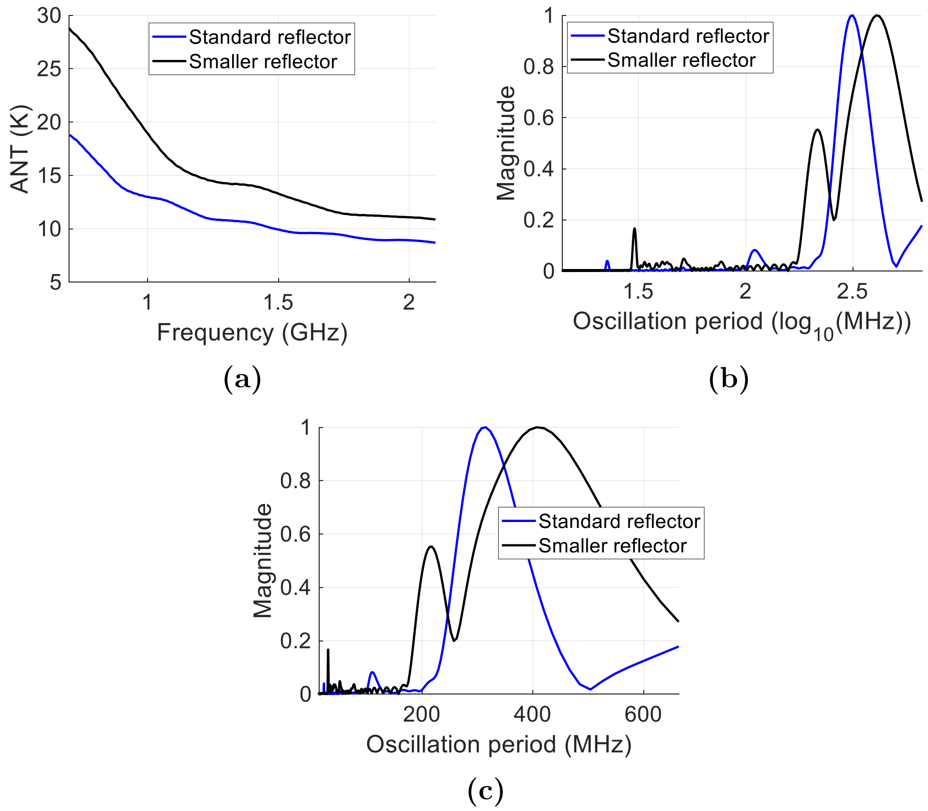

Figure 4.50: The fine model output in (4.1) is shown in (a), for a zenith pointing angle. A normalised FFT of the ANT ripple at zenith is shown in (b) on linear-log scale to highlight the frequency components of the ripple. In (c) the FFT is shown in linear scale. This is performed for the standard reflector and a smaller offset Gregorian dual reflector. The smaller reflector has maximum chord lengths of 4 m and 1 m for the primary reflector and subreflector, respectively. The primary reflector has a projected aperture diameter of 3 m. All other parameters are kept constant

4.4.2 ANT as a function of frequency range and electrical reflector size

An electric aperture diameter can be defined for a reflector, which describes the aperture diameter in wavelengths, and will grow as the frequency increases. A larger electric aperture diameter leads to a narrower main beam in the radiation pattern. This relation is shown in Fig. 4.54. As the main beam narrows, more power will be in the main beam and less in the far sidelobes. Recall that an ideally operating reflector, refers to an infinitely large reflector, with a Dirac delta main beam and no sidelobes. The amount of deviation from this ideal response is strongly correlated to the intensity of non-ideal effects present in the system, and can be seen in Fig. 4.55. Increasing the electrical size of a reflector will reduce the intensity of the non-ideal effects interfering, as the reflector can

Stellenbosch University https://scholar.sun.ac.za

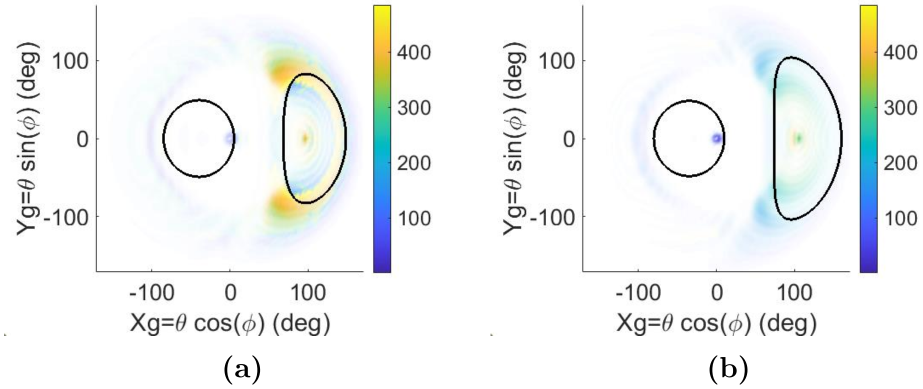

Figure 4.51: The dominant ripple periods of the radiation intensity in all directions, with an alpha map overlay. In (a) it is shown for the smaller reflector. In (b) it is shown for the standard reflector

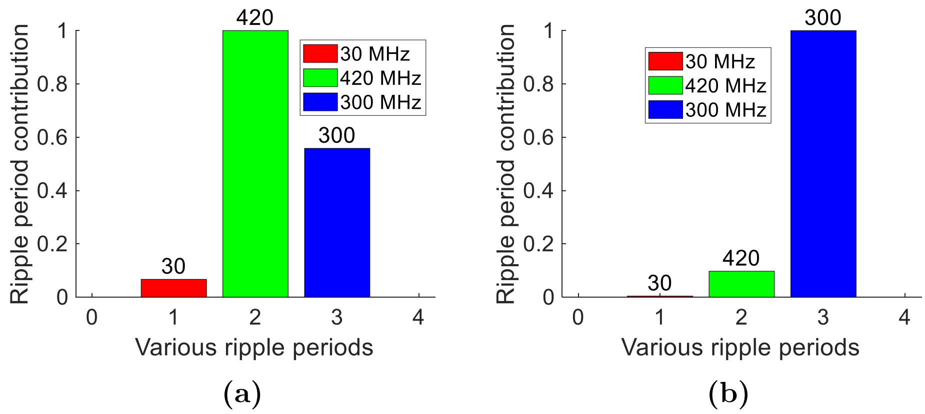

Figure 4.52: The contribution from each dominant ripple period is shown for a smaller reflector in (a), and the standard reflector in (b)

operate more ideally, and reduce the ripple in the radiation pattern and the ANT. An increase in the simulated frequency band can thus be used to emulate a larger reflector, without changing the physical properties of the reflector.

It is also important to note that in this case the electrical size of the entire system is discussed, however, the electrical size of each component will also influence the ripple in the ANT. An example would be if the subreflector reduces in size, but the primary reflector does not. In this case, the subreflector will generate more non-ideal effects, which will interfere with the full radiation pattern of the reflector system, and increase the ripple in the ANT.

A reflector will thus continue to have improved electrical performance as frequency increases, however, the same is not true for a practically designed feed. This characteristic of reflectors is only applicable to perfectly manufactured

Stellenbosch University https://scholar.sun.ac.za

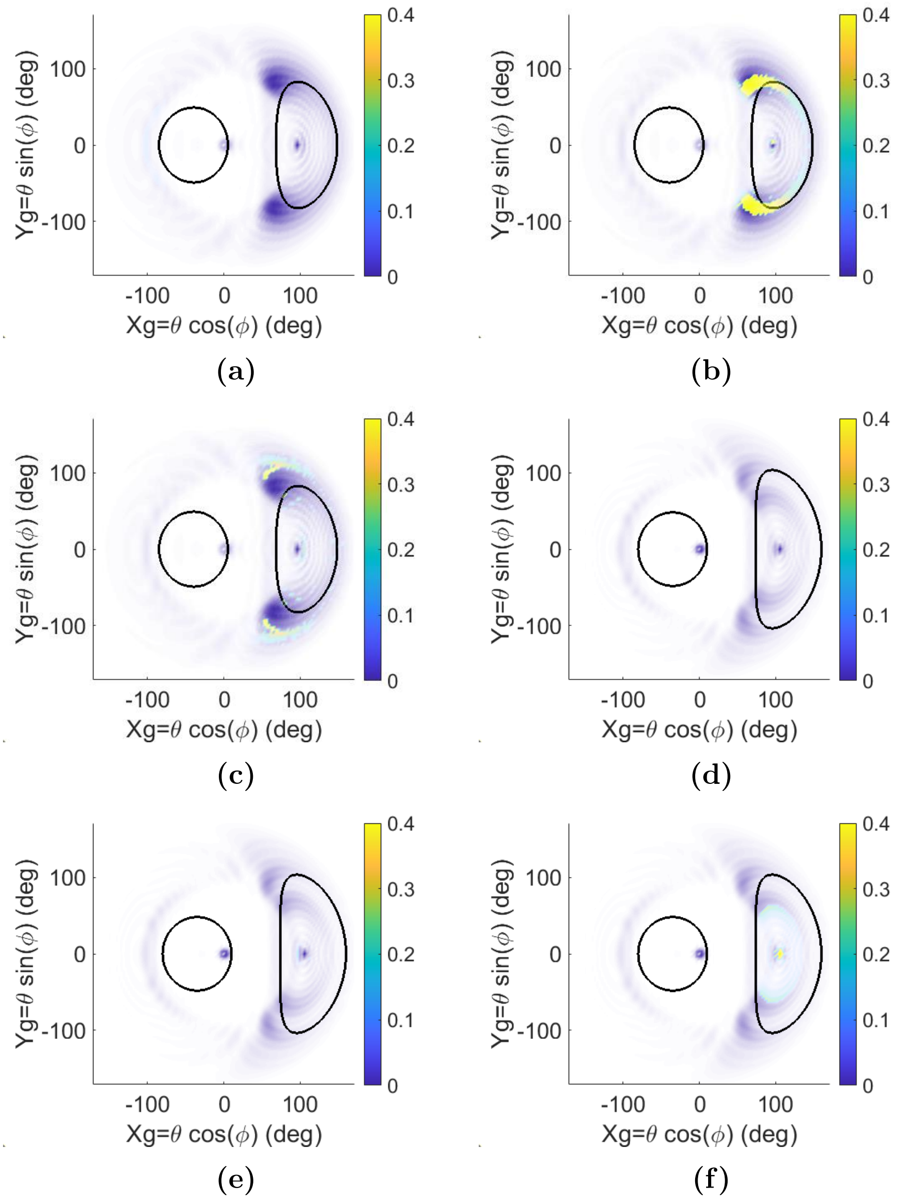

Figure 4.53: Contribution to the ANT ripple from various dominant ripple periods. The colour scale represents the contribution, with a maximum possible contribution of one. The contribution is directly correlated to the alpha map, normalised to the highest value of the alpha map. In (a) the contribution from the ∼30 MHz dominant ripple period is shown, for the smaller reflector. In (b) the contribution from the ∼420 MHz dominant ripple period is shown, for the smaller reflector. In (c) the contribution from the ∼300 MHz dominant ripple period is shown, for the smaller reflector. In (d) the contribution from the ∼30 MHz dominant ripple period is shown, for the standard reflector. In (e) the contribution from the ∼420 MHz dominant ripple period is shown, for the standard reflector. In (f) the contribution from the ∼300 MHz dominant ripple period is shown, for the standard reflector

Stellenbosch University https://scholar.sun.ac.za

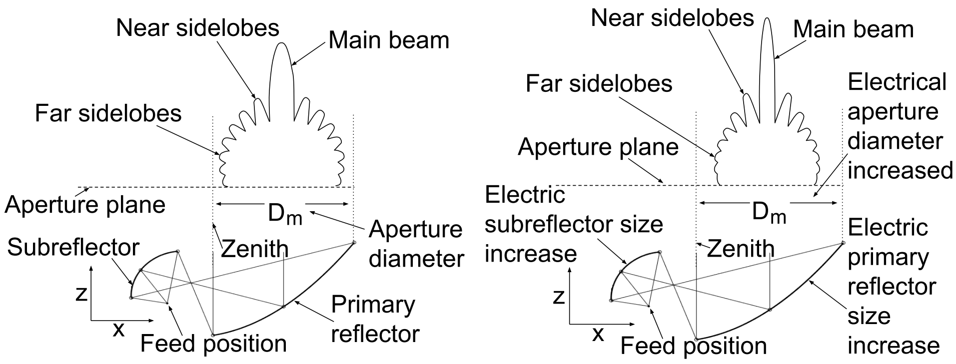

(a) (b)

Figure 4.54: Physical reflector size increase, or operating frequency band increase, leads to a similar effective result: Increasing the electrical size of the reflector, which leads to an increase in electric aperture diameter. This in turn leads to a more directive, or narrow, main beam

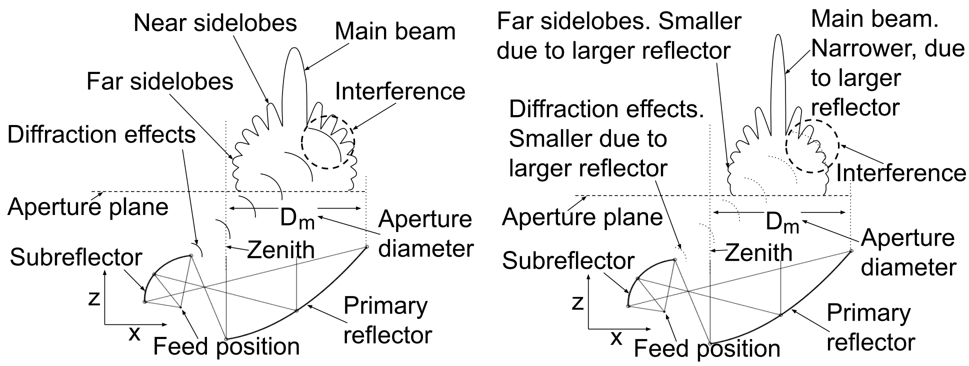

(a) (b)

Figure 4.55: Effect of increasing aperture diameter, or electrical size of reflector, on the ripple of ANT with frequency kept constant. A smaller aperture diameter, or electrical size, will result in a broader main beam and higher far sidelobes as seen in (a). A larger aperture diameter, or electrical size, will result in a narrower main beam and smaller far sidelobes as the directivity increases as seen in (b). The interference from diffraction effects will be less severe in (b) with a larger electrical size as the far sidelobes are smaller, compared to the smaller electrical size in (a)

reflectors, which follow the conic shape exactly, which is assumed in this dissertation. The radiation pattern of a practical feed is a function of frequency, however, a Gaussian feed is not. While using a Gaussian feed is standard in this dissertation, it is also useful in this case. A Gaussian feed has no effect on the ANT over frequency. This allows the effect on the ANT, from increasing the electrical size of the reflector, to be analysed in isolation.

The frequency band over which the ANT analysis is performed is now changed to [0.7 – 5.0] GHz. Fig. 4.56a shows the ANT, while Fig. 4.56b shows the

Stellenbosch University https://scholar.sun.ac.za

periods of the ripple components. It can be observed that the ripple becomes almost non-existent over this frequency range, as the ripple reduces over frequency. It is important to note that the ripple in the ANT will not completely disappear over the band. The ripple from the radiation pattern due to interference effects, and from the implicit ripple over frequency that the radiation pattern experiences, will both decay over frequency. These effects will, however, not completely disappear. In Fig. 4.56b, at the somewhat arbitrary range of $[4.0 - 5.0]$ GHz, the ripple decay is very low. At 4.0 GHz a soft break point can thus be defined, as the frequency from which the ripple will not change significantly.

At 4.0 GHz, the electric aperture diameter of the primary reflector is $A_{\mathrm{ed}} = \frac{D_{\mathrm{m}}}{\lambda} = \frac{D_{\mathrm{m}} f}{c} = 53.37$ wavelengths. The (physical) aperture diameter of the primary reflector is $D_{\mathrm{m}} = 4$ m, the wavelength is $\lambda = \frac{c}{f}$. Additionally the smallest diameter, that can enclose the primary reflector, is $D_{\mathrm{cl}} = 5$ m, or $A_{\mathrm{ecl}} = 66.71$ wavelengths. The ripple when using a reflector at this electric size is notably reduced, and increasing the electrical size of the reflector will not significantly reduce the ripple. From this analysis, it can be concluded that the ripple in an electrically larger reflector is much less relevant.

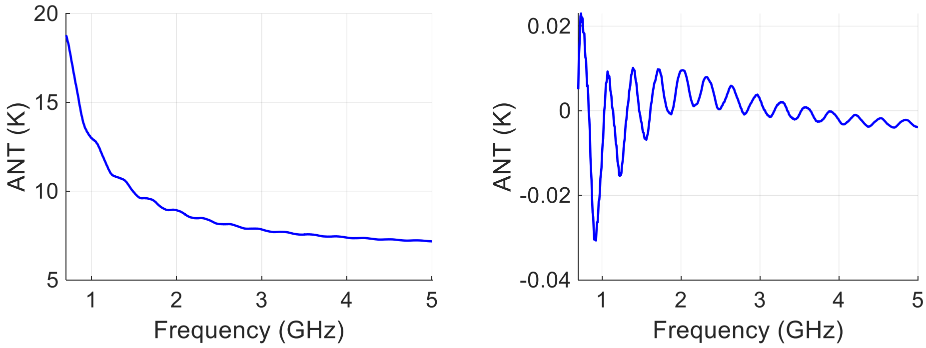

(a) (b)

Figure 4.56: In (a) the solid line indicates the fine model output of ANT, for a zenith pointing direction. The ripple of the ANT is shown in (b). In this case the frequency band over which the analysis is performed is changed to $[0.7 - 5.0]$ GHz. The electric aperture diameter of the primary reflector at 4.0 GHz is $A_{\mathrm{ed}} = 53.37$ wavelengths. The smallest diameter, that can enclose the primary reflector, is $A_{\mathrm{ecl}} = 66.71$ wavelengths. All other parameters are kept constant

The tipping angle is now changed to -80°, with the ANT shown in Fig. 4.57 below. For this tipping angle, the ripple also diminishes over frequency. This diminishing effect will apply to any tipping angle. For this tipping angle, the ANT starts to increase over the band near the frequency of 2.5 GHz. This did

Stellenbosch University https://scholar.sun.ac.za

not occur for the zenith tipping angle. This increase will be investigated next.

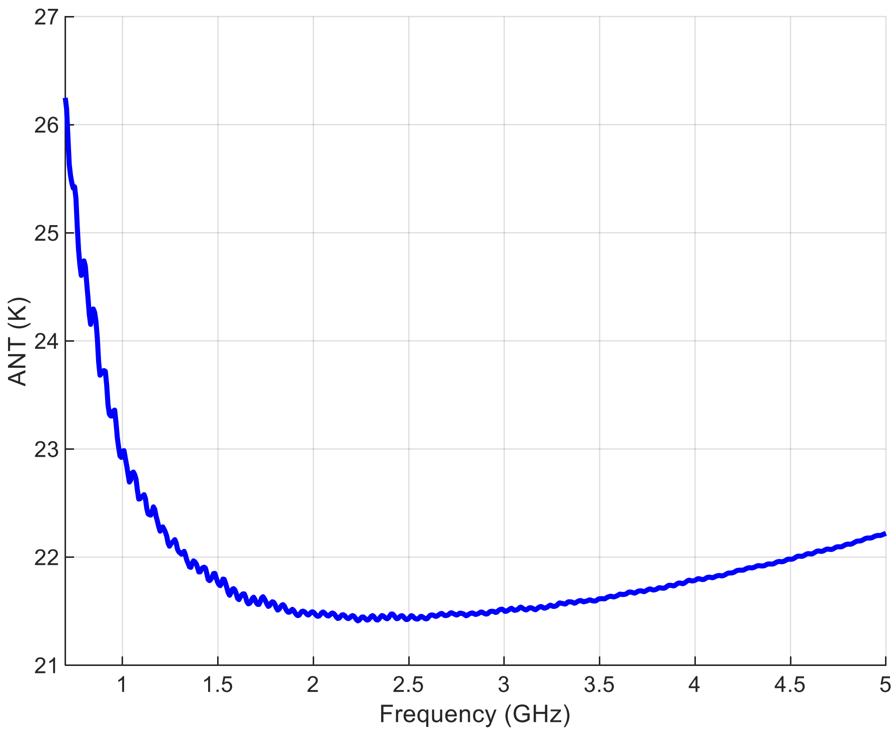

Figure 4.57: The solid line indicates the fine model output of ANT, for a -80° pointing direction. It can be seen that the ANT starts to increase over the band near the frequency of 2.5 GHz

The background noise temperature is shown below in Fig. 4.59, for a zenith tipping angle in Fig. 4.59a and a -80° tipping angle in Fig. 4.59b. In Fig. 4.59a the sky region background noise temperature increases from the marked centre point, to the marked outer point, and can be seen through the rise in the z value. The centre point is from the zenith observation direction, and the outer point from a $\sim$ -80° observation direction.

The radiation observed by the reflector, from an angle closer to the horizon, has to travel through more of the atmosphere compared to radiation observed from zenith. This increases the background noise temperature from angles closer to the horizon. This temperature increase can also be seen from Fig. 4.58 below. It shows the background noise temperature from both the sky and ground contribution. The dotted line represents the ground contribution and the solid line the sky contribution. They are separated at the horizon (90°). It can be seen from Fig. 4.58, that the temperature rises notably for angles

Stellenbosch University https://scholar.sun.ac.za

closer to the horizon.

Due to the background noise temperature being rotated for the calculations, instead of the radiation pattern, the radiation pattern main beam is located at the centre of both Fig. 4.59a and Fig. 4.59b. In Fig. 4.59b the reflector system is tipped in the -80° direction. The centre point in Fig. 4.59b is clearly much higher than the centre point in Fig. 4.59a. Thus, the main beam for the -80° tipping angle points into a much higher background noise temperature, compared to the main beam for the zenith tipping angle. The main beam has a high contribution to the ANT.

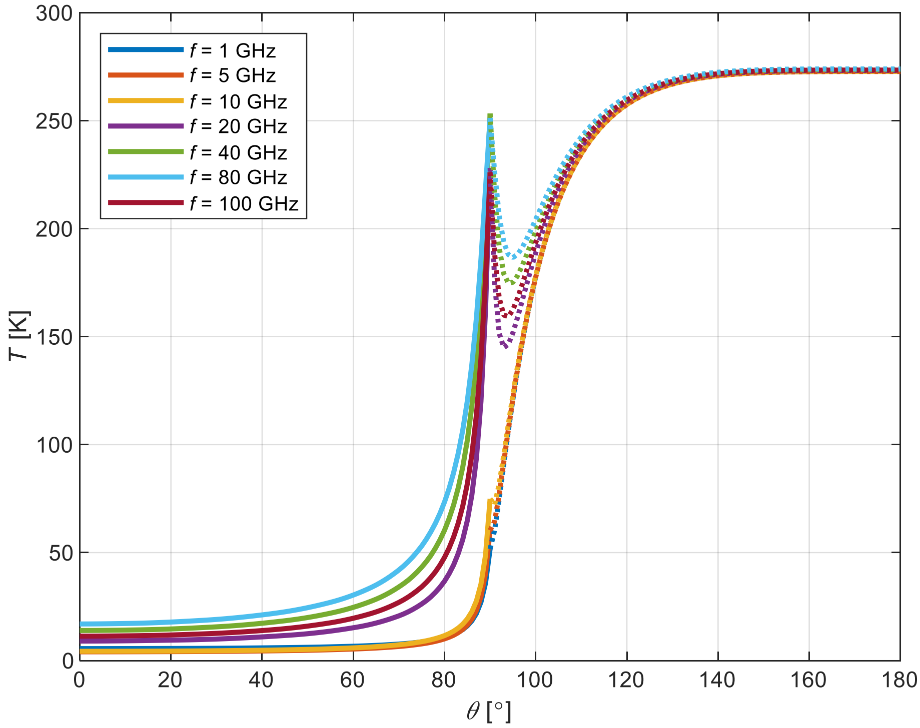

Figure 4.58: The sky and ground contribution to the background noise temperature over frequency. θ refers to the observation angle from zenith. The Cortes model is used, as described in [1]

More energy focuses into the main beam over frequency, which reduces the contribution to the ANT from other directions, and increases the contribution from the main beam. In Fig. 4.60 the dominant ripple components, over all angles, of the radiation pattern are shown with an alpha map applied over it. It is shown for the -80° tipping angle. In Fig. 4.60a the alpha map is constructed from M_{TbUS} calculated at 2.1 GHz, and in Fig. 4.60b at 3.5 GHz. The

Stellenbosch University https://scholar.sun.ac.za

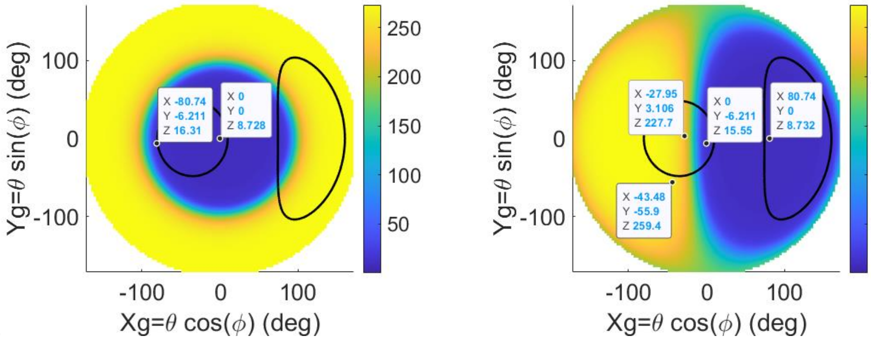

(a) (b)

Figure 4.59: The background noise temperature, for a zenith tipping angle in (a), and a -80° tipping angle in (b)

alpha map has to be scaled to notice any difference, as the change in the ANT over the $[2.1 - 3.5]$ GHz band is less than 0.5 kelvin. A scaling method is used which highlights the subtle difference clearly. This scaling method scales the alpha map regions to either fully transparent or fully opaque, from a chosen threshold value. This scaling will be referred to as cliff scaling. In Fig. 4.60 it can clearly be seen that the regions outside the main beam becomes less relevant for higher frequencies, as more energy is focused into the main beam, while the main beam direction becomes more relevant.

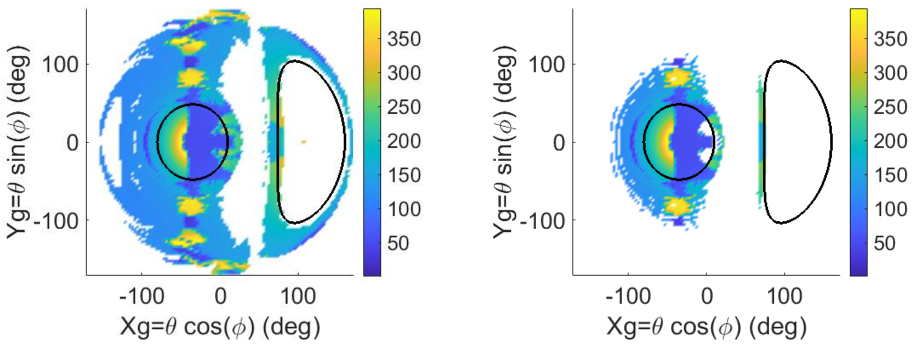

(a) (b)

Figure 4.60: The dominant ripple components, in all directions, of the radiation pattern can be seen with an alpha map overlay applied. In (a) the alpha map is constructed from M_{TbUS} calculated at 2.1 GHz. In (b) the alpha map is constructed from M_{TbUS} calculated at 3.5 GHz. Cliff scaling is applied to the alpha map

In the case of the -80° tipping angle, most of the other sky regions will likely have a lower temperature, compared to the main beam region. When the contributions from these regions reduce, while the contribution from the main beam region increases, the ANT will rise. The ground regions, however, will

Stellenbosch University https://scholar.sun.ac.za

likely have a higher temperature than the main beam region. When the contributions from these regions reduce, while the contribution from the main beam region increases, the ANT might reduce.

In the case of the zenith tipping angle, most of the other sky regions will likely have a higher temperature, compared to the main beam region. When the contributions from these regions reduce, while the contribution from the main beam region increases, the ANT will lower. This also contributes as to why the -80° tipping angle ANT rises over frequency and the zenith direction does not. It is expected that the influence on the ANT from more energy focusing into the main beam over frequency is relatively small, as strong scaling was required to see any difference.

In Fig 4.61, the sky region temperature is shown. In Fig 4.61b, the sky model for the zenith and the -80° observation angle is highlighted, over the frequency range [1.0 – 10.0] GHz. It can clearly be seen that the ANT for the -80° tipping angle, seen in Fig. 4.57, is similar to the sky model for the -80° observation angle, except for the ripple. This is expected, as the contribution to the ANT from the -80° observation angle is large, as this is the direction of the main beam. The contribution from the main beam also becomes larger over frequency, while the contribution from other directions becomes less, as previously explained. The sky region temperature at the -80° observation angle, is also relatively large, which amplifies the contribution even more. Furthermore, the sky model for the zenith observation angle starts to rise at a higher frequency compared to the -80° observation angle, which contributes as to why the ANT for zenith does not rise over the band [0.7 – 5.0] GHz.

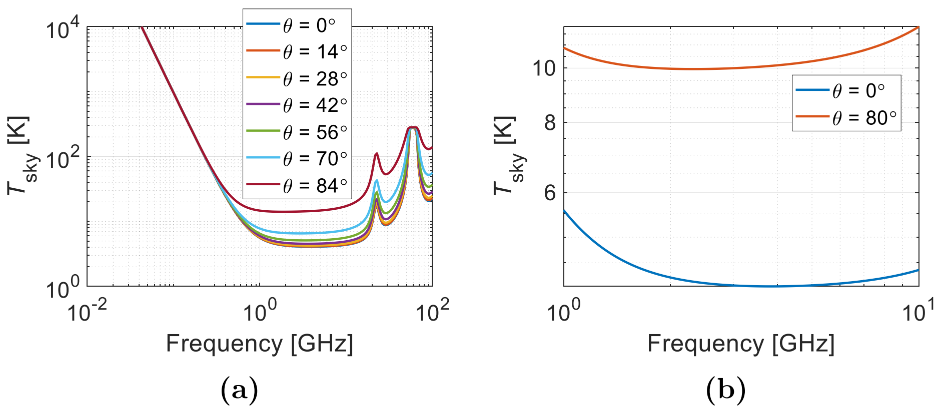

Figure 4.61: Sky noise model over frequency, or sky brightness temperature, over frequency. θ refers to the observation angle from zenith. The Cortes model is used, as described in [1]. In (b) the sky model for the zenith and -80° observation angle is highlighted, over the frequency range [1.0 – 10.0] GHz

Stellenbosch University https://scholar.sun.ac.za

The decrease in the ANT for both tipping angles, up to the somewhat arbitrarily chosen 2.5 GHz frequency position, is mostly due to Galactic synchrotron radiation power law response of the sky model. Some of the decrease might also be attributed to more energy focused into the main beam pointing into a colder sky, compared to the hot ground, as frequency increases. Calculating the ANT over a frequency band which include absorption lines in the sky model will also have a large impact on the ANT, at those frequencies, but they are higher near 20 GHz. Part of the success of the ANT approximation technique described in subsection 4.2.1, is due to the power law base form of the ANT. The ANT, however, does not always have a power law base form, as seen for the -80° tipping angle in Fig. 4.57. A power law does not model a non-monotonic function particularly well, and situations where the ANT base form is non-monotonic, occurs more easily over a larger band. An overall decrease of the ripple over frequency, however, can be assumed.

4.4.3 Aperture efficiency and ANT similarities

The ANT for a -80° tipping angle, and the AE, is shown in Fig. 4.62 below over the same band. The ANT and AE ripple is shown in Fig. 4.63. The ANT ripple resembles the AE ripple. The AE ripple will be discussed in more detail in Chapter 5, however, the AE ripple is determined from only the direction of maximum radiation intensity in the main beam of the radiation pattern.

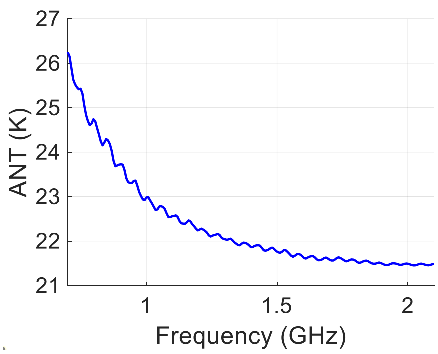

(a)

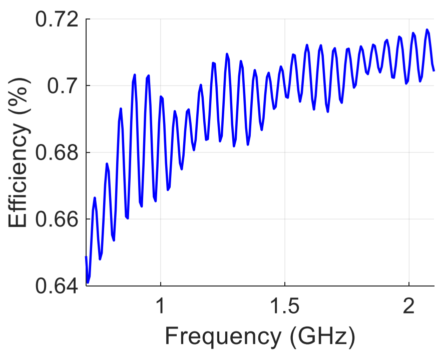

(b)

Figure 4.62: ANT at -80° tipping angle in (a). The reflector system efficiency response is shown through the high-fidelity AE in (b)

The dominant ripple periods of the radiation pattern in all directions, with an alpha map overlay, is shown in Fig 4.64 for a -80° tipping angle. Some similar angles are marked in Fig 4.64a, compared to the marked angles in Fig 4.59b. In Fig 4.64b the non-marked version is shown, for visual clarity and reference, because the marked information can obstruct parts of the plot. A $\sim$

Stellenbosch University https://scholar.sun.ac.za

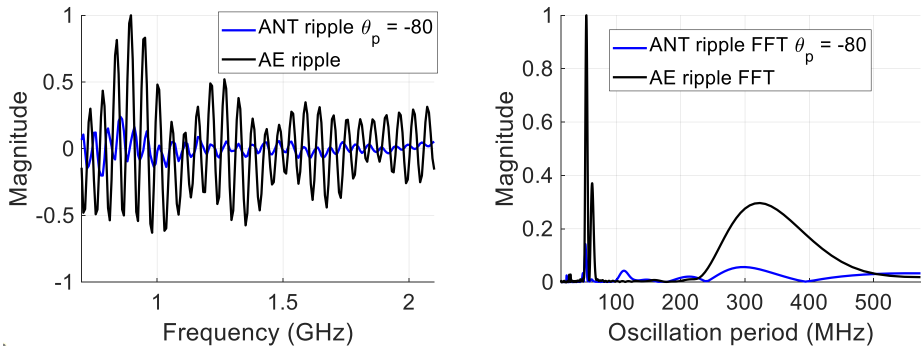

(a) (b)

Figure 4.63: Both ripples of the ANT and AE shown in (a). An FFT of the efficiency ripple, and the ANT ripple, is shown in (b) with a normalised magnitude on a linear scale to demonstrate their similarity

50 MHz ripple can be seen in the main beam near the centre of Fig 4.64a. The contribution from this component in the main beam is notably higher for a -80° tipping angle, compared to a zenith tipping angle, due to the main beam being in a hotter sky region. This is part of the reason why the ANT ripple in the zenith tipping angle does not resemble the AE ripple.

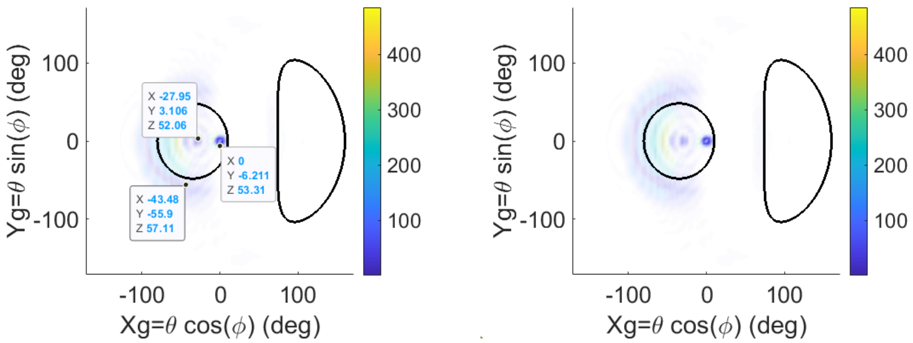

(a) (b)

Figure 4.64: The dominant ripple components, in all directions, of the radiation pattern can be seen with an alpha map overlay applied. In (a) similar angles are marked compared to the marked angles in Fig 4.59b. In (b) a non-marked version is shown for visual clarity and reference

In the case of the -80° tipping angle, the ANT ripple is similar to the AE ripple, mostly due to the higher main beam contribution. The other marked areas in Fig 4.64a, however, are inside the hot ground region of Fig 4.59b, and thus also contributes notably. In Fig 4.65 the $\sim$ 50 MHz ripple contribution is shown for the ANT in the -80° tipping angle, through the z value, for similarly marked angles as shown in Fig 4.59b. In Fig 4.65 it can be seen from the marked angle

Stellenbosch University https://scholar.sun.ac.za

near the centre, that the main beam contribution is notably higher than the contributions from the other marked angles.

Finally a smaller ~ 300 MHz ripple component can be seen for the AE, and the ANT in the -80° tipping angle. This ripple component is also present inside the main beam, but it is not as dominant as the ~ 50 MHz ripple.

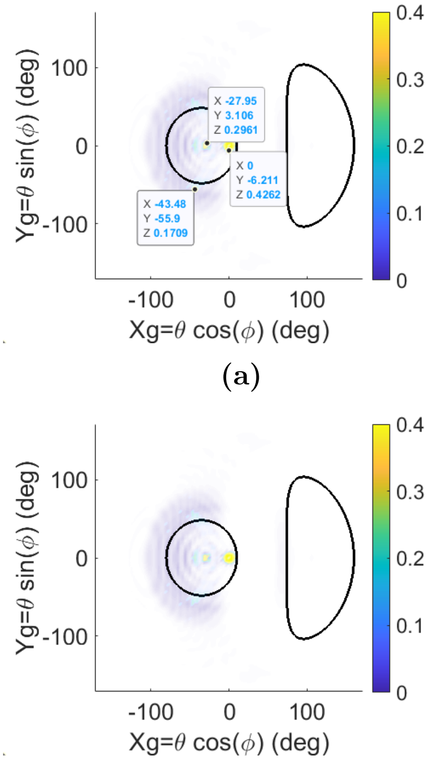

(a)

(b)

Figure 4.65: The ~ 50 MHz ripple contribution is shown for the ANT in the -80° tipping angle, through the z value. In (a) some angles are marked similarly to the marked angles as shown in Fig 4.59b, and the contribution from these angles are shown explicitly. In (b) a non-marked version is shown, for visual clarity and reference

4.4.4 Impact of hotter sky on ANT

The sky is hotter at a lower frequency band of $[0.3 - 0.9]$ GHz, compared to the $[0.7 - 2.1]$ GHz band, and thus a lower frequency band will be used to demonstrate the impact on the ANT of the hotter sky. The standard reflector is electrically scaled, and simulated over a frequency band of $[0.3 - 0.9]$ GHz. The reflector is electrically scaled through scaling all the lengths and physical

Stellenbosch University https://scholar.sun.ac.za

sizes of the standard reflector by a factor of $\frac{0.7}{0.3}$. This allows the electrically scaled reflector to have a similar full radiation pattern over the $[0.3-0.9]$ GHz band, compared to the standard reflector over the $[0.7-2.1]$ GHz band.

Comparing the standard reflector to a larger electrically scaled version allows the investigation of the impact of the background noise temperature on the ANT in a lower frequency range $[0.3-0.9]$ GHz, compared to a higher frequency range $[0.7-2.1]$ GHz, independent of the radiation pattern changes which would occur from simulating the same reflector in a different band. This is useful, as it allows the investigation of the background noise temperature on the ANT in isolation from the usual changes in the radiation pattern over frequency.

In Fig. 4.66 below, the electrically scaled reflector ANT is shown over $[0.3-0.9]$ GHz band, accompanied by the standard reflector ANT shown over the standard $[0.7-2.1]$ GHz band. In Fig. 4.66a it is shown for a 0° tipping angle, and in Fig. 4.66b for a -80° tipping angle.

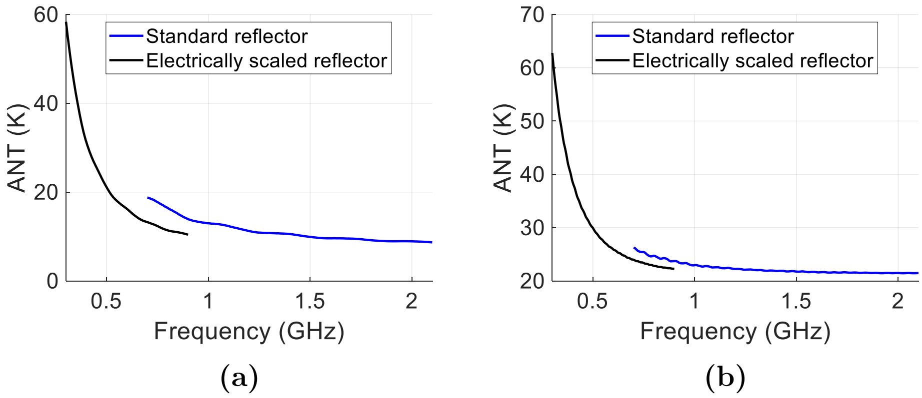

Figure 4.66: The electrically scaled reflector ANT is shown over $[0.3-0.9]$ GHz band, accompanied by the standard reflector ANT shown over the standard $[0.7-2.1]$ GHz band. In (a) it is shown for a 0° tipping angle, and in (b) for a -80° tipping angle

The x-axis is normalised, to allow both reflector ANTs to be compared, and is shown in Fig. 4.67 below. The normalisation is performed by adjusting both frequency bands independently to a range between zero and one. This normalisation and presentation allows investigating the impact of the background noise temperature in a low frequency range. In Fig. 4.67, the electrically scaled reflector has a significantly higher ANT in the lower part of the normalised frequency range. This is because the background noise temperature sky region is notably hotter around the frequency of 0.3 GHz, compared to around the frequency of 0.7 GHz. This can be seen in the sky model in Fig. 4.61. It is

Stellenbosch University https://scholar.sun.ac.za

also shown in Fig. 4.68 below.

In all sensible cases, the main beam will point into the sky region. A notably hotter sky will amplify the contribution of the main beam substantially, due to the high energy content of the main beam. Furthermore, many of the angles of the background noise temperature are in the sky region, and are clearly seen in Fig. 4.68. The contribution to the ANT, from an increase over this large region, will substantially rise the ANT. The ANT of both reflectors somewhat converges near the end of the band, as expected, due to the background noise temperature somewhat converging in the band $[0.9 - 2.1]$.

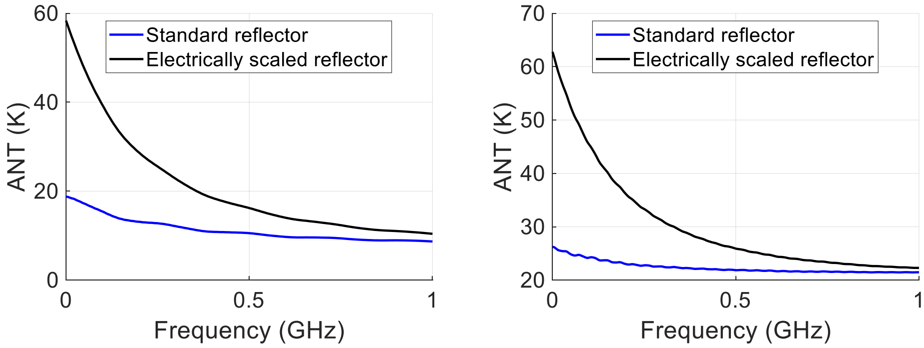

(a) (b)

Figure 4.67: The x-axis is normalised, to allow both reflector ANTs to be compared. The electrically scaled reflector, over the $[0.3 - 0.9]$ GHz band, has a significantly higher ANT in the lower part of the normalised frequency range, compared to the standard reflector over the $[0.7 - 2.1]$ GHz band

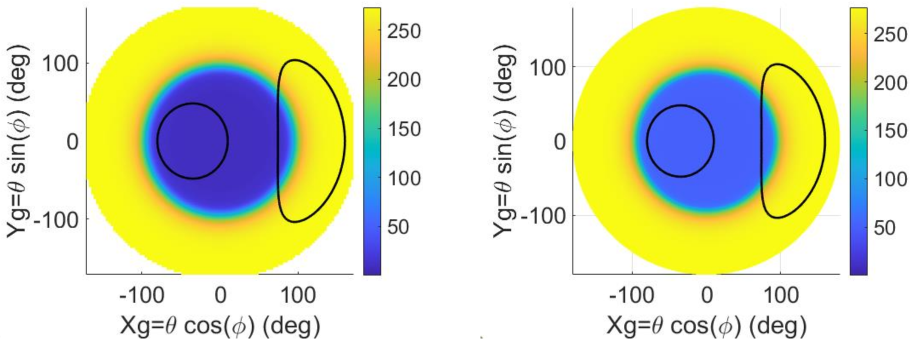

(a) (b)

Figure 4.68: The background noise temperature at 0.7 GHz in (a), and at 0.3 GHz in (b). The background noise temperature sky region is notably hotter around the frequency of 0.3 GHz, compared to around the frequency of 0.7 GHz

Stellenbosch University https://scholar.sun.ac.za

The ripple (non-FFT) of both reflectors are shown in Fig. 4.69 below. Remember, the electrically scaled reflector over the $[0.3 - 0.9]$ GHz band, has a similar full radiation pattern, compared to the standard reflector over the $[0.7 - 2.1]$ GHz band. The electrically scaled reflector has a lower ripple overall, compared to the standard reflector, even though the electrically scaled reflector has a higher ANT temperature. The reason for the lower ripple will be described soon.

In Fig. 4.70, the normalised FFT of both reflectors are shown. The normalisation is performed by adjusting both FFTs by the bandwidth of the highest band, thus by 1.4 GHz. This allows the ripples in both FFTs to be observed over a similar band. Both FFTs are then further normalised to the highest bandwidth, to observe the ripple components over a band of $0 - 1$.

The ANT of both reflectors have similar dominant ripple periods, and both reflectors have similar radiation patterns. While it could be expected that the electrically scaled reflector ANT ripple might look similar to the AE ripple, due to the main beam contribution increasing from the hotter sky, this does not occur. It does not occur, because the entire sky region becomes hotter, which increases the contribution from many more angles than just the main beam. This assumption will be investigated next, to confirm its validity.

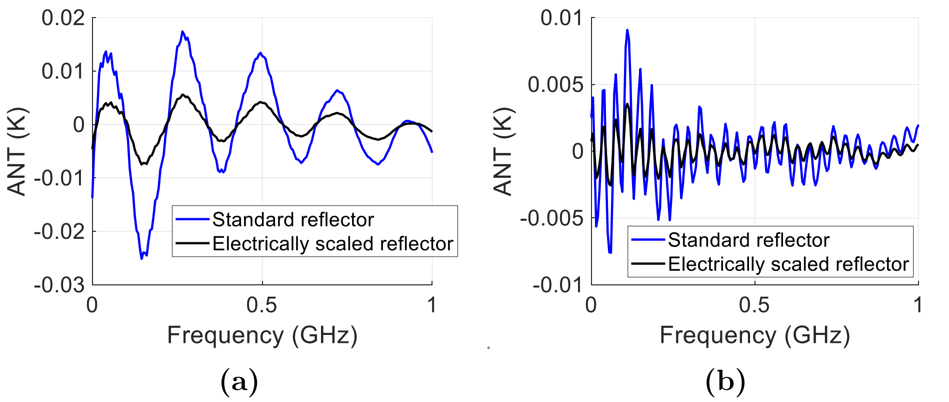

Figure 4.69: The ripple (non-FFT) of both reflectors are shown. In (a) for a zenith tipping angle and in (b) for a -80° tipping angle

Previously, it was shown that the electrically scaled reflector ([0.3 - 0.9] GHz) has a lower ripple overall, compared to the standard reflector ([0.7 - 2.1] GHz). Furthermore, there was the possible expectation that the electrically scaled reflector ANT ripple will be similar to the AE ripple, and the result proved otherwise. The reason for these results will be explained using using two tailored situations, which does not exist in reality, but allow for a clear and

Stellenbosch University https://scholar.sun.ac.za

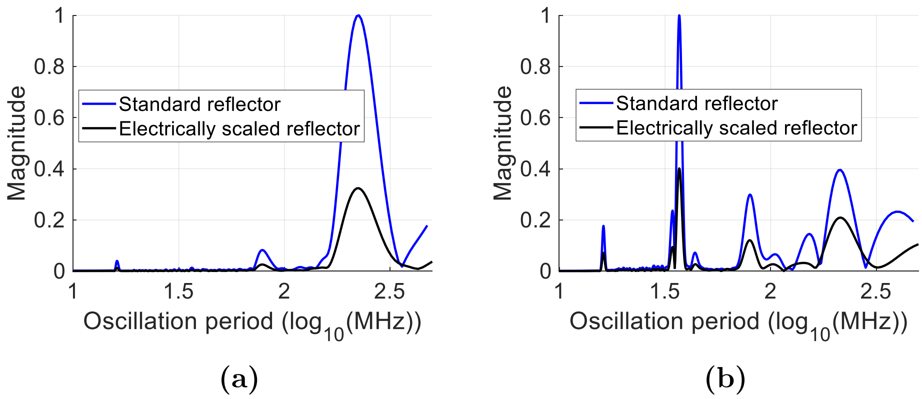

Figure 4.70: The ripple (FFT) of both reflectors are shown. In (a) for a zenith tipping angle and in (b) for a -80° tipping angle

systemic explanation. The first situation only accounts for contributions from the main beam. The second situation accounts for the entire sky region, to account for more contributions than just from the main beam.

In Fig. 4.71 the ANT and its ripple is shown when the contribution to the ANT from every region, except for the zenith direction, is zeroed. This is achieved by zeroing the background noise temperature of every region except for zenith, shown in Fig. 4.71d, and is shown only for the standard reflector for the sole purpose of highlighting which regions remain relevant. It is shown for the 0° tipping angle. It is shown for the standard and electrically scaled reflector, except for Fig. 4.71d.

In this case the use of HEALPix is not necessary to improve performance, as no fitting will be performed. In Fig. 4.71 the ANT has similar ripple characteristics as seen for the AE or the ANT for the -80° tipping angle, as expected, due to the main beam in the zenith direction being the only contributor.

In Fig. 4.71 it can be observed that the ANT ripple is larger for the electrically scaled reflector, compared to the standard reflector. This is expected, as the electrically scaled reflector has a hotter sky region temperature, due to its lower frequency band. This hotter sky amplifies the ANT contribution from the zenith direction in the main beam, which also includes the ripple in this direction. The ANT is also generally larger for the electrically scaled reflector, as the ANT contribution is increased. In both cases, however, the ripple components have similar frequencies or periods.

In Fig. 4.72 below the ANT and its ripple is shown when the contribution to the ANT from every ground region is zeroed, with only the sky region contribution remaining. This is achieved by zeroing the background noise temperature

Stellenbosch University https://scholar.sun.ac.za

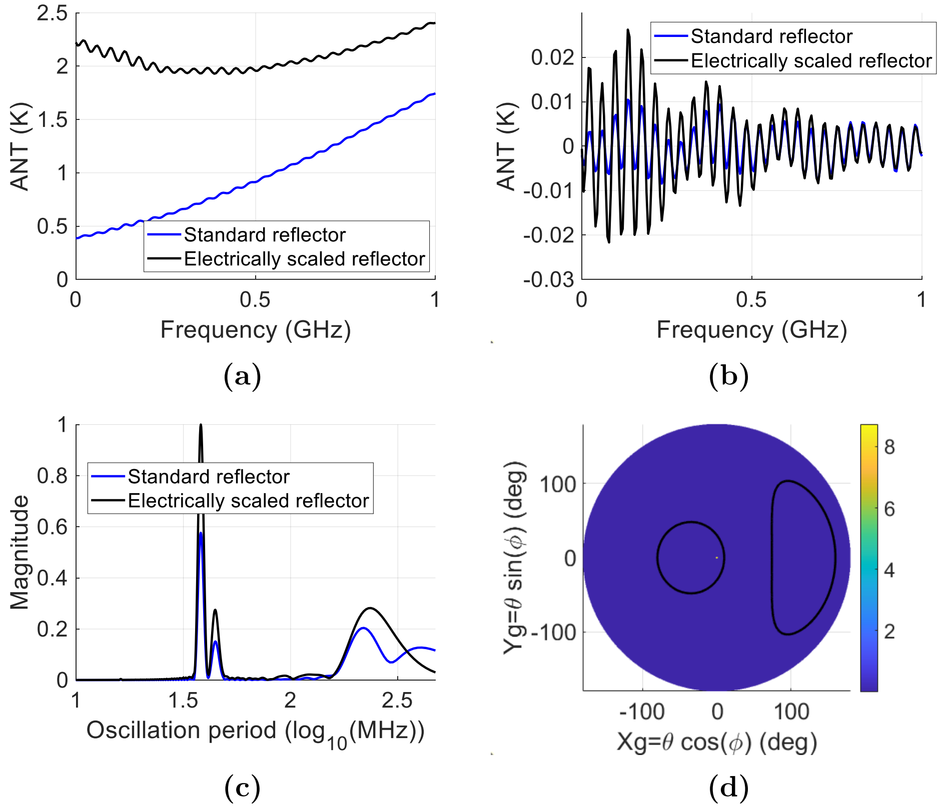

Figure 4.71: The ANT and its ripple is shown for the standard reflector when the contribution to the ANT from every region, except for the zenith direction, is zeroed. This is achieved by zeroing the background noise temperature of every region except for zenith, shown in (d). It is shown for the 0° tipping angle. In (a) the ANT is shown. In (b) the ripple is shown, and in (c) the ripple FFT

of every ground region, shown in Fig. 4.72d, and is shown only for the standard reflector for the sole purpose of highlighting which regions remain relevant. It is shown for the 0° tipping angle. It is shown for the standard and electrically scaled reflector, except for Fig. 4.72d.

In Fig. 4.72 the ANT ripple is lower for the electrically scaled reflector, compared to the standard reflector. When the contribution is extended to the entire sky region, and not just the zenith direction, the total ripple is no longer due to only the ripple in the zenith direction. The ripple is now influenced from the various different frequency components in all sky regions. The influence from all these frequency components combining, reduces the resultant dominant ripple observed. In the case of the electrically scaled reflector ([0.3 - 0.9] GHz), the sky is even hotter compared to the standard reflector ([0.7 - 2.1] GHz), and thus the influences of these frequency components are even larger, to reduces the resultant dominant ripple observed even more. The dominant ripple components, however, will still be dominant, and dominate

Stellenbosch University https://scholar.sun.ac.za

the total ripple. This is why these components are observed in the standard and electrically scaled reflector, even though the electrically scaled reflector has a hotter sky.

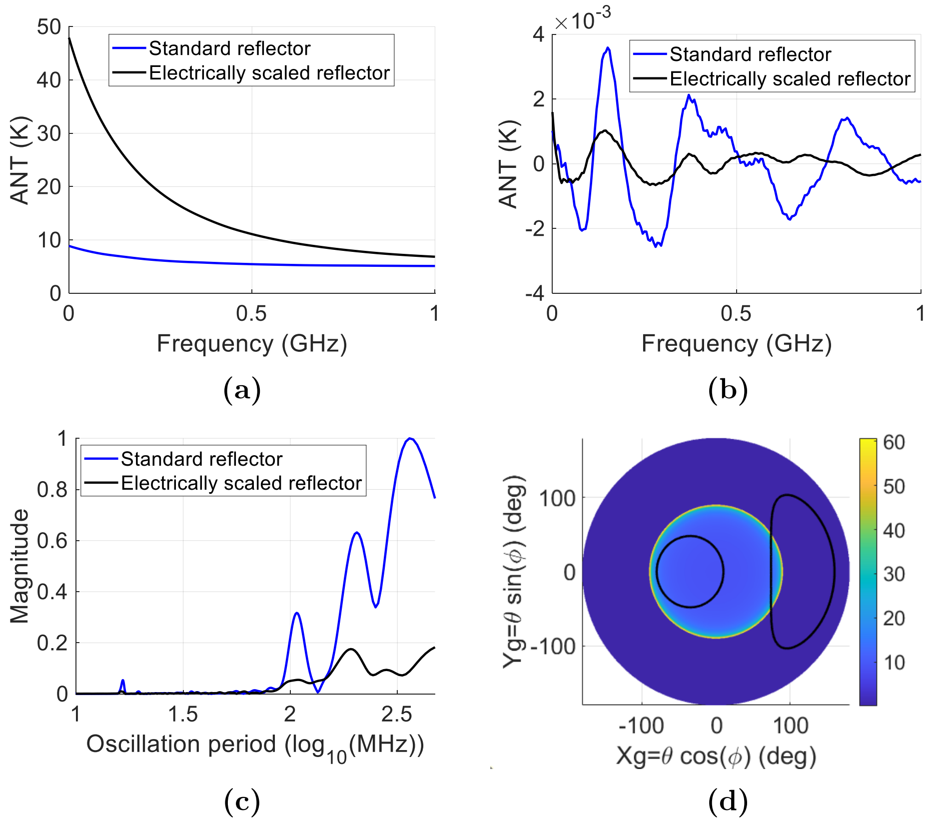

Figure 4.72: The ANT and its ripple is shown for the standard reflector when the contribution to the ANT from every region, except for the zenith direction, is zeroed. This is achieved by zeroing the background noise temperature of every region except for zenith, shown in (d). It is shown for the 0° tipping angle. In (a) the ANT is shown. In (b) the ripple is shown, and in (c) the ripple FFT

4.4.5 Effect of distance between PR and SR on ANT

In Fig. 4.73, the standard reflector is shown accompanied by a reflector setup similar to the standard reflector, with only the spacing increased between the reflectors. The x-axis spacing is increased to 2 m, from 1 m, between the reflectors. This distance is measured between the rightmost edge of the subreflector, compared to the leftmost edge of the primary reflector. In Fig. 4.73a the standard reflector is shown in 2D. In Fig. 4.73b the reflector with the increased spacing is shown in 2D. In Fig. 4.73c the standard reflector is shown

Stellenbosch University https://scholar.sun.ac.za

in 3D. In Fig. 4.73d the reflector with the increased spacing is shown in 3D.

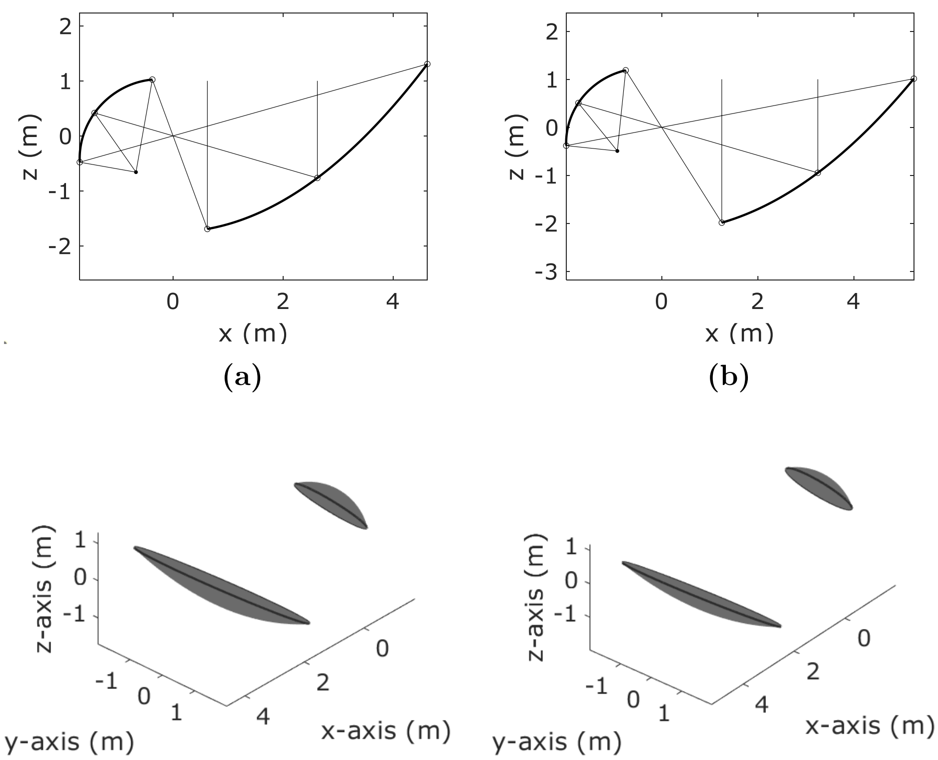

(a) (b) (c) (d)

Figure 4.73: The standard reflector is shown accompanied by a reflector setup similar to the standard reflector, with only the spacing increased between the reflectors. The x-axis spacing is increased to 2 m, from 1 m, between the reflectors. This distance is measured between the rightmost edge of the subreflector, compared to the leftmost edge of the primary reflector. In (a) the standard reflector is shown in 2D. In (b) the reflector with the increased spacing is shown in 2D. In (c) the standard reflector is shown in 3D. In (d) the reflector with the increased spacing is shown in 3D

The ANT of both reflector setups are shown in Fig. 4.74, for a 0° and -80° tipping angle. The ANT is higher for the 2 m spacing case, however, the amount it is higher depends on the tipping angle. The ANT is higher for the 2 m case, because more energy spillover from the subreflector around the primary reflector occurs, due to the increased spacing. Some of this energy spills into the hot ground for the zenith tipping angle, which raises the ANT notably.

For the -80° tipping angle, this energy spills into the cold sky instead, which is why the ANT contribution is lowered. In Fig. 4.75, where both reflectors are shown for the -80° tipping angle, it can be seen that the energy spillover, from

Stellenbosch University https://scholar.sun.ac.za

the subreflector around the primary reflector, spills into the cold sky instead. In Fig. 4.75a the standard reflector is shown in 2D. In Fig. 4.75b the reflector with the increased spacing is shown in 2D.

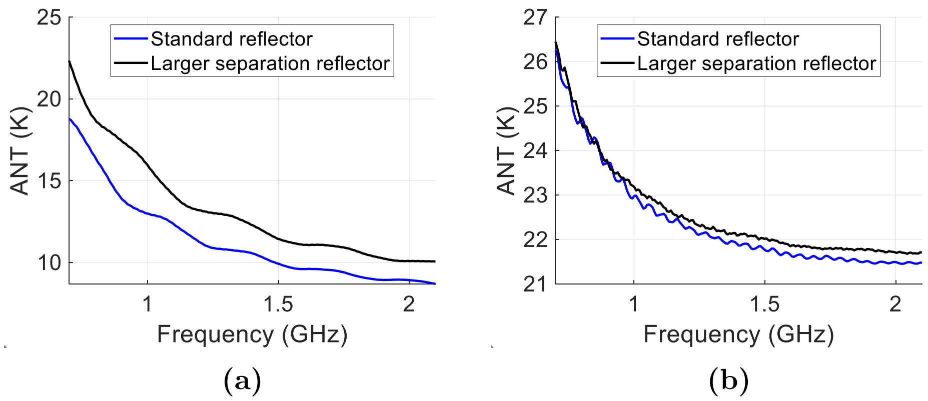

Figure 4.74: The ANT of both reflector setups are shown, for a 0° and -80° tipping angle. In (a) it is shown for a 0° tipping angle. In (b) it is shown for a -80° tipping angle

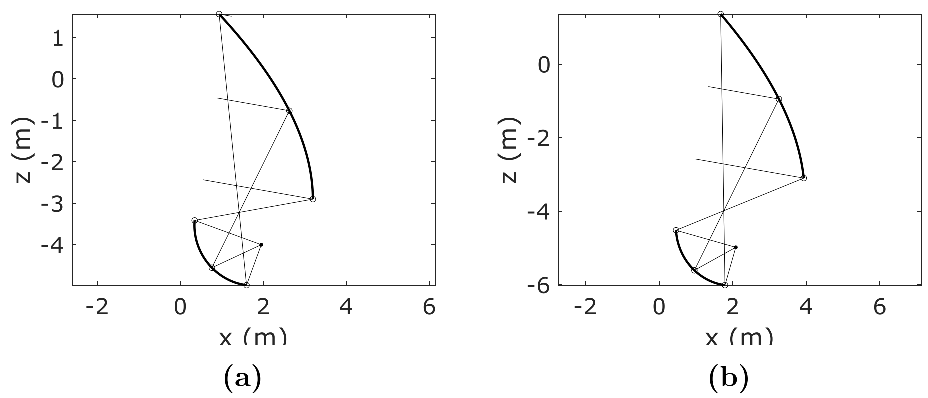

Figure 4.75: Both reflectors are shown for the -80° tipping angle. In (a) the standard reflector is shown in 2D. In (b) the reflector with the increased spacing is shown in 2D

In Fig. 4.76 M_{TbUS} is shown for both reflector setups, for a 0° and -80° tipping angle. In Fig. 4.76a $M_{\mathrm{TbUS_{SS0}}}$ is shown for the standard reflector, in the zenith direction. In Fig. 4.76b $M_{\mathrm{TbUS_{LS0}}}$ is shown for the reflector with the larger spacing, in the zenith direction, with the colour axis limited to the maximum of Fig. 4.76a. The colour axis is limited to compare the magnitude of both products, M_{TbUS}, with the colour axis. From the colour axis, the reflector with a larger spacing generally has a larger M_{TbUS}. It is especially noticeable around

Stellenbosch University https://scholar.sun.ac.za

the edges of the primary reflector. This corresponds with the statement that the spillover from the subreflector radiates into the hot ground, causing a large contribution to the ANT, as the region around the primary reflector is part of the hot ground as seen in Fig. 4.76e.

In Fig. 4.76c $M_{\mathrm{TbUS}_{\mathrm{SSm80}}}$ is shown for the standard reflector, in the -80° tipping angle. In Fig. 4.76d $M_{\mathrm{TbUS}_{\mathrm{LSm80}}}$ is shown for the reflector with the larger spacing, in the -80° tipping angle, with the colour axis limited to the maximum of Fig. 4.76c. The differences between $M_{\mathrm{TbUS}_{\mathrm{SSm80}}}$ and $M_{\mathrm{TbUS}_{\mathrm{LSm80}}}$ in this case is much smaller, as expected. This is because most of the spillover radiation from the subreflector radiates into the cold sky around the primary reflector, as seen in Fig. 4.76f. $M_{\mathrm{TbUS}_{\mathrm{LSm80}}}$ is still slightly larger, as there is some extra scattering behind the subreflector, due to the primary reflector. This scattering is in the hot ground region, and thus makes the contribution somewhat noticeable.

The ripple (non-FFT) of both reflectors are shown in Fig. 4.77, for a 0° and -80° tipping angle. The ripple (FFT) is shown in Fig. 4.78, for a 0° and -80° tipping angle. The ripple is different as expected, because the path lengths of the interfering waves will change, as the spacing between the reflectors changes. This will lead to different non-ideal effects, such as diffraction effects. The spacing between the reflectors can thus be used to change the ripple, to keep specific bands clear of ripple effects.

4.4.6 Antenna noise temperature ripple as a function of simulation method

In Fig. 4.79 the dominant ripple period of the radiation intensity is shown for PO and MoM. In Fig. 4.79a it is shown using the PO method. In Fig. 4.79b it is shown using the MoM method. It can clearly be seen that the methods generated different dominant ripple periods, although somewhat similar in many regions. This is expected, as MoM accounts for more non-ideal effects, specifically the self-coupling (which includes mutual coupling) and re-radiation non-ideal effects. The standard reflector is considered in this case, and since it is an offset system, the ripple similarity in many regions is a result of the coupling and re-radiation energy being much less outside of the main beam.

Various simulation component times, for four different electrical size setups and two different simulation methods, are shown in Fig. 4.80. A simulation component refers to a specific calculation required in the simulation. To complete a simulation, the currents needs to be calculated, followed by the radiation pattern from these currents, known as the field calculation.

Stellenbosch University https://scholar.sun.ac.za

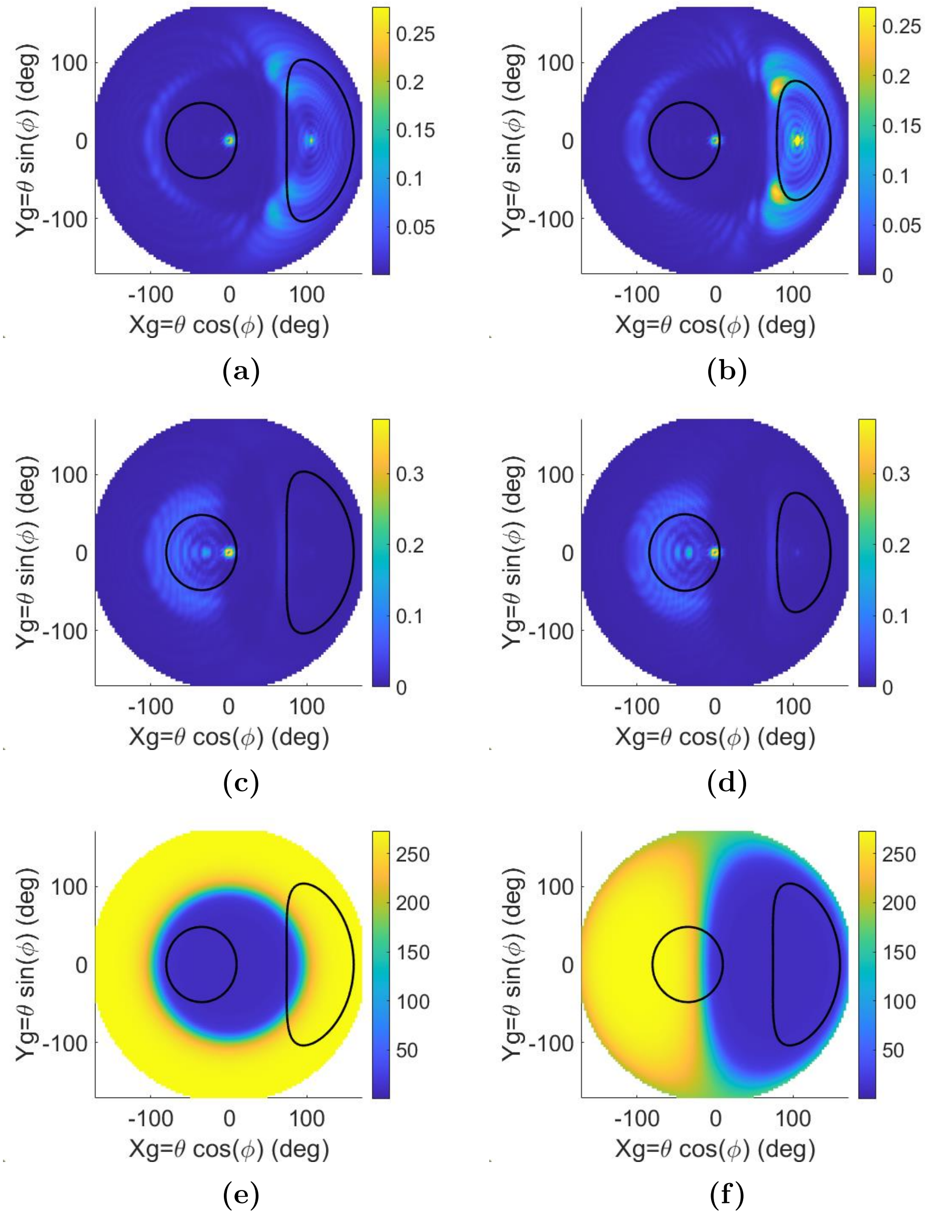

Figure 4.76: M_{TbUS} is shown for both reflector setups, for a 0° and -80° tipping angle. In (a) $M_{\mathrm{TbUS_{SS0}}}$ is shown for the standard reflector, in the zenith direction. In (b) $M_{\mathrm{TbUS_{LS0}}}$ is shown for the reflector with the larger spacing, in the zenith direction, with the colour axis limited to the maximum of (a). In (c) $M_{\mathrm{TbUS_{SSm80}}}$ is shown for the standard reflector, in the -80° tipping angle. In (d) $M_{\mathrm{TbUS_{LSm80}}}$ is shown for the reflector with the larger spacing, in the -80° tipping angle, with the colour axis limited to the maximum of (c). The background noise temperature, for a zenith tipping angle in (e), and a -80° tipping angle in (f)

The electrical sizes are determined through the electric aperture diameter of

Stellenbosch University https://scholar.sun.ac.za

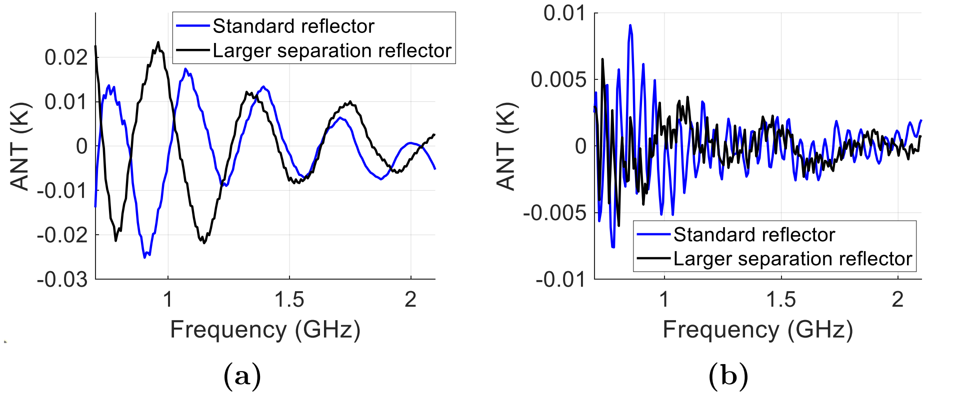

Figure 4.77: The ripple (non-FFT) of both reflectors are shown, for a 0° and -80° tipping angle

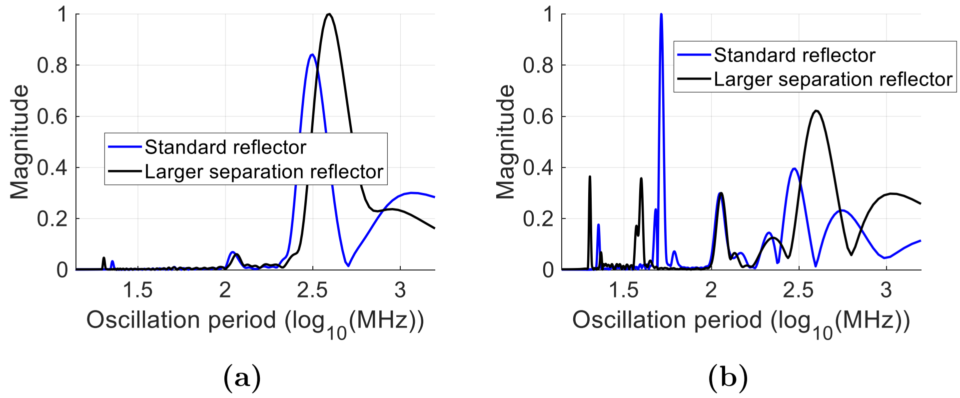

Figure 4.78: The ripple (FFT) of both reflectors are shown, for a 0° and -80° tipping angle

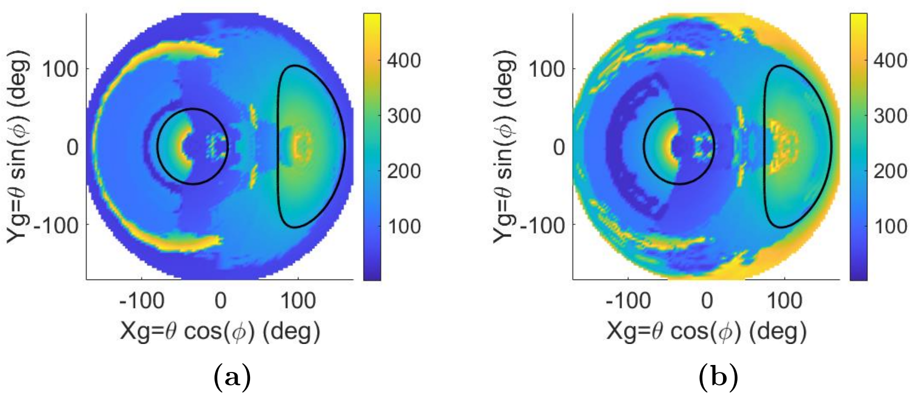

Figure 4.79: The dominant ripple period of the radiation intensity is shown for PO and MoM. In (a) it is shown using the PO method. In (b) it is shown using the MoM method

Stellenbosch University https://scholar.sun.ac.za

the primary reflector $A_{\mathrm{ed}} = \frac{D_{\mathrm{m}}}{\lambda} = \frac{D_{\mathrm{m}} f}{c}$. The setups are chosen to have ascending electrical size, and are denoted by $A_{\mathrm{e}r}$, $r \in 1, 2, 3, 4$. At 2.1 GHz and $D_{\mathrm{m}} = 3$ m, $A_{\mathrm{e1}} = 21.01$ wavelengths. At 2.1 GHz and $D_{\mathrm{m}} = 4$ m, $A_{\mathrm{e2}} = 28.02$ wavelengths. At 3.5 GHz and $D_{\mathrm{m}} = 4$ m, $A_{\mathrm{e3}} = 46.70$ wavelengths. At 5.0 GHz and $D_{\mathrm{m}} = 4$ m, $A_{\mathrm{e4}} = 66.71$ wavelengths. Outside of these changes, all other physical properties remain identical to the standard reflector, except for $r = 1$, where the subreflector chord length changes to 1 m. The simulations are performed with a desktop personal computer (PC), with a Intel(R) Core(TM) i7-9700K CPU processor @ 3.60 GHz, 8 Core(s), 8 Logical processor(s). The PC has 32 GB memory.

It is expected from the ascending electrical sizes, that the computation time required for each simulation component will also increase monotonically. From Fig. 4.80, this expectation is generally met. Furthermore, the PO current calculation time scales less with electric size, compared to the MoM current calculation time, which is also expected.

It is interesting, however, to note that the field calculation of PO requires notably more time, compared to the field calculation of MoM, especially at higher frequencies. The reason for this is explained comprehensively in [44], however, a short summary will be provided, for brevity. In summary, the PO calculation time is an exponential function of the frequency. From [44], the electric far-field, $\boldsymbol{E}_{\mathrm{far}}(\theta, \phi)$, can be computed as,

$$\boldsymbol{E}_{\mathrm{far}}(\theta, \phi) = \frac{jk\eta_0}{4\pi} \hat{\boldsymbol{k}} \times \left[\hat{\mathbf{k}} \times \iint \boldsymbol{J}_S(\boldsymbol{r}') e^{jk\hat{\boldsymbol{k}} \cdot \boldsymbol{r}'} dS' \right], \tag{4.42}$$

where the surface current distribution is denoted as $\boldsymbol{J}_S$, the wavenumber is defined as $k = \frac{2\pi}{\lambda}$, the wave vector is $\hat{\boldsymbol{k}} = \sin\theta\cos\phi\hat{\boldsymbol{x}} + \sin\theta\sin\phi\hat{\boldsymbol{y}} + \cos\theta\hat{\boldsymbol{z}}$, and the integration point is $\boldsymbol{r}' = x'\hat{\boldsymbol{x}} + y'\hat{\boldsymbol{y}} + z'\hat{\boldsymbol{z}}$.

The electric far-field, $\boldsymbol{E}_{\mathrm{far}}(\theta, \phi)$ in (4.42) has to be evaluated at a certain number of observation points, N_{obs}, where each observation point is $X_{\mathrm{p}}(\theta, \phi)$. The grid resolution determines N_{obs}. Furthermore, each observation point, X_{p}, requires a summation over all the integration points, N_{int}. The density of points chosen over the surface for integration influences the number of integration points, N_{int}, and the resolution has to be high enough for the integral to converge. Both N_{obs} and N_{int} usually have a order complexity of $\mathcal{O}(f^2)$. Thus, the order complexity of (4.42), is $\mathcal{O}(N_{\mathrm{obs}} N_{\mathrm{int}})$, or $\mathcal{O}(f^4)$.

The commercial solver GRASP [39] implements improvements to the PO method, and does not suffer from such a severe slowdown in computation time, at higher frequencies. These improvements, however, are beyond the scope of this dissertation. Even with these improvements, when simulating electrically larger structures, it might be more time efficient to rather use MoM, instead

Stellenbosch University https://scholar.sun.ac.za

of PO, to extract the ANT ripple in GRASP.

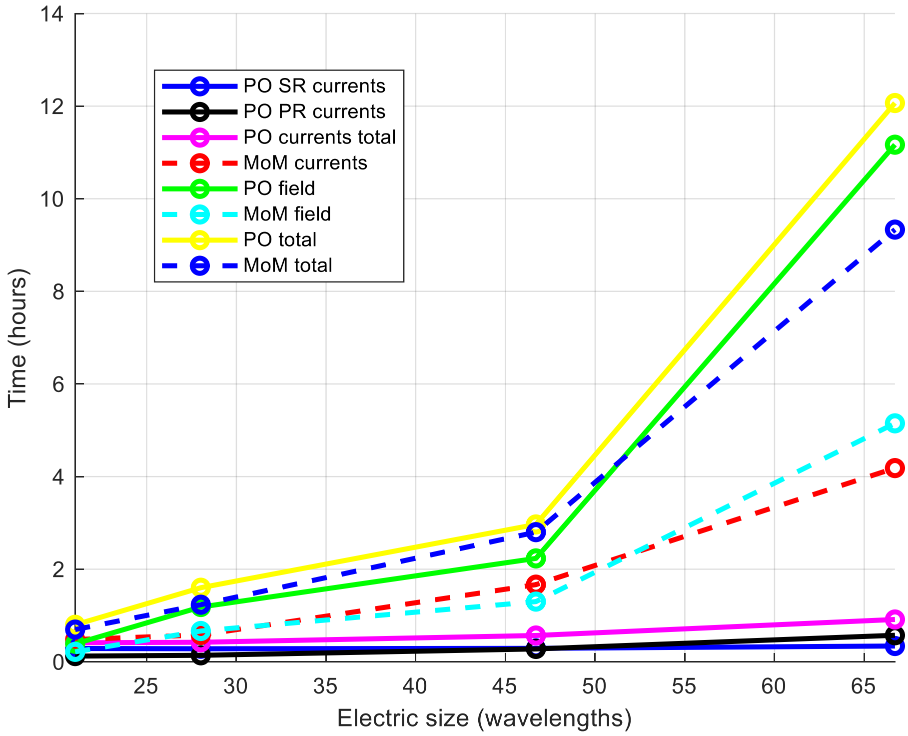

Figure 4.80: Various simulation component times, for four different electrical size setups and two different simulation methods, are shown

In Fig. 4.81a the ANT is calculated for both MoM and PO over the [0.7 - 5.0] GHz band, and in Fig. 4.81b the ripple (non-FFT) is displayed. It is calculated for the zenith tipping angle, using the the standard reflector. The ripple (FFT) is calculated over the [0.7 - 5.0] GHz band for both MoM and PO in Fig. 4.81c.

By comparing Fig. 4.81a and Fig. 4.81b, it is apparent that the MoM and PO simulations have a different ripple in the ANT, as expected, and that the ANT calculated from both simulation techniques start to converge around the 3 GHz frequency. It is expected that the ANTs will start to converge over frequency, as the electric size increases. An electric size increase leads to less non-ideal effects, which would make both simulation methods provide a more similar radiation pattern. In both cases, the ripple also decreases over frequency. Thus, for larger electrical sizes, there is less need for a MoM simulation over a PO simulation, to accurately account for the ANT ripple.

Stellenbosch University https://scholar.sun.ac.za

While in Fig. 4.81c the simulation methods have different strength ripple periods, the dominant ripple period is similar. Thus, the PO technique accounts for the highest impact non-ideal effects on the ANT ripple, and largely models the underlying ripple behaviour of the ANT. This proves that using the PO method for the ripple analysis in this dissertation is valid, although not entirely descriptive of the ANT behaviour .

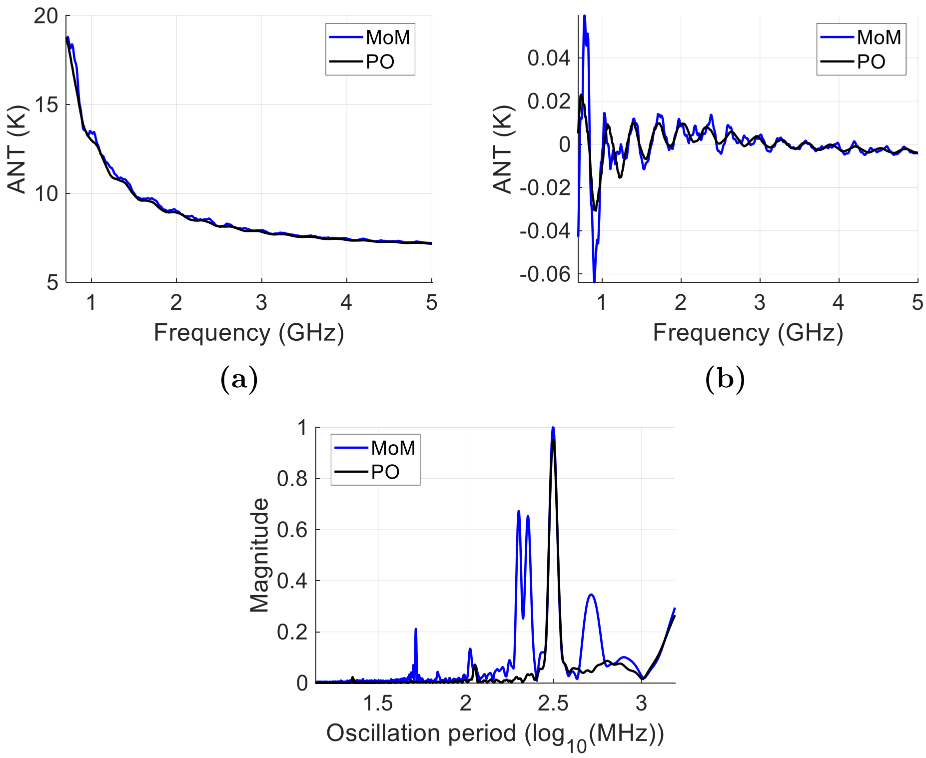

(a) (b) (c)

Figure 4.81: In (a) the ANT is calculated for both MoM and PO over the [0.7 - 5.0] GHz band, and in (b) the ripple (non-FFT) is displayed. It is calculated for the zenith tipping angle, using the the standard reflector. The ripple (FFT) is calculated over the [0.7 - 5.0] GHz band for both MoM and PO in (c)

4.4.7 Spillover from feed effect on the ANT

Spillover is a non-ideal effect, which will influence the ripple of the ANT. Increased spillover from the feed, will lead to increased interference on the radiation pattern of the full reflector system, which will lead to more ripple in the ANT. In Fig. 4.82 the increased interference from higher feed spillover is shown conceptually.

Stellenbosch University https://scholar.sun.ac.za

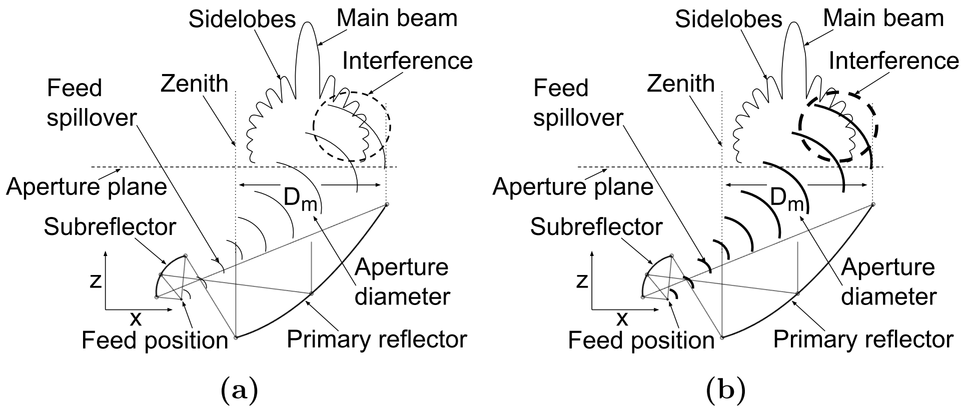

Figure 4.82: More spillover from the feed will lead to more interference on the radiation pattern of the full reflector system, which will lead to higher ripple in the ANT. In (a) there is less feed spillover, compared to (b)

In Fig. 4.83, the Gaussian feed taper is stepwise changed from -24 dB, to -4 dB taper, to characterise the effect on the ANT ripple. A smaller feed taper will lead to less spillover from the feed. The ANT for each taper is shown in Fig. 4.83a, with its ripple (non-FFT) shown in Fig. 4.83b and its ripple (FFT) in Fig. 4.83c. The spillover efficiency can be seen in Fig. 4.83d. The spillover efficiency is discussed in detail in Chapter 5, however, in short it accounts for the loss in AE due to spillover. It is expected that as spillover efficiency increases, less energy is lost to spillover, and thus the spillover non-ideal effect becomes less. By comparing Fig. 4.83b to Fig. 4.83d, it is clear that as the spillover efficiency increases, the ripple becomes less, as the spillover non-ideal effect reduces. Finally, it is interesting to note that some other frequency components become larger in Fig. 4.83c, as the taper becomes larger. This is also expected, as interference from various other angles will increase as the taper becomes larger, due to more spillover, which will increase the ripple contribution from these angles.

4.4.8 A low ripple case

A situation where almost no ripple is observed, is shown in Fig. 4.84. In Fig. 4.84, the ANT is shown in Fig. 4.84a, and $M_{\mathrm{TbUS_{LR}}}$ in Fig. 4.84b. It is shown for the zenith tipping angle. In this case, an offset single reflector is simulated, with a projected aperture diameter of 5 m, an $\frac{F}{D} = 0.4$ and an $\frac{H}{D} = 0.5$. A -12 dB edge taper Gaussian feed is used, and there are no support struts. For an offset single reflector, little feed spillover interference is experienced from a Gaussian feed in the radiation pattern of the reflector system, as Gaussian patterns have no sidelobes and back radiation. The struts needed to mount the feed on the single reflector would also scatter and interfere. Without a subreflector, the non-ideal diffraction effect interference is also less. Re-radiation

Stellenbosch University https://scholar.sun.ac.za

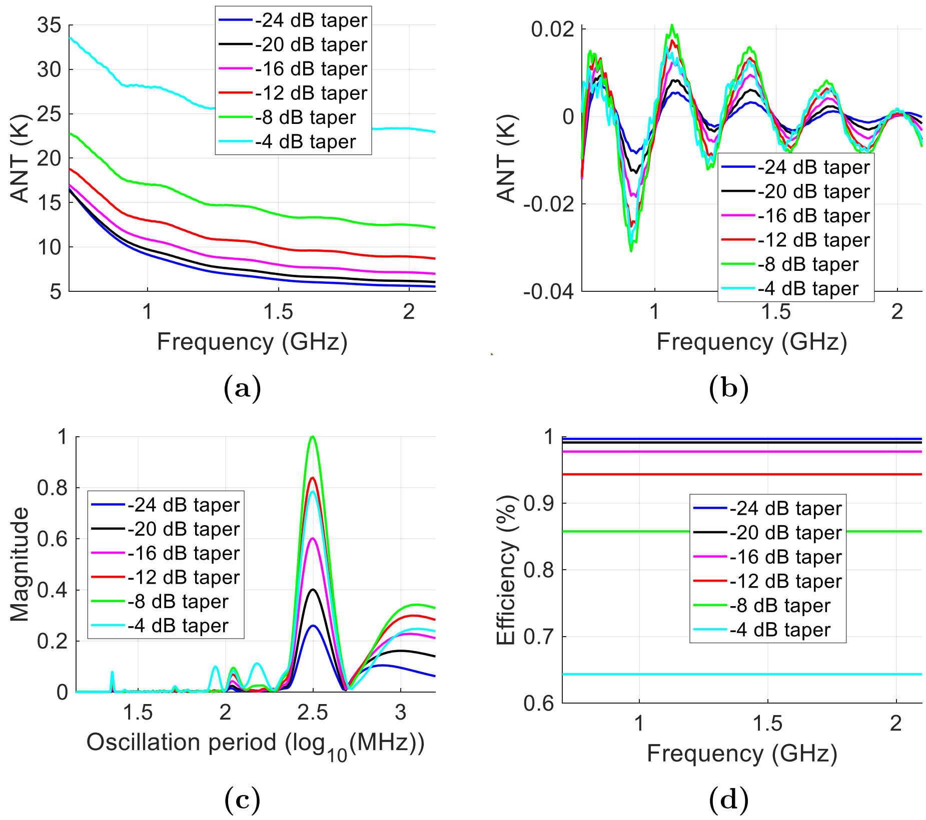

Figure 4.83: The Gaussian feed taper is stepwise changed from -24 dB, to -4 dB taper, to characterise the effect on the ANT ripple. A smaller feed taper will lead to less spillover from the feed. The ANT for each taper is shown in (a), with its ripple (non-FFT) shown in (b) and its ripple (FFT) in (c). The spillover efficiency can be seen in (d)

interference is less, as the feed is offset. Less selfcoupling occurs, as there is no subreflector. Thus without dominant non-ideal effect interference, ripple would not easily be observed on the ANT.

4.4.9 Effect of physical feed vs Gaussian feed on ANT ripple

The low ripple case is changed to use a Quad Ridge Flared Horn (QRFH) feed, instead of a Gaussian feed. The purpose of this is to show the effect of using a practical feed on the ripple of the ANT, instead of an idealised feed. In Fig. 4.85 the normalised radiation intensity of an arbitrary QRFH feed is compared to a Gaussian feed. In Fig. 4.85a the radiation intensity is plotted in 2D. It is plotted in 3D for the QRFH in Fig. 4.85b, and for the Gaussian in Fig. 4.85c. It can clearly be seen that the QRFH has back radiation and sidelobes, where the Gaussian pattern does not.

Stellenbosch University https://scholar.sun.ac.za

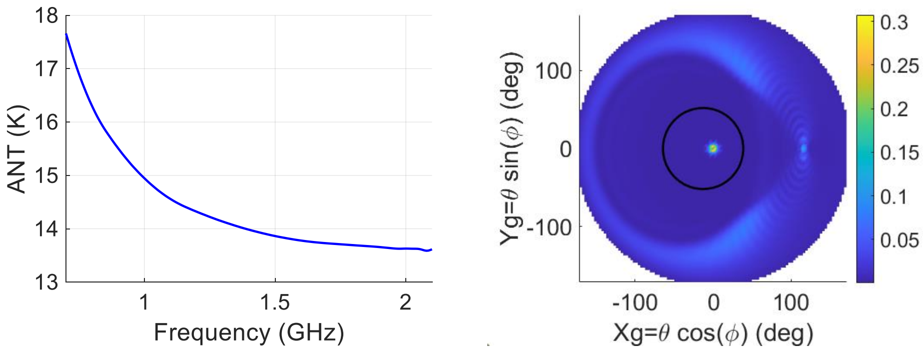

(a) (b)

Figure 4.84: A situation where almost no ripple is observed. In (a) the ANT is shown. In (b) $M_{\mathrm{TbUS_{LR}}}$ is shown. It is shown for the zenith tipping angle. In this case, an offset single reflector is simulated, with a projected aperture diameter of 5 m, an $\frac{F}{D} = 0.4$ and an $\frac{H}{D} = 0.5$. A -12 dB edge taper Gaussian feed is used, and there are no support struts

In Fig. 4.86 the low ripple case is compared to a similar situation, with only the feed adjusted to an arbitrary Quad Ridge Flared Horn (QRFH) design. The analysis is performed using a PO simulation technique, which neglects mutual coupling effects between the feed and the reflector. The back radiation and sidelobes of the QRFH, compared to a Gaussian feed, increases the spillover non-ideal effect. This occurs, because the sidelobes and backlobe interferes with the radiation pattern, which increases the ripple seen in the ANT. The spillover is especially noticeable, when viewing M_{TbUS} of both cases. In the case of the Gaussian feed, the radiation outside the main beam is lower than in the case of the QRFH, which confirms the increased spillover.

4.4.10 Strategies for rapid ANT approximation effect on ANT

Recall that in subsection 4.2.1 a strategy for rapid ANT approximation was discussed. This strategy [24], uses a masking technique to accelerate the calculation of the ANT by using approximations. To account for diffraction effects, not included through the masking technique, simulations have to be performed. These simulations include the far-field radiation pattern of the full reflector system (which includes the primary reflector), at up to three frequencies, uniformly separated over the band. Usually only the lowest frequency is simulated. Using the simulated data, the strategy then adjusts the background noise temperature, in the direction of the main beam, to change the ANT over frequency. It is adjusted until the ANT at the simulated frequencies, match

Stellenbosch University https://scholar.sun.ac.za

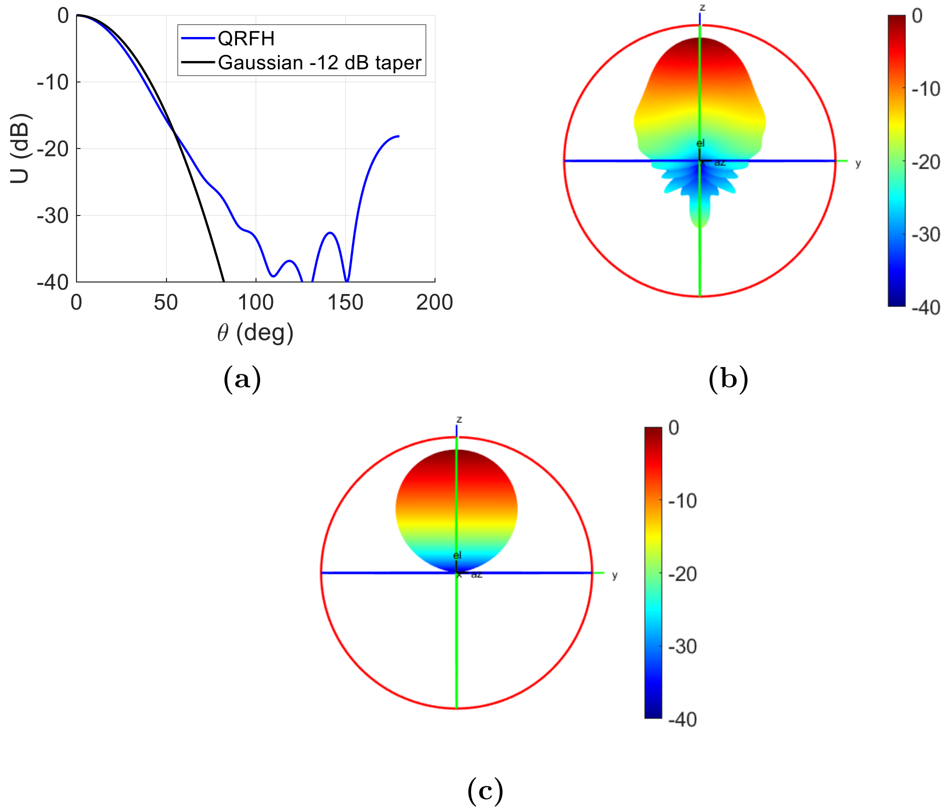

Figure 4.85: The normalised radiation intensity of an arbitrary QRFH feed is compared to a Gaussian feed. In (a) the radiation intensity is plotted in 2D, and in (b) it is plotted in 3D, for both feeds. It can clearly be seen that the QRFH has back radiation and sidelobes, where the Gaussian pattern does not

the ANT calculated through the simulated data.

Part of the success of this strategy is due to the power law base form of the ANT. Remember, the base form refers to the form of the ANT, without its ripple included. This allows the ANT to be relatively accurately predicted, from only a few simulated frequencies, as a power law requires only a few points to be accurately described. The power law, however, is more accurately described if a few frequencies are simulated, instead of only one. The ANT can thus be predicted from simulating the radiation pattern of the full reflector system at a single frequency, however, using three will increase the accuracy of the predicted ANT.

While the mathematics is described fully in 4.2.1, a summary of the method to correct the ANT approximation by using simulations is provided, as it is central to the discussion in this subsection. The correction method changes the sky temperature in the pointing direction, to correct the approximated ANT, to the validation ANT, at a certain number of frequencies. A power

Stellenbosch University https://scholar.sun.ac.za

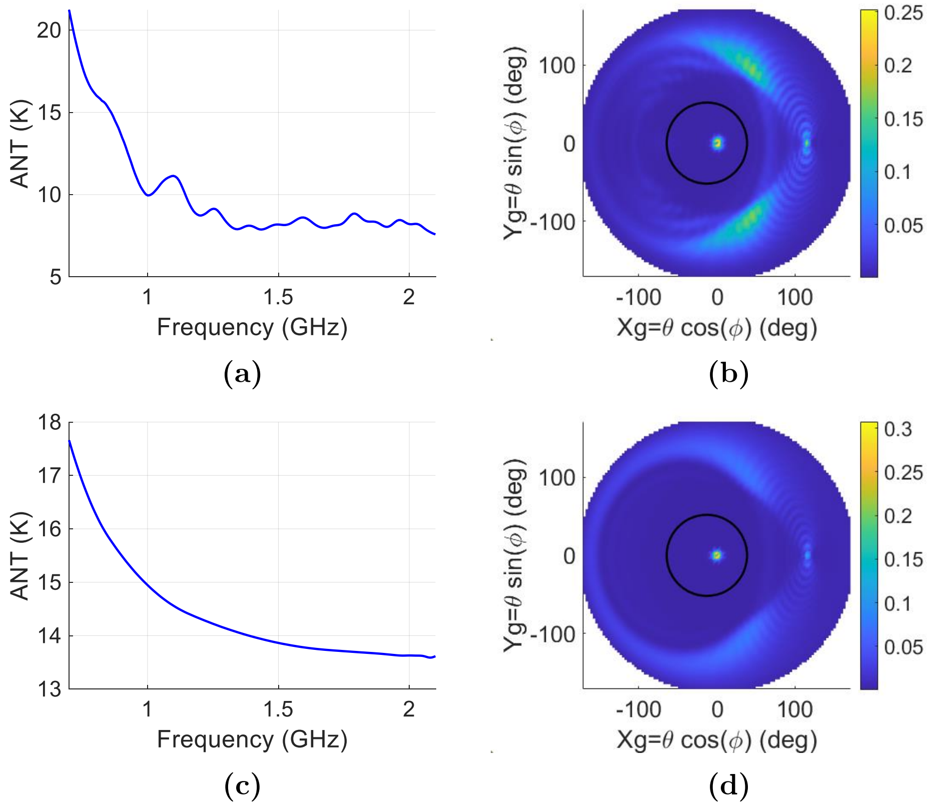

Figure 4.86: The low ripple case is compared to a similar situation, with only the feed adjusted to an arbitrary Quad Ridge Flared Horn (QRFH) design. The analysis is performed using a PO simulation technique, which neglects mutual coupling effects between the feed and the reflector. In (a) the ANT is shown, when using a QRFH design. In (b) $M_{\mathrm{TbUS_{LQ}}}$ is shown, when using a QRFH design. In (c) the ANT is shown, when using a Gaussian feed. In (d) $M_{\mathrm{TbUS_{LR}}}$ is shown, when using a Gaussian feed. It is shown for the zenith tipping angle. In this case, an offset single reflector is simulated, with a projected aperture diameter of 5 m, an $\frac{F}{D}=0.4$ and an $\frac{H}{D}=0.5$. A -12 dB edge taper Gaussian feed is used, and there are no support struts

law is then applied to generate correction factors over the rest of the band, using interpolation and extrapolation. The correction factor application can be defined as,

$$T_{\alpha}(f,\theta_p) = [1-\alpha(f,\theta_p)]T_{\mathrm{r}}(f,\theta_p) + \alpha(f,\theta_p)T_{\mathrm{d}}(f,\theta_p), \tag{4.43}$$

where $T_{\alpha}(f,\theta_p)$ represents the temperature allocated to the masked region. The masked region refers to a concept introduced by the masking technique. The masking technique uses ray tracing from the feed position to predict where most of the energy will radiate, by calculating the reflection of the rays through the reflecting surfaces, without simulating these surfaces. The masked region is defined as the angles in which rays have successfully reflected through all the excluded reflectors. The sky temperature in the main beam direction is

Stellenbosch University https://scholar.sun.ac.za

$T_{\mathrm{r}}(f,\theta_p) = T_{\mathrm{b}}(f,\theta_p)$, and behind the reflector is $T_{\mathrm{d}}(f,\theta_p) = T_{\mathrm{b}}(f,\theta_d)$, where $\theta_d = \theta_p + \pi$ (wrapped). The correction factor calculation can be defined for any $m \in 0,1,2$ and $n \in 1,2$ as,

$$\alpha_{\mathrm{mn}}(f,\theta_p) = \frac{T_{\mathrm{A}m}(f)I_{\mathrm{tn}}(f) - I_{\mathrm{wn}}(f,\theta_p) - I_{\mathrm{rn}}(f,\theta_p)}{I_{\mathrm{dn}}(f,\theta_p) - I_{\mathrm{rn}}(f,\theta_p)}, \tag{4.44}$$

where the goal is to calculate a correction factor that sets the approximated temperature equal to a temperature calculated from a more accurate approximation, at a specified number of frequency samples, f_i. To do this, it requires $T_{\mathrm{A}m}(f_i,\theta_p) = T_{\mathrm{A}n}(f_i,\theta_p)$, where m is a more accurate approximation compared to n, thus $m < n$. Each integral in (4.44) is defined as,

$$I_{\mathrm{tn}}(f) = \iint_{4\pi} U_n(f,\Omega_n)\sin\theta_n d\Omega_n, \tag{4.45}$$

$$I_{\mathrm{wn}}(f,\theta_p) = \iint_{4\pi} W_n(\Omega_n)T_{\mathrm{b}}(f,\theta_p)U_n(f,\Omega_n)\sin\theta_n d\Omega_n, \tag{4.46}$$

$$I_{\mathrm{rn}}(f,\theta_p) = \iint_{4\pi} M_n(\Omega_n)T_{\mathrm{r}}(f,\theta_p)U_n(f,\Omega_n)\sin\theta_n d\Omega_n, \tag{4.47}$$

$$I_{\mathrm{dn}}(f,\theta_p) = \iint_{4\pi} M_n(\Omega_n)T_{\mathrm{d}}(f,\theta_p)U_n(f,\Omega_n)\sin\theta_n d\Omega_n, \tag{4.48}$$

where $M_n(\Omega_n)$ is,

$$M_1(\Omega_1) = \begin{cases} 1 & \text{rays intercept the primary reflector} \\ 0 & \text{rays miss the primary reflector,} \end{cases} \tag{4.49}$$

for a single reflection approximation where $n = 1$, and

$$M_2(\Omega_2) = \begin{cases} 1 & \text{rays intercept both reflectors} \\ 0 & \text{rays miss one or both reflectors,} \end{cases} \tag{4.50}$$

for a dual reflection approximation where $n = 2$. A reflection approximation refers to the application of the masking technique. If a single reflector is excluded from simulation, then a single reflection approximation, where $n = 1$, is performed. When both reflectors are excluded, a dual reflection approximation, where $n = 2$, is performed. Furthermore, $W_n(\Omega_n) = 1 - M_n(\Omega_n)$, where $\Omega_n = \theta_n, \phi_n$ is defined for each ANT approximation in the global coordinate system. Finally, $U_n(f,\Omega_n)$ for a single reflection approximation $U_1(f,\Omega_1)$, is the radiation intensity from the feed illuminating only the subreflector, defined in the global coordinate system. For a dual reflection approximation $U_2(f,\Omega_2)$, it is radiation intensity of the feed, defined in the feed coordinate system.

Two levels of approximation is available in the case where a single reflection approximation, and a dual reflection approximation is available. A single

Stellenbosch University https://scholar.sun.ac.za

reflection approximation can be calculated when simulations of the far-field radiation pattern of the reflector system, excluding the primary reflector, is performed. A dual reflection approximation is available, when simulations of the radiation pattern, excluding the primary reflector and subreflector, is performed, which is simply the feed pattern.

When two levels of approximation is available, an efficient strategy to correct the ANT involves simulating the validation ANT, T_{A0}, at the lowest frequency in the band. Then simulating T_{A1} at three uniformly spaced frequencies over the band, and T_{A2} at all frequencies where the feed is available. Using the simulated data, two levels of correction can be performed. This includes correcting T_{A1} to T_{A0} at one frequency and using a power law extrapolation for the other frequencies. Then correcting T_{A2} to the corrected T_{A1}, at three frequencies, with a polynomial power law interpolation for the other frequencies. Instead of using only T_{A0} at the lowest frequency, it can instead be simulated at three uniformly spaced frequencies over the band, to increase the modeling accuracy, which is investigated next.

It is somewhat intuitive that a larger modeling error will occur when only a single frequency is simulated for the radiation pattern of the full reflector system to calculate T_{A0}, when approximating the ANT, instead of simulating three frequencies to calculate T_{A0}. The modeling error from using only a single frequency, however, is influenced by a larger degree from others factors, such as the feed taper, compared to using three frequencies. Only the effect of the feed taper will be investigated, for brevity.

In Fig. 4.87, the modeling error when using a single full radiation pattern simulation is compared to the error when using three instead, especially in regards to the impact of factors such as the feed taper on this error. In this case the standard reflector setup is used, except the Gaussian feed is changed to a -16 dB taper, instead of the standard -12 dB taper. All results are shown for the zenith tipping angle. In Fig. 4.87a the ANT is shown, where the solid lines indicate the validation high-fidelity ANT, and the dashed lines the low-fidelity approximation. The approximation is calculated using only a single full radiation pattern simulation, at the lowest frequency, using the strategy. The frequencies where the full radiation pattern was simulated, is shown through the circles. In Fig. 4.87b the ripple is shown. In Fig. 4.87c the approximation is calculated using three full radiation pattern simulations, uniformly spaced over the band. In Fig. 4.87d the ripple is shown from Fig. 4.87c.

From Fig. 4.87a and Fig. 4.87b, the ANT modelling error is higher for the -16 dB taper, compared to the -12 dB taper. In Fig. 4.87c and Fig. 4.87d, the modelling error difference between using a -16 dB taper, compared to the -12 dB taper, is less impactful. Thus, there is less of an impact from other

Stellenbosch University https://scholar.sun.ac.za

factors, such as the feed taper, when using three frequency simulations of full radiation pattern. Furthermore, the general modelling error when is also less when using three frequency simulations, as seen from the comparison of Fig. 4.87b and Fig. 4.87c. From this, it is recommended to use at least three full radiation pattern simulations.

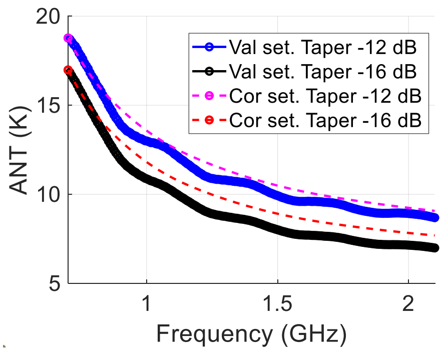

(a)

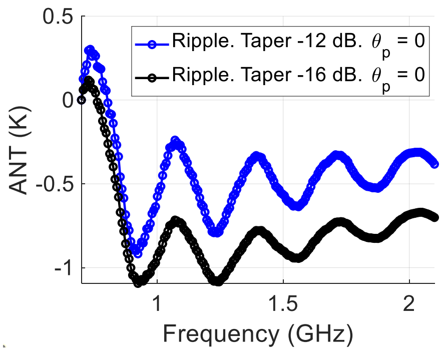

(b)

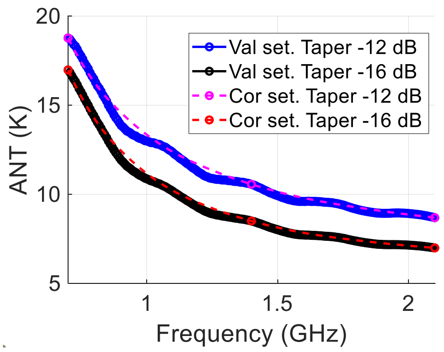

(c)

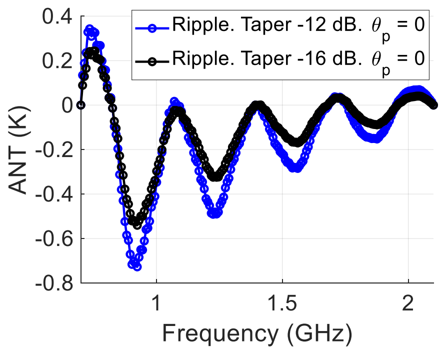

(d)

Figure 4.87: In this case the standard reflector setup is used, except the Gaussian feed is changed to a -16 dB taper, instead of the standard -12 dB taper. All results are shown for the zenith tipping angle. In (a) the ANT is shown, where the solid lines indicate the validation high-fidelity ANT, and the dashed lines the low-fidelity approximation. The approximation is calculated using only a single full radiation pattern simulation, at the lowest frequency, using the strategy. The frequencies where the full radiation pattern was simulated, is shown through the circles. In (b) the ripple is shown. In (c) the approximation is calculated using three full radiation pattern simulations, uniformly spaced over the band. In (d) the ripple is shown from (c)

Stellenbosch University https://scholar.sun.ac.za

4.4.11 Impacts of many other causes

Clearly the examples shown up to now are simplifications of actual reflector systems, and several effects have not been considered. Chief among these effects are the influence of the supporting structure of the feed, and the coupling between the feed and reflector. These have been discussed in literature [45],[46],[47],[48],[49] and thus omitted here for clarity.

Furthermore, a physical feed antenna could be mismatched to the receiver, which is ignored during this dissertation. The standing wave between the reflector and the feed will cause additional currents on the feed antenna, which changes its impedance, and is especially more noticeable when using a prime-focused reflector. This impedance change causes additional mismatches to the receiver, which leads to an impedance ripple, and by extension a ripple in the receiver noise temperature [50]. This can cause additional ripple effects in the sensitivity. The sensitivity will be discussed in the next chapter.

A shield can also be positioned around the edge of a reflector, to prevent feed spillover into the ground, which will lower the ANT. Furthermore, subreflector extensions will also influence the ANT ripple. It will increase the size of the subreflector, while also protecting the feed spillover from the hot ground. This will reduce the ripple on the ANT. Instead of considering all these effects, the work in this dissertation focused more on the general effects of interference, and how they relate to frequency ripple behaviour in ANT.

4.5 Conclusion

In this chapter it was confirmed that the radiation pattern ripple is responsible for the ripple in the ANT. Furthermore, certain directions are more important than others in the calculation of the ANT ripple, for each specific pointing angle. The ANT integral can also be calculated using a summation process over a heatmap, which is explained in more detail in Appendix A. Furthermore, in Appendix A it is proven that the angular resolution used for the full radiation pattern, in this dissertation, is high enough for the ANT integral to converge.

Tools were developed to extract the ripple from the radiation pattern. The extracted ripple was investigated using heatmaps, to characterise the impact of the pointing angle on the ANT ripple, and also confirm the radiation pattern ripple causes the ANT ripple. Finally, the effect on the ANT and its ripple in various cases in section 4.4 were investigated and characterised, using the tools developed in this dissertation. The examples shown in section 4.4 are simplifications of actual reflector systems, and several effects have not been

Stellenbosch University https://scholar.sun.ac.za

considered. Some of these effects are discussed in subsection 4.4.11. This work instead focused more on the general effects of interference, and how they relate to frequency ripple behaviour in ANT.

From these previous investigations, and the practical considerations, it is apparent that the ANT ripple is a function of many factors. This raises the model complexity of the ANT ripple significantly and increases the difficulty of creating a simple and relatively accurate model of it. Creating fast and efficient models of the ANT, is key in strategies used for rapid sensitivity approximation. Next, the impact of the ANT ripple on the sensitivity will be discussed.

Stellenbosch University https://scholar.sun.ac.za

Chapter 5

Characterization of receiver sensitivity ripple

In this chapter the implication of ripple in the ANT on the sensitivity will be shown. Additionally, the effect of the aperture efficiency ripple (AE) on the sensitivity will also be investigated. Many of the concepts reported in this chapter, has already been published in [51].

5.1 Sensitivity

Radio astronomy projects currently being planned or developed, including the SKA [52], DSA-2000 [53], and next generation Very Large Array (ngVLA) [54], are all planned for ambitious science goals. This requires radio telescopes that are designed and optimised for maximum performance, and thus their design requires a careful consideration of the important figures of merit (FoM). The receiving sensitivity is a primary FoM that is often maximised [51].

Sensitivity relates to a radio telescopes signal-to-noise ratio (SNR) available for observation [55]. This sensitivity is generally expressed in system equivalent flux density (SEFD) and can be determined as follows [56],

$$\mathrm{SEFD} = \frac{2k_B T_{\mathrm{sys}}}{A_{\mathrm{eff}}}, \tag{5.1}$$

where the total system noise temperature is denoted as T_{sys} and finally the effective reflector area is A_{eff}. The system noise temperature, denoted as T_{sys}, represents the total noise in a receiver system. The system noise temperature for a single-pixel receiver can be determined from [1],

$$T_{\mathrm{sys}} = \eta_{\mathrm{rad}} T_{\mathrm{A}} + (1 - \eta_{\mathrm{rad}}) T_{\mathrm{phy}} + T_{\mathrm{rec}}, \tag{5.2}$$

Stellenbosch University https://scholar.sun.ac.za

where the receiver noise temperature is denoted as T_{rec}, the physical antenna temperature is T_{phy}, the ANT is T_{A} and finally the antenna radiation efficiency is denoted as η_{rad}. The receiver noise temperature also includes the noise contributions from the receiver components such as low-noise amplifiers (LNAs), couplers for calibration and possible bandpass-filters as seen in the Fig. 5.1. The receiver noise temperature additionally includes potential mismatches. The noise contribution, from brightness sources surrounding the reflector system, to the system temperature is represented by the ANT, T_{A}.

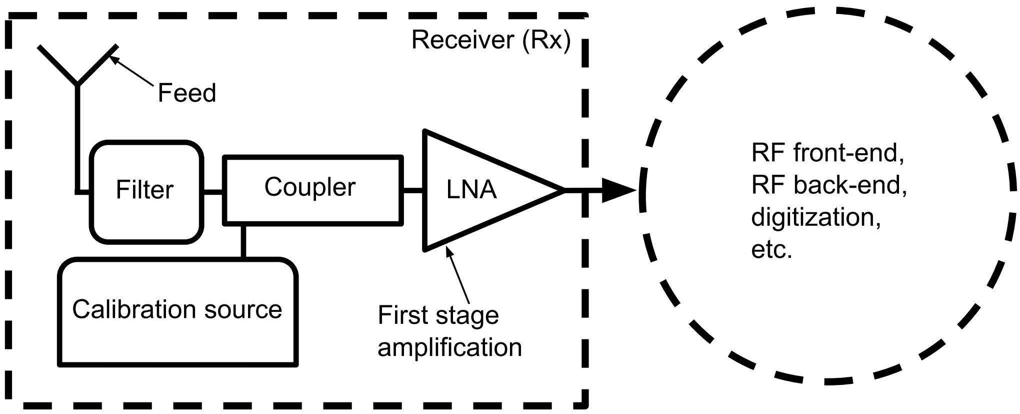

Figure 5.1: The general receiver chain

The effective area of the reflector, A_{eff}, describes how well the physical projected area of a reflector, A_{phy}, is being illuminated. The effective area can be calculated according to

$$A_{\text{eff}} = \eta_{\text{loss}}\eta_{\text{ap}}A_{\text{phy}}, \tag{5.3}$$

where η_{ap} represents the AE of the reflector system [57]. The losses in the reflector system is denoted by η_{loss}. Surface error, jitter in pointing, transparency losses in the reflector, blockage, dielectric losses and ohmic losses are some of the sub-efficiencies that make up the combined factor η_{loss}. These

Stellenbosch University https://scholar.sun.ac.za

losses are strong functions of the reflector structure and system and can thus vary greatly [58]. An example of this is how offset reflectors can have almost no blockage. System specifications are generally given with a specific AE that has a determined margin that accounts for η_{loss}.

The physical projected area of a reflector, A_{phy}, can be calculated as,

$$A_{\text{phy}} = \frac{\pi D^2}{4}, \tag{5.4}$$

where D is the aperture diameter of the antenna.

The AE of a reflector can be approximated with [59],

$$\eta_{\text{f}}(f) = \eta_{\text{BOR1}}\eta_{\text{ill}}\eta_{\text{sp}}\eta_{\text{pol}}\eta_{\text{ph}}\eta_{\text{st}}\eta_{\text{ab}}\eta_{\text{d}}, \tag{5.5}$$

where each of these sub-efficiencies will be described in detail, shortly. This formulation of the AE is known as the feed efficiency, η_{f}, [59]. This is because these sub-efficiencies can be determined from the feed pattern. To calculate the feed efficiency, a description of the reflector geometry is still required. It is not entirely accurate, as it can not include the ripple from the full radiation pattern, as thus serves as a first order approximation of the AE. This can also be regarded as the low-fidelity approximation of the AE. Despite this limitation, this approximation has been shown to yield fairly accurate results in many cases, $\eta_{\text{f}} \approx \eta_{\text{ap}}$.

To calculate the low-fidelity approximation of the AE, the feed radiation pattern needs to be known. The feed far-field pattern can be described as [31],

$$\bar{E}(r,\theta,\phi) = \frac{1}{r}e^{-jkr}\bar{G}(\theta,\phi), \tag{5.6}$$

where r is the distance from the feed phase centre, to an observational point in the far-field radiation pattern $\bar{G}(\theta,\phi)$. The radiation pattern, $\bar{G}(\theta,\phi)$, can further be expanded to,

$$\bar{G}(\theta,\phi) = G_\theta(\theta,\phi)\hat{\theta} + G_\phi(\theta,\phi)\hat{\phi}. \tag{5.7}$$

The first sub-efficiency, η_{BOR1}, is the Body Of Revolution Type 1 (BOR1) (azimuth mode) efficiency. It is an efficiency regarding the rotational symmetry of the feed pattern. The feed pattern is periodic in its azimuth angle, ϕ, and can be expanded using a Fourier series expansion. This expansion factorises the feed pattern into azimuth modes. The BOR1 efficiency can be calculated by determining the ratio of the power in the first-order azimuth mode, compared to the total radiated power from the feed [60] as,

Stellenbosch University https://scholar.sun.ac.za

$$\eta_{\text{BOR1}} = \frac{\iint_{4\pi}(|\bar{G}_{\theta 1}|^2 + |\bar{G}_{\phi 1}|^2)\sin\theta d\Omega}{\iint_{4\pi}(|\bar{G}_{\theta}(\Omega)|^2 + |\bar{G}_{\phi}(\Omega)|^2)\sin\theta d\Omega}, \tag{5.8}$$

where the first-order azimuth modes are denoted by $\bar{G}_{\theta 1}$ and $\bar{G}_{\phi 1}$. These modes can be calculated from a Fourier expansion in ϕ of the feed pattern as,

$$G_{\theta 1}(\theta,\phi) = A_1(\theta)\sin\phi + B_1(\theta)\cos\phi, \tag{5.9}$$

$$G_{\phi 1}(\theta,\phi) = C_1(\theta)\cos\phi - D_1(\theta)\sin\phi. \tag{5.10}$$

The Fourier coefficients can be calculated from the inverse fast Fourier transform (IFFT) as,

$$A_1(\theta) = \frac{2}{N}\sum_{k=0}^{N-1} G_\theta\left(\theta, k\frac{2\pi}{N}\right)\sin\left(k\frac{2\pi}{N}\right), \tag{5.11}$$

$$B_1(\theta) = \frac{2}{N}\sum_{k=0}^{N-1} G_\theta\left(\theta, k\frac{2\pi}{N}\right)\cos\left(k\frac{2\pi}{N}\right), \tag{5.12}$$

$$C_1(\theta) = \frac{2}{N}\sum_{k=0}^{N-1} G_\phi\left(\theta, k\frac{2\pi}{N}\right)\cos\left(k\frac{2\pi}{N}\right), \tag{5.13}$$

$$D_1(\theta) = \frac{2}{N}\sum_{k=0}^{N-1} G_\phi\left(\theta, k\frac{2\pi}{N}\right)\sin\left(k\frac{2\pi}{N}\right). \tag{5.14}$$

Furthermore, a dual polarised antenna is implied when the BOR1 efficiency is calculated. The y-polarisation can be described as,

$$\bar{E}_y(r,\theta,\phi) = \frac{1}{r}e^{-jkr}(A_1(\theta)\sin(\phi)\hat{\theta} + C_1(\theta)\cos(\phi)\hat{\phi}), \tag{5.15}$$

and the x-polarisation as,

$$\bar{E}_x(r,\theta,\phi) = \frac{1}{r}e^{-jkr}(B_1(\theta)\cos(\phi)\hat{\theta} - D_1(\theta)\sin(\phi)\hat{\phi}). \tag{5.16}$$

By using Ludwig's third definition [61], $\bar{E}_y(r,\theta,\phi)$ can be expressed in its co- and cross-polar components as,

$$\text{CO}_y(\theta) = \frac{A_1(\theta) + C_1(\theta)}{2}, \tag{5.17}$$

$$\text{XP}_y(\theta) = \frac{A_1(\theta) - C_1(\theta)}{2}. \tag{5.18}$$

The same process can be applied to $\bar{E}_x(r,\theta,\phi)$, to provide the co- and cross-polar components as,

Stellenbosch University https://scholar.sun.ac.za

$$\mathrm{CO}_x(\theta) = \frac{D_1(\theta) + B_1(\theta)}{2}, \tag{5.19}$$

$$\mathrm{XP}_x(\theta) = \frac{D_1(\theta) - B_1(\theta)}{2}. \tag{5.20}$$

A BOR1 type feed can have its co- and cross-polar components fully described, using only the $\phi = 45°$ plane, as described in [32]. In short, the far-field function for a y-polarized BOR1 antenna is,

$$\mathbf{G}_y(\theta, \phi) = A_1(\theta) \sin\phi \hat{\boldsymbol{\theta}} + C_1(\theta) \cos\phi \hat{\boldsymbol{\phi}}, \tag{5.21}$$

where this form allows the construction of the entire far-field function from the E- and H-plane patterns only. Its co- and cross-polar far-field function can be described using Ludwig's third definition,

$$G_{\mathrm{co}}(\theta, \phi) = G_{\mathrm{co45°}}(\theta) - G_{\mathrm{xp45°}}(\theta) \cos(2\phi), \tag{5.22}$$

$$G_{\mathrm{xp}}(\theta, \phi) = G_{\mathrm{xp45°}}(\theta) \sin(2\phi), \tag{5.23}$$

with the co and cross-polar far-field function in the $\phi = 45°$ plane described as,

$$G_{\mathrm{co45°}}(\theta) = \frac{1}{2}(A_1(\theta) + C_1(\theta)), \tag{5.24}$$

$$G_{\mathrm{xp45°}}(\theta) = \frac{1}{2}(A_1(\theta) - C_1(\theta)). \tag{5.25}$$

The spillover efficiency, η_{sp}, quantifies the effect of feed spillover on the AE. Specifically, it involves calculating the power radiated within the taper angle of the feed, compared to total power radiated by the feed. As mentioned before, spillover is a non-ideal effect. It also reduces the AE, and increases the ANT. The spillover efficiency can be calculated as,

$$\eta_{\mathrm{sp}} = \frac{\int_{\theta_{\mathrm{e}}} (|\mathrm{CO}(\theta)|^2 + |\mathrm{XP}(\theta)|^2) \sin\theta d\theta}{\int_{\pi} (|\mathrm{CO}(\theta)|^2 + |\mathrm{XP}(\theta)|^2) \sin\theta d\theta}, \tag{5.26}$$

where θ_{e} is the feed taper angle, for a non-shaped system. The definitions provided in this chapter are for reflector systems with an equivalent parabola, also known as non-shaped systems. Ideally, the aperture field must be uniform in phase and amplitude (for maximum aperture directivity) with no energy spillover past the reflectors [62]. This is practically impossible, and the illumination efficiency, η_{ill}, determines the uniformity of the field amplitude distribution over the surface of the reflector. The illumination efficiency can be determined as,

Stellenbosch University https://scholar.sun.ac.za

$$\eta_{\mathrm{ill}} = 2\cot^2\left(\frac{\theta_{\mathrm{e}}}{2}\right)\frac{\left(\int_{\theta_{\mathrm{e}}}|\mathrm{CO}(\theta)|\tan\left(\frac{\theta}{2}\right)d\theta\right)^2}{\int_{\theta_{\mathrm{e}}}|\mathrm{CO}(\theta)|^2\sin\theta d\theta}. \tag{5.27}$$

Since it is impossible for a uniform distribution, with no spillover, a trade-off exists in the product of $\eta_{\mathrm{ill}}\eta_{\mathrm{sp}}$. This trade-off determines the uniformity of the illumination, compared to the amount of energy in spillover. If a system is designed only for large AE, η_{ap}, then the optimal edge taper-level at θ_{e} to achieve this is found as the highest value of the product $\eta_{\mathrm{ill}}\eta_{\mathrm{sp}}$. For a monotonic feed power pattern, the edge taper can be determined, when the taper angle is known, for the best trade-off. This will result in the highest AE contribution, from the product $\eta_{\mathrm{ill}}\eta_{\mathrm{sp}}$ [63].

The (cross) polarisation efficiency, η_{pol}, determines the amount of power radiated in the co-polar component, relative to the total power radiated, in the designed taper angle of the feed. The polarisation efficiency can be determined as,

$$\eta_{\mathrm{pol}} = \frac{\int_{\theta_{\mathrm{e}}}|\mathrm{CO}(\theta)|^2\sin\theta d\theta}{\int_{\theta_{\mathrm{e}}}(|\mathrm{CO}(\theta)|^2+|\mathrm{XP}(\theta)|^2)\sin\theta d\theta}, \tag{5.28}$$

The phase efficiency, η_{ph}, examines the uniformity of the phase distribution in the aperture plane, to determine the effect on the AE. The phase efficiency, η_{ph}, is correlated to the proximity of the phase center of the feed, relative to the focus point of the reflector. A higher phase efficiency is expected from a closer proximity. From this, the phase centre of the feed can be identified from the feed position which maximizes the phase efficiency. Additionally, the ideal situation includes a phase centre which is frequency independent, to yield a high phase efficiency over the entire band. The phase efficiency can be calculated as,

$$\eta_{\phi} = \frac{|\int_{\theta_{\mathrm{e}}}\mathrm{CO}(\theta)\tan\left(\frac{\theta}{2}\right)d\theta|^2}{(\int_{\theta_{\mathrm{e}}}|\mathrm{CO}(\theta)|\tan\left(\frac{\theta}{2}\right)d\theta)^2}. \tag{5.29}$$

The surface tolerance efficiency, η_{st}, accounts for errors in the surface. In this dissertation this efficiency will be disregarded, and chosen to be $\eta_{\mathrm{st}} = 1$, as the assumption is that the reflector surface is a perfect conic section. This efficiency accounts for manufacturing errors, and is out of the scope of this dissertation.

The aperture blockage efficiency, η_{ab}, accounts for physical reflector system components which blocks part of the aperture. This reduces AE. The aperture blockage efficiency, for rotationally symmetric antennas, can be calculated as,

Stellenbosch University https://scholar.sun.ac.za

$$\eta_{\text{ab}} = \left| 1 - C_b \left(\frac{d}{D} \right)^2 \right|^2, \tag{5.30}$$

where d is the blockage diameter, and C_b can be calculated as,

$$C_b = \frac{\tan^2\left(\frac{\theta_\text{e}}{2}\right)\text{CO}(0)}{\int_{\theta_\text{e}} \text{CO}(\theta)\tan\left(\frac{\theta}{2}\right)d\theta}. \tag{5.31}$$

This definition neglects the blockage from struts and is also not defined for offset systems. In this dissertation struts are neglected, and blockage efficiency for offset systems are assumed $\eta_{\text{ab}} = 1$, as it is expected to be minimal.

The diffraction efficiency, η_d, accounts for the diffraction losses, such as edge diffraction. For brevity, the diffraction efficiency is only defined for the offset Gregorian reflector case in this dissertation, as this is the reflector setup most investigated. In cases where other reflector types are used in the dissertation, an appropriate diffraction efficiency is used [64]. The diffraction efficiency can be calculated as,

$$\eta_\text{d} = \left| 1 + \frac{(j-1)\Delta\rho E_{\text{CO}}(\theta_\text{e})\sin\theta_\text{e}}{\sqrt{2\pi}D_m\sqrt{\eta_{\text{par}}}} \right|^2, \tag{5.32}$$

where in this case $E_{\text{CO}}(\theta_\text{e})$ is,

$$E_{\text{CO}}(\theta_\text{e}) = \sqrt{n+1}\cos^n\left(\frac{\theta_\text{e}}{2}\right), \tag{5.33}$$

as a theoretical radiation pattern is assumed, which approximates a Gaussian beam within the 10 dB beamwidth. It is useful to use this theoretical radiation pattern, instead of a Gaussian, so that a analytical solution can be derived for the diffraction efficiency. Furthermore, the diffraction efficiency will change if a physical feed is used, however, this diffraction efficiency serves as a good approximation. The approximated parabolic efficiency can be described as,

$$\eta_{\text{par}} = 4\cot^2\left(\frac{\theta_\text{e}}{2}\right)\left(1 - \cos^n\left(\frac{\theta_\text{e}}{2}\right)\right)^2\left(\frac{n+1}{n^2}\right), \tag{5.34}$$

where θ_e is the taper angle of the feed, n is,

$$n = \frac{|A_0|_{dB}}{-20\log\left(\cos\left(\frac{\theta_\text{e}}{2}\right)\right)}, \tag{5.35}$$

Stellenbosch University https://scholar.sun.ac.za

and $|A_0|_{dB}$ is,

$$|A_0|_{dB} = -20\log\left(|A_0|\right), \tag{5.36}$$

where A_0 is the amplitude taper of the feed pattern at θ_e,

$$A_0 = \frac{\mathrm{CO}(\theta_\mathrm{e})}{\mathrm{CO}(0)}. \tag{5.37}$$

Furthermore, $\Delta\rho$ can be described as,

$$\Delta\rho = \sqrt{\lambda\frac{(\rho_\mathrm{m}+\rho_\mathrm{s})}{\pi}\left|1-\frac{(\rho_\mathrm{m}+\rho_\mathrm{s})}{\rho_\mathrm{s}}\right|}, \tag{5.38}$$

with ρ_m and ρ_s described as,

$$\rho_\mathrm{m} = \sqrt{(Q_{0x})^2+(Q_{0y})^2+(Q_{0z})^2}, \tag{5.39}$$

$$\rho_\mathrm{s} = \sqrt{(P_{0x})^2+(P_{0y})^2+(P_{0z})^2}, \tag{5.40}$$

where Q_{0x}, Q_{0y}, and Q_{0z}, respectively represent the x, y, and z coordinate of the centre of the primary reflector, in the global coordinate system. Finally, P_{0x}, P_{0y}, and P_{0z}, respectively represent the x, y, and z coordinate, of the centre of the secondary reflector, in the global coordinate system.

The feed efficiency, η_f, described previously, is a low-fidelity approximation of the AE. This approximation does not include the ripple on the AE. The high-fidelity AE, which includes the ripple, can be calculated as [65],

$$\eta_\mathrm{ap}(f) = \frac{\lambda^2|\mathbf{G}_\mathrm{co}(f,0,0)|^2}{A_\mathrm{phy}\iint_{4\pi}U(f,\Omega)\mathrm{sin}\theta d\Omega}, \tag{5.41}$$

where the frequency is f, the direction of maximum radiation intensity is defined as $\Omega = (0,0)$ and the wavelength is λ. Furthermore, the projected aperture area is A_phy, and is determined through the design process and by the primary reflector size. The reflector system main beam co-polarisation component is defined by $\mathbf{G}_\mathrm{co}(f,0,0)$, through Ludwig's third definition [66]. The AE thus require the radiation pattern of the full reflector system in only one direction, instead of in all directions as is required for the ANT calculation. Finally, (5.41) can be used in (5.3) to determine the effective area of the

Stellenbosch University https://scholar.sun.ac.za

reflector, A_{eff}, when losses in the reflector system are neglected, $\eta_{\text{loss}} = 1$.

In [30] a method to accurately predict the AE ripple is provided, using a geometric argument approach. In summary, it suggests that the cause of the ripple is due to interference between the diffracted fields of the subreflector and the main beam of the primary reflector. By calculating the path length differences between the diffracted fields and the main beam, it is possible to predict this ripple component.

This technique works, because the AE ripple is due to one direction and narrowband, as can be seen in the FFT of this ripple in Fig. 5.2b. This means that the single geometric argument predicting ripple in that direction is enough to characterise the ripple adequately, unlike the case for the ANT ripple prediction. Modeling the ripple of the AE is thus significantly easier than modeling the ripple of the ANT.

In Fig. 5.2a the high-fidelity efficiency response, η_{ap} in (5.41) and the feed efficiency, η_{f}, as calculated in [59] is shown. The ripple can be extracted by taking the difference between them.

From Fig. 5.2a, it can be observed that the diffraction efficiency, η_{d}, is correlated to the ripple amplitude. A lower diffraction efficiency, occurring at the lower frequencies, leads to a larger ripple amplitude. Conversely, the amplitude of the ripple decreases, as the diffraction efficiency increases with higher frequencies. The diffraction efficiency, η_{d}, can be calculated using the methods in [67] or as described in the dissertation. The AE ripple thus reduces as the electrical size of the reflector increases.

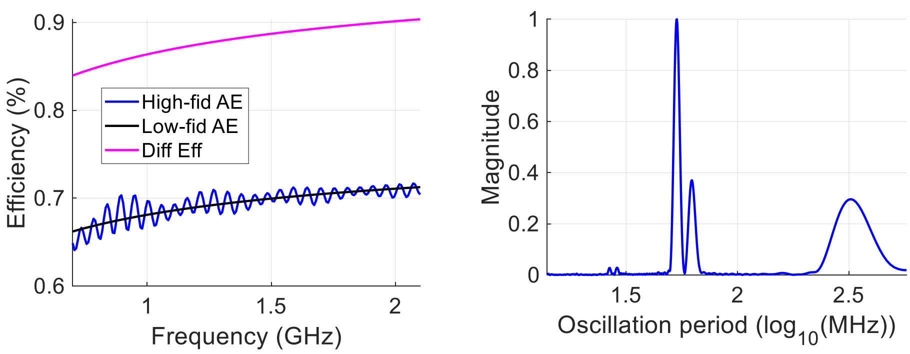

(a) (b)

Figure 5.2: The low-fidelity approximation (feed efficiency) is compared to the high-fidelity AE from (5.41) in (a), with the diffraction sub-efficiency also displayed. A normalised magnitude FFT of the high-fidelity AE ripple is shown on a linear-log scale in (b), to illustrate the response being relatively band limited

Stellenbosch University https://scholar.sun.ac.za

The sensitivity calculation can be refined more. The signal-to-noise ratio (SNR) can be calculated using the equation below,

$$\mathrm{SNR} = \frac{S_\mathrm{v}\sqrt{t\Delta v}}{\mathrm{SEFD}}, \tag{5.42}$$

where the available bandwidth is Δv and the integration time is denoted as t. The integration time refers to the time in seconds over which the signal is measured. Thus to achieve a higher SNR, which means lower RMS fluctuation, SEFD has to be minimized. This also results in needing shorter integration time for detection. When the available bandwidth, Δv, in the receiver is increased, it also reduces the integration time needed for detection and increases the signal-to-noise ratio. Occasionally, the sensitivity is expressed as $\frac{A_\mathrm{eff}}{T_\mathrm{sys}}$ in the units of $\mathrm{m}^2\mathrm{K}^{-1}$. This form is just (5.1) rewritten as,

$$\frac{A_\mathrm{eff}}{T_\mathrm{sys}} = \frac{2k_B}{\mathrm{SEFD}}. \tag{5.43}$$

To simplify for proportional expressions of array sensitivity, the SKA project selected this notation as expressed in (5.43). Notably, from both (5.1) as well as (5.43), the effective area A_eff is included. This has the implication that increasing the size (or efficiency) of the reflector would yield a higher sensitivity. In certain cases the reflector area is not even included in the comparison of the sensitivity of different receiver systems by using the ratio $\frac{T_\mathrm{sys}}{\eta_\mathrm{ap}}$ to compare.

Sensitivity, in this dissertation, is defined as a ratio of the effective aperture area to the system noise temperature as,

$$\text{sensitivity} = \frac{A_\mathrm{eff}}{T_\mathrm{sys}} = \frac{\eta_\mathrm{ap}A_\mathrm{phy}}{T_\mathrm{A} + T_\mathrm{rec}}, \tag{5.44}$$

where η_ap represents the AE, A_phy is the main-reflector physical projected aperture area and their product describes how effective the aperture area is being used. T_A is the ANT and T_rec denotes the receiver noise temperature.

In many cases, and in this dissertation, the system noise temperature is simplified as $T_\mathrm{sys} = T_\mathrm{A} + T_\mathrm{rec}$, where the antenna radiation efficiency $\eta_\mathrm{rad} = 1$. It is known that the ANT, T_A, will have a ripple over frequency. The receiver temperature T_rec is often considered as constant, and in this dissertation T_rec is simplified to a constant contribution from only the LNA, and can thus not have a ripple. It is possible for the LNA to introduce a ripple, if the antenna and LNA is not well matched, but this situation is not investigated in this dissertation. The physical projected aperture area does also not contribute to the ripple, as it is a constant and not a function of frequency.

Stellenbosch University https://scholar.sun.ac.za

It is thus only the AE ripple and the ANT ripple that can contribute to the ripple in the sensitivity, and the sensitivity ripple is the quotient of the AE ripple over the ANT ripple. The impact of the AE ripple and ANT ripple on the sensitivity will be investigated and discussed next.

5.2 Ripple impact on sensitivity

To keep the discussion tractable, it is first performed for the standard case, while the other parameters remain constant. The high-fidelity approximation of the sensitivity, M_{H}, is compared to the low-fidelity approximation, M_{L}. M_{H} calculates the sensitivity using the validation data, $\boldsymbol{\upsilon}$, where M_{L} calculates the sensitivity using first order approximations of AE and ANT.

A 7 K receiver noise temperature, T_{rec}, is assumed. High quality modern LNA temperatures can be as low as 7 K at ambient temperatures where they are not cryogenically cooled [68]. The resulting receiving sensitivity calculations are shown in Fig. 5.3. The sensitivity calculation was done on the standard reflector setup, and the sensitivity ripple looks similar to the AE ripple in Fig. 5.2a, so it is largely dominated by it.

The error function over frequency for each pointing angle is calculated as,

$$\mathrm{Error} = 100\left(\frac{|M_{\mathrm{H}} - M_{\mathrm{L}}|}{M_{\mathrm{H}}}\right), \tag{5.45}$$

and it is shown in Fig. 5.4.

The largest error of about 8% occurs at the zenith pointing angle. This pointing angle also has the highest mean error of 2.76% over frequency. The other 2 pointing angles have a 1.10% and 1.22% mean error, respectively. Thus, the total mean error over all pointing angles is about 1.70%.

The calculation time for the standard case, using the same PC setup described in Chapter 4, is described next. This is done to give an indication of the relative computation time, between the high-fidelity and low-fidelity sensitivity calculation. The calculation time is separated into the time required for simulations involving GRASP, which will be discussed first, followed by the time required to use this simulated data to calculate the sensitivity.

The calculation time for the high-fidelity set is dominated by the total PO full field calculation, which required 1 hour, 36 minutes, 19 seconds. It is followed by the feed radiation calculation time of 18 minutes, 28 seconds, which is also required for the low-fidelity set, over 201 frequency points. For the low-fidelity

Stellenbosch University https://scholar.sun.ac.za

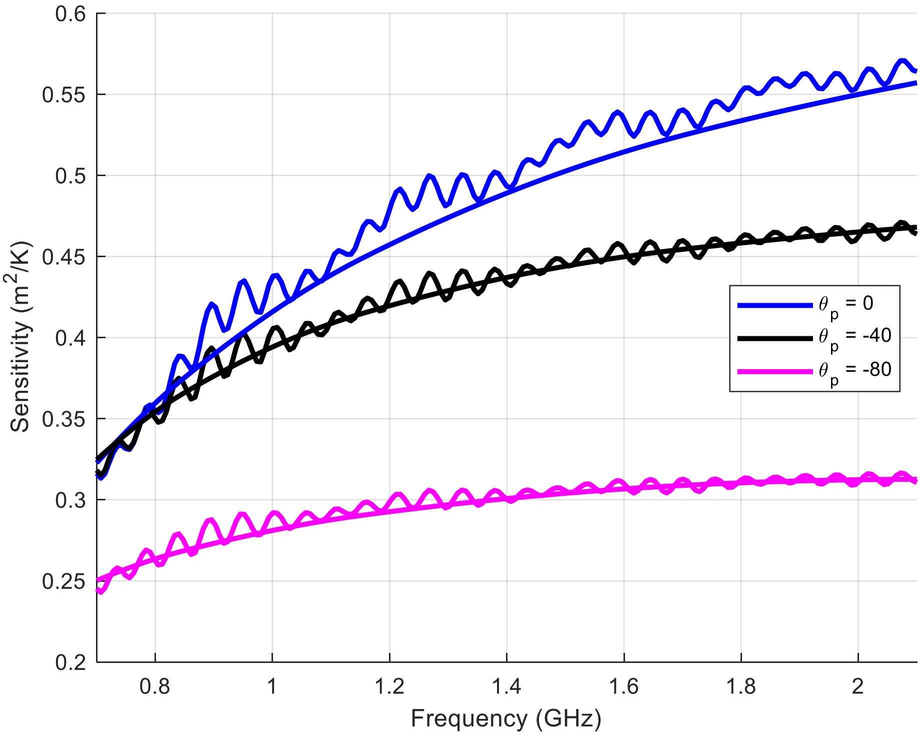

Figure 5.3: The high-fidelity approximation is compared to the low-fidelity approximation, for the receiving sensitivity, over three pointing angles. The rapidly varying solid lines display the high-fidelity approximation. The slowly varying solid lines display the low-fidelity approximation, which excludes the ripple

set, the full field at a single frequency point required 17.9 seconds, and the mask at three frequency points required 10.51 seconds. The combined simulation time required for the high-fidelity set is 1 hour, 54 minutes, 47 seconds. The combined simulation time required for the low-fidelity set is 18 minutes, 56.4 seconds. The high-fidelity simulation time requires more than six times as long to complete.

The calculation of the sensitivity using the simulated data is much faster, compared to the time spent creating the simulated data, for both the high- and low-fidelity cases. The sensitivity is calculated using (5.44), which includes calculating the ANT using the simulated data. The low-fidelity ANT also has to be created using masks, and be corrected, as described in Chapter 4. The high-fidelity sensitivity requires 39.26 seconds to calculate, and the low-fidelity requires 79.7 seconds to calculate. It is expected that the low-fidelity set will require more time due to the masking and correction processes. In any case, these calculation times are negligible compared to the simulation time required.

From Fig. 4.80 in Chapter 4, it is apparent that for larger reflectors, the to-

Stellenbosch University https://scholar.sun.ac.za

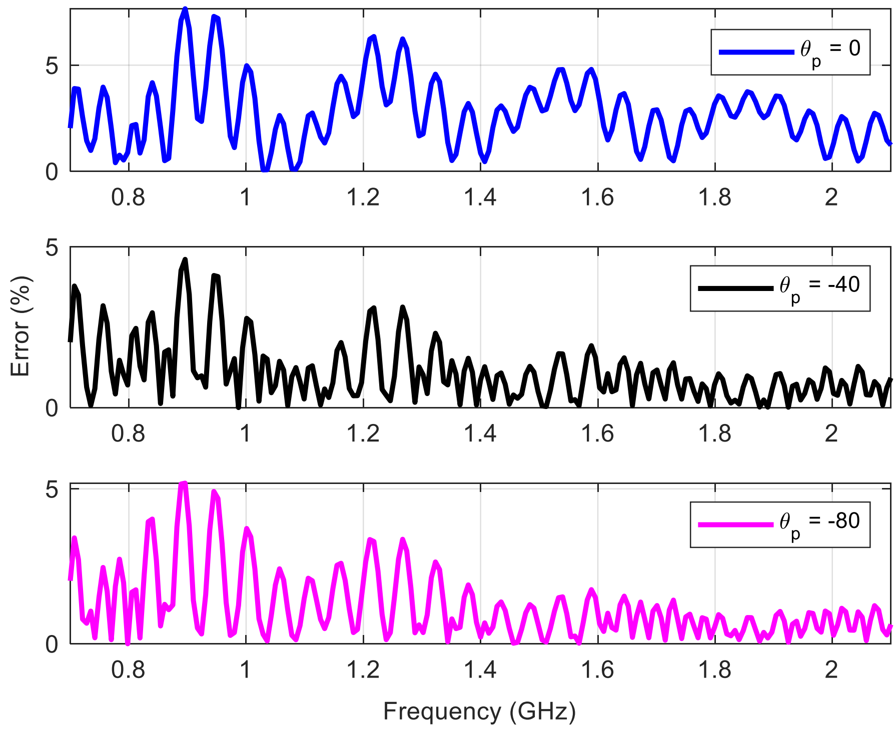

Figure 5.4: The error function as similarly calculated in (5.45), is shown over frequency for each pointing angle, and is used to compare the low- and high-fidelity set of the sensitivity

tal full field PO calculation time scales significantly. In turn, the calculation time ratio will rise significantly. A 1.70% average error, is relatively low for such a cold receiver. The reduction in calculation time, due to the low-fidelity approximation of the sensitivity requiring only a few simulations, is likely a worthwhile trade-off in the optimisation phase for losing 1.70% in accuracy.

Recall that the ripple is worse for electrically smaller reflectors. As the reflector becomes electrically larger these errors will also become smaller, and the sensitivity will be even more accurate if the ripple is ignored. The effect the receiver noise temperature has on the AE ripple and ANT ripple, and their respective impact on the sensitivity ripple, is discussed next.

Assume that the error on the sensitivity of not modeling a specific ripple is found through subtracting the full ripple including set R_{include}, from the ripple excluding set R_{exclude}, and then normalising to the full set as,

$$\text{Error}_{\text{comp}} = \frac{R_{\text{include}} - R_{\text{exclude}}}{R_{\text{include}}}. \tag{5.46}$$

Note that this is a general form for the error calculation, and the specific form

Stellenbosch University https://scholar.sun.ac.za

of R_{include} and R_{exclude} will differ, depending on the context. The error on the sensitivity of not modeling the ripple in the AE can then be calculated as follows,

$$\text{Error}_{\text{AE}} = \frac{\frac{A_{\text{e}}A_{\text{phy}}}{T_{\text{A}}+T_{\text{rec}}} - \frac{a_{\text{e}}A_{\text{phy}}}{T_{\text{A}}+T_{\text{rec}}}}{\frac{A_{\text{e}}A_{\text{phy}}}{T_{\text{A}}+T_{\text{rec}}}}, \tag{5.47}$$

where A_{e} represents the full AE model with ripple included, and a_{e} excludes the ripple. The error can simplify to,

$$\text{Error}_{\text{AE}} = \frac{A_{\text{e}}A_{\text{phy}} - a_{\text{e}}A_{\text{phy}}}{A_{\text{e}}A_{\text{phy}}}, \tag{5.48}$$

which can simplify to,

$$\text{Error}_{\text{AE}} = \frac{A_{\text{e}} - a_{\text{e}}}{A_{\text{e}}}, \tag{5.49}$$

and further to,

$$\text{Error}_{\text{AE}} = 1 - \frac{a_{\text{e}}}{A_{\text{e}}}, \tag{5.50}$$

where the ripple contribution can explicitly be written as,

$$\text{Error}_{\text{AE}} = 1 - \frac{a_{\text{e}}}{a_{\text{e}} + A_{\text{e ripple}}}. \tag{5.51}$$

The ripple excluding AE can further be defined as $a_{\text{e}} = \eta_{\text{f}}(f)$, and the ripple including $A_{\text{e}} = \eta_{\text{ap}}(f)$. Finally, for the set only including the ripple, $A_{\text{e ripple}} = \eta_{\text{ap}}(f) - \eta_{\text{f}}(f)$. From this, it can be concluded that the error on the sensitivity from not modeling the AE ripple is independent of the receiver noise temperature and only a function of the AE and the AE ripple.

The same analysis can be performed for the ANT ripple contribution. The error on the sensitivity of not modeling the ripple in the ANT can be calculated as follows,

$$\text{Error}_{\text{Ta}} = \frac{\frac{A_{\text{e}}A_{\text{phy}}}{T_{\text{A}}+T_{\text{rec}}} - \frac{A_{\text{e}}A_{\text{phy}}}{t_{\text{A}}+T_{\text{rec}}}}{\frac{A_{\text{e}}A_{\text{phy}}}{T_{\text{A}}+T_{\text{rec}}}}, \tag{5.52}$$

where T_{A} includes the ripple for ANT and where T_{A} excludes the ripple. This error can simplify to,

$$\text{Error}_{\text{Ta}} = \frac{A_{\text{e}}A_{\text{phy}}(t_{\text{A}} + T_{\text{rec}}) - A_{\text{e}}A_{\text{phy}}(T_{\text{A}} + T_{\text{rec}})}{A_{\text{e}}A_{\text{phy}}(t_{\text{A}} + T_{\text{rec}})}, \tag{5.53}$$

which factorises to,

Stellenbosch University https://scholar.sun.ac.za

$$\text{Error}_{\text{Ta}} = \frac{A_{\text{e}}A_{\text{phy}}(t_{\text{A}} + T_{\text{rec}} - (T_{\text{A}} + T_{\text{rec}}))}{A_{\text{e}}A_{\text{phy}}(t_{\text{A}} + T_{\text{rec}})}, \tag{5.54}$$

and finally simplifies to,

$$\text{Error}_{\text{Ta}} = \frac{t_{\text{A}} - T_{\text{A}}}{t_{\text{A}} + T_{\text{rec}}}. \tag{5.55}$$

If the receiver noise temperature were to tend to infinity $\lim_{T_{\text{rec}}\to\infty}$ then,

$$\text{Error}_{\text{Ta}} = \lim_{T_{\text{rec}}\to\infty} \frac{t_{\text{A}} - T_{\text{A}}}{t_{\text{A}} + T_{\text{rec}}} = 0, \tag{5.56}$$

the error on the sensitivity of not modeling the ANT will be completely insignificant, as the receiver noise temperature completely dominates the contribution. If the receiver noise temperature were to tend to zero $\lim_{T_{\text{rec}}\to 0}$ then,

$$\text{Error}_{\text{Ta}} = \lim_{T_{\text{rec}}\to 0} \frac{t_{\text{A}} - T_{\text{A}}}{t_{\text{A}} + T_{\text{rec}}} = \frac{t_{\text{A}} - T_{\text{A}}}{t_{\text{A}}} = 1 - \frac{T_{\text{A}}}{t_{\text{A}}} = 1 - \frac{t_{\text{A}} + T_{\text{Aripple}}}{t_{\text{A}}}, \tag{5.57}$$

the error caused on the sensitivity of not modeling the ANT ripple will simply be a function of the ANT and the ANT ripple, similar to the error the AE ripple causes.

Thus, as the receiver noise temperature rises, the relevance of modeling the ANT ripple for the sensitivity calculation will becomes less relevant. The importance of the ripple in the sensitivity calculations for receiver noise temperatures over $T_{\text{rec}} \in [0 - 300]$ K, is investigated. The high temperature values simulates low quality LNAs bought off-the-shelf, where the low temperature values simulates either high quality LNAs or those that have been cryogenically cooled. The purpose of the analysis is to determine at which LNA temperature the ANT ripple becomes less important to model. A higher LNA temperature will be required to cause a higher amplitude ANT ripple, to have the same relative impact on the sensitivity ripple, as a lower amplitude ANT ripple for a lower LNA temperature.

A root mean square error (RMSE) between the high-fidelity approximation, M_{H}, and some low-fidelity approximations, is calculated to combine the error over frequency. The ripple contributions to the sensitivity error are then factorised.

The RMSE between M_{H} and M_{L} is first compared, which is denoted as ξ_{all}, and ignores both the AE ripple and ANT ripple when calculating the sensitivity. Secondly, the RMSE from ignoring the ANT ripple in the sensitivity calculations, is denoted as ξ_{TA}. Finally, the RMSE from ignoring the AE ripple in the

Stellenbosch University https://scholar.sun.ac.za

sensitivity calculations, is denoted as ξ_{ap}. The results are displayed in Fig. 5.5.

From Fig. 5.5, it is apparent that ignoring the ripple when calculating the sensitivity at lower receiver noise temperatures, leads to the largest RMSE. At these temperatures T_{rec} is somewhat similar to T_{A}. Furthermore, it is less important to model the ANT ripple as the receiver noise temperature rises, as the receiver noise temperature starts to dominate the system temperature, causing the ANT ripple to become more negligible. Recall that predicting the ANT ripple is difficult, and in this case neglecting the ANT ripple would not result in a large error in the sensitivity.

The relevance of the AE ripple in the sensitivity calculation over receiver noise temperature is also displayed. The RMSE from ignoring the AE ripple is independent of the receiver noise temperature. Thus, ignoring all ripple when calculating the sensitivity when the receiver noise temperature is high, leads to a similar RMSE when only ignoring the AE ripple. Since calculating the AE ripple is easier, it might be practical to calculate it to improve the sensitivity accuracy.

When the ANT ripple is modeled, the information is available to model the AE ripple as well, and practical designs will consider both the ANT and the AE at the same time. This is because the accurate ANT calculation requires the calculation of the main beam, which is also necessary for the accurate calculation of the AE.

5.3 Additional examples

In this section some additional examples will be considered, to inspect the impact of the ripple on the sensitivity in these cases. There are an inexhaustible list of permutations of the influences which will change the sensitivity, and thus not all of them can be investigated.

5.3.1 Smaller reflector

It is expected that the ripple impact will be more severe for an electrically smaller reflector. In this case, a smaller dish is used with maximum chord lengths of 4 m and 1 m for the primary reflector and subreflector, respectively. The primary reflector has a projected aperture diameter of 3 m. All other parameters, compared to the standard reflector, remain constant.

Stellenbosch University https://scholar.sun.ac.za

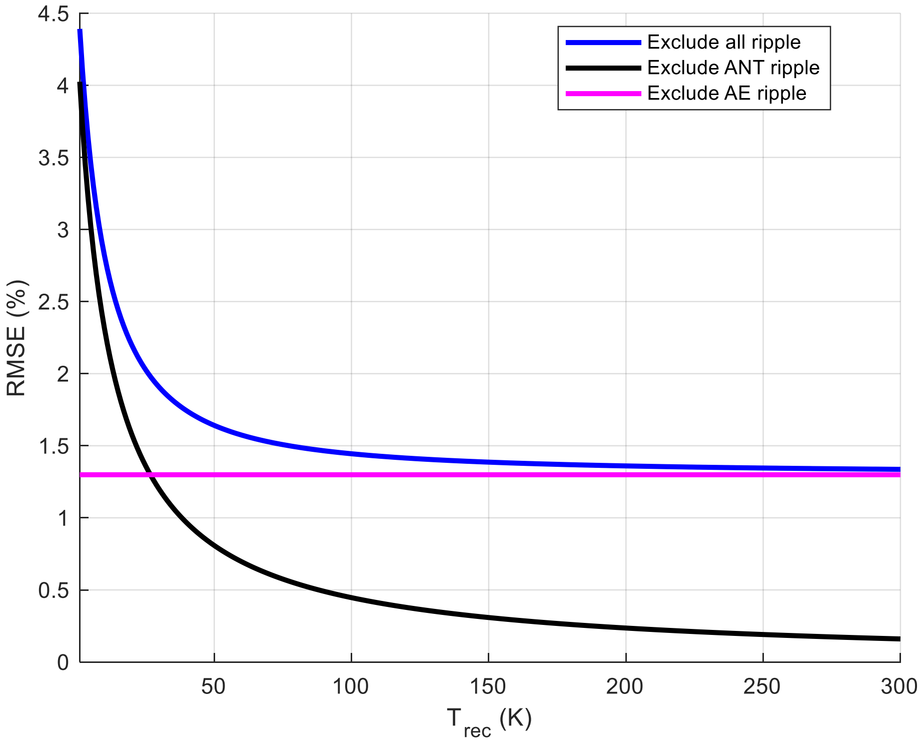

Figure 5.5: The RMSE is compared for three different situations of excluding specific ripple components from the receiving sensitivity calculations, over receiver noise temperature

In Fig. 5.6, the AE is shown. This includes the high-fidelity AE, η_{ap}, the low-fidelity AE, η_{f}, and the diffraction efficiency. The diffraction efficiency, η_{f}, calculated in this chapter uses GO, and thus the accuracy of η_{f} reduces, as the electric size of the system reduces. From Fig. 5.6, the high-fidelity AE is substantially different, compared to the low-fidelity AE, especially at the lower part of the frequency band. This is expected, as the lower band will cause the reflector to have a smaller electric size, compared to the higher part of the band. The diffraction efficiency is also lower, compared to the standard reflector, which is expected, and contributes to the difference between the high-fidelity AE vs the low-fidelity AE. At around 85 % diffraction efficiency, the AE calculations are somewhat similar, and perhaps the diffraction efficiency can give an indication when the low-fidelity AE is accurate enough.

In Fig. 5.7a, the high- and low-fidelity sensitivity is compared, for various tipping angles, over frequency. A 7 K receiver noise temperature, T_{rec}, is assumed. In Fig. 5.7b, the error function as similarly calculated in (5.45), is shown for each pointing angle. From Fig. 5.7 the sensitivity error, between the low- and high-fidelity set, is also much larger in the lower part of the band. This occurs for similar reasons as explained for the AE comparison previously. The

Stellenbosch University https://scholar.sun.ac.za

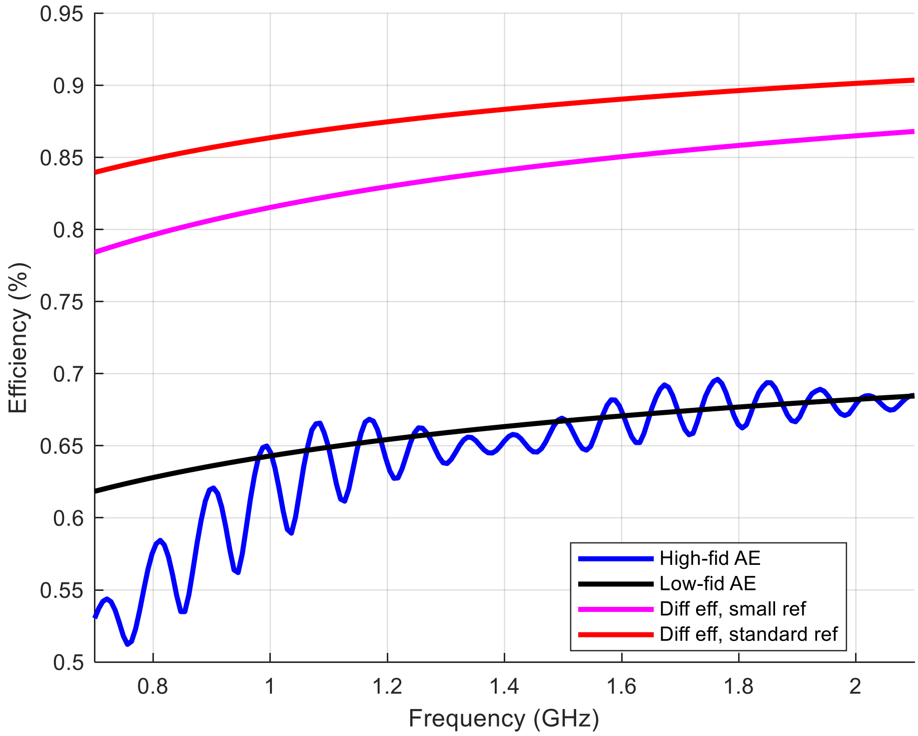

Figure 5.6: The low-fidelity approximation (feed efficiency) is compared to the high-fidelity AE from (5.41), with the diffraction sub-efficiency also displayed

error at the start of the band has a higher oscillation amplitude, which relates to the larger ripple, due to a smaller electric size. While the error becomes substantially less over the band, the error at the start of the band is perhaps too large to qualify the low-fidelity set as usable. For very small reflectors, it might become necessary for high-fidelity calculations of the sensitivity, even during the optimisation phase.

Finally, a RMSE is calculated, similarly to previously explained. In Fig. 5.8 the importance of including the AE ripple, compared to the ANT ripple, is apparent for this smaller reflector. The exclusion of the AE ripple leads to a relatively high error over the band, compared to excluding the ANT ripple, which is only comparative at almost zero receiver noise temperature. Thus for this smaller reflector, it is even more important to model the AE ripple, compared to the standard reflector. Besides this change, the RMSE behaviour is somewhat similar to that which was seen with the use of the standard reflector, except that the errors are generally higher.

Stellenbosch University https://scholar.sun.ac.za

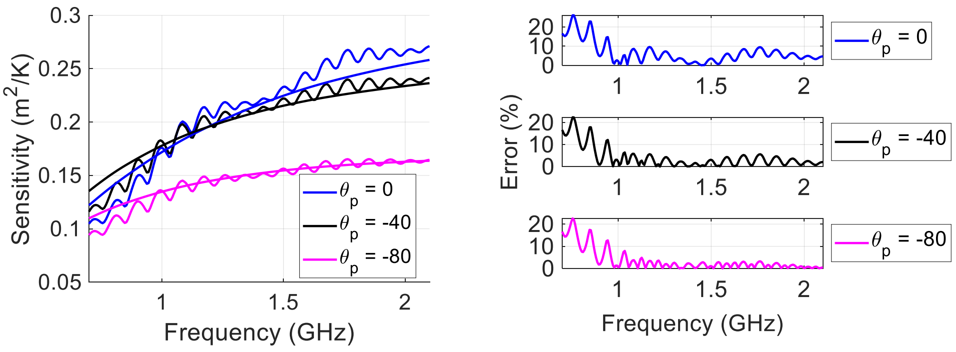

(a) (b)

Figure 5.7: In (a) the high-fidelity approximation is compared to the low-fidelity approximation, for the receiving sensitivity, over three pointing angles. The rapidly varying solid lines display the high-fidelity approximation. The slowly varying solid lines display the low-fidelity approximation, which excludes the ripple. In (b), the error function as similarly calculated in (5.45), is shown over frequency for each pointing angle, and is used to compare the low- and high-fidelity set of the sensitivity

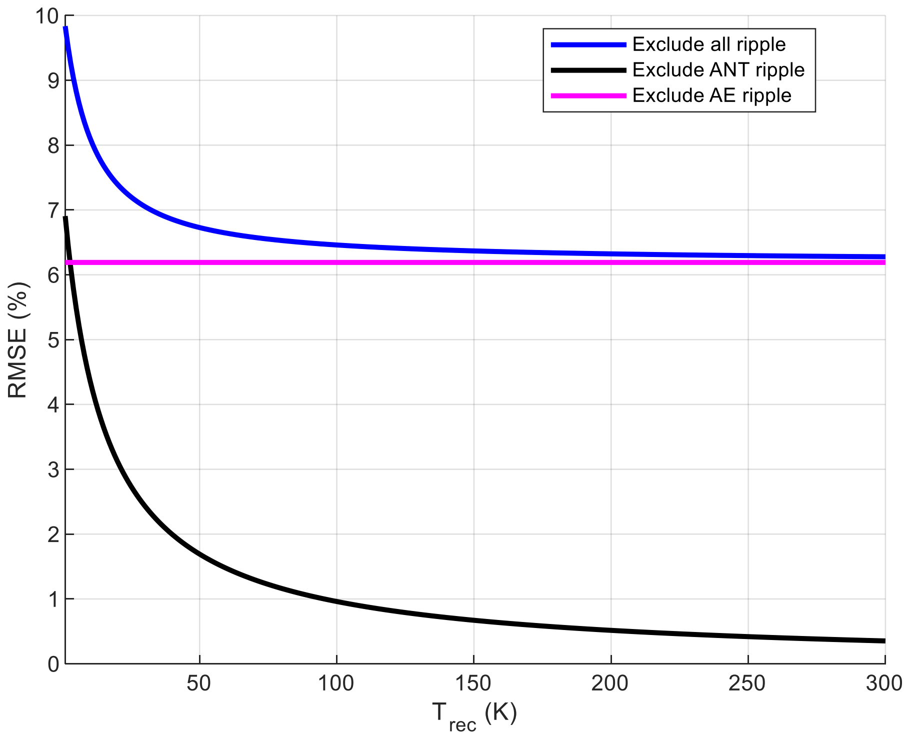

Figure 5.8: The RMSE is compared for three different situations of excluding specific ripple components from the receiving sensitivity calculations, over receiver noise temperature

Stellenbosch University https://scholar.sun.ac.za

5.3.2 Higher frequency

It is expected that the ripple impact will be less severe for a higher frequency band, as the reflector electric size will increase. The impact is analysed for the standard reflector, with only a shift in the frequency band.

In Fig. 5.9, the AE is shown. This includes the high-fidelity AE, η_{ap}, the low-fidelity AE, η_{f}, and the diffraction efficiency. From Fig. 5.9, the high-fidelity AE is mostly similar to the low-fidelity AE, except for the ripple. The diffraction efficiency is also higher, compared to the standard reflector, which is expected, and contributes to the similarity between the high-fidelity AE vs the low-fidelity AE.

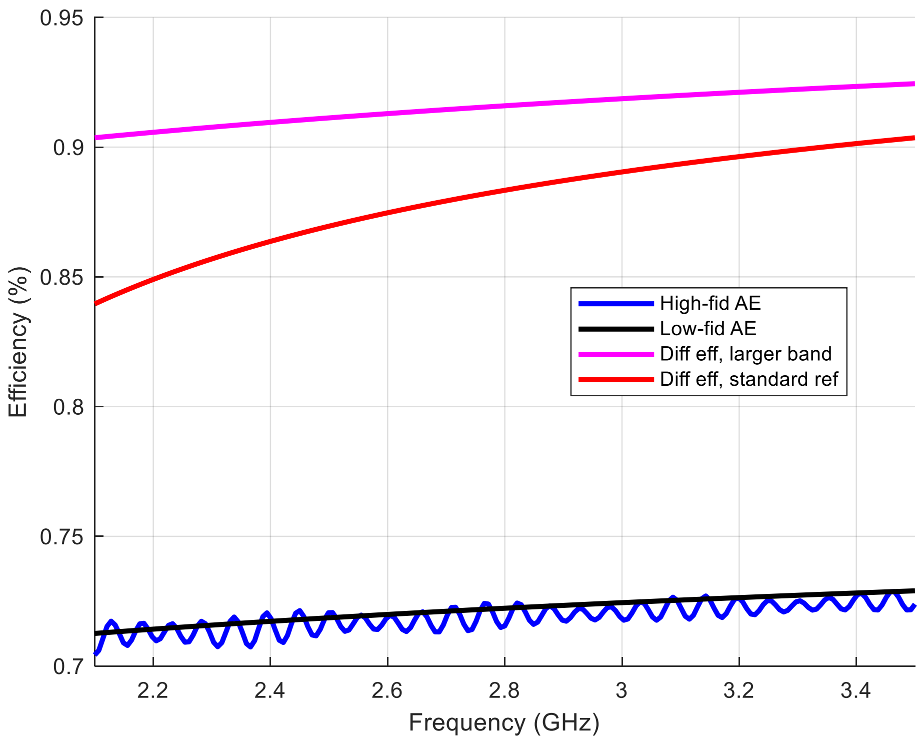

Figure 5.9: The low-fidelity approximation (feed efficiency) is compared to the high-fidelity AE from (5.41), with the diffraction sub-efficiency also displayed

In Fig. 5.10a, the high- and low-fidelity sensitivity is compared, for various tipping angles, over frequency. A 7 K receiver noise temperature, T_{rec}, is assumed. In Fig. 5.10b, the error function as similarly calculated in (5.45), is shown for each pointing angle. From Fig. 5.10 the sensitivity error, between the low- and high-fidelity set, is very small. This occurs, as seen from the

Stellenbosch University https://scholar.sun.ac.za

diffraction efficiency, because the reflector size is large enough to limit the influence of non-ideal effects. For this case, it is likely that the sensitivity does not need to be accounted for during the optimisation phase, but perhaps still in the final design.

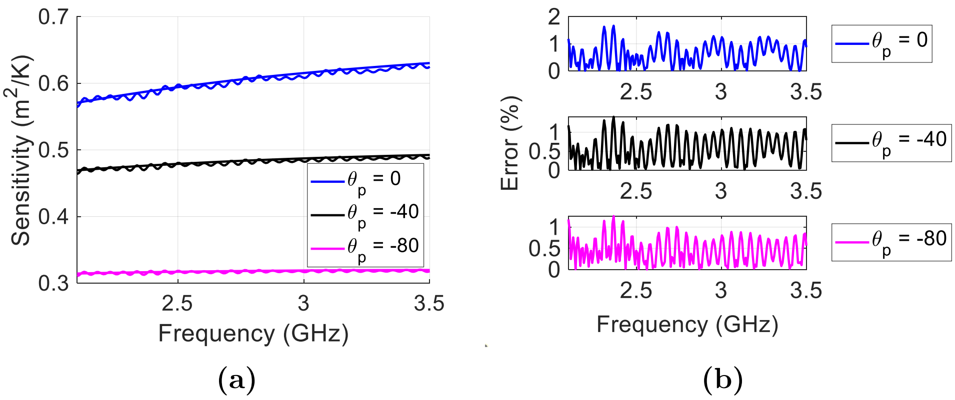

Figure 5.10: In (a) the high-fidelity approximation is compared to the low-fidelity approximation, for the receiving sensitivity, over three pointing angles. The rapidly varying solid lines display the high-fidelity approximation. The slowly varying solid lines display the low-fidelity approximation, which excludes the ripple. In (b), the error function as similarly calculated in (5.45), is shown over frequency for each pointing angle, and is used to compare the low- and high-fidelity set of the sensitivity

Finally, a RMSE is calculated, similarly to previously explained. In Fig. 5.11 the AE ripple is more important to include, compared to the ANT ripple, over the entire band for this higher frequency band. Besides this change, the RMSE behaviour is somewhat similar to that which was seen with the use of the standard reflector, except that the errors are generally smaller. Exclusion of any ripple, is thus mostly insignificant in this case, for this band.

5.4 Conclusion

Sensitivity ripple is influenced by the AE ripple and the ANT ripple, and is the result of their quotient. The significance of accurately modelling this ripple factor is investigated for the standard case, with the other parameters kept constant, to keep the discussion tractable. It is shown that low-fidelity approximations can be used to accelerate the sensitivity calculation process, with only an average error of 1.70% for a 7 K receiver noise temperature system.

Furthermore, including the AE ripple improves the accuracy of the sensitivity calculation, over receiver noise temperature. The ANT ripple is only important

Stellenbosch University https://scholar.sun.ac.za

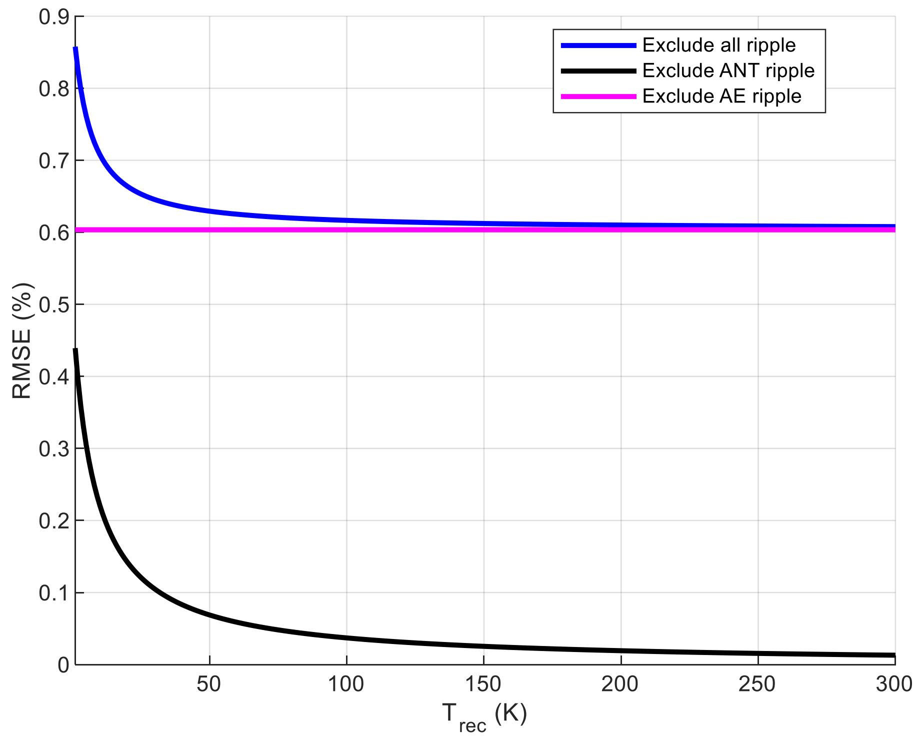

Figure 5.11: The RMSE is compared for three different situations of excluding specific ripple components from the receiving sensitivity calculations, over receiver noise temperature

when the receiver noise temperature is similar to the ANT, or lower. Additionally, the ANT ripple is notably more complicated to model compared to AE ripple, which results in significantly more difficulty to build accurate and reliable models for the ANT ripple. For higher receiver noise temperatures, omitting the ANT ripple does not have a severe impact on the accuracy of the sensitivity. For lower temperatures it becomes more relevant to model it. Finally, the ripple impact on the sensitivity is analysed for various other cases, where the importance of modeling the ripple is discussed from the results.

Stellenbosch University https://scholar.sun.ac.za

Chapter 6

Conclusion

Radio astronomy requires antennas to detect emissions from celestial objects in the universe, to characterise them. Sensitivity is used as a primary figure of merit to optimise these antennas (SKA, ngVLA, DSA-2000) for radio astronomy, and they are often reflectors. Some modern radio astronomy projects choose to use many electrically smaller reflectors, instead of fewer traditional larger ones.

Non-ideal effects become more dominant in the total radiation pattern of the reflector system, due to the reflector performing less ideally, as the electrical size of the reflector reduces. The MoM can most effectively simulate these non-ideal effects, as it is a full wave solution, while the asymptotic PO technique can simulate only a subset of them. The PTD can be used with the PO analysis to increase the ability to simulate non-ideal effects.

These non-ideal effects influence the radiation pattern of the reflector system through interference, which causes a ripple over frequency in the radiation pattern. This ripple in the radiation pattern, leads to a ripple over frequency in the antenna noise temperature (ANT). The magnitude of this ripple is correlated to the electric size of the reflector system, and is thus less relevant for larger reflector designs.

The ANT is a function of all directions, as it requires an integral over the entire sphere of the product of the background noise temperature, the radiation pattern and a sinus function. The background noise temperature, and radiation pattern, is a function of all directions. The background noise temperature thus weighs the radiation pattern differently in each direction. This leads to certain directions or regions being significantly more important than others for the ANT calculation, in a specific pointing angle. In these regions, the ripple in the radiation pattern is observed in the ripple of the ANT, as expected. It is shown that the ANT is a function of many physical parameters. Some of these parameters, and their effect, on the ANT is investigated.

Stellenbosch University https://scholar.sun.ac.za

It is shown that the ripple observed in the sensitivity is due to the ripple in the ANT and the ripple in the AE. The impact of the ripple in the sensitivity is investigated on a relatively electrically small offset Gregorian dual reflector, to determine the relevance of modeling it. The electric size of this reflector ranges from about a dozen, to a few dozen in wavelength, in the band it is analysed. It is concluded to only cause a small error of a few percent. Ignoring the ripple in the optimisation phase might be safe, but a highly accurate final design would require the ripple to be modeled. Strategies for rapid sensitivity approximation often times ignore the ripple to facilitate significantly faster sensitivity calculations, which is crucial during the optimisation phase of antenna design for radio astronomy.

The impact of the LNA temperature is also investigated together with the relevance of the ripple of the ANT, or the ripple of the AE, individually. Higher LNA temperatures are common with cheaper low quality LNAs. Cryogenically cooling the LNA will reduce the temperature, but raises operation and capital costs.

It is observed that for high LNA temperatures, it is less important to model the ANT ripple. The ANT ripple will also become less relevant, as the electrical size of the reflector increases. The AE ripple relevance remains constant, independent of the LNA temperature. The relevance to model the AE ripple is thus dependent on the electrical size of the reflector and not the LNA quality or temperature. Generally it is more important to model the ripple in the case of low LNA temperature, for the final design. If the ripple is not modeled, it is not necessary to model all the non-ideal effects. PO + PTD is then sufficient to analyse electrically small reflectors.

Thus in conclusion, small reflectors can in most cases be developed without modeling the ripple, during the optimisation phase. The ripple can be modeled for the final design, to ensure stringent requirements can be met.

6.1 Future Work

6.1.1 Using near-field in sensitivity calculation

The calculation of the receiving sensitivity requires the calculation of the far-field radiation pattern (technically the radiation intensity) of the full reflector system. This might, however, not be completely accurate. In any sensible case, the reflector system observes in the direction of the sky, and thus the main beam is pointing into the sky. The main beam receives the most power,

Stellenbosch University https://scholar.sun.ac.za

and it is thus largely contributing to the ANT. The sky is in the far-field, and the main beam contribution is thus accurately accounted for in the ANT. It is thus expected that the current sensitivity calculation approach is still relatively accurate, however, the possible near-field impacts will be discussed next.

As the reflector is tipped towards the horizon, the larger sidelobes closer to the main beam start to receive radiation from the ground, which is in the near-field. This is generally ignored and far-field radiation is still assumed. Reactive effects largely disappear for far-fields, but they are relevant for near-fields. The near-field radiation patterns will likely be different to their assumed far-field counterparts, which might influence the ANT and sensitivity. Recall that electromagnetic waves are spherical waves in the near-field, and not plane waves. Interference effects involving them might no longer cause a similar ripple over frequency effect on the radiation pattern, as it is no longer plane waves interfering over frequency.

A possible method to account for the near-field, could be to calculate both the near-field and the far-field, for the angles associated with the ground directions. Radiation intensity does not strictly exist for the near-field, so a power per unit solid angle calculation would have to be developed for the near-field that resembles radiation intensity, to be usable in the ANT calculation. These radiation intensities can be compared, as well as their FFT outputs. If they contain similar ripple, then the current ripple is modeled correctly. If the radiation intensities themselves are similar, then there is no need to model in the near-field at all.

6.1.2 Ripple in the optimisation

6.1.2.1 VEXPA ripple prediction

A possible solution to ripple prediction in the ANT, is by using Validated Exponential Analysis or VEXPA [69], with other associated techniques. Estimation of Signal Parameters via Rotational Invariance Techniques (ESPRIT) [70], Multiple Signal Classification (MUSIC) [71] and Matrix Pencil (MP) [72] are all techniques that can be used to extract the frequency composition of a signal. It assumes and requires the signals to be defined as a sum of exponential functions. These techniques require dense sampling, above the Nyquist sampling rate, otherwise aliasing starts to occur. VEXPA removes aliasing from the results of these techniques, if undersampled, to give unique solutions for sparse sampling. This enables these techniques to recover a unique signal composition from a sampling rate under the Nyquist rate.

Stellenbosch University https://scholar.sun.ac.za

The ANT ripple is determined from the radiation intensity ripple, which is determined from the co- and cross-polar electric field components. If the ANT, radiation intensity, or co- and cross-polar electric field components can be defined as an exponential series, then these techniques could possibly reconstruct them, including the ripple. A possible test could include performing an FFT on these functions, and using the FFT output to produce an exponential series, to attempt to reconstruct these functions. If the reconstruction compares well with the original function, the function can likely be described by an exponential series.

While the applicability of this technique would require a lot of research and development, it might allow the ripple in the ANT to be predicted from only a few samples.

6.1.2.2 Preprocessed applied ripple

A possible method for ripple prediction, during the optimisation phase, is discussed next. During optimisation, the reflector system is generally kept constant, while the feed is constantly adjusted. In this method, a single fine model of the ANT is created using a Gaussian ideal feed, which will include the ripple. This model will implicitly model the ripple impact of all of the components of the reflector system, including the Gaussian feed. If the feed were to be replaced by a physical feed, which is at least somewhat similar to the Gaussian feed, it is expected to not change the ripple significantly. The Gaussian feed is an idealised feed, and thus most practical physical feeds will be a similar, but worse version of the Gaussian feed. This includes the QRFH feed. After the fine model, the ANT is then consecutively calculated using a low-fidelity model, with a physical feed instead. This model excludes the ripple. The ripple calculated from the fine model, is then applied to the low-fidelity model.

6.1.2.3 Geometric argument ripple prediction

In Chapter 5, it was stated that the AE ripple can be predicted using a geometric argument, but predicting the ANT ripple using a geometric argument approach is significantly more difficult. Geometric arguments infers information from only the geometry of the reflector setup, making them independent of simulations, and thus very fast. In summary, a geometric argument uses a geometric optics approach to ray trace the path lengths of interfering waves, to predict the resultant ripple, due to effects described in Chapter 3.

Stellenbosch University https://scholar.sun.ac.za

A geometric argument in this sense, can only predict the ripple in a single direction. This is because the non-ideal effects interfering with the full radiation pattern, and the path lengths of interfering waves, are functions of angle. For the ANT, a geometric argument would be required to predict the ripple in every high contributing direction, which changes for every tipping angle, and for every reflector setup. If each high contributing direction has multiple dominant ripple periods, then a geometric argument has to be found for each one.

These high contributing directions can be identified using the heatmap tools developed and presented in this dissertation. It is also important to identify which type of non-ideal effect causes the ripple, so that the adequate path lengths can be compared. For the AE ripple, it is identified to be a diffraction non-ideal effect, and thus specific path lengths from the subreflector and primary reflector are compared. The non-ideal effect can sometimes be derived from the presented heatmaps, such as edge diffraction near the edges of the reflectors, but in some cases it is more difficult. The ripple can also be caused by a combination of non-ideal effects, which increases the difficulty in identifying them.

Geometric arguments are not completely accurate, as it uses a geometric optics ray tracing approach, and thus optimisation techniques are required to correct the predicted ripple. A possible approach can be to extract the power law base form of the ANT, which do not require many samples, and then adding the predicted ripple. An alternative ANT can then be calculated at a few specific frequency points, using the full radiation pattern, to provide a sparse high-fidelity ANT over the band. This alternative ANT will require much less samples than a dense high-fidelity set. These two ANT calculations can then be fitted on each other, using a simplex search method, to correct the ripple. An incorrectly predicted ripple will become out of phase with the correct ripple, over the band, and will occur quicker for a faster ripple. This leads to a larger error than ignoring the ripple. Using geometric arguments to solve the ripple in the ANT is thus very difficult to do, but could perhaps be attempted.

Stellenbosch University https://scholar.sun.ac.za

Appendices

Stellenbosch University https://scholar.sun.ac.za

Appendix A

Adding true-view regions, to approximate integral

The integral of the product, M_{TbUS}, of the factors required to calculate the ANT, can be calculated by the summation of M_{TbUS} over the entire projection, and will be discussed next. Recall that the ANT is described as follows,

$$T_{\mathrm{A}}(f|\hat{\mathbf{r}}_0) = \frac{\iint_{4\pi} T_{\mathrm{b}}(f,\Omega)U(f,\Omega|\hat{\mathbf{r}}_0)\sin\theta d\Omega}{\iint_{4\pi} U(f,\Omega)\sin\theta d\Omega}. \tag{A.1}$$

This can be rewritten as,

$$T_{\mathrm{A}}(f|\hat{\mathbf{r}}_0) = \frac{\int_{\pi}\int_{2\pi} T_{\mathrm{b}}(f,\phi,\theta)U(f,\phi,\theta|\hat{\mathbf{r}}_0)\sin\theta d\theta d\phi}{\iint_{4\pi} U(f,\Omega)\sin\theta d\Omega}, \tag{A.2}$$

which in turn can be rewritten as,

$$T_{\mathrm{A}}(f|\hat{\mathbf{r}}_0) = \frac{\int_{\pi}\int_{2\pi} F(f,\phi,\theta|\hat{\mathbf{r}}_0) d\theta d\phi}{\iint_{4\pi} U(f,\Omega)\sin\theta d\Omega}, \tag{A.3}$$

where

$$F(f,\phi,\theta|\hat{\mathbf{r}}_0) = T_{\mathrm{b}}(f,\phi,\theta)U(f,\phi,\theta|\hat{\mathbf{r}}_0)\sin\theta. \tag{A.4}$$

The surface area element of a sphere is $A_s = r^2\sin(\theta)d\theta d\phi$. When surface integration is performed over a unit sphere, with $r = 1$, the surface area element becomes $A_{s2} = \sin(\theta)d\theta d\phi$. This is the case for the surface integral performed in (A.5), when calculating the ANT. If the sin in the surface area element A_{s2} is removed, then the surface area element $A_3 = d\theta d\phi$ is a rectangle on a rectangular grid, as seen in Fig. A.1. This is the case for (A.5), with the normalising denominator removed, which can be rewritten as,

$$T_{\mathrm{AUN}}(f|\hat{\mathbf{r}}_0) = \int_{\pi}\int_{2\pi} F(f,\phi,\theta|\hat{\mathbf{r}}_0)A_3. \tag{A.5}$$

Stellenbosch University https://scholar.sun.ac.za

The numerator format in (A.4) thus casts the evaluation of the integral into a summation of the product of the function F at the centre of each grid element, with each grid element having sides of size $d\theta$ and $d\phi$, respectively. This is shown in Fig. A.1. This means that the integral can be evaluated by adding these regions together.

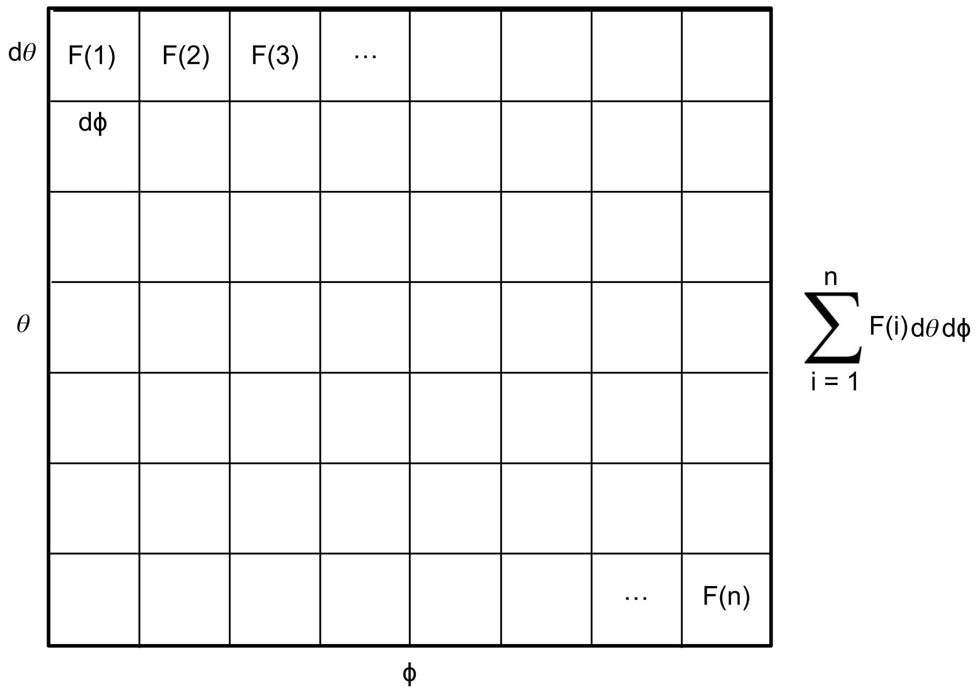

Figure A.1: Integral cast into a format where its evaluation reduces to a summation of the product of the function at the centre of each grid element with each grid element, over the entire grid

When the function, F, is transformed through a true-view projection, the integral area element will become the same format as the polar coordinate area element, since the transformation casts the function into a circular area. This can be seen in Fig. A.2.

The variables ρ and α will be derived in relation to the spherical coordinates, to evaluate the impact on the integral in (A.5), due to the true-view projection. Consider the definition of ρ in polar coordinates,

$$\rho = \sqrt{x^2 + y^2}, \tag{A.6}$$

Stellenbosch University https://scholar.sun.ac.za

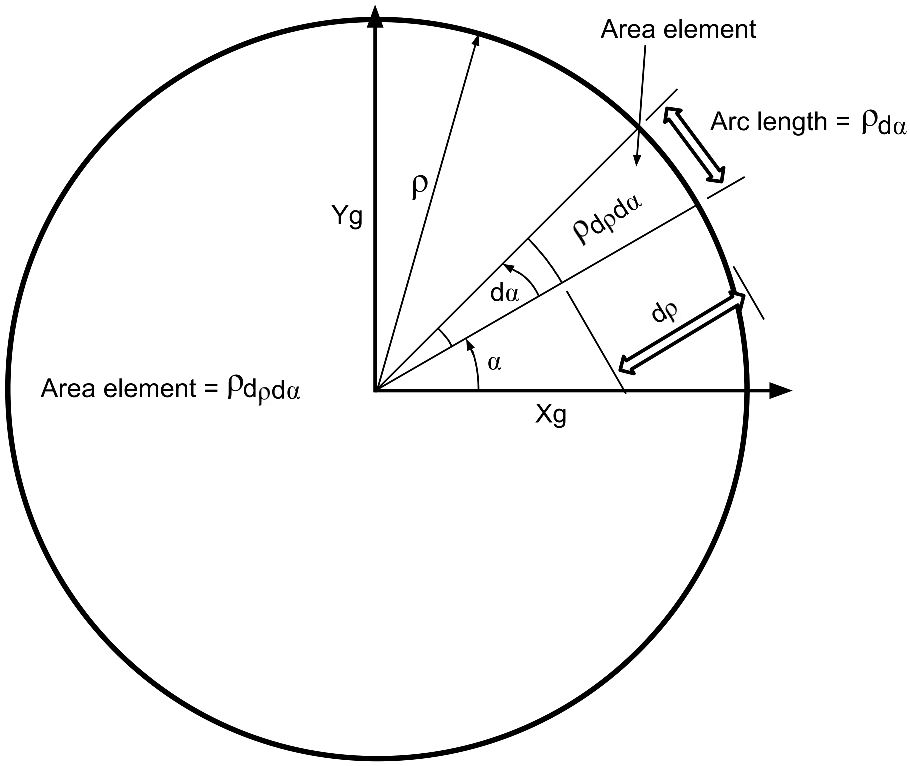

Figure A.2: True-View projection of the function casts it into a circular area, resulting in the integral area element changing to a format similar to the polar coordinate area element

which directly relates to true-view coordinates,

$$\rho = \sqrt{X_g^2 + Y_g^2}, \tag{A.7}$$

expanding the true-view projections,

$$\rho = \sqrt{\theta^2 \mathrm{sin}^2(\phi) + \theta^2 \mathrm{cos}^2(\phi)}, \tag{A.8}$$

factorising θ^2 out and using the trigonometric identity $\sin^2(\phi) + \cos^2(\phi) = 1$,

$$\rho = \sqrt{\theta 2}, \tag{A.9}$$

which equates ρ to θ,

$$\rho = \theta. \tag{A.10}$$

Stellenbosch University https://scholar.sun.ac.za

From this, $d\rho = d\theta$, and θ is the same θ from the spherical coordinate system. The angle α can be calculated as,

$$\alpha = \arctan\left(\frac{y}{x}\right), \tag{A.11}$$

which translates in true-view to,

$$\alpha = \arctan\left(\frac{Y_g}{X_g}\right), \tag{A.12}$$

and then expands using the true-view projection definitions to,

$$\alpha = \arctan\left(\frac{\theta \sin\phi}{\theta \cos\phi}\right), \tag{A.13}$$

which then simplifies to,

$$\alpha = \arctan(\tan\phi), \tag{A.14}$$

where the function and its inverse simplifies to the argument,

$$\alpha = \phi, \tag{A.15}$$

thus, α is ϕ from the spherical coordinate system, and $d\alpha = d\phi$.

The area element is thus transformed from $pd\rho d\alpha$ to $\theta d\theta d\phi$, in terms of spherical coordinates. This can be rewritten in terms of,

$$\theta d\theta d\phi = \theta A_3. \tag{A.16}$$

For the true-view projection, the integral changes to,

$$T_{\text{AUN}}(f|\hat{\mathbf{r}}_0) = \int_{\pi}\int_{2\pi} F(f,\phi,\theta|\hat{\mathbf{r}}_0)\theta d\theta d\phi, \tag{A.17}$$

or using (A.16),

$$T_{\text{AUN}}(f|\hat{\mathbf{r}}_0) = \int_{\pi}\int_{2\pi} F(f,\phi,\theta|\hat{\mathbf{r}}_0)\theta A_3. \tag{A.18}$$

Thus if (A.4) is multiplied by θ, then it would produce,

$$F(f,\phi,\theta|\hat{\mathbf{r}}_0)\theta = T_{\text{b}}(f,\phi,\theta)U(f,\phi,\theta|\hat{\mathbf{r}}_0)\sin(\theta)\theta, \tag{A.19}$$

which can be rewritten as,

Stellenbosch University https://scholar.sun.ac.za

$$V(f, \phi, \theta|\hat{\mathbf{r}}_0) = F(f, \phi, \theta|\hat{\mathbf{r}}_0)\theta, \tag{A.20}$$

and finally,

$$T_{\mathrm{AUN}}(f|\hat{\mathbf{r}}_0) = \int_{\pi}\int_{2\pi} V(f, \phi, \theta|\hat{\mathbf{r}}_0)A_3. \tag{A.21}$$

This means that the area element would be reduced back to the rectangular area element A_3, if the function F is multiplied by θ, and thus this would once again cast the integral into a summation over a rectangular grid. If the area element is kept as $\theta A_3 = \theta d\theta d\phi$, then the integrated region would not be transformed into a rectangular grid, but remain a circular area. This follows intuitively by considering that removing ρ from the area element of the the polar coordinate system, changes the area element into a rectangular grid element, as shown in Fig. A.3. By removing θ, from the area element $\theta d\theta d\phi$, the same will effect will occur. The integral can still be calculated as a summation over the grid, whether it is rectangular or circular. Thus, no change to F needs to occur, and the area element can be kept as $\theta A_3 = \theta d\theta d\phi$.

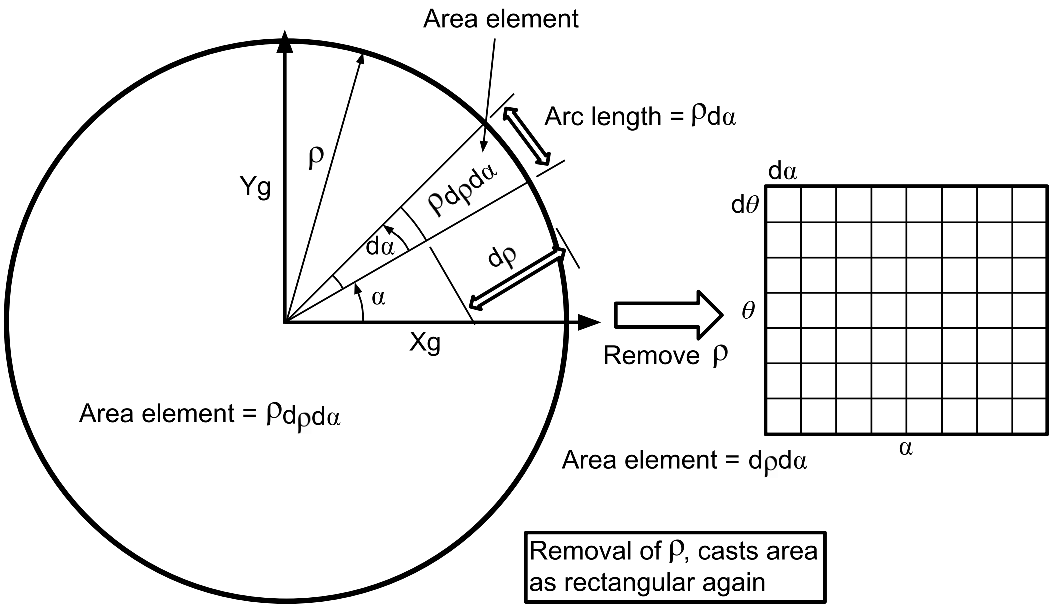

Figure A.3: Removal of ρ changes the area element to a rectangular grid element

Stellenbosch University https://scholar.sun.ac.za

A.1 ANT integral convergence resolution

In order for the ANT integral to converge, a high enough angular resolution is required for the full radiation pattern. The resolution used in this dissertation is based on the recommendations provided in [73]. While it is expected that the resolution will allow the ANT integral to converge, due to following the recommendation, it is explicitly tested. The required resolution for convergence depends on the frequency and the reflector setup, however, only convergence for the standard band [0.7 - 2.1] GHz and standard reflector setup will be tested, for brevity.

For the standard case, the resolution of the full radiation pattern, $U(f, \Omega)$, is calculated at a resolution of 289 samples in ϕ, uniformly sampled from $\phi = 0°$ to $\phi = 360°$. The resolution in θ is 1441 samples uniformly sampled from $\theta = 0°$ to $\theta = 180°$. To prove that the resolution used in this dissertation is enough for convergence, the ANT is calculated at a lower resolution and compared. The resolution is lowered in both ϕ and θ by half, thus reduced to 145 and 721 sampled, respectively.

In Fig. A.4 the true-view projection, with HEALPix applied, of the full radiation pattern, $U(f, \Omega)$, and M_{TbUS} is shown. In Fig. A.4a and Fig. A.4b, the full radiation pattern is shown, calculated at the resolution used in this dissertation, and the lower resolution, respectively. M_{TbUS} is similarly shown for both cases in Fig. A.4c and Fig. A.4d, respectively. In Fig. A.5 the ANT is calculated using the resolution used in this dissertation, and the lower resolution, and the ripple of both cases is shown. Clearly, by comparing the results of each resolution used, there is very little difference by using a lower resolution. This proves that the resolution used in this dissertation converges the ANT integral.

Stellenbosch University https://scholar.sun.ac.za

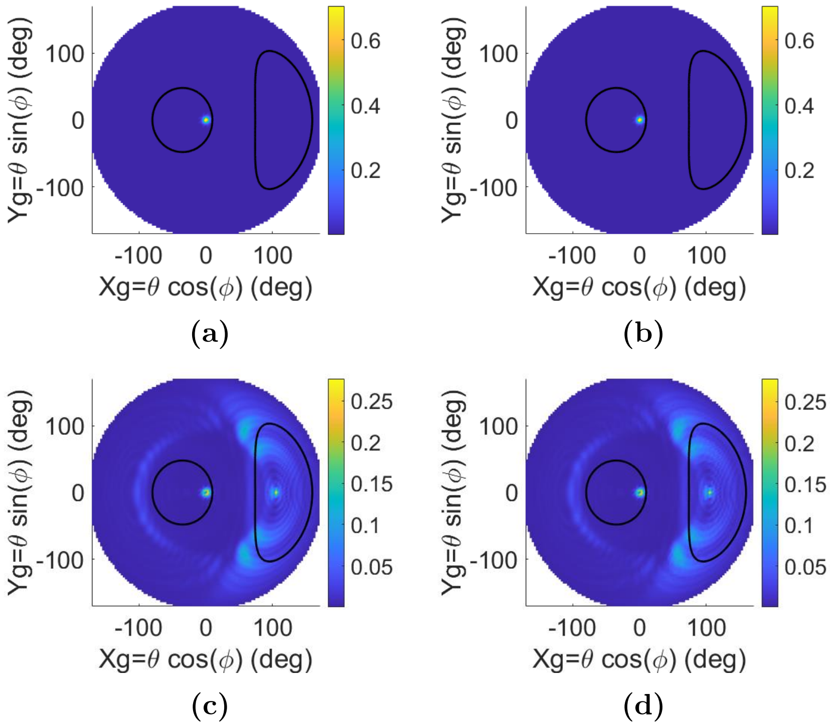

Figure A.4: The true-view projection, with HEALPix applied, of the full radiation pattern, $U(f, \Omega)$, and M_{TbUS}. In (a) and (b), the full radiation pattern is shown, calculated at the resolution used in this dissertation, and the lower resolution, respectively. M_{TbUS} is similarly shown for both cases in (c) and (d), respectively

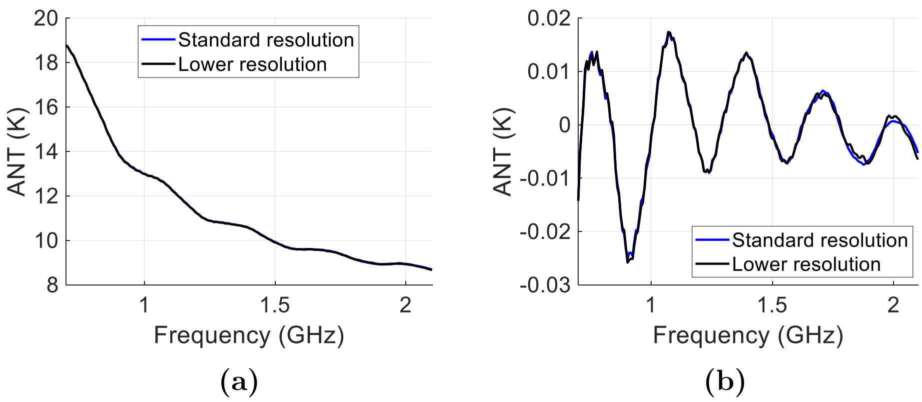

Figure A.5: The ANT is calculated using the resolution used in this dissertation, and the lower resolution, and the ripple of both cases is shown

Stellenbosch University https://scholar.sun.ac.za

List of References

[1] Medellin, G.C.: Antenna noise temperature calculations. In: *SKA Memo 95*. July 2007.
Available at: https://cornell.academia.edu/GermanCortes

[2] J. J. Condon, S. M. Ransom: *Essential Radio Astronomy*. 1st edn. Princeton University Press, 41 William Street, Princeton, New Jersey 08540, 2016.

[3] D. K. Milne: *Parkes: Thirty Years of Radio Astronomy*. 1st edn. CSIRO Publishing, 1994.

[4] Arecibo Observatory.
Available at: https://www.naic.edu/ao/landing

[5] Five-hundred-meter Aperture Spherical radio Telescope.
Available at: https://fast.bao.ac.cn/

[6] L. R. D'Addario, A. R. Thompson, J. W. M. Baars: Advances in radio telescopes. *Proceedings of the IEEE*, vol. 97, no. 8, August 2009.

[7] J. W. M. Baars, L. R. D'Addario, A. R. Thompson: Radio astronomy in the early twenty-first century. *Proceedings of the IEEE*, vol. 97, no. 8, August 2009.

[8] A Crash Course in Radio Astronomy and Interferometry: 2. Aperture Synthesis.
Available at: https://science.nrao.edu/science/meetings/presentation/jdf.webinar.2.pdf

[9] A. R. Thompson, J. M. Moran, G. W. Swenson Jr: *Interferometry and Synthesis in Radio Astronomy*. 3rd edn. Springer Nature, 2017.

[10] T. J. Cornwell: Hogbom's clean algorithm. impact on astronomy and beyond. *Astronomy Astrophysics*, vol. 500, no. 1, June 2009.

[11] O. Smirnov: Interferometric Imaging, Calibration and the RIME. November 2019. Presentation given for course at Stellenbosch University.

[12] Chapter 9: Interferometry and Aperture Synthesis.
Available at: http://ircamera.as.arizona.edu/Astr_518/interferometry1.pdf

Stellenbosch University https://scholar.sun.ac.za

[13] The SKA Project.
Available at: https://www.skatelescope.org/the-ska-project/

[14] de Villiers, D.I.L. and Lehmensiek, R.: SKA Reflector Design. June 2018. Presentation at Caltech, ngVLA Workshop.

[15] G. Hallinan, V. Ravi, S. Weinreb, J. Kocz, Y. Huang, D. P. Woody, J. Lamb, L. DâAddario, M. Catha, J. Shi, C. Law, S. R. Kulkarni, E. S. Phinney, M. W. Eastwood, K. L. Bouman, M. A. McLaughlin, S. M. Ransom, X. Siemens, J. M. Cordes, R. S. Lynch, D. L. Kaplan, S. Chatterjee, J. Lazio, A. Brazier, S. Bhatnagar, S. T. Myers, F. Walter, B. M. Gaensler: Astro2020 APC White Paper. The DSA-2000 - A Radio Survey Camera. July 2019. DSA White paper.

[16] Design Considerations for Radio Astronomy.
Available at: http://www.dunlap.utoronto.ca/wp-content/uploads/2016/08/Longwavelength-Design-Consideration.pdf

[17] The DSA-2000.
Available at: https://www.deepsynoptic.org/overview

[18] Radio astronomy.
Available at: https://www.sarao.ac.za/outreach/radio-astronomy/

[19] D. Cuadrado-Calle, D. George, G. A. Fuller, K. Cleary, L. Samoska, P. Kangaslahti, J. W. Kooi, M. Soria, M. Varonen, R. Lai, X. Mei: Broadband mmic lnas for alma band 2+3 with noise temperature below 28 k. *IEEE Transactions On Microwave Theory And Techniques*, vol. 65, no. 5, May 2017.

[20] Cryogenic Systems and Receiver Maintenance.
Available at: https://www.haystack.mit.edu/wp-content/uploads/2020/07/conf_TOW2019_operations_Ploetz.OW_.CryogenicsSystemsandReceiverMaintenance.pdf

[21] M. A. McCulloch, J. Grahn, S. J. Melhuish, P. Nilsson, L. Piccirillo, J. Schleeh, N. Wadefalk: Dependence of noise temperature on physical temperature for cryogenic low-noise amplifiers. *Journal of Astronomical Telescopes, Instruments, and Systems*, March 2017.

[22] S. Weinreb, H. Mani: Low Cost 1.2 to 116 GHz Receiver System â a Benchmark for ngVLA. June 2017. Presentation at Soccoro.

[23] J. Jonas: Radio Telescopes and Radiometry. November 2019. Presentation given for course at Stellenbosch University.

[24] de Villiers, D.I.L. and Lehmensiek, R.: Rapid calculation of antenna noise temperature in offset Gregorian reflector systems. *IEEE Trans. Antennas Propag.*, vol. 63, no. 4, pp. 1564–1571, April 2015.

[25] C. A. Balanis: *Advanced Engineering Electromagnetics*. 3rd edn. Hoboken, New Jersey, USA: John Wiley & Sons, 2012.

Stellenbosch University https://scholar.sun.ac.za

[26] Rusch, W. and Sorensen, O.: The geometrical theory of diffraction for axially symmetric reflectors. *IEEE Transactions on Antennas and Propagation*, vol. 23, no. 3, pp. 414–419, May 1975. ISSN 1558-2221.

[27] Mizugutch, Y., Akagawa, M. and Yokoi, H.: Offset dual reflector antenna. In: *1976 Antennas and Propagation Society International Symposium*, vol. 14, pp. 2–5. 1976.

[28] Moreira, F. and Jr, A.: Generalized classical axially symmetric dual-reflector antennas. *Antennas and Propagation, IEEE Transactions on*, vol. 49, pp. 547 – 554, 05 2001.

[29] Granet, C.: Designing classical offset cassegrain or gregorian dual-reflector antennas from combinations of prescribed geometric parameters. *IEEE Antennas and Propagation Magazine*, vol. 44, no. 3, pp. 114–123, 2002.

[30] de Villiers, D.I.L.: Prediction of aperture efficiency ripple in clear aperture offset Gregorian antennas. *IEEE Trans. Antennas Propag.*, vol. 61, no. 5, pp. 2457–2465, 2013.

[31] Fahmi T. T. Mokhupuki: *Efficient Optimisation of Wideband Reflector Feed Antennas*. Ph.D. thesis, Stellenbosch University, 2021.

[32] Kildal, P. S.: *Foundations of Antenna Engineering: A Unified Approach for Line-of-Sight and Multipath*. Kildal Antenn AB, 2015.

[33] Xiang, D.P. and Botha, M.M.: Mlfmm-based, fast multiple-reflection physical optics for large-scale electromagnetic scattering analysis. *Journal of Computational Physics*, vol. 368, pp. 69–91, 2018. ISSN 0021-9991.
Available at: https://www.sciencedirect.com/science/article/pii/S0021999118302870

[34] William R. Dommisse: Extensions to the domain green's function method for antenna array analysis. 2021.

[35] C. A. Balanis: *Advanced Engineering Electromagnetics*. Wiley, 1989.

[36] Zhao, G., Zhou, Y., Li, W.Z. and Tong, M.S.: A generalized point-matching method for solving electromagnetic problems. In: *2021 International Conference on Electromagnetics in Advanced Applications (ICEAA)*, pp. 065–067. Aug 2021.

[37] Synchrotron Emission.
Available at: https://astronomy.swin.edu.au/cosmos/s/synchrotron+emission

[38] de Villiers, D.I.L.: Prediction of aperture efficiency ripple in clear aperture offset gregorian antennas. *IEEE Transactions on Antennas and Propagation*, vol. 61, no. 5, pp. 2457–2465, May 2013. ISSN 1558-2221.

[39] TICRA, Copenhagen, Denmark. Ticra Tools, Version 20.1.
Available at: http://www.ticra.com

Stellenbosch University https://scholar.sun.ac.za

[40] Masters, G.F. and Gregson, S.F.: Coordinate system plotting for antenna measurements. In: *Antenna Measurement Techniques Association*. 2007. Available at: https://www.nsi-mi.com/library/technical-papers/2007-technical-papers?start=14

[41] McEwan, N. and Goldsmith, P.: Gaussian beam techniques for illuminating reflector antennas. *IEEE Transactions on Antennas and Propagation*, vol. 37, no. 3, pp. 297–304, March 1989. ISSN 1558-2221.

[42] de Villiers, D.I.L. and Lehmensiek, R.: Multi-level approximations for fast and accurate antenna noise temperature calculation of dual-reflector antennas. *IEEE Transactions on Antennas and Propagation*, pp. 1–1, 2022.

[43] Górski, K.M., Hivon, E., Banday, A.J., Wandelt, B.D., Hansen, F.K., Reinecke, M. and Bartelmann, M.: Healpix: A framework for high-resolution discretization and fast analysis of data distributed on the sphere. *The Astrophysical Journal*, vol. 622, no. 2, p. 759, apr 2005.
Available at: https://dx.doi.org/10.1086/427976

[44] Borries, O., Viskum, H.-H., Meincke, P., Jørgensen, E., Hansen, P.C. and Schmidt, C.H.: Analysis of electrically large antennas using fast physical optics. In: *2015 9th European Conference on Antennas and Propagation (EuCAP)*, pp. 1–5. April 2015. ISSN 2164-3342.

[45] Barnes, D.G., Briggs, F.H. and Calabretta, M.R.: Postcorrelation ripple removal and radio frequency interference rejection for parkes telescope survey data. *Radio Science*, vol. 40, 2005.

[46] Goldsmith, P.F. and Scoville, N.Z.: Reduction of baseline ripple in millimeter radio spectra by quasi-optical phase modulation. *Astronomy & Astrophysics*, vol. 82, pp. 337–339, 1980.

[47] Morris, D.: Chromatism in radio telescopes due to blocking and feed scattering. *Astronomy & Astrophysics*, vol. 67, pp. 221 – 228, 1978.

[48] Padman, R.: Reduction of the baseline ripple on spectra recorded with the parkes radio telescope. *Proceedings of the Astronomical Society of Australia*, vol. 3, pp. 111–113, 08 1977.

[49] Poulton, G.T.: *Minimisation of Spectrometer Ripple in Prime Focus Radiotelescopes*. 1974.

[50] Iupikov, O.A., Maaskant, R., Ivashina, M.V., Young, A. and Kildal, P.-S.: Fast and accurate analysis of reflector antennas with phased array feeds including multiple reflections between feed and reflector. *IEEE Transactions on Antennas and Propagation*, vol. 62, no. 7, pp. 3450–3462, July 2014. ISSN 1558-2221.

Stellenbosch University https://scholar.sun.ac.za

[51] Cerfonteyn, W.J., Mokhupuki, F.T.T. and de Villiers, D.I.L.: Frequency ripple in antenna noise temperature of small offset gregorian reflector systems. In: *2022 International Conference on Electromagnetics in Advanced Applications (ICEAA)*, pp. 207–211. Sep 2022.

[52] Dewdney, P.E., Hall, P.J., Schilizzi, R.T. and Lazio, T.J.L.W.: The square kilometre array. *Proc. IEEE*, vol. 97, no. 8, pp. 1482 – 1496, August 2009.

[53] Hallinan, G. *et al.*: The DSA-2000 — A Radio Survey Camera. In: *Bulletin of the American Astronomical Society*, vol. 51. Sep 2019.

[54] Selina, R.: The next-generation very large array: Reference design overview. In: *Proc. URSI Asia-Pacific Radio Science Conference (URSI AP-RASC)*. New Delhi, India, Mar 2019.

[55] T. L. Wilson, K. Rohlfs, S.H.: *Tools of Radio Astronomy*. 6th edn. Springer-Verlag Berlin Heidelberg, 2013.

[56] S. W. Ellingson: Sensitivity of antenna arrays for long-wavelength radio astronomy. *IEEE Transactions On Antennas And Propagation*, vol. 59, no. 6, June 2011.

[57] J. Flygare: Ultra-wideband feed design and characterization for next generation radio telescopes. 2018. Thesis for the degree of licentiate of engineering.

[58] J. W. M. Baars: *The Paraboloidal Reflector Antenna in Radio Astronomy and Communication*. 1st edn. Springer, New York, NY, 2007.

[59] Kildal, P.S.: Factorization of the feed efficiency of paraboloids and Cassegrain antennas. *IEEE Trans. Antennas Propag.*, vol. AP-33, no. 8, pp. 903–908, August 1985.

[60] Kildal, P.S. and Sipus, Z.: Classification of rotationally symmetric antennas as types bor /sub 0/ and bor /sub 1/. *IEEE Antennas and Propagation Magazine*, vol. 37, no. 6, pp. 114–, Dec 1995. ISSN 1558-4143.

[61] Ludwig, A.: The definition of cross polarization. *IEEE Transactions on Antennas and Propagation*, vol. 21, no. 1, pp. 116–119, January 1973. ISSN 1558-2221.

[62] P. Meincke: Reflector Antennas in Radio Astronomy. November 2019. Presentation given for course at Stellenbosch University.

[63] Akgiray, A.H.: *New technologies driving decade-bandwidth radio astronomy: Quad-Ridged Flared Horn Compound-Semiconductor LNAs*. Ph.D. thesis, California Institute of Technology, Pasadena, CA, USA, 2013.

[64] Rao, K.S. and Kildal, P.S.: A study of the diffraction and blockage effects on the efficiency of the cassegrain antenna. *Canadian Electrical Engineering Journal*, vol. 9, no. 1, pp. 10–15, Jan 1984. ISSN 0700-9216.

Stellenbosch University https://scholar.sun.ac.za

[65] Yang, J.: Calculation of aperture efficiency of reflector antenna with the measured far-field function of its feed in Ludwig's third definition. In: *15th European Conference on Antennas and Propagation (EuCAP)*, pp. 1–4. Dusseldorf, Germany, 2021.

[66] Ludwig, A.: The definition of cross polarization. *IEEE Trans. Antennas Propag.*, vol. 21, no. 1, pp. 116–119, 1973.

[67] de Villiers, D.I.L.: Offset dual-reflector antenna system efficiency predictions including subreflector diffraction. *IEEE Antennas and Wireless Propagation Letters*, vol. 10, pp. 947–950, 2011.

[68] Weinreb, S. and Shi, J.: Low noise amplifier with 7-k noise at 1.4 ghz and 25 ° c. *IEEE Transactions on Microwave Theory and Techniques*, vol. 69, no. 4, pp. 2345–2351, April 2021. ISSN 1557-9670.

[69] Briani, M., Cuyt, A., Lee, W.-s. and Knaepkens, F.: Vexpa: Validated exponential analysis through regular sub-sampling. *Signal Processing*, vol. 177, 09 2017.

[70] Roy, R. and Kailath, T.: Esprit-estimation of signal parameters via rotational invariance techniques. *IEEE Transactions on Acoustics, Speech, and Signal Processing*, vol. 37, no. 7, pp. 984–995, July 1989. ISSN 0096-3518.

[71] Huang, X. and Liao, B.: One-bit music. *IEEE Signal Processing Letters*, vol. 26, no. 7, pp. 961–965, July 2019. ISSN 1558-2361.

[72] Assiimwe, E., Mwangi, E. and Konditi, D.: A matrix pencil method for the efficient computation of direction of arrival estimation for weakly correlated signals using uniform linear array in a low snr regime. *International Journal of Engineering Research and Technology*, vol. 11, pp. 1347–1361, 01 2018.

[73] de Villiers, D.I.L. and Lehmensiek, R.: Efficient simulation of radiometric noise in offset gregorian antenna systems. In: *2013 7th European Conference on Antennas and Propagation (EuCAP)*, pp. 3357–3359. April 2013.